Multi-wavelenght Observations of INTEGRAL sources & the parameter space occupied by soft ?-ray emitting objects

Bodaghee, Arash

How to cite

BODAGHEE, Arash. Multi-wavelenght Observations of INTEGRAL sources & the parameter space occupied by soft ?-ray emitting objects. Doctoral Thesis, 2007. doi: 10.13097/archive-ouverte/unige:477

This publication URL: https://archive-ouverte.unige.ch/unige:477
Publication DOI: 10.13097/archive-ouverte/unige:477

UNIVERSITÉ DE GENÈVE
Département d'astronomie

FACULTÉ DES SCIENCES
Professeur T. J.-L. Courvoisier

Multi-wavelength Observations of INTEGRAL Sources & the Parameter Space Occupied by Soft γ-ray Emitting Objects

THÈSE

présentée à la Faculté des sciences de l'Université de Genève
pour obtenir le grade de Docteur ès sciences,
mention astronomie et astrophysique

par

Arash BODAGHEE

de

Téhéran, Iran, et Los Angeles, USA

Thèse N° 3849

GENÈVE
Atelier de reproduction de la Section de physique
2007

.

CETTE THÈSE A FAIT L'OBJET DES PUBLICATIONS SUIVANTES:
voir Appendice B.

for Isabelle

RÉSUMÉ EN FRANÇAIS

Cette thèse sur les résultats de la mission *INTEGRAL* (INTErnational Gamma-Ray Astrophysics Laboratory) de l'Agence Spatiale Européenne (ESA) a été produite au centre de données astronomiques ISDC (*INTEGRAL* Science Data Centre) attaché à l'Observatoire de Genève. Les sujets principaux qui sont traités dans cette thèse sont les analyses multi-longueurs d'ondes des nouvelles sources détectées par *INTEGRAL*, et une étude sur les paramètres spatiaux, spectraux et temporels des différentes classes de sources gamma vues au cours des 4 premières années de la mission (fevrier 2003 à mars 2007).

INTRODUCTION

La plupart des $\sim$ 500 sources détectées par *INTEGRAL* sont classifiées comme des noyaux actifs de galaxies (AGN) qui sont composés d'un trou noir supermassif au coeur d'une galaxie, ou des binaires X de petite et grande masse (respectivement, LMXB et HMXB). Les binaires X sont des systèmes où un objet compact (CO) tel qu'une étoile de neutrons (NS) ou un trou noir (BH) accrète de la matière perdue par un compagnon stellaire. Tous sont des puissants émetteurs de rayons X et gamma avec des luminosités qui peuvent atteindre 10^{36}–10^{38} ergs s^{-1} pour les LMXB et les HMXB, voire plus pour les AGN.

Les rayons X et gamma occupent presque la moitié du spectre électromagnétique. Pourtant, l'astronomie des hautes énergies, contrairement à l'astronomie optique et radio, n'a pu décoller qu'à partir de l'ère spatiale. En effet, l'atmosphère terrestre bloque la majorité des photons X/γ. Il faut rappeler que cet écran est bénéfique puisqu'il diminue la quantité de dommages génétiques soufferts par un organisme, ce qui a permis à la vie d'évoluer au niveau de complexité requis pour que des astronomes puissent se poser la question de savoir à quoi ressemble l'univers en rayons gamma.

Dans les années 1950 et 1960, les astronomes ne s'attendaient pas à trouver d'autre sources de rayonnement gamma que la terre (du aux armes atomiques) ou éventuellement la Lune. Pour chaque fréquence ν, le flux décroit comme $f_\nu \propto \nu^{-1}$. L'extrapolation des valeurs solaires amène à la conclusion qu'un signal lointain serait trop faible pour être détecté avec la technologie actuelle. Ce fut donc une surprise quand le LMXB Sco X-1 et le fond X diffus furent détectés lors d'observations de la Lune (Giacconi et al. 1962).

Depuis, les télescopes *Uhuru*, *Einstein*, *EXOSAT*, et plus récemment *CGRO*, *ASCA*, *Beppo-SAX* et *ROSAT* ont repéré $\sim$100,000 objets qui émettent au dessus de 0.1 eV. L'astronomie des hautes énergies est dans un Age d'Or avec plusieurs satellites

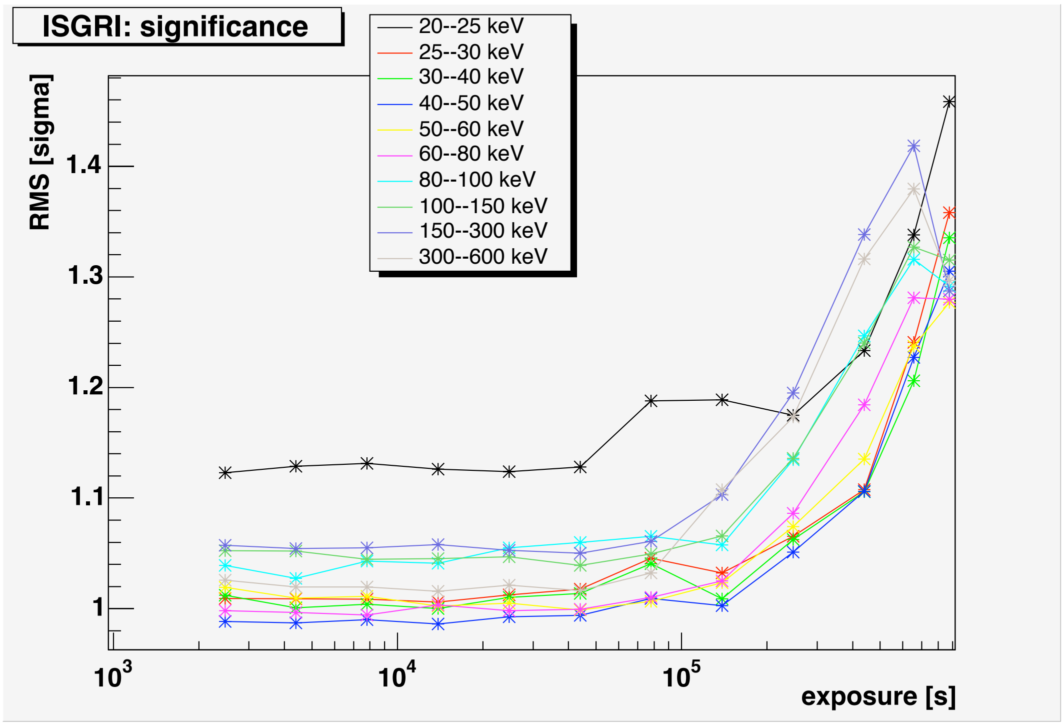

Figure *0.1: Significance (en σ) du bruit de fond en fonction du temps d'exposition pour les images mosaïques du plan galactique prises par ISGRI en différentes bandes d'énergie.*

opérant en même temps: *Chandra*, *INTEGRAL*, *RXTE*, *Swift*, *Suzaku* et *XMM-Newton*. Pour déterminer la nature d'une source gamma, les astrophysiciens doivent aussi prendre en compte les observations dans d'autres bandes d'énergie telles que l'optique, l'infrarouge et les ondes radio.

Plusieurs mécanismes peuvent créer des photons gamma, mais il s'agit essentiellement de rayonnement produit par une charge accélérée. En général, ceci implique de la matière (électrons) tombant dans un puits de potentiel gravitationnel (p.ex. un CO qui agglomère de la matière). Les électrons peuvent aussi être accélérés par un champ magnétique puissant (p.ex. rayonnement cyclotron/synchrotron), par le champ électrostatique d'ions (c-à-d Bremsstrahlung), ou par des photons énergétiques (diffusion de Compton). Les chocs violents entre nuages ou les régions de nucléosynthèse peuvent aussi produire des rayons gamma.

L'agglomération (ou l'accrétion) transforme l'énergie potentielle de la matière qui tombe en rayonnement électromagnétique. Dans certains cas, ce processus représente une manière beaucoup plus efficace pour convertir la matière en énergie que les réactions de nucléosynthèse. Pour le soleil, l'efficacité de la fusion d'hydrogène en hélium est de l'ordre de $\Delta E_{\text{nuc}} = 0.007 \cdot c^2 \sim 6 \cdot 10^{18}$ ergs g^{-1}. L'efficacité de l'accrétion s'écrit $\Delta E_{\text{acc}} = \frac{GM}{R} \sim \frac{M}{R}$, ce qui veut dire qu'elle dépend de la compacité $\frac{M}{R}$. Ceci est faible par rapport à la nucléosynthèse dans les étoiles de type solaire: $E_{\rm acc} \ll E_{\rm nuc}$. Donc les réactions nucléaires sont la source principale d'énergie dans les étoiles de type solaire. Par contre, dans les objets beaucoup plus denses tels que les étoiles de neutrons: $\Delta E_{\rm acc} = 10^{20}$ ergs g^{-1} $\sim 17 \times \Delta E_{\rm nuc}$.

Au delà d'une certaine limite, appelée la limite d'Eddington, la luminosité produite est si grande que la force de pression radiative empêche la matière de tomber sur le CO. A la luminosité d'Eddington, la force radiative poussant la matière vers l'extérieur de l'étoile, est égale à la force gravitationnelle dirigée vers l'intérieur:

$$\begin{aligned} L_{\rm Edd} &= \frac{4\pi G M m_{\rm p} c}{\sigma_{\rm T}} \\ &= 10^{38}\,(\frac{M}{M_\odot})\ {\rm ergs\ s^{-1}} \end{aligned}$$

Les binaires X ont 3 mécanismes d'accrétion principaux: l'accrétion par un disque autour du CO qui est fourni en matière via un point Lagrangien suite au remplissage de la lobe de Roche de l'étoile secondaire; le mécanisme Be; et l'accrétion par le vent stellaire. Le premier est très important pour les LMXB alors que l'agglomération dans les HMXB procède en général par le mécanisme Be où à travers les vents stellaires (équatoriaux lents et polaires rapides) qui sont parfois modérés par un disque. Dans quelques HMXB qui ont un compagnon super-massif (SG) de type spectral O ou B, le CO est enfoui dans le vent radial du compagnon alors l'accrétion est dominée par un vent stellaire quasi-isotrope.

Vu la grande masse du compagnon stellaire ($M \geq 10\ M_\odot$), les HMXB sont des systèmes jeunes ($\lesssim 10^7$ ans), donc ils se trouvent proches des régions de formation stellaire récentes, c-à-d le plan galactique et les bras spiraux. Leur spectre est dur ($kT \gtrsim 15$ keV) avec un continu en forme de loi de puissance avec une coupure à haute énergie. Ce genre de spectre est souvent interprété physiquement comme une Comptonisation thermique où des photons arrivant sur un plasma d'électrons sont diffusés à plus hautes énergies. Une densité de colonne importante, des raies de fer, ou un excès à basse énergie sont d'autres caractéristiques qui peuvent se présenter dans le spectre X d'un HMXB. L'émission est soit éphémère pour les HMXB avec compagnon Be, ou persistante pour les HMXB qui ont des compagnons OB. Le NS peut produire un champ magnétique très fort qui dirige l'accrétion vers les pôles magnétiques. Si les axes de rotation et de magnétisme ne sont pas alignés, un observateur peut voir une pulsation dans l'émission avec une période égale à la rotation du NS.

Par contre, les LMXB ont des compagnons de faible masse ($M \leq 1\ M_\odot$). Ces objets sont donc vieux ($\sim 10^{10}$ ans) et se trouvent principalement dans le bulbe galactique proche des amas globulaires. Le spectre est plus mou ($kT \lesssim 10$ keV) caractérisé par un continu fait d'un ou de plusieurs corps noirs. Une petite minorité de LMXB présente des pulsations, mais presque tous subissent des sursauts qui sont des explosions nucléaires pas loin du CO. Le disque d'accrétion domine le spectre optique, et pour ceux qui ont des NS comme CO, l'évolution de l'émission X suit des tracés précis dans les diagrammes de couleur–couleur reflétant les changements

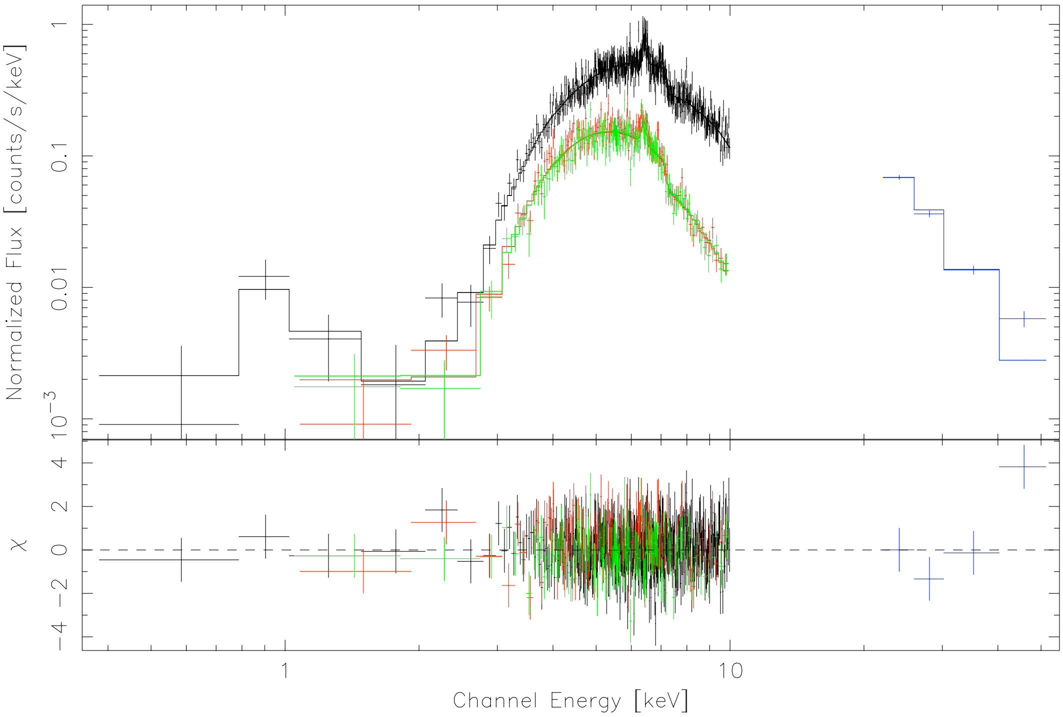

Figure *0.2: Spectre de IGR J16393−4643 provenant de PN (noir), MOS-1 (vert), MOS-2 (rouge), et ISGRI (bleu) avec application d'un modèle de Comptonisation thermique.*

dans le taux d'accrétion.

La Voie Lactée contient d'autres classes d'objets telles que les variables cataclysmiques (CV), les restes de supernova (SNR), les nuages moléculaires (MC), etc. qui sont regroupées et appelées *Miscellaneous* (pour divers). Au delà de notre galaxie et des Nuages de Magellan, les principales sources de rayons gamma sont les AGN, les amas de galaxies, et les sursauts gamma (GRB).

Pour détecter les sources, *INTEGRAL* se sert de 4 télescopes qui fonctionnent de façon simultanée, opérant sur plusieurs bandes d'énergie, et qui sont orientés dans la même direction. Ces instruments sont l'OMC (optique: Mas-Hesse et al. 2003), JEM-X (3–30 keV: Lund et al. 2003), IBIS (15 keV–10 MeV: Lebrun et al. 2003; Ubertini et al. 2003) et SPI (20 keV–8 MeV: Vedrenne et al. 2003). A part l'OMC qui est une caméra CCD avec un filtre optique, les autres télescopes d'*INTEGRAL* fonctionnent sur le principe du masque codé. Comme les rayons gamma sont trop énergétiques pour être déviés par une lentille ou par des miroirs, un masque avec une distribution connue de pixels ouverts ou fermés à la lumière est placé à une certaine distance d'un plan détecteur. Chaque source dans le champ de vue (FOV) projette alors l'ombre du masque sur le détecteur. Si l'on connait les positions des sources dans le FOV, on peut déduire une image du champ par déconvolution. Un des avantages du masque codé est que les sources et le bruit de fond sont mesurés en même temps évitant ainsi l'introduction d'un biais observationnel. Un autre

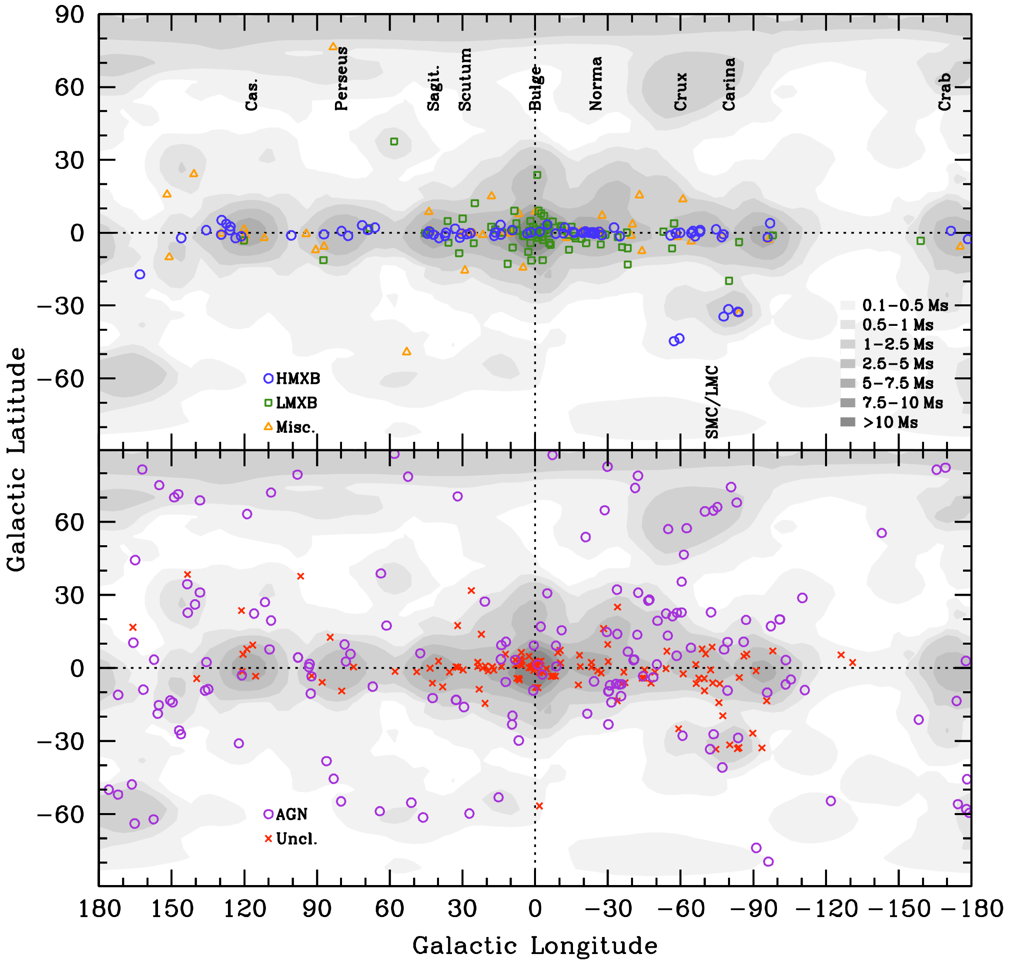

Figure *0.3: Distribution spatiale des sources détectées par ISGRI.*

avantage important est que la taille du FOV est nettement plus grande dans un télescope à masque codé que dans un télescope classique (quelques degrés au lieu de quelques minutes d'arc).

INTEGRAL orbite autour de la terre une fois tous les 3 jours et envoie ses données continuellement aux stations réceptrices de Belgique et de Californie, qui les transmet à l'ISDC. Ces données sont sauvegardées et analysées pour vérifier le fonctionnement des instruments et pour réagir aux évènements parfois transitoires, mais qui sont importants au niveau scientifique. La création de logiciels d'analyse scientifique (OSA) et l'archivage et la distribution des données d'*INTEGRAL* sont assurées par l'ISDC. Ainsi, l'ISDC sert de lien entre le satellite et la communauté scientifique.

MOSAÏQUES ET SURVEYS

La stratégie d'observation adoptée par *INTEGRAL* permet de créer des images mosaïques du ciel gamma à partir de plusieurs centaines ou quelques milliers d'images individuelles. Un an après le lancement d'*INTEGRAL*, chaque partie du plan galactique a été observée pendant au moins 50 ks. Dans ces premières images mosaïques profondes, nous avons détecté des dizaines de sources qui étaient déjà connues et presque autant de sources inconnues au dessus de 20 keV (Walter et al. 2004a). Pour certaines de ces sources, une observation avec *XMM-Newton* ou *RXTE* a été obtenu afin de suivre l'objet à basse énergie. Ces observations ont donné des résultats surprenants tels que des absorptions très élevées et des pulsations dont on parlera plus tard.

L'équipe du Survey d'ISGRI a produit des catalogues de source détectées après la première et deuxième année d'observation, respectivement Bird et al. (2004) et Bird et al. (2006). Ce dernier contient $\sim$ 210 sources avec des positions et des flux pour les bandes allant de 20 à 100 keV. Le flux limite d'une détection à 6σ se situe autour de 1 mCrab pour 1 Ms.

En augmentant le temps d'exposition, c-à-d en créant des images mosaïques de plus en plus profondes, on pourrait s'attendre à ce que la sensibilité augmente. Nos analyses ont montré que ceci n'était clairement pas le cas dans les premières années de la mission (Bodaghee et al. 2004). Même si les incertitudes statistiques diminuent avec le temps, l'accumulation des effets systématiques du aux déconvolutions de champs denses comme le centre galactique (GC) domine à partir de 1 Ms (Fig. 0.1). Ces résultats ont finalement servi à améliorer les logiciels qui génèrent les mosaïques.

ANALYSES DES SOURCES IGR

Les études décrites ci-dessus ont permis la découverte de nombreux nouveaux objets appelés sources IGR pour *INTEGRAL* Gamma-Ray. La première à être découvert fut IGR 16318−4848 (Courvoisier et al. 2003b). Une observation pointée avec *XMM-Newton* a montrée la présence d'une densité de colonne énorme ($N_{\mathrm{H}} \sim 10^{24}\,\mathrm{cm}^{-2}$) qui peut seulement provenir de matière obscurcissante située proche de la source puisque la valeur interstellaire attendue dans cette direction est presque 2 ordres de grandeur moins importante. En plus, le spectre présente deux raies de fer bien définies.

Par la suite, d'autres sources IGR ont étés vues avec *XMM-Newton*, *Chandra*, etc. Parmi celles-ci, j'ai étudié IGR J16393−4643 en détail, et j'ai contribué aux analyses de IGR J16320−4751, IGR J17252−3616 et IGR J17497−2821.

IGR J16393−4643 est aussi connue sous le nom d'AX J163904−4642 puisqu'elle a été découverte à plus basse énergie par *ASCA* (Sugizaki et al. 2001). Sa pente de

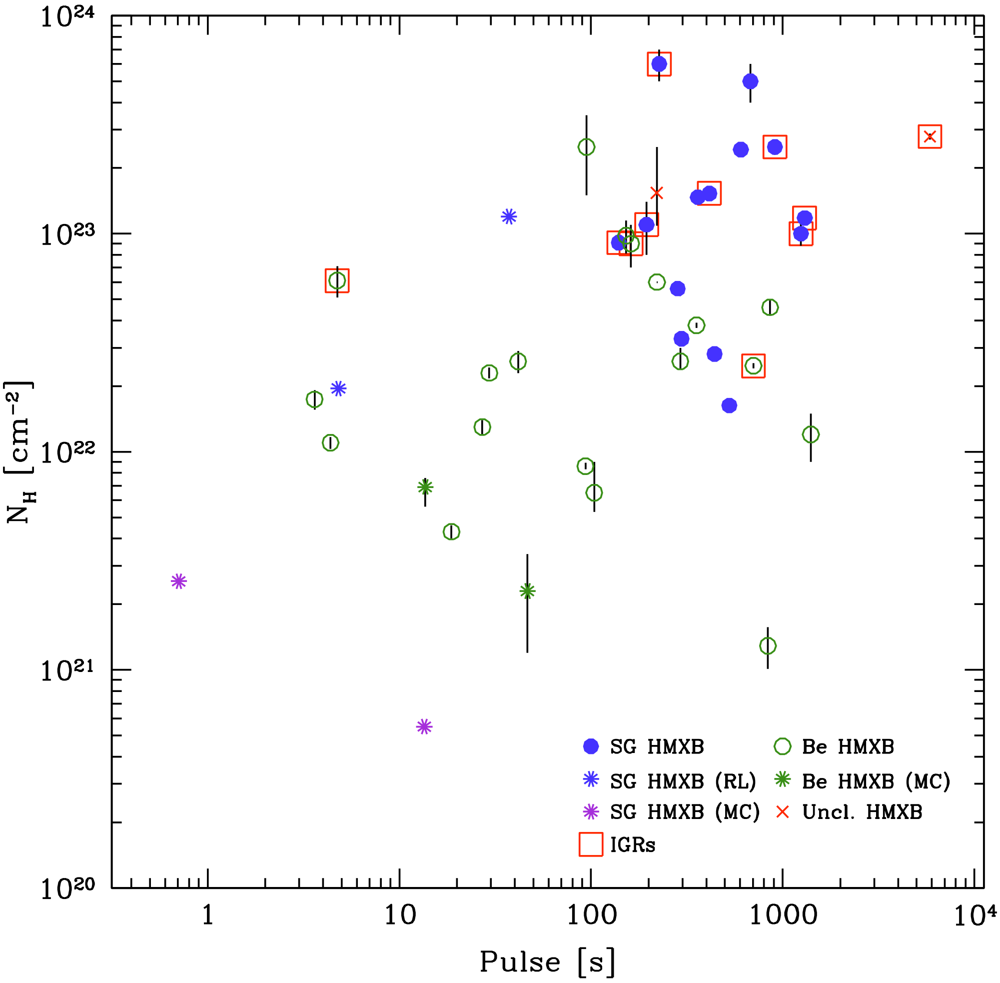

Figure *0.4: Période de pulsation en fonction du N_H pour les HMXB qui ont des compagnons OB (16, cercles bleus remplis), des compagnons Be (19, cercles verts vides), ou avec des compagnons non-classifiés (2, croix rouges). Les sources IGR sont encadrées et les sources appartenant aux nuages de Magellan sont indiquées. Deux HMXB OB (Cen X-3 et OAO 1657−415) qui sont des systémes avec agglomération par le remplissage du lobe de Roche (RL) sont symbolisés par des étoiles bleues.*

loi de puissance nulle ($\Gamma = -0.01$), son absorption élevée ($N_H = 13^{+9}_{-7} \cdot 10^{22}$ cm^{-2}), l'absence d'émission radio, et sa position très proche du plan galactique ($b = 0.07°$) conduisent Sugizaki et al. (2001) de classifier la source comme un HMXB.

Le 21 avril 2003, nous avons détecté IGR J16393−4643 avec un flux moyen de 0.85 coups par seconde (cps) dans une image mosaïque de la bande 15–40 keV des révolutions 50–59. L'annonce de Malizia et al. (2004) note aussi la comptabilité de la position avec la source non-identifiée 3EG J1639−4702 (Hartman et al. 1999).

Combi et al. (2004) trouve en plus de l'émission radio/IR qui suggère une combinaison jet/disque que l'on trouve dans les micro-quasars, et qui pourrait solidifier l'association avec la source *EGRET*.

Les données *INTEGRAL* regroupent les 244 premières révolutions (~ 2 ans, ou ~ 1500 pointages). Ces données provenant d'ISGRI ont été analysées avec OSA 4.2–5.0 à partir de la version 20 du catalogue de référence général de l'ISDC (GRC: voire plus loin) qui a été modifié pour n'inclure que les sources détectées précédemment par ISGRI (c-à-d `ISGRI_FLAG==1`). Afin de mieux connaître la nature d'IGR J16393−4643, nous avons obtenu une observation de 8.5 ks le 21 mars 2004 avec *XMM-Newton*.

L'image mosaïque d'ISGRI a fourni une position R.A. (J2000) = $16^{h}39^{m}05^{s}$ et Dec. = $-46°42'16''$ avec une incertitude de $26''$. Cette position est compatible avec (et améliore) les positions données par Sugizaki et al. (2001) et Bird et al. (2004). En plus, la source est bien détectée par *XMM-Newton* et la position de R.A. = $16^{h}39^{m}05.41^{s}$ et Dec. = $-46°42'11.9''$ a une incertitude de seulement $4''$. Ceci est la meilleure position connue pour cette source et elle permet d'exclure les contreparties proposées par Combi et al. (2004), c-à-d l'intersection des boîtes d'erreurs de la source infrarouge IRAS 16353−4636 et la source radio MOST J1639.0−4642. La seule contrepartie qui est désormais possible est 2MASS J16390535−4642137.

IGR J16393−4643 est une source persistante dans la bande 20–40 keV avec une forte variabilité, mais elle n'est pas détectée dans la bande plus élevée (60–100 keV). Une pulsation qui dure 912.0 ± 0.1s est mise en évidence dans les courbes de lumière provenant de PN et d'ISGRI. Cette pulsation correspond à la rotation de l'étoile de neutrons et rejette formellement l'hypothèse du trou noir dans un micro-quasar. La longueur de la période indique un NS qui est accompagné d'une étoile super-géante de type OB.

Le spectre de la source (Fig. 0.2) suggère également la présence d'un pulsar évoluant dans un système HMXB et qui agglomère le vent d'un compagnon stellaire OB. La densité de colonne ($N_{\rm H} = (25 \pm 2) \cdot 10^{22}\,{\rm cm}^{-2}$) est beaucoup plus élevé que l'absorption galactique attendue dans cette direction. Ceci indique, avec la présence de raies de fer à 6.4 et 7.1 keV, que le CO est enfoui dans une coquille de matière froide et neutre. Cette matière absorbe l'essentiel de l'émission X, et ne laisse passer que les photons plus énergétiques que ~ 5 keV. Un excès de flux à basse énergie est aussi observé.

Ces résultats permettent de classifier IGR J16393−4643 comme un HMXB composé d'un NS et d'une étoile supergéante OB (Bodaghee et al. 2006). Ces objets étaient en minorité comparé aux HMXB avec des compagnons Be. Grâce à la capacité d'*INTEGRAL* de voir ces sources absorbées, une nouvelle population de pulsars enfouis a été mis en évidence.

Une analyse similaire sur les sources IGR J16320−4751 (Rodriguez et al. 2006), IGR J17252−3616 (Zurita Heras et al. 2006) et IGR J17497−2821 (Rodriguez et al. 2007) a démontré que les 2 premières sources sont des pulsars HMXB avec des compagnons OB, et que la dernière est un trou noir en LMXB.

UNE VISION SYNTHÉTIQUE DES SOURCES IGR

Avec ces nouveaux membres de la classe des pulsars absorbés accrétant par le vent, nous avons construit un catalogue de leurs paramètres spatiaux, spectraux et temporels. Ceci nous permettra d'étudier l'espace des paramètres occupé par ces sources. Parmi les outils mis à notre disposition, il y a le catalogue de référence général de l'ISDC (GRC: Ebisawa et al. 2003), et la page web des sources IGR. Ces bases de données ont été créées à partir de données publiées dans les articles, ou les annonces telles que les ATels. Le GRC contient toutes les sources détectables par *INTEGRAL* ($\sim$ 1600), et la page IGR sur le web est un sous-ensemble de ce catalogue qui collectionne les paramètres et références des quelques 200 sources IGR.

Pour chacune des 500 sources détectées par ISGRI, les paramètres tels que les positions, et si possible, la classification, la densité de colonne ($N_{\rm H}$) d'un spectre X, l'orbite, la pulsation et la distance ont été trouvés dans la littérature et répertoriés dans un indexe de paramètres. Les buts principaux sont de regrouper dans un même endroit ce que l'on connait sur les sources gamma détectées par ISGRI, d'examiner l'espace de paramètres des différentes classes d'objets émetteurs de rayons γ, d'utiliser ces paramètres dans les modèles galactiques ou de pulsation, et peut-être de découvrir des nouvelles relations entre les paramètres.

En opérant au dessus de 20 keV, ISGRI n'est pas affecté par l'absorption, ce qui a permis la découverte de nouveaux HMXB et AGN avec des fortes densités de colonnes ($N_{\rm H} \sim 10^{22}$–$10^{24}\,{\rm cm}^{-2}$). En moyenne, les nouvelles sources galactiques détectées par ISGRI sont 4 fois plus absorbées que les sources galactiques connues avant ISGRI. La moyenne des pulsations pour les sources IGR se situe entre 100 et 1000 s ce qui est plus long que les rotations des pulsars connus avant ISGRI. L'absorption et les longues périodes de pulsations sont des preuves qu'*INTEGRAL* a trouvé beaucoup de nouveaux membres de la classe des HMXB avec compagnons OB.

Grâce au plus grand échantillon à notre disposition, nous avons pu tester la dépendance entre le $N_{\rm H}$, c-à-d la matière proche de la source X, et les périodes de pulsation ou orbitale. Il y a des tendances possibles dans les diagrammes $P_{\rm S}$–$N_{\rm H}$ et $P_{\rm O}$–$N_{\rm H}$ (Figs. 0.4–0.5). De plus, les populations de HMXB OB et Be se séparent en des régions distinctes des diagrammes permettant ainsi de proposer une contrepartie OB ou Be à un HMXB qui est non-classifié (p.ex. IGR J16358−4726 et IGR J19140+0951 sont probablement des HMXB OB vu leurs positions dans les diagrammes.

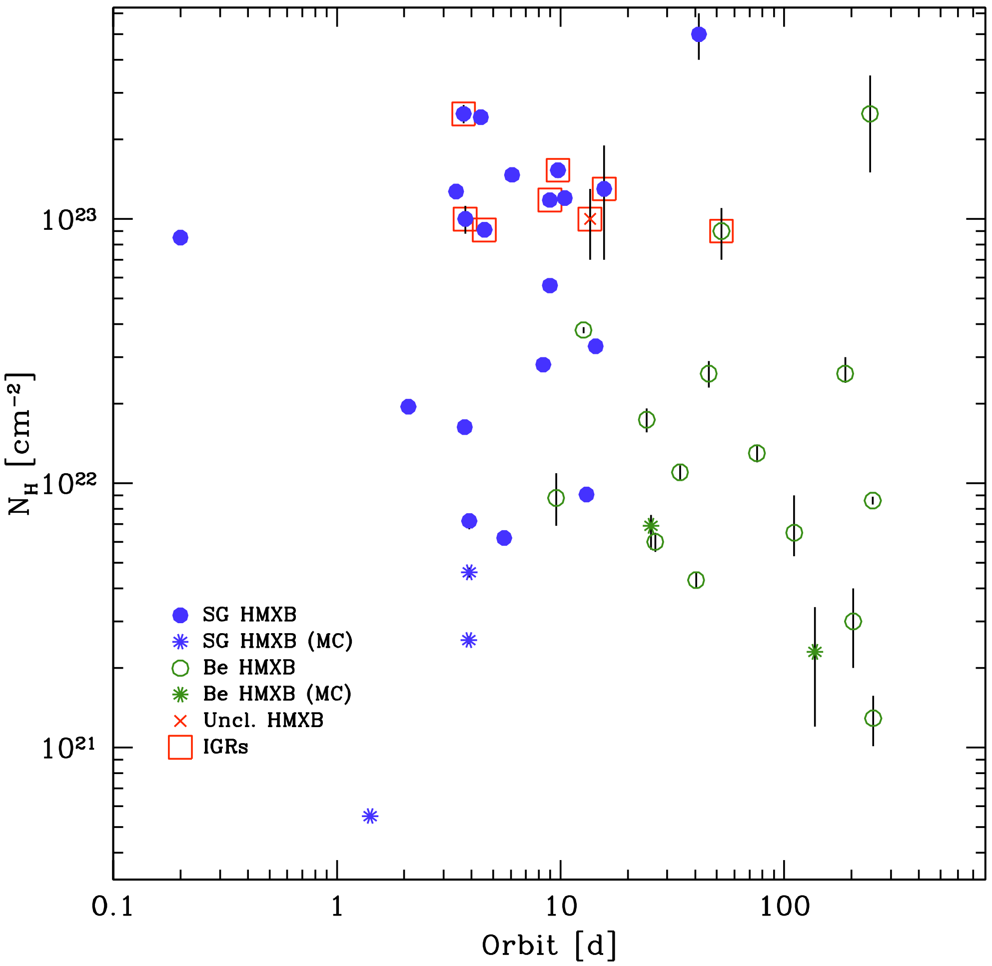

Figure *0.5: Période orbitale en fonction du N_H pour les HMXB qui ont des compagnons OB (20, cercles bleus remplis), des compagnons Be (15, cercles verts vides), ou avec des compagnons non-classifiés (1, croix rouge). Les sources IGR sont encadrées et les sources appartenant aux nuages de Magellan sont indiquées.*

Des signatures d'évolution stellaire ressortent des distributions spatiales des sources. Les HMXB se trouvent proche du plan galactique avec des pics de densité qui correspondent à peu près aux tangentes des bras spiraux. Alors que l'on trouve le même léger décalage entre les pics de distribution des HMXB et les tangentes qu'ont trouvé Lutovinov et al. (2005a) et Dean et al. (2005), la rotation galactique ne semble pas améliorer l'alignement entre les HMXB et les tangentes. Par contre, la distribution des HMXB est compatible avec la distribution des complexes les plus actifs en formation d'étoiles OB de Russeil (2003). Ce sont ce genre d'étoiles qui donneront naissance à des HMXB.

Les LMXB suivent une distribution similaire aux amas globulaires, c-à-d proche du bulbe et à haute latitudes. Une association avec la barre de la galaxie est possible. Bien que seulement 6 LMXB aient été découverte par *INTEGRAL*, il existe une centaine de sources non-identifiées. La distribution spatiale de ces dernières, et la transience de leur émission, rappelle une population de sources galactiques composée essentiellement de LMXB. Les raisons pour lesquelles elles ne sont pas identifiées comme telles sont: les LMXB ont une émission souvent transitoire qui complique les observations ultérieures; les contreparties sont très faibles quand le système n'est pas en sursaut X; et ces contreparties ne sont pas facilement identifiables dans les champs denses et poussiéreux du centre galactique.

Ce travail est présenté sous Bodaghee et al. (2007) publié dans A&A.

Table of contents

Part I

Introduction

Chapter 1
Introduction

This thesis is the product of work performed at the *INTEGRAL* Science Data Centre (ISDC) of the University of Geneva Observatory between February, 2003, and March, 2007. The aim of this thesis is to describe the types of high-energy sources that have been detected by *INTEGRAL* in its first 4 years of observations. *INTEGRAL* is an X-ray and γ-ray space telescope that provides high-resolution imaging, spectral, and timing data for energies typically above 20 keV.

Most of the $\sim$ 500 sources that *INTEGRAL* has detected have been classified as either active galactic nuclei (AGN), which are supermassive black holes at the heart of other galaxies, or Galactic low and high-mass X-ray binaries (LMXB and HMXB, respectively), which are systems composed of a compact object (CO) such as a neutron star (NS), a black hole (BH), or in some cases a white dwarf (WD), that accretes from a companion star. All of these objects are powerful X-ray emitters with luminosities reaching 10^{38} ergs s^{-1} for X-ray binaries, and even higher for AGN. Their emission is generally characterized by short and long-term variability, and their spectra sometimes present absorption and line features.

The 4 years that were dedicated to this thesis correspond roughly to the first 4 years of *INTEGRAL* observations. Most of the initial year was spent generating and scrutinizing the first mosaic images of the Galactic Plane as seen by ISGRI, the soft γ-ray imager aboard *INTEGRAL*. In these images, we were able to detect dozens of new sources, some of which we later observed in the soft X-rays with other telescopes. These multi-wavelength analyses of IGRs yielded surprising results such as large intrinsic column densities and long pulsation periods.

In the last 2 years, the scope of research broadened to include all sources detected by ISGRI. We constructed a catalog listing the most accurate positions known for each source, and, when available, the source's classification, photoelectric absorption value, distance or redshift, and pulsation and orbital periods. This information was updated as soon as new results were available in the literature. The fruit of this effort, besides its importance for *INTEGRAL* data analysis, is the publication of the most extensive catalog of *INTEGRAL* source parameters to date. Parameters in this catalog were used to define new tools enabling most HMXBs to be distinguished in plots of intrinsic absorption versus spin and orbital periods. They also served to highlight the signatures of evolution in Galactic X-ray binaries.

After a brief introduction to high-energy astrophysics, the various classes of X/γ-ray emitters are reviewed, and the *INTEGRAL* mission is outlined. Part II describes the IBIS Survey campaigns and the source catalogs that were produced. Results from multi-wavelength observations of individual sources, specifically, IGR J16393−4643, IGR J16320−4751, IGR J17252−3616, and IGR J17497−2821, are presented in Part III. In Part IV, we expand our field of view in order to examine the global properties of *INTEGRAL* sources. Finally, Part V discusses other scientific contributions that I have provided during my time at the ISDC. The conclusion summarizes the main points of each chapter.

1.1 Accretion & Emission

X-rays and γ-rays occupy nearly half of the total electromagnetic spectrum ($\lambda \lesssim 100$ Å). However, the Earth's atmosphere effectively blocks most high-energy photons from space from reaching the surface. Depending on the wavelength, half of the radiation is absorbed ~20–120 km above the surface. Because of this, high-energy astronomy flourished only after the space age made it possible for telescopes to be placed in orbit. Of course, by blocking energetic X/γ-rays, the atmosphere helps diminish the amount of genetic damage suffered by organisms, thereby enabling life to develop to such an advanced level of complexity as to enable astronomy in the first place.

Astronomers in the 1950s and '60s did not expect to detect high-energy sources. Theoretically, the energy flux of a source in the γ-rays follows $f_\nu \propto \nu^{-1}$ which leads to a photon flux that is $\propto \nu^{-2}$. Extrapolation of Solar values to nearby stars led to the realization that there would not be enough of a signal given the state of technology. It was a surprise, therefore, when a series of X-ray observations of the Moon aboard rocket flights revealed Sco X-1 and the bright X-ray background (Giacconi et al. 1962).

Since then, space telescopes like *Uhuru*, *Einstein*, *EXOSAT*, and more recently *CGRO*, *ASCA*, *Beppo-SAX*, and *ROSAT*, have found ~100,000 objects that emit above 0.1 eV. High-energy astrophysics is currently in its Golden Age with several X/γ-ray missions operating simultaneously: *Chandra*, *INTEGRAL*, *RXTE*, *Swift*, *Suzaku*, and *XMM-Newton*. Astrophysicists studying high-energy sources routinely complement X/γ-ray data with observations taken from lower energies such as the radio, infrared and optical bands. Indeed, a broad spectral analysis offers the most reliable way to identify the nature of a high-energy source.

There are many different types of objects that emit in the X/γ-ray domain. In most cases, their high-energy emission stems from an accelerated charge. Usually, this involves matter falling into a deep gravitational field, as in the case of an accreting CO. Electrons can also be accelerated by strong magnetic fields (e.g. cyclotron/synchrotron emission), the electrostatic fields of ions (i.e. Bremsstrahlung), or by energetic photons (Compton scattering). Violent shocks between clouds, and nucleosynthesis regions can also produce high-energy photons.

Accretion transforms the stored gravitational potential energy of infalling material into electromagnetic radiation. One possibility is for the surface of the accretor to radiate the accretion luminosity as a thermal blackbody with a characteristic temperature:

$$T_\mathrm{b} = \frac{L}{4\pi R^2 \sigma} \tag{1.1}$$

Or, the gravitational energy of an accreted electron-proton pair is converted into heat of a given shock temperature:

$$3kT_\mathrm{s} = \frac{GM(m_\mathrm{p} + m_\mathrm{e})}{R} \tag{1.2}$$

Here, $m_\mathrm{p} \gg m_\mathrm{e}$ represent proton and electron masses.

For a neutron star (NS: $M \sim M_\odot$, $R \sim 10\,\mathrm{km}$) accreting at the Eddington limit ($L = 10^{38}$ ergs s^{-1}, see below), the typical photon energies ($h\nu$) are:

$$1\mathrm{keV} \sim 10^7\mathrm{K} \sim kT_\mathrm{b} \lesssim h\nu \lesssim kT_\mathrm{s} \sim 5 \cdot 10^{11}\mathrm{K} \sim 50\mathrm{MeV} \tag{1.3}$$

Hence, accretion onto a CO generates X/γ-ray emission. In certain cases, this mechanism can be a much more efficient source of energy than nucleosynthesis reactions. To demonstrate, consider the nuclear (H, He) fusion efficiency of the Sun:

$$\Delta E_\mathrm{nuc} = 0.007 \cdot c^2 \sim 6 \cdot 10^{18}\,\mathrm{ergs\,g^{-1}} \tag{1.4}$$

The accretion efficiency can be written:

$$\Delta E_\mathrm{acc} = \frac{GM}{R} \sim \frac{M}{R} \tag{1.5}$$

In other words, the accretion yield increases with the compactness $\frac{M}{R}$. For Solar values, $E_\mathrm{acc} \ll E_\mathrm{nuc}$ which means that nuclear reactions are the primary source of energy in a star such as the Sun. For a neutron star, however, the accretion efficiency is:

$$\Delta E_\mathrm{acc} = 10^{20}\,\mathrm{ergs\,g^{-1}} \sim 17 \times \Delta E_\mathrm{nuc} \tag{1.6}$$

Thus, under certain conditions, accretion is the most efficient way of converting mass into energy. Compactness determines the conversion efficiency. For a black hole, the typical accretion yields are roughly 10% of the rest mass which makes them very luminous:

$$L_{\mathrm{acc}} = \frac{GM}{R}\dot{M} \quad (\sim 10^{46}\,\mathrm{ergs\,s^{-1}} \text{ for quasars with } \dot{M} = \frac{1M_{\odot}}{\mathrm{yr}}) \tag{1.7}$$

A higher accretion rate leads to an increase in luminosity. At a certain point, though, the luminosity can be so strong that instead of falling towards the CO, matter is blown away. The Eddington luminosity (L_{Edd}) is the limit at which the outward force of radiative pressure (F_{rad}) exactly counters the inward gravitational pull of matter (F_{g}):

$$F_{\mathrm{rad}} = \frac{L_{\mathrm{acc}}\sigma_{\mathrm{T}}}{4\pi R^2 c} \tag{1.8}$$

$$F_{\mathrm{g}} = \frac{GM(m_{\mathrm{p}} + m_{\mathrm{e}})}{R^2} \tag{1.9}$$

$$\Rightarrow L_{\mathrm{Edd}} = \frac{4\pi GMm_{\mathrm{p}}c}{\sigma_{\mathrm{T}}} = 10^{38}\,(\frac{M}{M_{\odot}})\,\mathrm{ergs\,s^{-1}} \tag{1.10}$$

where σ_{T} is the Thomson cross section.

The mechanism by which accretion proceeds depends on the type of system. The main accretion scenarios for Galactic objects are: disk accretion via Roche-lobe overflow; the Be mechanism; and wind-driven accretion.

A star that has grown to fill its Roche lobe (defined as the innermost volume encompassing the gravitational potentials of the stars in a binary system) will transfer matter to its companion's potential well via the first Lagrangian point. Since the star rotates, the transferred material carries angular momentum. Thus, matter settles into a disk around the CO, losing angular momentum as it spirals onto the CO.

Stars of spectral class B that rotate rapidly can develop a torus-like region of material which produces emission lines. X-rays are generated whenever this Be star and its torus approach the CO during the periastron of a wide and eccentric orbit. As with Roch-lobe overflow, matter is accreted via a disk that forms around the CO. Once this passage is complete, the accretion rate diminishes and the luminosity drops. The X-ray emission is therefore sporadic (or transient).

Supergiant O or B stars can shed significant quantities of material due to radiation-driven wind (up to $10^{-4}\ M_{\odot}\,\mathrm{yr}^{-1}$). Compact objects in these systems have short orbital periods, with negligible angular momentum gained from the wind. Even though this process is less efficient than the other mechanisms, the accretion rate is still large enough (and consistent enough) to radiate near the Eddington limit persistently.

The velocity with which acceting matter arrives on the NS, and the direction of its angular momentum vector, will affect the spin of the NS. The Alfvén radius defines the region where the magnetic and ram pressures are equal:

$$R_{\mathrm{A}} = 2.9 \cdot 10^{8} M_{\mathrm{X}}^{1/7} R_{6}^{-2/7} L_{37}^{-2/7} \mu_{30}^{4/7} \text{ cm} \tag{1.11}$$

The X-ray source has a mass M_{X} ($M_{\odot}$) and luminosity L_{37} (10^{37} ergs s^{-1}), with a NS radius R_6 (10^6 cm) and dipolar magnetic moment of μ_{30} (10^{30} G cm^3).

The corotation radius is defined as the boundary at which the magnetic field regulates the motion of matter:

$$R_{\mathrm{c}} = 1.5 \cdot 10^{8} P_{S}^{2/3} M_{\mathrm{X}}^{1/3} \text{ cm} \tag{1.12}$$

Material arriving with a Keplerian velocity that is less than the velocity at the corotation radius will be spun away, taking angular momentum with it, and the NS spin (P_S in seconds) will slow down due to the "propellor mechanism" (Illarionov & Sunyaev 1975). For Keplerian velocities greater than the corotation velocity, material can accrete onto the NS magnetosphere which will either spin up or spin down the NS depending on whether the angular momentum of the accreted material has the same or an opposite direction as the NS spin (Waters & van Kerkwijk 1989). In other words, accretion will occur onto a NS if $R_{\mathrm{A}} < R_{\mathrm{c}}$.

1.2 High-Energy Objects

1.2.1 Galactic Sources

As discussed above, X-ray emitters in the Milky Way generally involve a CO consuming its companion star. Such objects are called X-ray binaries (XRBs). The CO is usually a NS, but a BH or WD are possible. The subclassification of an XRB is based on the mass (i.e. spectral type) of the companion star, but the geometry of the system (i.e. the way matter is distributed around the CO), or a strong magnetic field emanating from the NS, can influence the emission properties, and hence its subcbelassification.

When a CO is paired with a star that has $M \leq 1\, M_{\odot}$, the system is called a low mass X-ray binary (LMXB). Because of the small mass of the companion star, these systems are generally old ($\sim 10^{10}$ yr) and so are found predominantly in the Galactic Bulge. Formation of a LMXB requires an asymmetry in the initial masses of the stars in the binary system. One of the stars must begin with $M \geq 10\, M_{\odot}$ (or more) in order to form a NS or BH. Since it evolves faster, the core of the massive star collapses to a CO, releasing a prodigious amount of energy that expels the outer layers of the massive star. If the companion survives this explosion, the newly-formed CO then accretes from a disk of matter that is replenished by the companion's Roche-lobe overflow.

The photon spectrum can be fit with single or multiple blackbodies for the soft disk contribution, and a thermal Comptonization model for the hard portion of the spectrum. Their X-ray emission is usually soft ($kT \lesssim 10\,\mathrm{keV}$) and is punctuated by flares which are thermonuclear explosions from material bunched near the surface of the NS. The thick accretion disk dominates the optical spectrum. For LMXBs with a NS, the evolution of the X-ray spectrum in a color-color diagram can follow precise tracks (described as Z or Atoll shaped) that reveal changes in the mass accretion rate.

If the CO has a companion of $M \geq 10\,M_{\odot}$, the system is called a high-mass X-ray binary (HMXB). Given the mass of the companion, HMXBs are young systems ($\lesssim 10^7$ yr) and so are located close to regions of recent star formation, i.e. close to the Galactic Plane with peaks at the spiral arm tangents. Their spectra are relatively harder than for LMXBs ($kT \gtrsim 15\,\mathrm{keV}$). The continuum is usually described by thermal Comptonization whereby injected photons are scattered to higher energies by an electron plasma. Spectral features such as a soft excess emission, absorption, iron lines, and an exponential cutoff energy can also be seen depending on the type of HMXB.

Before a HMXB is created, both stars begin with $M \geq 12\,M_{\odot}$. The more massive star of the pair quits the MS and fills its Roche lobe. Material is transferred to the companion which grows in mass. The evolved core of the shedding star will form a CO, and the ensuing supernova will eject large quantities of material away from the system if not onto the companion. Mass transferred in this way carries angular momentum which could be the initial kick that spins the companion into forming a decretion torus.

In HMXBs where the companion is a Be star, matter is lost through a combination of slow, dense equatorial outflows, and fast, thin polar winds. These systems represent the majority of known HMXBs, and their X/γ-ray emission is generally transient. Outbursts in these systems are due primarily to the CO accreting material whenever it approaches the Be star in its sometimes wide and eccentric orbit.

More and more HMXBs are being found whose companions are evolved O or B-type supergiant (SG) stars. Because the orbit of the CO places it within the radial wind of the SG, matter is accreted nearly continuously leading to persistent X/γ-ray emission. This also means that the high-energy emitting source is nestled within a cocoon of material so the soft X-ray spectrum is heavily absorbed. As we will see later, this is the main reason why many of these sources went unnoticed before *INTEGRAL.*

Strong magnetic fields ($B \sim 10^{12}$–10^{14} G) emanating from inside certain neutron stars can funnel accreted material to the magnetic poles. The emission will be pulsed if the magnetic and rotation axes are misaligned. The pulse profile is single-peaked if one cap is visible along the line of sight, or double-peaked when both caps can be seen during a rotation. Magnetic fields such as these are found mainly in the neutron stars of HMXBs. Given the type of precursor star that underwent a supernova that gave rise to the NS, and given the advanced age of the system, there are only a handful of LMXBs that have neutron stars with magnetic fields that are strong enough to produce pulsations (generally, they have $B \lesssim 10^{11}$ G). If the corotation and magnetospheric radii are roughly equal (the so-called "equilibrium rotator" regime), the X-ray luminosity that results from accretion is proportional to $(\frac{B}{10^{11}\,\mathrm{G}})^2 P_S^{-7/3}$ (Ghosh & Lamb 1979). So for LMXBs radiating at $\sim 10^{36}$ ergs s^{-1}, pulsations on the order of a few seconds or less are expected. Pulsation periods tend to last a few 10–100 s for HMXBs, while the neutron stars in a few LMXBs (e.g. millisecond pulsars) spin at much higher frequencies.

Besides XRBs, the Milky Way hosts other types of X/γ-ray sources such as cataclysmic variables (CVs), molecular clouds (MCs), supernova remnants (SNRs), radio pulsars (RPs), pulsar wind nebulae (PWN), anomalous X-ray pulsars (AXPs), soft-gamma repeaters (SGRs), and others. In many of these sources, additional processes (other than accretion onto a CO) are invoked to explain a portion of the high-energy emission: i.e. shocks between clouds, an isolated but rapidly-rotating NS, etc. In later chapters (i.e. Part IV), these sources are categorized as "Miscellaneous."

1.2.2 Extragalactic Sources

Beyond the Milky Way and the Magellanic Clouds, the principal sources of X/γ-rays are AGN (e.g. quasars or QSOs) and γ-ray bursts (GRBs). These sources are among the most luminous objects in the Universe. Clusters of galaxies can emit at high energies through Bremsstrahlung.

An AGN is a galaxy whose core is a suppermassive BH ($M \sim 10^8\,M_\odot$). Stars, gas, and dust are consumed by the BH after being spun and heated in a disk. The size of the disk, which is sometimes visible in the IR/optical/UV/X-rays, can be so important that its magnetic field triggers an outflow of disk material. Instead of being accreted, some of the matter in the inner disk can also be ejected through the jets. In the radio, these jets are seen to extend to lobes located several Mpc away from the galaxy. The CO and its disk are embedded in a giant torus of molecular gas.

The standard model classifies the different types of AGN based on the orientation of the system with respect to the observer. If the jet is active (i.e. radio loud), then the 4 classes of AGN are: blazars, where the jet and line of sight are aligned; radio-loud QSOs and broad-line radio galaxies, where the jet is slightly misaligned, the accretion disk is visible, and broad emission lines are observed; and narrow-line radio galaxies, where the line of sight is nearly perpendicular to the disk which is hidden by the molecular torus. In the absence of jets (i.e. radio quiet), there are 3 classes of AGN: radio-quiet QSOs, where the system is viewed face-on so that the accretion disk is visible; Seyfert I galaxies, where the viewing angle is slightly offset with respect to the normal vector, but the disk and broad emission lines are still visible; and Seyfert II, where the AGN is viewed nearly edge-on, so its spectrum is more absorbed with narrow emission lines only.

A GRB is a tremendous release of energy from a random direction that, for a short time (~0.1–20 s) can be as luminous as all other objects in the Universe combined. These sources are believed to be merging BHs where the high-energy emission stems from shocks between its ejected shells. Being unique and ephemeral events, they are clearly different from the other classes of sources discussed thus far. Hence, they are not considered in this research.

Chapter 2

The *INTEGRAL* Mission

INTEGRAL stands for the INTErnational Gamma-Ray Astrophysics Laboratory Winkler et al. (2003), which is an X and γ-ray space telescope of the European Space Agency's (ESA) "Horizon 2000" program. A successful lift-off from the Baikonur spaceport in Kazakhstan, on October 17, 2002, capped nearly 20 years of pre-launch planning of an ambitious mission that opens a new window to the cosmos.

With 4 co-aligned instruments aboard, *INTEGRAL* is able to observe the local Universe in a spectrum that stretches from the optical band to the γ-rays. A large spectral coverage is necessary to understand the mechanisms that produce emission above $\sim$1 keV. Among the topics that can be explored using *INTEGRAL* science are compact objects, AGN, diffuse emission, clusters of galaxies, GRBs, nucleosynthesis, and source populations.

Aspects of the *INTEGRAL* mission are presented in this chapter. The mission is composed of a 4-ton spacecraft and its ground segment. We begin by explaining the different components of the spacecraft and coded-mask imaging. Next, the ground segment of the mission and observation strategies are described, We conclude with a brief introduction to scientific analysis of *INTEGRAL* data.

2.1 The Spacecraft

There are 2 main components to the spacecraft (SC: Jensen et al. 2003): a service module, which forms the base of the SC, and a payload module (see Fig. 2.1). The service module hosts the computers and electronics that regulate the power, operating temperatures, telecommunications, and attitude and orbital parameters. Solar panels are attached to the service module as is the *INTEGRAL* Radiation Environment Monitor (IREM: Hajdas et al. 2003) which measures the amount of particles (electrons, protons, and cosmic rays) hitting the SC.

Mounted on the payload module, the scientific instruments point in the same direction in order to observe across a wide spectral range simultaneously. They are supplemented by the Star Trackers, which allow the telescope to fix a position in

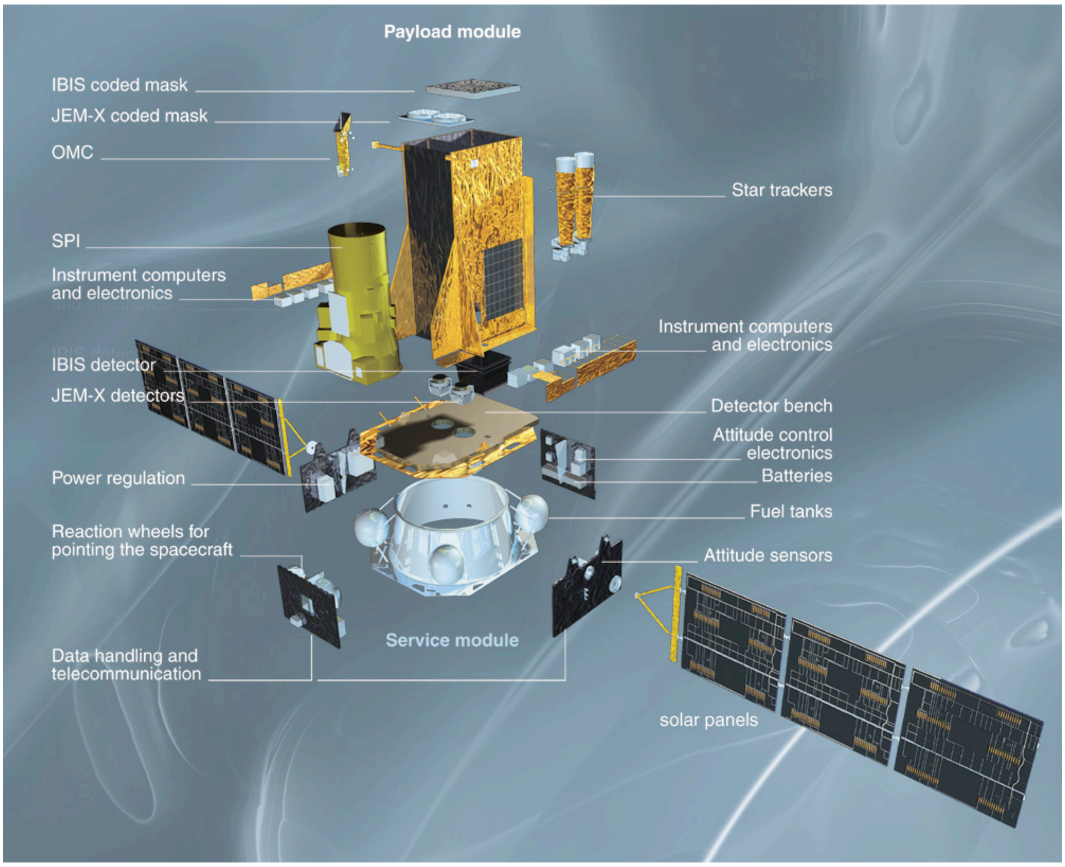

Figure *2.1: Schematic view of the* INTEGRAL *space telescope. Operational systems are located in the service module at the bottom of the satellite, while the main scientific instruments (OMC, JEM-X, IBIS, SPI, and the Star trackers) are loaded onto the payload module at the top (ESA, 2002).*

the sky. The instruments are listed below in order of increasing energy. Their characteristics are described later in the chapter:

- OMC: Optical Monitoring Camera (Mas-Hesse et al. 2003);
- JEM-X: Joint European Monitor for X-rays (Lund et al. 2003);
- IBIS: Imager on Board *INTEGRAL* Satellite (Ubertini et al. 2003); and
- SPI: Spectrometer on board *INTEGRAL* (Vedrenne et al. 2003).

INTEGRAL orbits the Earth about once every 72 hours in a highly-eccentric trajectory. With an apogee of ~154,000 km, *INTEGRAL* spends the bulk of its time in orbit (~90%) at altitudes far above the Van Allen radiation belts. This orbit was chosen so that deep, uninterrupted exposures (~200 ks) could be made with minimal contamination from the background. When count rates from IREM are too high, such as during perigee passage or during prolonged solar flares, the SC halts all non-vital operations and enters a so-called “safe mode.” Assuming there are no on-board failures, and assuming that current consumption rates continue, there is enough fuel for the satellite to operate in orbit for 15 years.

2.1.1 Coded-Mask Imaging

Gamma-rays are notoriously difficult to focus or reflect. They will simply pass through traditional lenses and mirrors, or be absorbed by the material that tries to deviate them. Using the latter fact, one could place a semi-transparent mask between a γ-ray source and a detector, and deduce the properties of the source based on its shadow. This is the basic idea behind the coded-mask technique employed by all high-energy instruments on *INTEGRAL.*

A coded-aperture mask is an array of elements that are transparent or opaque to photons of a given energy range. The shape and size of the cells and their distribution are arbitrary, but certain patterns work better than others. The mask is placed a certain height above a detector of similar dimensions (or smaller).

Light from each source in the instrument's field of view (FOV) illuminates the coded-mask pattern (which can be represented by the matrix M having entries of 0 or 1 for opaque or transparent elements) onto the detector plane in a specific way. The sum of these projections is called the shadowgram image (D). The detector records the x-y coordinates on the plane, the arrival time, and the energy of every photon that it receives. Even though the sides of the instrument are shielded, an unmodulated background term (B) considers photons that manage to come through the walls. Via deconvolution, an image of the sky (S) can then be generated using the relation:

$$\mathrm{D} = \mathrm{S} \otimes \mathrm{M} \oplus \mathrm{B} \tag{2.1}$$

Emission from a source is represented by its point spread function (PSF) which is usually Gaussian in shape and has a size equivalent to the angular accuracy of the instrument (on the order of an arcminute for IBIS and JEM-X). Given the PSF and the detector's spectral response and calibrations, the source position, error, significance, exposure, and flux can be determined. The source location error from the PSF is:

$$\delta \sim \frac{1}{R \times S/N} \tag{2.2}$$

Here, R is the ratio of mask element size to pixel size (~2.43 for ISGRI), and S/N is the signal-to-noise ratio for reconstructed source count rate (c_s) and background count rate c_b:

$$\frac{S}{N} = \frac{c_s}{\sqrt{c_s + c_b}} \tag{2.3}$$

One of the advantages of coded-mask imaging is that source and background information are recorded simultaneously. Indeed, for any given source direction, the set of detector pixels that are opaque to the source define a background that is measured under identical conditions. Other telescopes require an additional background measurement that is usually an average of observations performed before and after the source is viewed.

Another benefit is a much wider FOV for coded-mask instruments (~ degrees) than for classical telescopes (~ arcmins). The FOV of a coded-mask imager is described as fully-coded (FCFOV) for regions of the sky where the shadowgram completely illuminates the detector, and partially-coded (PCFOV) for regions where part of the shadowgram lands outside the detector limits (e.g. a source with a large off-axis angle). A bright source in the PCFOV can produce ghosts in an image from a coded mask that relies on cyclical geometry (such as IBIS). Fortunately, the positions of these artifacts can be anticipated, so they can be accounted for in the image reconstruction process. In the image, they would appear at the corners of a 10.7°-wide square (roughly equal to the size of the IBIS FCFOV) when one of its corners is placed at the position of the bright source.

2.1.2 OMC

The OMC represents the first optical camera working in tandem with X and γ-ray instruments. It features CCD optics and a Johnson V-band filter (λ ~500–600 nm ~5500 Å). The instrument has a nominal FOV of 5° × 5° with an imaging area of 1024×1024 pixels. One of the aims of the OMC is to detect the elusive optical afterglow of a GRB. Typical targets, however, include known high-energy sources that are bright. They are observed in a series of short expsoures with a few selected regions of the FOV actually being sent to the ground due to telemetry restrictions.

2.1.3 JEM-X

The Joint European Monitor for X-rays is a pair of identical telescopes that are meant to supplement the high-energy imager (IBIS) and spectrometer (SPI) by extending the spectral range to the 3–35 keV band, with an angular resolution on the order of an arcminute. The FOV of JEM-X is circular with a diameter of 13.2° for the PCFOV, and 4.8° for the FCFOV. The pattern of the coded mask is a hexagonal uniformly redundant array with a cell size of 3.3 mm and a transparency of 25%. This mask sits 3.2 m above a detector which is a chamber filled with Xe and CH_4 gases (90% and 10%, respectively). High-energy photons ionize atoms in the chamber. The ions are drawn to high-voltage anodes resulting in an amplified signal (the nominal gas gain is ~1500).

Unfortunately, some of the strips of anodes deteriorated prematurely. In order to prolong the lifetime of the instrument, it was decided that JEM-X1 and JEM-X2 would relay shifts. Another protective measure involved lowering the operating voltage at the cost of reduced sensitivity.

2.1.4 IBIS

The IBIS telescope is optimized for high-angular resolution imaging in the 15 keV to 10 MeV range. It has a low-energy layer called the *INTEGRAL* Soft Gamma-Ray Imager (ISGRI: Lebrun et al. 2003) and a high-energy layer named the Pixellated Cesium-Iodide Telescope (PICsIT: Di Cocco et al. 2003). Having 2 detector planes means that each detector can be finely tuned for its spectral range, and that photons can be tracked in 3-D space.

Scintillating crystals of CdTe arranged in an array of 128 × 128 pixels cover the detector plane of ISGRI (2600 cm^2), while PICsIT has a 64 × 64-pixel array of CsI crystals (3100 cm^2). The FOV of IBIS is a box of 29° × 29° where 9° × 9° are fully-coded. The pattern of the tunsgten mask and its supporting structure is a modified uniformly redundant array optimized for high angular resolution, with 50% of the cells transparent and a cell size of 11.2 mm. Given the distance to the detector plane (3.2 m), the typical angular resolution is a few arcminutes, with sub-arcminute positions possible in certain cases. The temporal resolution of ISGRI is $\sim$1 ms and its spectral resolution is $\sim$10% at 100 keV.

In every aspect, IBIS is a telescope designed for observing large regions of the γ-ray sky, and locating high-energy sources in crowded fields such as the Galactic Plane and Center. By operating above 15 keV, IBIS can peer through the intervening dust and gas that absorb photons below this limit. It is therefore instrumental for discovering sources where column densities are too large for other telescopes to see them. Science with IBIS has produced some of the largest catalogs of γ-ray sources to date (e.g. Bird et al. 2007), and assisted in the discovery of new members of a class of absorbed X-ray pulsars (Walter et al. 2006).

2.1.5 SPI

Operating in the 20 keV–8 MeV range, SPI is geared towards high-resolution γ-ray spectroscopy of e.g. nucleosynthesis regions and the electron-positron annihilation line (511 keV). One of the highlights of the *INTEGRAL* mission so far has been the distribution of Al^{26} from massive stars in the Milky Way (Diehl et al. 2006). A tungsten mask of 60 mm-large hexagonal elements that form a symmetrical pattern is placed 1.7 m above a honeycomb-like array of 19 detectors made of germanium crystals. This yields a FOV with a diameter of 31°, a 16.5°-diameter FCFOV, and an angular resolution of 2.5° for a point source. The spectral resolution of 2.2 keV (FWHM) at 1.33 MeV makes SPI 100 times more sensitive than previous telescopes in this domain.

A shield of bismuth germanate oxide (BGO) crystals surrounds SPI. This Anti-Coincidence Shield (ACS) records photon events from nearly every direction, thereby serving as a large-area detector for GRBs occuring outside the FOV. Since ACS acts as a photon counter, all spatial information for a potential GRB is lost. The temporal characteristics of a GRB, however, are well defined since the timing resolution of ACS is around 0.5 ms.

Not long after launch, detectors #2 and #17 were lost which reduced the instrumental effective area below the nominal value of 500 cm^2. Their absence can be circumvented by software, and a periodic annealing process ensures that an acceptable level of sensitivity is maintained for a long time.

2.2 The Ground Segment & The ISDC

Data streams to and from *INTEGRAL* are provided continuously and in real-time by stations in Redu, Belgium, and in Goldstone, California, USA. Satellite data are received in telemetry packets by the Mission Operations Center (MOC: Much et al. 2003). The MOC controls *INTEGRAL*'s performance and flight, and relays scientific and housekeeping data to the *INTEGRAL* Science Data Center (ISDC: Courvoisier et al. 2003a).

Located near Geneva in Versoix, Switzerland, the ISDC is responsible for rapidly assessing the scientific quality of incoming satellite data (see Chapter 16), to archive all the data that it receives, and to distribute the data to interested parties (i.e. the PIs of the observations, and then the public). The ISDC develops *INTEGRAL*-related software and hosts workshops that teach astronomers how to analyze *INTEGRAL* data. Therefore, the ISDC serves as the link between *INTEGRAL* and the scientific community.

2.3 Observation Strategies

When *INTEGRAL* observes the sky, the overlapping FCFOVs of the instruments represent an area of 4.8° in diameter for JEM-X, $5^\circ \times 5^\circ$ for OMC, $9^\circ \times 9^\circ$ for IBIS, and 16 ° from corner to corner in SPI.

Given the limited number of detectors for each instrument, and the large number of unknowns, the only way to reconstruct an image is to observe the region many times. To account for possible variations in detector responses, and to better estimate the background, the observation strategy consists of individiual pointings (called science windows or ScWs) that are offset by 2° with respect to the target position. This process is called dithering, and for *INTEGRAL*, it can be a rectangular pattern (baseline) of 25 points (i.e. SPI), or a hexagonal pattern of 7 points (i.e. JEM-X). The former works best for regions where multiple sources are expected in the FOV (e.g. mosaics of the Galactic Center), and the latter is suited for a lone bright source, with no other sources expected just outside the FOV.

During the initial planning phase in 1989, *INTEGRAL* was expected to be serviceable for 2 years, with a possible extension of up to 5 years. In the opening

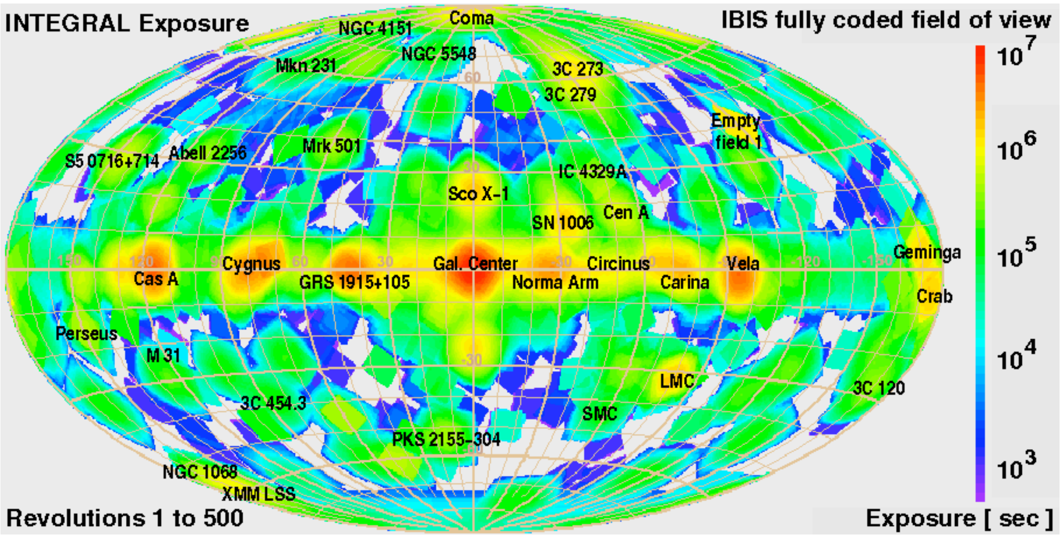

Figure *2.2:* INTEGRAL *exposure map using the IBIS FCFOV from observations performed during the first 500 revolutions (N. Mowlavi & M. Türler, 2007).*

Announcement of Opportunity (AO-1), ~9.3 Ms of the first year of observations (~26.6 Ms) were guaranteed for the Core Program (CP) as a return on the investment made by the *INTEGRAL* Science Working Team (ISWT), i.e. the scientists and institutes that contributed to designing the mission.

The ISWT devoted 4.3 Ms of their CP time to the Galactic Center Deep Exposure (GCDE), and 2.3 Ms were spent on Galactic Plane Scans (GPS). A GCDE consists of rectangular pointings (each lasting ~1.8 ks) in a grid bound by the Galactic coordinates $|l| \lesssim 30^\circ$ and $|b| \lesssim 20^\circ$. Residuals in the background image are better accounted for (post AO-2) by the introduction of a small offset angle between scans. During a GPS, *INTEGRAL* points at a target for ~2.2 ks, then slews diagonally, and repeats to draw a saw-tooth pattern inside a region with l free and $|b| \lesssim 10^\circ$.

Remaining CP time was used for pointed observations (e.g. 3C 273, Cyg X-1, and the Vela region) and for Targets of Opportunity (ToOs) which are follow-up observations of interesting events. Recently, the CP allocated some of its time to perform deep observations of the Norma Arm and the Scutum/Sagittarius Arms, as well as a deep extragalactic exposure. While the CP continues its regular monitoring of the GPS and GCDE, its share of the total observing time has been reduced (35% in AO-1, 30% in AO-2, and 20–25% in AO-3+) in favor of the General Program (GP) and Key Program (KP).

Most of *INTEGRAL*'s total observing time is awarded to the scientific community as the GP (65% in AO-1, 70% in AO-2, 75% in AO-3+). Scientists propose targets for a total exposure time that generally lasts from 100 ks to 1 Ms. The Time Allocation Committee (TAC) selects observations based on merit and feasibility.

Beginning with AO-4, the KP serves as a complement to CP and GP. Key Program time is reserved for interesting and ambitious proposals that do not fit the traditional CP and GP formats. For example, upcoming KP observations will monitor the SMC or the extragalactic sources in the region of Cas A. The data rights of KP observations are shared among the different Principle Investigators (PIs) who lead KP campaigns.

While the data rights to some observations are made public immediately (e.g., *INTEGRAL* observations of the Earth), almost all observations are private for the PIs and groups during the first year, and public thereafter. This is intended to reward the scientists who proposed the observation by giving them exclusive access to analyze the data and to announce discoveries.

INTEGRAL has now been in orbit for over 4 years. An increasing portion of the observing time has gone to extragalactic fields. The intention is to homogenize the exposure map (see Fig. 2.2) to not only observe underexposed regions and to hopefully detect new sources there, but also to facilitate studies of populations of γ-ray sources. Currently, the uneven exposure map impedes direct comparisons between objects located in different areas of the sky.

2.4 Offline Science Analysis

Analysis of *INTEGRAL* data is made possible with the software package called Offline Science Analysis (OSA). Components of OSA are developed by members of the various instrument teams in collaboration with the ISDC. The ISDC integrates the components into the OSA suite, tests the software, and distributes it. The current version of OSA is 6.0, but some of the initial tests and analyses that led to scientific results in this thesis were performed using OSA 3.0, and a significant portion of this thesis relied on OSA versions 4.2 and 5.0.

Incorporating housekeeping data (e.g. good and bad-time intervals), calibration data (e.g. instrumental response files, calibration files), and auxiliary data (e.g. ephemerides), OSA converts raw science data into images, spectra, and light curves. The large FOV captures more sources leading to a more complex deconvolution, and thus a heavy demand on computing resources during the image reconstruction and source cleaning processes.

The smallest element of an OSA analysis is a ScW which is a single pointing. It is packaged as a Flexible Image Transport System (FITS) which is the astronomical data file standard recognized by OSA. An analysis usually concerns a group of ScWs called an Observation Group (OG). For example, the OG could be the list of ~50 ScWs around the time of a source outburst, or the OG could combine the hundreds of ScWs from an entire GPS. A detailed example of *INTEGRAL* analysis of IGR J16393−4643 with OSA is presented in Chapter 7.

Part II

Galactic Surveys

Chapter 3

The First ISGRI and JEM-X Mosaics

3.1 New Sources

By the end of the first year of observations, *INTEGRAL* had devoted $\sim$ 50 ks of exposure time to almost every region of the Galactic Plane, with the Galactic Center receiving as much as $\sim$ 1 Ms of exposure. Most ISGRI pointings last $\sim$ 2 ks which is only enough for the brightest sources to be detected. Faint but persistent sources are much easier to detect in mosaic images that stack individual pointings.

The coded-mask technique presents a number of different challenges when creating mosaic images, such as deconvolving images of crowded fields and accurately representing the average fluxes of sources in them. Artifacts of the deconvolution process can appear in the mosaic images as streaks of bright or dark pixels, or as ghosts (i.e. a single source that is replicated 8 times at regular intervals of 10.7°).

Our early experiments at source and image cleaning resulted in a steady improvement of the quality of the output mosaics. Some of the methods that we used to create the cleanest mosaic images possible included: rejecting ScWs that lasted less than 1 ks or that appeared noisy upon visual inspections; focusing on energy bands in which ISGRI is most sensitive and which are likely to correspond to the peak spectral domain of new γ-ray sources (i.e. 20–80 keV); and employing a catalog during the source extraction phase that was designed explicitly to include only sources that were detected in previous trials. Only a few months into the mission, we were able to generate relatively clean mosaic images of the Galactic Plane with ISGRI and JEM-X that were featured in a poster and proceedings of The 5th *INTEGRAL* Workshop in Munich (February, 2004).

We examined mosaic images such as these by eye in order to locate known γ-ray sources and their ghosts, to flag known X-ray sources that that are detected for the first time in the ISGRI energy range, and to identify possible new source candidates. In ATel #229 (Walter et al. 2004a), we announced the discovery of around a dozen new sources (Table 3.1). These sources are called IGRs for *INTEGRAL*

Table 3.1: Positions (J2000, error=2') and significances (20–40 keV) of new γ-ray sources detected in ISGRI mosaic images of core program data between February 27 and October 19, 2004. Also provided is the source type as determined from the literature published after our announcement in ATel #229. IGR J17460−3047 turned out to be a false detection (Dr. Anthony J. Bird, private communication). AGN ≡ Active Galactic Nucleus; B ≡ Burster; BHC ≡ Black Hole Candidate; CV ≡ Cataclysmic Variable; E ≡ Eclipsing; HMXB ≡ High-Mass X-ray Binary; IP ≡ Intermediate Polar; LMXB ≡ Low-Mass X-ray Binary; P ≡ Pulsar; SFXT ≡ Supergiant Fast X-ray Transient; SG ≡ Supergiant; T ≡ Transient

Name	R.A.	Dec.	Sig.	Type
IGR J16167−4957	16:16.7	−49:57	9	CV (IP)
IGR J16195−4945	16:19.5	−49:45	10	HMXB (SG, SFXT?)
IGR J16207−5129	16:20.7	−51:29	11	HMXB (SG)
IGR J16558−5203	16:55.8	−52:03	6	AGN (Seyfert 1.2)
IGR J17195−4100	17:19.5	−41:00	8	CV (IP)
IGR J17200−3116	17:20.0	−31:16	8	HMXB (T)
IGR J17252−3616	17:25.2	−36:16	39	HMXB (SG, P, E)
IGR J17254−3257	17:25.4	−32:57	11	LMXB (B)
IGR J17285−2922	17:28.5	−29:22	5	Unclassified (T, BHC?)
IGR J17303−0601	17:30.3	−06:01	8	CV (IP)
IGR J17460−3047	17:46.0	−30:47	6	false detection
IGR J17488−3253	17:48.8	−32:53	8	AGN (Seyfert 1)
IGR J18027−1455	18:02.7	−14:55	10	AGN (Seyfert 1)
IGR J21247+5058	21:24.7	+50:58	7	AGN (Seyfert 1)

Gamma-Ray sources. A number of other sources that were not known to emit above 20 keV were also detected. Their results were reported in ATel #232 (Bassani et al. 2004).

For a few IGR sources, Dr. Roland Walter obtained observation time with *XMM-Newton*. These follow-up observations enabled us to detect iron lines and photoelectric absorption, to obtain a more precise position, and to discover pulsations. The IGR sources from this campaign (as well as others) are discussed further in Part III and in Walter et al. (2006).

3.2 Source Variability

The large amount of exposure time dedicated to certain regions of the Galaxy allowed us to subdivide the mosaic images into epochs without losing too much sensitivity. Figure 3.1 presents the Norma Arm region as seen by ISGRI in the 30–50 keV band during 5 consecutive observation periods (GCD1a: 2003-01-29 to 2003-03-15; GCDE 1b: 2003-03-15 to 2003-04-17; GCDE 2a: 2003-08-02

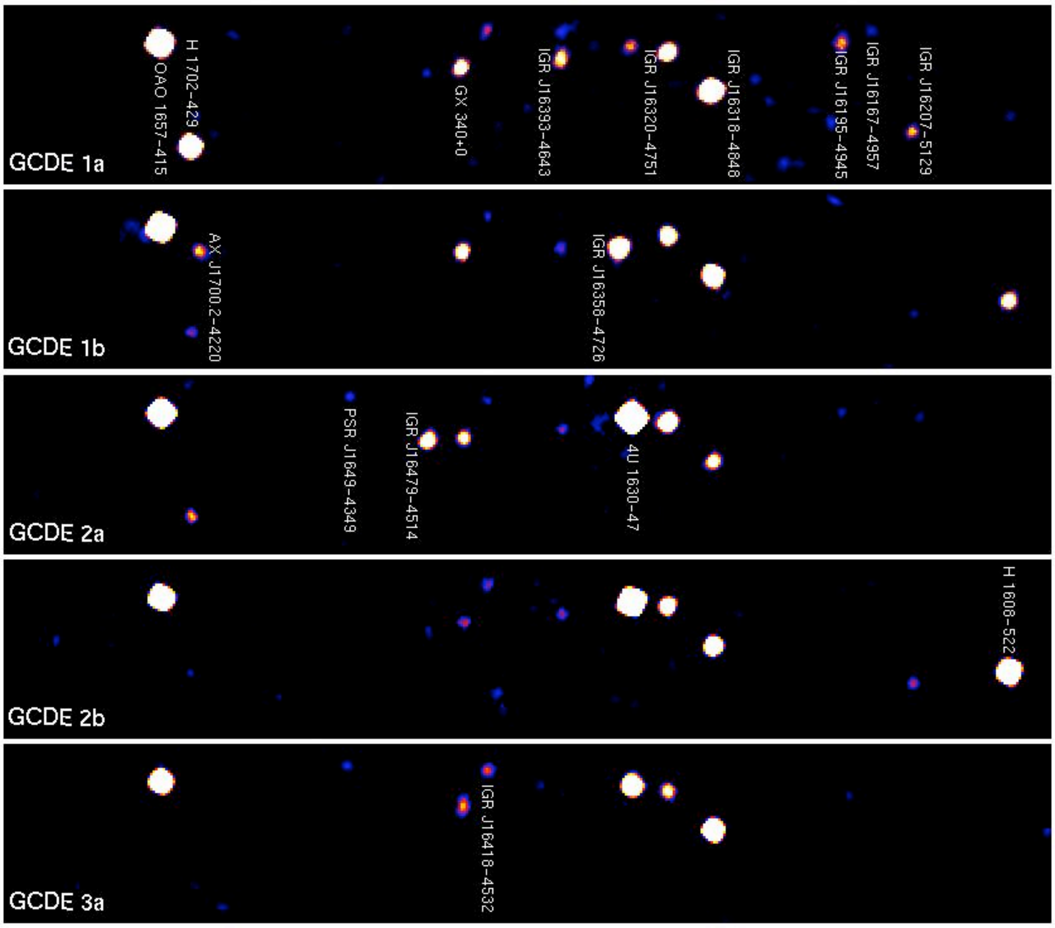

Figure *3.1: ISGRI significance map of the Norma Arm region in the 30–50 keV band during 5 successive observation periods. From top to bottom, the images collect 261, 117, 188, 158, and 93 ks of exposure time, respectively. The area of each image is about* 15° × 3° *in Galactic coordinates.*

to 2003-08-19; GCDE 2b: 2003-08-19 to 2003-10-08; GCDE 3a: 2004-02-16 to 2004-03-17). The images were derived from mosaics of the significance map and they collect (from top to bottom) 261, 117, 188, 158, and 93 ks of exposure time, respectively. Each image represents an area of about 15° × 3° in Galactic coordinates.

The figure illustrates well the variable nature of high-energy sources. Some objects are almost always seen but at varying significances, while others appear briefly only to disappear again. Almost all of the sources were detected for the first time above 20 keV by *INTEGRAL*. A few of them are members of the class of highly-absorbed high-mass X-ray binaries that are typically found in the spiral arms of the Milky Way (see Parts III–IV).

In the next chapter, we examine the level of sensitivity that can be reached in ISGRI and JEM-X mosaic images of the GPS and GCDE. This analysis should help us minimize the number of false detections such as was the case for IGR J17460−3047 which we detected at 6σ, but was ultimately shown to be a residual of nearby bright sources.

Chapter 4
Imaging Systematics

In Chapter 3, we showed that dozens of faint persistent sources were revealed in the first mosaic images of the GCDE and GPS, demonstrating how the accumulation of exposure time tends to improve the statistical accuracy. However, there is a point at which overexposure actually causes the quality of the image to suffer rather than to improve. This is because the deconvolution of crowded fields of bright sources add systematic uncertainties to the mosaic images. By studying the distributions of intensity and significance values from ISGRI and JEM-X mosaic images of the GPS and GCDE across different energy bands, we found that regardless of energy, systematic uncertainties dominated statistical uncertainties for exposure times $\gtrsim$ 1 Ms.

The aims of this research were to help improve the statistical quality of mosaic images of deep and busy fields such as the GPS and GCDE, to assess the level of confidence in faint candidate sources found in the most exposed regions, and to help define a significance cutoff for the IBIS Survey (see Chapter 5).

Images of CP pointings of the GCDE and GPS were generated in several energy bands for both ISGRI and JEM-X. In the case of ISGRI, the pointing images were created with OSA 3 software using a catalog of detected sources in order to clean the images. These images were then assembled into a mosaic on a fine sky grid with a full analysis of the flux spread, and weighting that relied on the variance map of each individual image. The JEM-X mosaic images were created with software by Dr. Niels Lund that implemented an improved vignetting correction.

For the mosaic image of each energy band, we fitted Gaussians to the distribution of intensities (and significances) of all pixels in a given interval of exposure time. An example of this presented in Fig. 4.1 where the distribution of intensities is shown in the 40–50 keV band for exposure times between 177.8 and 316.2 ks. Then, we collected the root-mean-square (rms) coefficients from the Gaussians to examine their dependence on exposure time. Since we were only interested in the background fluctuations, we excluded sources from the fits (defined here as excesses over 5σ).

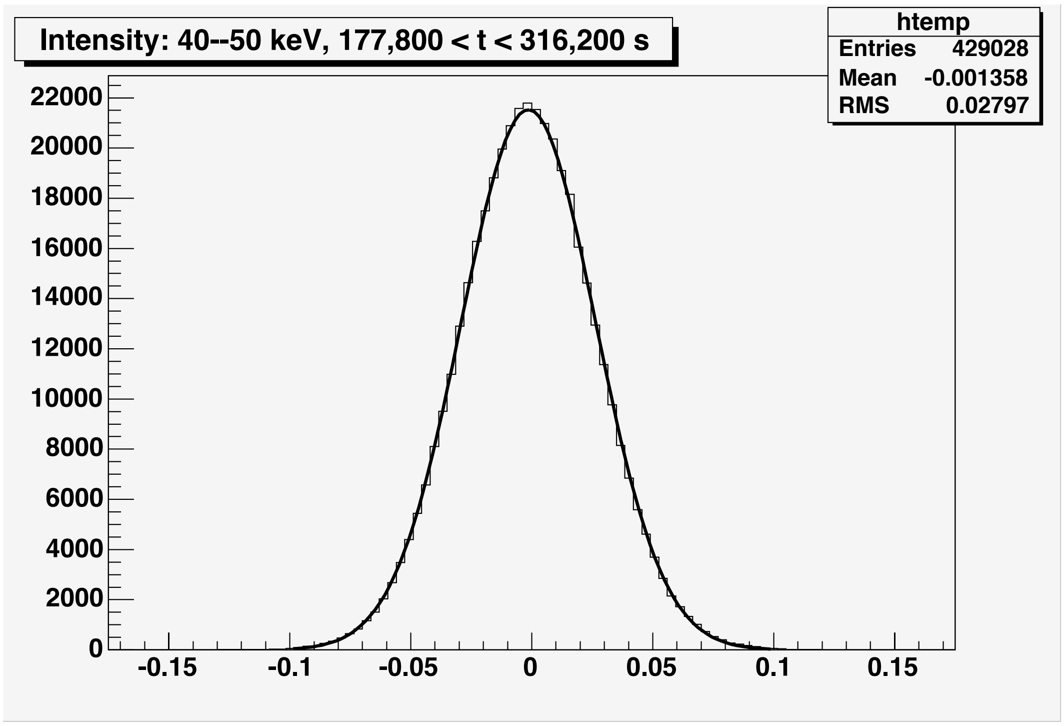

Figure *4.1: The distribution of intensity values for 40–50 keV over an interval of exposure time (177,800–316,200 s). The y-axis represents the number of pixels for a given intensity (in cts/s) along the x-axis. The solid curve and its parameters reflect the best Gaussian fit to the distribution up to* 5σ.

4.1 Significance & Intensity vs. Exposure Time

One way to ascertain the statistical quality of mosaic images involves checking whether significance values of all background pixels remain close to 1 regardless of exposure time:

$$n_\sigma \sim \frac{N_c}{S_c}\left(\frac{2\Delta E}{E}\right)^{\frac{1}{2}}\left(\frac{t}{10^5}\right)^{\frac{1}{2}} \tag{4.1}$$

This implies that the measurement of the background continuum (N_c) is equivalent to the expected sensitivity limit (S_c). Note that a background significance of 1 was acceptable just after launch, but thanks to fine tuning of the software and steady improvements in the background maps, current significance levels for the background are less than 1.

In Fig. 4.2, rms values from ISGRI significance images are plotted as a function of exposure time. As expected, the rms of the background is close to 1 for exposure times up to 10^5 s. Beyond this, the reinforcement of coding noise becomes a factor, and systematic effects dominate statistical uncertainties. High exposure times are typical of the GCDE. The deconvolution of many bright sources in this crowded region leads to coding noise and a degradation of sensitivity. In the first energy band (20–25 keV), the cleaning of sources is not optimal yet since the rms of the

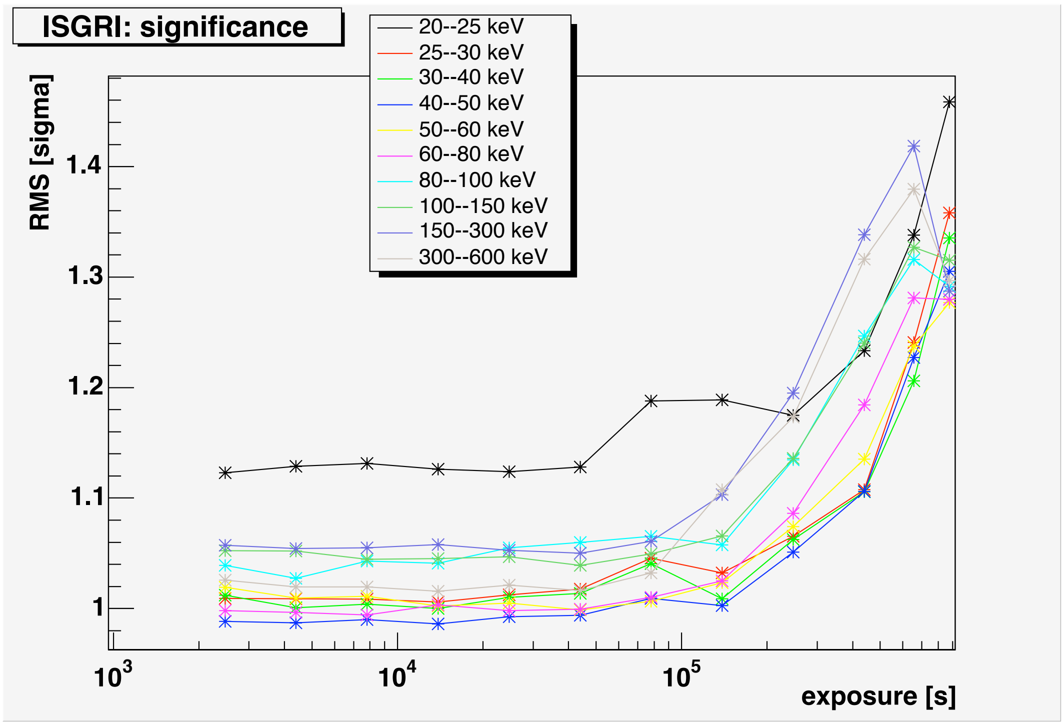

Figure *4.2: Significance (in σ) of the background as a function of exposure time for ISGRI mosaics.*

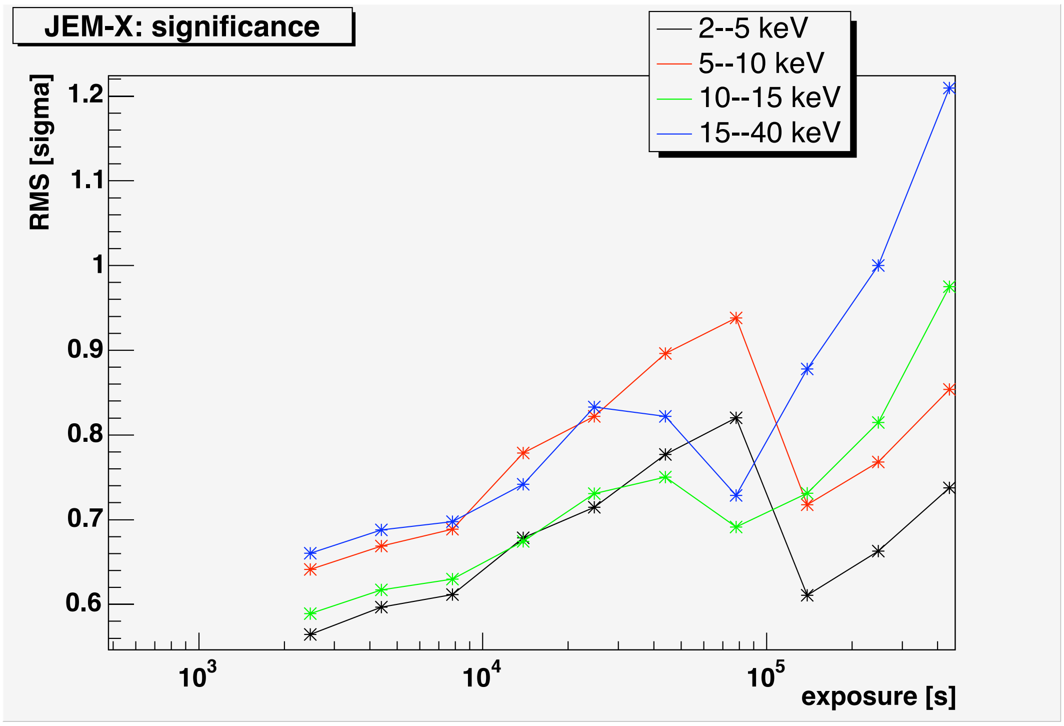

Figure *4.3: Significance (in σ) of the background as a function of exposure time for JEM-X mosaics.*

background significance is greater than 1.

For JEM-X, the rms value of the background significance we derive is less than 1 in many cases which indicates that the variance of the JEM-X images are not yet fully consistent (see Fig. 4.3). As with ISGRI, the rms of significance images from JEM-X increases with the exposure time, demonstrating the effects of systematics. The reinforcement of coding noise in the GCDE could impact the sensitivity of intensity images as well.

Figure 4.4 illustrates the dependence of the rms of the background intensity on the exposure time for ISGRI mosaics. There appears to be two slopes in the distribution: the rms varies inversely with exposure time up to about $4 \cdot 10^4$ s, then the rms decreases with the square-root of the exposure time, as expected. The change in slope is not yet understood. For exposures longer than $2 \cdot 10^5$ s, and at low energies, the rms of the background fluctuations is less than 1 mCrab. We performed a similar analysis excluding the GCDE. Although the exposure time was shorter, the distribution was similar and an eventual change in slope was imperceptible.

The rms of the JEM-X background intensity decreases with the exposure time (Fig. 4.5). However, there is an unexpected bump in the distribution for exposure times between 10^4 and 10^5 s. JEM-X mosaics have their highest exposure times associated with the Vela region. The GCDE extends up to only about 10^5 s. In the neighborhood of Vela, an optimum sensitivity can be reached since bright sources are less numerous, whereas the GCDE remains above the limit of sensitivity due to the coding noise residuals of its crowded field.

To reiterate, we believe that the cumulative effects of coding noise from multiple bright sources in the GCDE are responsible for the bump between 10^4 and 10^5 s in Fig. 4.5. We can determine how much influence the GCDE has by extracting this region geometrically (e.g.: removing pixels with galactic longitudes between 30–330°) and replotting. Fig. 4.6 shows that the exclusion of the GCDE improves the sensitivity in the two time bins before 10^5 s (i.e.: the bins are no longer affected by coding noise from the GCDE). The deterioration witnessed in the two prior bins is still unexplained. The edges of the GCDE, which correspond to these exposure times, might be responsible. Notice that for an exposure time of around $3 \cdot 10^4$ s, the amplitude of the shift from a linear dependence is equivalent for both low and high energies.

4.2 Comparison with Advertised Fluxes

We compared our ISGRI sensitivities with values provided in the ISGRI AO-2 documentation (Barr & Kuulkers, 2003). Since we were free to choose any exposure time in our comparison, we selected one exposure time that was representative of the GCDE ($1.4 \cdot 10^5$ s), and another that reflected the rest of the GPS mosaic ($7.8 \cdot 10^4$ s). This way, we were able to distinguish pixels that belonged to the

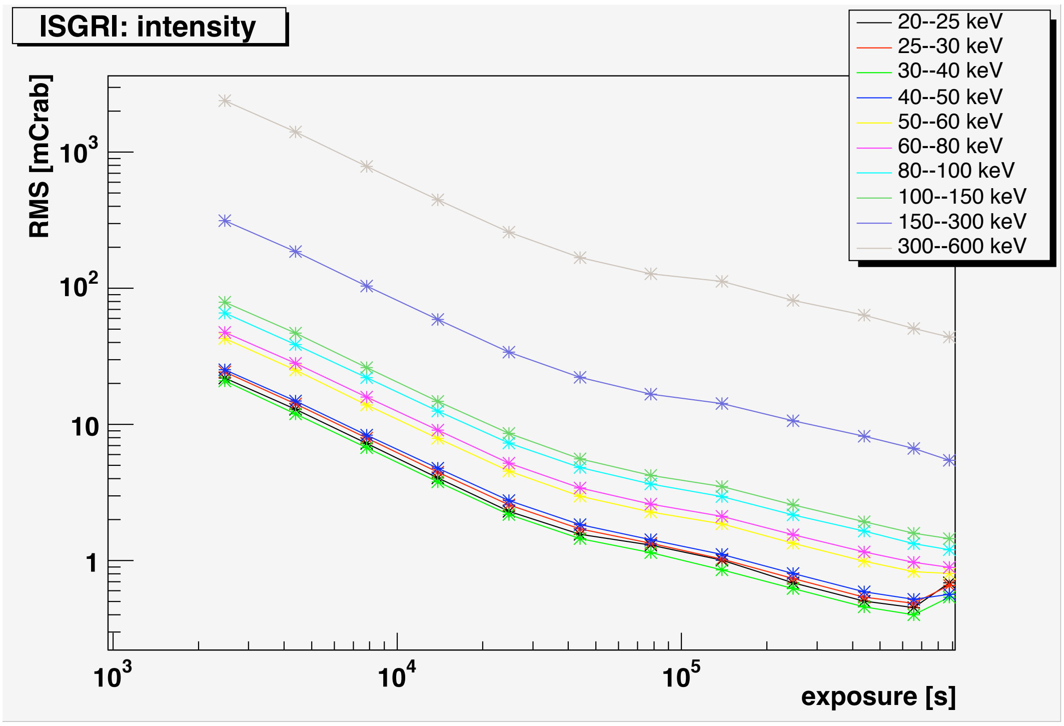

Figure *4.4: Intensity (in mCrabs) of the background as a function of exposure time for ISGRI mosaics.*

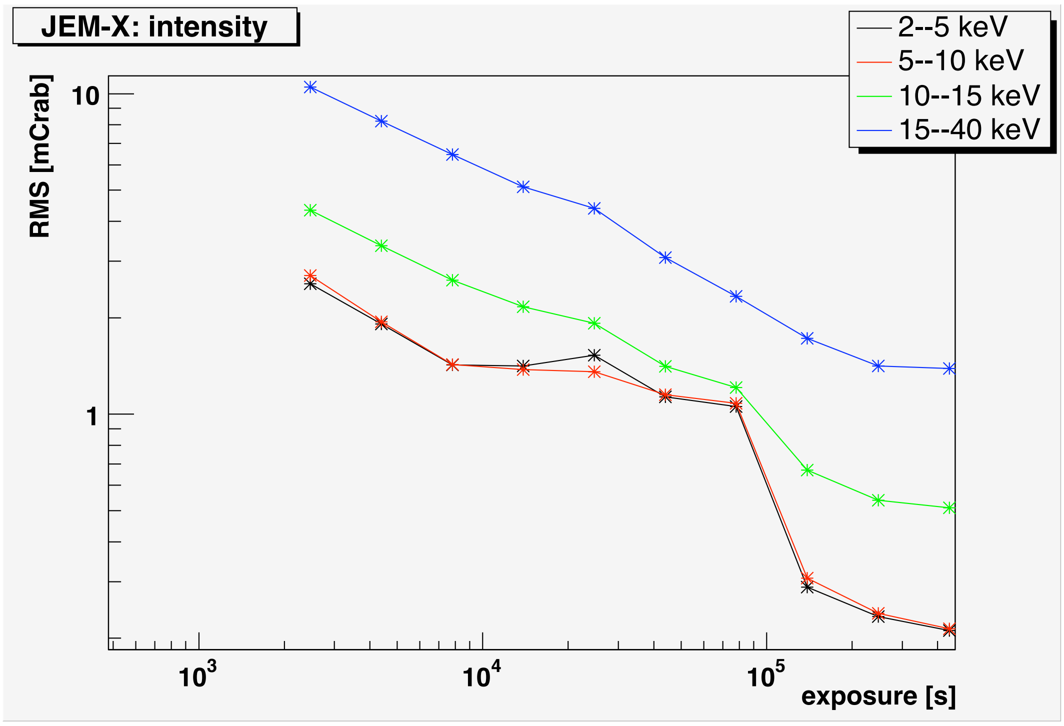

Figure *4.5: Intensity (in mCrabs) as a function of exposure time for JEM-X mosaics.*

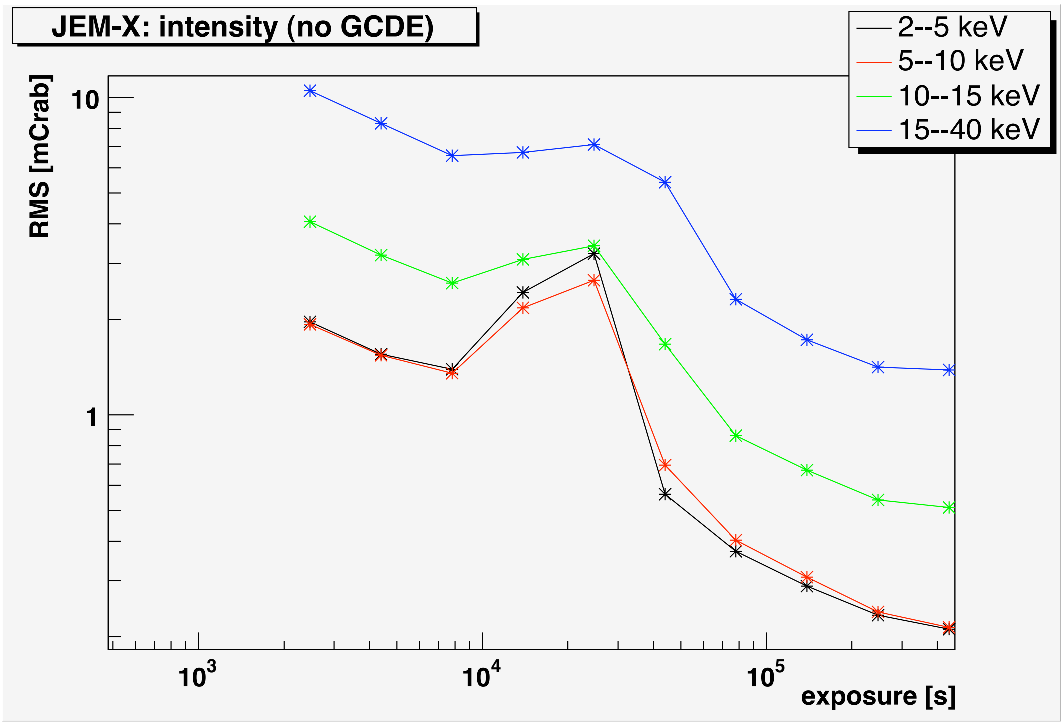

Figure *4.6: Intensity (in mCrabs) as a function of exposure time for JEM-X mosaics without the GCDE (i.e.: pixels with galactic longitudes between 30–330°).*

GCDE from the rest of the sky, in order to compare each region of the mosaic to the AO-2 documentation.

The 1σ-sensitivities of the ISGRI mosaics and the advertised rates as a function of energy are presented in Fig. 4.7. The ratios of 1σ-sensitivities to advertised values in different parts of the mosaic (GCDE, and GPS without the GCDE), are plotted against energy in Fig. 4.8. Compared with advertised fluxes, there is little difference between ISGRI mosaics that include or exclude the GCDE. The mosaics matched the advertised sensitivities for energies above 150 keV (see Figs. 4.7–4.8). At low energies, where the coding noise of the sources dominates, the sensitivities achieved in the mosaic images are not as good as anticipated. Hopefully, this will be better accounted for in future versions of the software.

Finally, we compared the sensitivities advertised in the JEM-X AO-2 documentation (Orr, 2003) with the rms of the JEM-X mosaic background for an exposure time of $7.8 \cdot 10^4$ s. The advertised sensitivity was derived from simulations that included the effect of the imaging software. Figure 4.9 shows that the measured 1σ-sensitivity for JEM-X is close to what was expected. When the GCDE is excluded geometrically, the sensitivity is enhanced.

It is worth remembering that our JEM-X mosaics had significances that were lower than 1 in this time bin ($7.8 \cdot 10^4$ s, see Fig. 4.3) which means that we are probably

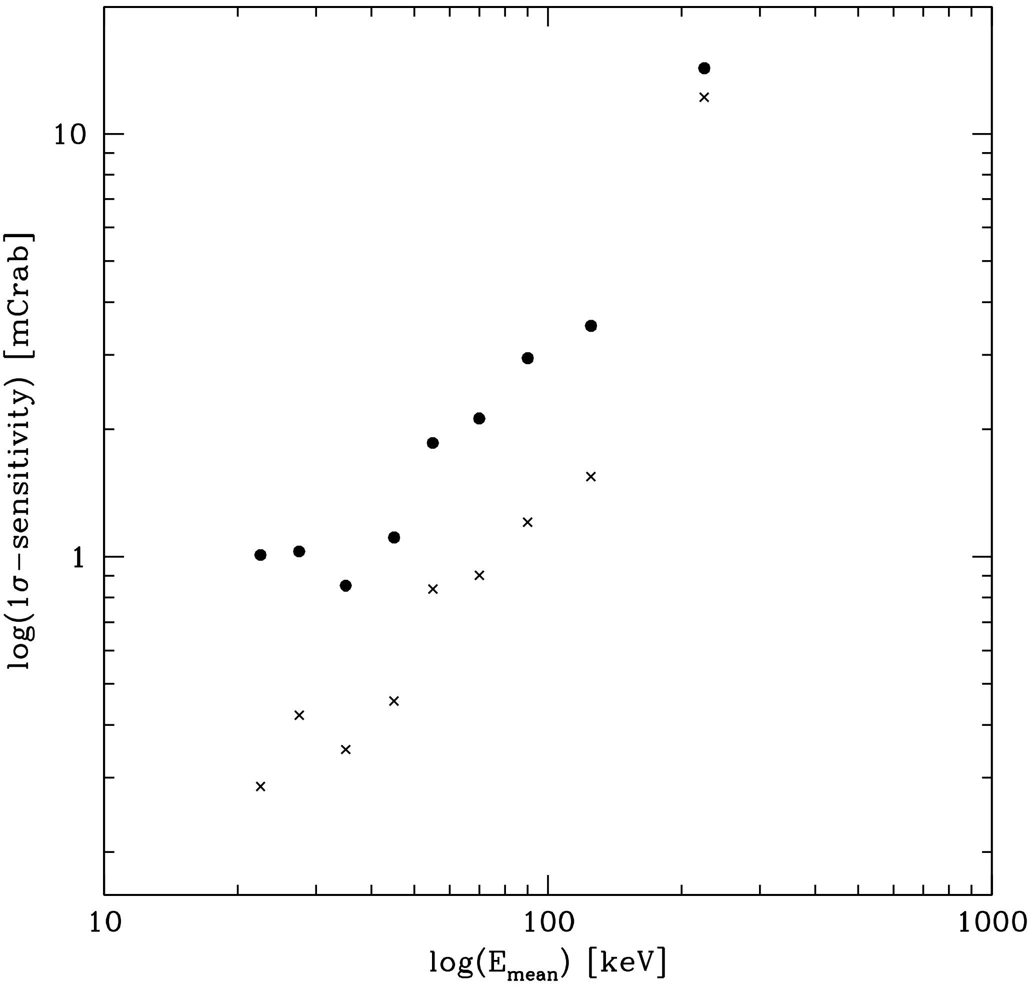

Figure *4.7: Comparison between mosaic fluxes (disks) and fluxes advertised for* $1.4 \cdot 10^5$ *s (crosses) in the ISGRI AO-2 documentation (Barr & Kuulkers, 2003).*

overestimating our sensitivity. Furthermore, the advertised fluxes relied on a simulation that considered a single energy band (2–10 keV).

4.3 Conclusions

Analyses of mosaic images obtained with ISGRI and JEM-X show that systematic effects dominate statistical uncertainties in the region of the sky where the density of sources is greatest (Galactic Plane and GCDE), and for exposure times longer than 10^5 s. We find that the statistics are acceptable for ISGRI when exposure times are less than 10^5 s, but the significance of JEM-X mosaics is less than 1 for most exposure times. The sensitivities of mosaic images from ISGRI and JEM-X are only a factor of 1–2 away from the optimum instrumental sensitivities.

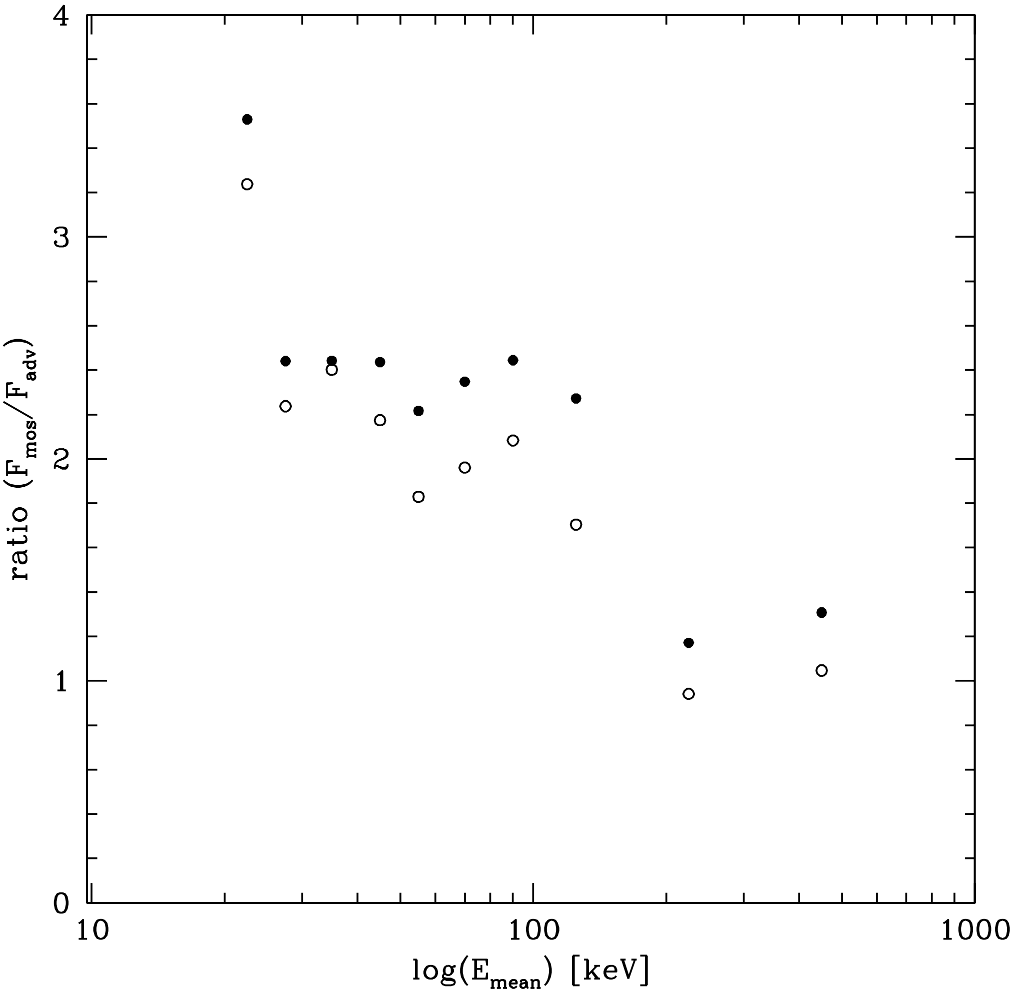

Figure *4.8: Ratios of mosaic to advertised fluxes from the ISGRI AO-2 documentation (Barr & Kuulkers, 2003). Disks represent mosaics that include the GCDE at* $1.4 \cdot 10^5$ *s, and circles refer to mosaics without the GCDE for an exposure time of* $7.8 \cdot 10^4$ *s.*

These results were presented as Bodaghee et al. (2004):

- Bodaghee A., Walter R., Lund N. & Rohlfs R.
  Systematics of ISGRI and JEM-X mosaic images
  Proceedings of the 5th *INTEGRAL* Workshop, ESA-SP 552, pp. 833–836, 2004

This research helped Bird et al. (2004) estimate a cutoff significance for faint sources in the IBIS GPS, and it led to refinements in the imaging software. At the time of this study, OSA 3 could not match the advertised instrumental sensitivities in deep mosaics from ISGRI and JEM-X. Current versions of OSA (5–6)

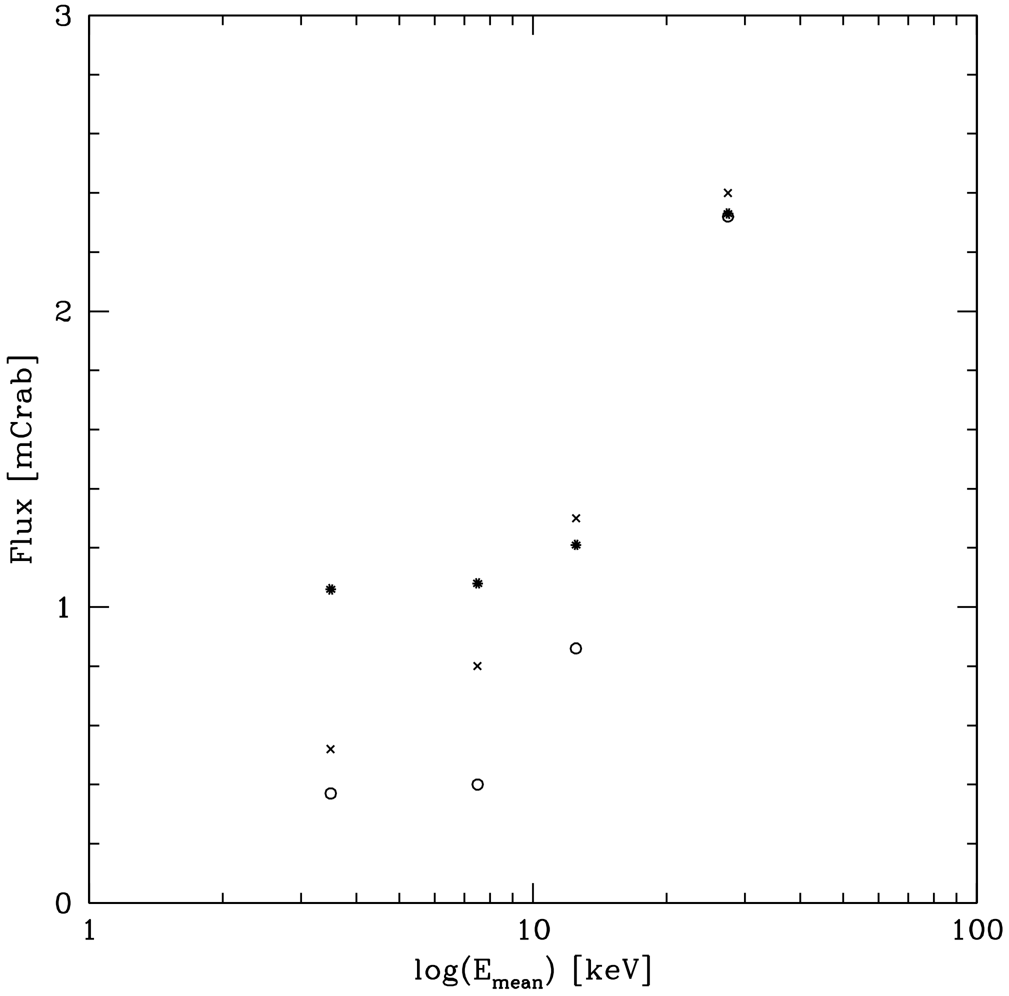

Figure *4.9: Comparison between JEM-X mosaics of the GPS (disks), mosaics without the GCDE (circles), and advertised fluxes (crosses) from the JEM-X AO-2 documentation (Orr, 2003). The exposure time is* $7.8 \cdot 10^4$ *s. The exclusion of the GCDE is geometrical (see caption for Fig. 4.6), and is not based on exposure time.*

are able to generate mosaics much deeper than the ones analyzed here, and achieve background sensitivities that are better than advertized. This is due to a combination of improved background maps, precise positions in an input catalog of relevant sources, and better source/ghost cleaning.

Chapter 5

The ISGRI Survey Catalogs

Results from Chapters 3–4 were presented at meetings of the IBIS-ISGRI Survey Team held at the University of Southampton in March, 2004, and in IASF, Rome, in June, 2005.

The ISGRI Survey Team is composed of scientists from institutes responsible for the ISGRI instrument: CEA-Saclay, IASF Bologna, IASF Roma, the University of Southampton, and the ISDC. Members of the ISGRI Survey Team have access to the CP data which, in the first 2 years, devoted ~30% of all observation time to the GPS and GCDE.

The ISGRI Survey Team established a cutoff significance of 6σ for source detections in the initial catalogs. Two wide energy bands were chosen for position determination and 10 narrow energy bands for spectral analyses. With these criteria, lists of sources detected in all-sky mosaic images were published as the 1st and 2nd IBIS Survey Catalogs of Bird et al. (2004) and Bird et al. (2006):

Bird A.J., Barlow E.J., Bassani L., Bazzano A., Bodaghee A., Capitanio F., Cocchi M., Del Santo M., Dean A.J., Hill A.B., Lebrun F., Malaguti G., Malizia A., Much R., Shaw S.E., Stephen J.B., Terrier R., Ubertini P. & Walter R.
The first IBIS/ISGRI soft gamma-ray galactic plane survey catalog
The Astrophysical Journal, Vol. 607-1, pp. L33–L37, 2004

Bird A.J., Barlow E.J., Bassani L., Bazzano A., Bélanger G., Bodaghee A., Capitanio F., Dean A.J., Hill A.B., Lebrun F., Malizia A., Mas-Hesse J.M., Molina M., Moran L., Renaud M., Sguera V., Shaw S.E., Stephen J.B., Terrier R., Ubertini P., Walter R., Willis D.R. & Winkler C.
The 2nd IBIS/ISGRI soft gamma-ray survey catalog
The Astrophysical Journal, Vol. 636-2, pp. 765–776, 2006

A copy of the 1st IBIS Survey can be found at the end of this chapter. These catalogs contain ~ 120 and ~ 210 sources, respectively, many of which are new at these energies. We provided X-ray positions with uncertainties as low as 0.7', soft (20–40 keV) and hard (40–80 keV) source fluxes, significances, and effective exposure times.

XMM-Newton observations were obtained for a subset of the new sources with the aim of clarifying their nature. The multiwavelength analyses of some of these IGR sources are presented in Part III. The 2^{nd} and 3^{rd} IBIS Survey Catalogs (Bird et al. 2006, 2007) were among the main catalogs that were used to populate the *INTEGRAL* General Reference Catalog, as well the catalog of the parameters of ISGRI-detected sources presented in Part IV.

The Astrophysical Journal, 607:L33–L37, 2004 May 20

THE FIRST IBIS/ISGRI SOFT GAMMA-RAY GALACTIC PLANE SURVEY CATALOG[1]

A. J. Bird,[2] E. J. Barlow,[2] L. Bassani,[3] A. Bazzano,[4] A. Bodaghee,[5] F. Capitanio,[2,4] M. Cocchi,[4] M. Del Santo,[4]
A. J. Dean,[2] A. B. Hill,[2] F. Lebrun,[6,7] G. Malaguti,[3] A. Malizia,[3] R. Much,[8] S. E. Shaw,[2,5] J. B. Stephen,[3]
R. Terrier,[6,7] P. Ubertini,[4] and R. Walter[5]

Received 2004 March 4; accepted 2004 April 12; published 2004 April 27

ABSTRACT

We report the first high-energy survey catalog obtained with the IBIS gamma-ray imager on board *INTEGRAL*. The analysis has been performed on the first-year Core Program ISGRI data comprising both Galactic Plane Scan and Galactic Centre Deep Exposure pointings for a total exposure time exceeding 5 Ms. This initial survey has revealed the presence of ∼120 sources detected with the unprecedented sensitivity of ∼1 mcrab in the energy range 20–100 keV. Each source is located to an accuracy between 1′ and 3′, depending on its brightness. The outstanding IBIS capability to locate soft γ-ray emitters has allowed us to identify most of the detected sources with already known Galactic X-ray binary systems, while 28 of the objects are of unknown nature.

Subject headings: Galaxy: general — gamma rays: observations — surveys

1. INTRODUCTION

A key strategic objective of the *INTEGRAL* (*I NTErnational Gamma-Ray Astrophysics Laboratory*) mission (Winkler et al. 2003) is a regular survey of the Galactic plane, for a total exposure of ∼2.3 Ms yr^{-1}, complemented by a deep exposure of the central radian of ∼4.8 Ms yr^{-1}. Technically this is made possible by the large field of view of the γ-ray instruments exceeding 30°. The survey is achieved by scanning as much of the Galactic plane as is possible within the Sun constraints. These scans are performed roughly every 12 days corresponding to about 9% of the total observational time, rising to 26% when the Galactic Centre Deep Exposure is included. Each exposure lasts, on average, 2150 s and covers a sky region of ∼900 deg^2, taking advantage of the IBIS's (Imager on Board *INTEGRAL*) wide field of view and capability to resolve each point source in the field, in terms of sky position, spectral shape, and time behavior (Ubertini et al. 2003). The discovery of transient sources within the field of view is ensured by the high sensitivity of the instrumentation, which allows Eddington luminosity stellar objects to be detected throughout the Galaxy within a short (∼1000 s) observation period.

The recent *ASCA* survey of the Galactic center (GC) region ($|l| \leq 45^\circ$ and $|b| \leq 0\overset{\circ}{.}4$), over the energy range of 0.7–10 keV (Sugizaki et al. 2001), has resolved 163 discrete sources with $F_{\mathrm{X}} \geq 10^{-12.5}$ ergs cm^{-2} s^{-1}, with a log N–log S distribution with a power-law index of ~ -0.79 ($E > 2$ keV). In the hard X-ray range (2.8–30 keV), all-sky coverage was achieved with the *BeppoSAX* Wide Field Camera (WFC; Jager et al. 1997). The WFC discovered ∼21 transients via 1 Ms yr^{-1} monitoring of the GC region and, in all, more than 50 transient and recurrent sources clustered along the plane down to a few mcrab sensitivity. These comprised ∼80% low magnetized neutron stars (in 't Zand et al. 2004) and ∼20% black hole candidates, most of them in low-mass X-ray binary systems (Ubertini et al. 1999). In the soft γ-ray band (13–180 keV range), the *HEAO 1* A4 catalog (Levine et al. 1984) contains 72 sources at a flux sensitivity of 14 mcrab. Information to pinpoint the high-energy components of the GC has been obtained with the SIGMA telescope (40–800 keV) on the French-Russian *Granat* mission, even if limited to ∼30 mcrab sensitivity (Vargas et al. 1996). Analysis of BATSE data can use the Earth occultation technique to survey the whole sky (Harmon et al. 2002). A recent all-sky survey (25–160 keV), based on ∼500 days of background-subtracted data, locates ∼25 known gamma-ray sources, including several extragalactic objects. This survey has a sensitivity ∼3 mcrab but suffers some source confusion due to the 2° angular resolution (Shaw et al. 2004).

2. THE IBIS SURVEY

In this Letter, we report the first results of the *INTEGRAL*/IBIS Galactic Plane survey, in order to provide a prompt release of information to the community. Further catalogs, employing better source location and spectral response, on larger data sets will be released later in the mission. The data are collected with the low-energy array, ISGRI (*INTEGRAL* Soft Gamma-Ray Imager; Lebrun et al. 2003), consisting of a pixilated 128 × 128 CdTe solid-state detector that views the sky through a coded aperture mask. IBIS generates images of the sky with a 12′ FWHM resolution over an ∼30° field of view in the energy range 15–1000 keV. This first catalog uses mosaic image data from the Core Program observations of the Galactic plane for the first year of operation. The source fluxes are integrated over two energy bands (20–40 and 40–100 keV), and the limiting sensitivity for this survey is around 1 mcrab.

3. DATA ANALYSIS

The data set consists of all Core Program observations (the Galactic Plane Scan and the Galactic Centre Deep Exposure) performed between 2003 February 28 (revolution 46) and October 10 (revolution 120), a total of 2529 point-

---

[1] Based on observations with *INTEGRAL*, an ESA project with instruments and science data centre funded by ESA member states (especially the PI countries: Denmark, France, Germany, Italy, Switzerland, and Spain), the Czech Republic and Poland, and with the participation of Russia and the US.

[2] School of Physics and Astronomy, University of Southampton, Highfield, Southampton, SO17 1BJ, UK.

[3] IASF/CNR, Via Gobetti 101, I-40129 Bologna, Italy.

[4] IASF/CNR, Via Fosso del Cavaliere 100, I-00133 Rome, Italy.

[5] Geneva Observatory, *INTEGRAL* Science Data Centre, Chemin d'Ecogia 16, 1291 Versoix, Switzerland.

[6] CEA-Saclay, DAPNIA/Service d'Astrophysique, F-91191 Gif sur Yvette Cedex, France.

[7] Federation de recherche APC, College de France 11, place Marcelin Berthelot, F-75231 Paris, France.

[8] ESA-ESTEC, Research and Scientific Support Department, Keplerlaan 1, 2201 AZ, Noordwijk, Netherlands.

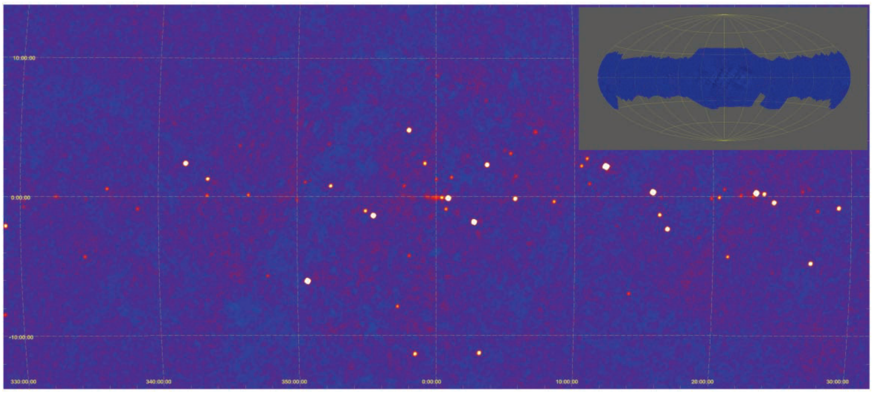

FIG. 1.—Significance map in the 30–50 keV band for the Galactic center region ($-30° < l < 30°$). The inset shows the all-sky image.

ings. ISGRI images were generated for each selected pointing in 10 narrow energy bands with the ISDC offline scientific analysis software version 3 (Courvoisier et al. 2003; Goldwurm et al. 2003), including background uniformity corrections (Terrier et al. 2003). The source ghosts have been cleaned in each image even when a source was not formally detected in a single pointing. The source catalog used for the image cleaning was built iteratively, finally including all sources significantly detected.

The images of the various pointings have been combined together in all-sky mosaics in Aitoff coordinates with sky pixels of 2′.4 at the center. For each sky pixel, the mosaic software weights each input image contribution according to the number of events detected and the variance of the signal in each input pixel. Detected events are fully redistributed in the final sky pixels assuming a flat distribution of the events in the original pixels. The resulting number of counts is divided by the effective (off-axis response–corrected) exposure time in each pixel to obtain a count rate image. Variance and significance mosaic images are also generated in the process. Figure 1 shows the all-sky significance map obtained for the 30–50 keV energy band.

Two energy bands have been used for peak detection. The primary detection band is 30–50 keV since this provides the best compromise between high source flux versus detector background, maximizing the signal-to-noise ratio for the majority of sources and good removal of imaging artefacts. However, it was found essential to also search the 20–40 keV band, which exhibits a higher degree of source-related structure, in order to detect sources with particularly soft spectra. Two peak search algorithms have been applied to the significance maps. The primary search tool used was SExtractor (Bertin & Arnouts 1996), employing a simple Gaussian point-spread function filter. The significance maps (20–40 and 30–50 keV) were searched independently, each providing a full list of all excesses detected above the $3.5\,\sigma$ level. A second method, using a basic search for excesses above a certain threshold level and a simple deblending algorithm for use in crowded source regions, was used to cross-check the SExtractor results. In cases of doubt, the possible sources were visually inspected.

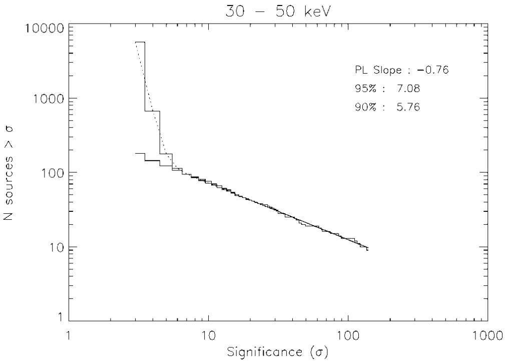

FIG. 2.—Distribution of significances of excesses found in the 30–50 keV all-sky map.

Source positions were derived using a barycentering method to determine the centroid of the source profile; this method was found to provide a better mean location accuracy than use of the brightest pixel (a mean error of 0′.72 and 1′.2, respectively). Source mean fluxes and uncertainties in two energy bands were determined from the count rate and variance images at the position of the source maximum significance. The ISGRI off-axis response is not yet fully calibrated. We estimate that the relative systematic uncertainties on the average count rates are not larger than 10% for well-exposed sources (>20 ks). Flux uncertainties derived from the variance only account for statistics, so fluxes derived from low significance ($<6\,\sigma$) detections are quoted as $2\,\sigma$ upper limits.

In order to investigate at what pixel significance levels true sources "emerge" from the (statistical and systematic) distribution of the background, it is possible to create a type of "log *N*–log *S*" figure, albeit not taking into account variations in exposure across the map (Bodaghee et al. 2004). This is shown in Figure 2 for the 30–50 keV significance mosaic, where we plot the number of excesses above a certain significance as a function of significance, taking into account the point-spread function of the image. The dotted line is a fit (Gaussian+power law) to the data, while the lower solid line is the extrapolation of the power law (PL). The fit parameters of the Gaussian component (center $= -0.5$, $\sigma = 1.08$) indicate

TABLE 1
The First IBIS Catalog: 20–100 keV

No.	Name	R.A. (deg)	Decl. (deg)	F_{20-40} (count s^{-1})	F_{40-100} (count s^{-1})	Significance[a]	T[b] (ks)	Type[c]
1	1A 0114+650	19.545	65.298	0.87 ± 0.09	<0.59	9.3*	43	HMXB
2	4U 0352+30	58.842	31.038	11.40 ± 0.58	9.72 ± 0.75	14.9	7	HMXB, XP
3	Crab	83.640	22.009	93.64 ± 0.07	69.12 ± 0.08	1021.2	94	PWN, PSR
4	4U 0614+091	94.284	9.109	2.90 ± 0.14	2.21 ± 0.19	15.6	29	LMXB, B, A
5	Vela pulsar	128.836	−45.196	0.84 ± 0.08	0.74 ± 0.11	8.4	61	PWN, PSR
6	4U 0836−429	129.355	−42.908	1.68 ± 0.08	1.35 ± 0.11	16.9	64	LMXB, T, B
7	Vela X-1	135.537	−40.561	21.09 ± 0.09	3.78 ± 0.12	116.5	58	HMXB, XP
8	Cen X-3	170.334	−60.610	2.84 ± 0.08	<0.40	11.6	55	HMXB, XP
9	A1145.1−6141	176.863	−61.971	2.75 ± 0.09	1.09 ± 0.11	22.2	54	HMXB, XP
10	GX 301−2	186.682	−62.767	22.46 ± 0.09	2.00 ± 0.12	89.3	51	HMXB, XP, T
11	Cen A	201.376	−43.059	20.51 ± 2.75	<14.65	6.5	1	AGN
12	Circinus galaxy	213.292	−65.323	1.77 ± 0.12	1.17 ± 0.16	11.1	29	AGN
13	PSR 1509−58	228.496	−59.141	1.21 ± 0.13	1.62 ± 0.17	9.6	74	PSR
14	4U 1516−569	230.174	−57.158	3.05 ± 0.10	<0.72	29.7*	113	LMXB, T, B, A
15	4U 1538−522	235.584	−52.376	2.53 ± 0.05	<0.32	26.4	308	HMXB, XP
16	IGR J15479−4529	237.055	−45.471	0.58 ± 0.03	<0.27	12.6	441	CV
17	XTE J1550−564	237.757	−56.458	0.61 ± 0.06	0.63 ± 0.07	8.6	240	LMXB, T, BHC
18	4U 1608−522	243.197	−52.420	2.13 ± 0.03	1.23 ± 0.04	44.6	469	LMXB, T, B, A
19	IGR J16167−4957	244.171	−49.957	0.27 ± 0.03	<0.17	6.2	577	?
20	IGR J16195−4945	244.844	−49.719	0.29 ± 0.03	<0.29	8.7	579	?
21	Sco X-1	244.990	−15.643	90.86 ± 0.12	2.33 ± 0.13	111.6	76	LMXB, Z
22	IGR J16207−5129	245.156	−51.510	0.36 ± 0.03	<0.28	10.0	528	?
23	4U 1624−49	246.983	−49.187	0.46 ± 0.03	<0.09	16.3*	589	LMXB, D
24	IGR J16318−4848	247.953	−48.801	2.31 ± 0.03	0.86 ± 0.03	61.9	658	HMXB
25	AX J1631.9−4752	248.009	−47.859	1.69 ± 0.03	0.47 ± 0.03	35.9	683	HMXB?
26	4U 1626−67	248.085	−67.480	2.75 ± 0.16	<0.60	17.3*	46	LMXB, XP
27	4U 1630−47	248.524	−47.390	8.32 ± 0.03	4.31 ± 0.03	202.4	713	LMXB, T, U, D
28	IGR J16358−4726	248.990	−47.407	0.44 ± 0.03	0.21 ± 0.03	16.4*	696	LMXB?, T
29	IGR J16393−4643	249.757	−46.676	0.82 ± 0.03	<0.16	12.7	727	?
30	4U 1636−536	250.231	−53.739	2.48 ± 0.03	1.13 ± 0.04	49.4	501	LMXB, B, A
31	IGR J16418−4532	250.437	−45.520	0.50 ± 0.03	<0.08	10.1	752	?
32	GX 340+0	251.450	−45.603	3.93 ± 0.03	<0.19	21.8	760	LMXB, Z
33	IGR J16479−4514	251.994	−45.217	0.48 ± 0.03	0.19 ± 0.03	11.9	768	?
34	PSR J1649−4349	252.409	−43.818	0.20 ± 0.03	<0.22	6.3	782	PSR
35	IGR J16558−5203	254.004	−52.075	<0.19	<0.20	6.1	572	?
36	AX J1700.2−4220	255.075	−42.326	0.20 ± 0.03	<0.19	6.8	798	?
37	OAO 1657−415	255.199	−41.653	9.90 ± 0.03	4.02 ± 0.03	248.3	800	HMXB, XP
38	GX 339−4	255.700	−48.783	0.78 ± 0.03	0.55 ± 0.03	21.9	687	LMXB, T, U, BHC
39	4U 1700−377	255.982	−37.841	23.49 ± 0.03	10.64 ± 0.03	571.6	793	HMXB
40	GX 349+2	256.439	−36.408	5.46 ± 0.03	<0.14	18.8	781	LMXB, Z
41	4U 1702−429	256.557	−43.029	1.42 ± 0.03	0.65 ± 0.03	31.8	794	LMXB, B, A
42	4U 1705−32	257.213	−32.333	0.36 ± 0.03	0.32 ± 0.03	10.2	737	?
43	4U 1705−440	257.223	−44.090	3.25 ± 0.03	1.49 ± 0.03	74.6	780	LMXB, B, A
44	IGR J17091−3624	257.289	−36.405	0.73 ± 0.03	0.49 ± 0.03	19.7	787	?
45	XTE J1710−281	257.583	−28.145	0.21 ± 0.03	0.33 ± 0.04	7.3	661	LMXB, T, B
46	EXMS B1709−232	258.122	−23.357	0.52 ± 0.03	<0.15	16.5*	568	Cluster
47	SAX J1712.6−3739	258.136	−37.632	0.52 ± 0.03	0.28 ± 0.03	12.1	800	LMXB, T, B
48	V2400 Oph	258.152	−24.270	0.40 ± 0.03	<0.18	7.5	592	CV
49	NGC 6300	259.209	−62.792	0.51 ± 0.06	<0.47	7.6	157	AGN, Sy2
50	IGR J17195−4100	259.878	−41.012	0.23 ± 0.03	<0.15	8.3*	786	?
51	XTE J1720−318	259.978	−31.748	0.45 ± 0.03	0.50 ± 0.03	15.0	773	LMXB, T, BHC
52	IGR J17200−3116	260.008	−31.274	0.24 ± 0.03	<0.24	6.8	768	?
53	IGR J17252−3616	261.309	−36.274	1.13 ± 0.03	0.27 ± 0.03	20.3	801	?
54	IGR J17254−3257	261.381	−32.961	0.32 ± 0.03	0.28 ± 0.03	8.6	797	?
55	GRS 1724−308	261.879	−30.790	2.33 ± 0.03	1.65 ± 0.03	65.1	788	LMXB, G, B, A
56	IGR J17303−0601	262.594	−6.000	0.28 ± 0.03	<0.18	8.3*	330	?
57	GX 9+9	262.939	−16.948	1.11 ± 0.03	<0.13	39.8*	580	LMXB, A
58	GX 354−0	262.990	−33.826	3.19 ± 0.03	0.75 ± 0.03	46.4	800	LMXB, B, A
59	GX 1+4	263.009	−24.735	2.34 ± 0.03	1.34 ± 0.03	64.8	741	LMXB, XP
60	GRS 1734−292	264.369	−29.131	0.64 ± 0.03	0.31 ± 0.03	15.8	796	AGN, Sy1
61	SLX 1735−269	264.571	−26.978	1.04 ± 0.03	0.68 ± 0.03	28.6	787	LMXB, B
62	4U 1735−444	264.741	−44.444	3.09 ± 0.03	<0.11	14.1	657	LMXB, B, A
63	SLX 1737−282	265.168	−28.313	0.39 ± 0.03	0.25 ± 0.03	10.8	797	LMXB, B, XP
64	1E 1740.7−2943	265.984	−29.735	4.68 ± 0.03	4.32 ± 0.03	147.3	799	LMXB, BHC
65	M1741−293	266.240	−29.336	0.86 ± 0.03	0.60 ± 0.03	24.4	800	LMXB, T, B
66	1E 1742.5−2859	266.490	−28.910	0.57 ± 0.03	0.28 ± 0.03	14.0	800	LMXB
67	1E 1742.9−2929	266.500	−29.491	0.63 ± 0.03	<0.10	22.4*	797	LMXB, B
68	IGR J17464−3213	266.562	−32.223	7.53 ± 0.03	4.01 ± 0.03	179.8	789	LMXB, T, BHC
69	IGR J17460−3047	266.580	−30.791	0.14 ± 0.03	<0.26	6.0	794	?
70	1E1743.1−2843	266.587	−28.752	0.55 ± 0.03	<0.22	8.9	800	LMXB
71	IGR J17475−2822	266.799	−28.444	0.28 ± 0.03	0.22 ± 0.03	10.0*	800	?
72	SLX 1744−299	266.844	−30.012	0.85 ± 0.03	0.40 ± 0.03	18.2	796	LMXB, B

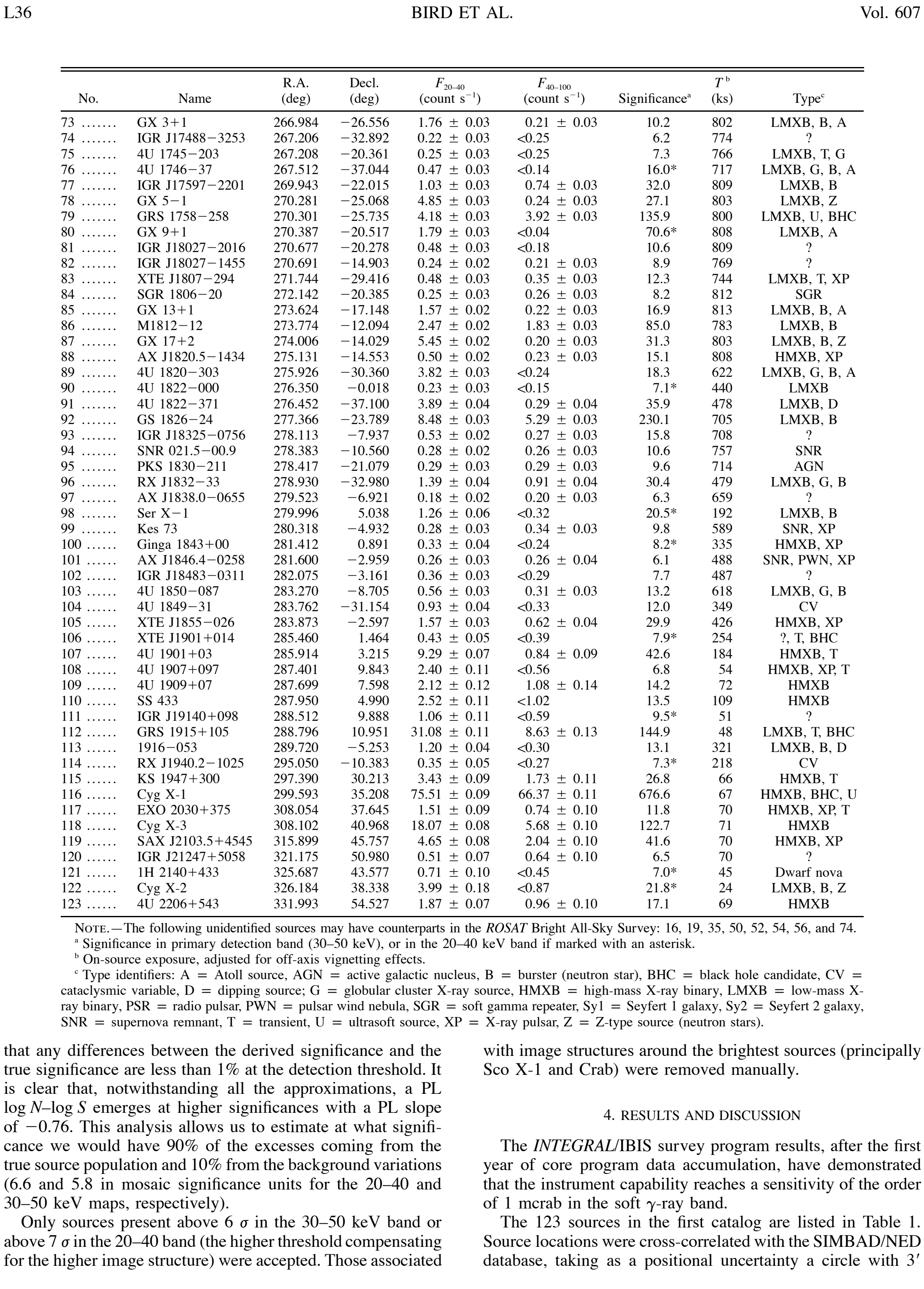

No.	Name	R.A. (deg)	Decl. (deg)	$F_{20–40}$ (count s^{-1})	$F_{40–100}$ (count s^{-1})	Significance[a]	T[b] (ks)	Type[c]
73	GX 3+1	266.984	−26.556	1.76 ± 0.03	0.21 ± 0.03	10.2	802	LMXB, B, A
74	IGR J17488−3253	267.206	−32.892	0.22 ± 0.03	<0.25	6.2	774	?
75	4U 1745−203	267.208	−20.361	0.25 ± 0.03	<0.25	7.3	766	LMXB, T, G
76	4U 1746−37	267.512	−37.044	0.47 ± 0.03	<0.14	16.0*	717	LMXB, G, B, A
77	IGR J17597−2201	269.943	−22.015	1.03 ± 0.03	0.74 ± 0.03	32.0	809	LMXB, B
78	GX 5−1	270.281	−25.068	4.85 ± 0.03	0.24 ± 0.03	27.1	803	LMXB, Z
79	GRS 1758−258	270.301	−25.735	4.18 ± 0.03	3.92 ± 0.03	135.9	800	LMXB, U, BHC
80	GX 9+1	270.387	−20.517	1.79 ± 0.03	<0.04	70.6*	808	LMXB, A
81	IGR J18027−2016	270.677	−20.278	0.48 ± 0.03	<0.18	10.6	809	?
82	IGR J18027−1455	270.691	−14.903	0.24 ± 0.02	0.21 ± 0.03	8.9	769	?
83	XTE J1807−294	271.744	−29.416	0.48 ± 0.03	0.35 ± 0.03	12.3	744	LMXB, T, XP
84	SGR 1806−20	272.142	−20.385	0.25 ± 0.03	0.26 ± 0.03	8.2	812	SGR
85	GX 13+1	273.624	−17.148	1.57 ± 0.02	0.22 ± 0.03	16.9	813	LMXB, B, A
86	M1812−12	273.774	−12.094	2.47 ± 0.02	1.83 ± 0.03	85.0	783	LMXB, B
87	GX 17+2	274.006	−14.029	5.45 ± 0.02	0.20 ± 0.03	31.3	803	LMXB, B, Z
88	AX J1820.5−1434	275.131	−14.553	0.50 ± 0.02	0.23 ± 0.03	15.1	808	HMXB, XP
89	4U 1820−303	275.926	−30.360	3.82 ± 0.03	<0.24	18.3	622	LMXB, G, B, A
90	4U 1822−000	276.350	−0.018	0.23 ± 0.03	<0.15	7.1*	440	LMXB
91	4U 1822−371	276.452	−37.100	3.89 ± 0.04	0.29 ± 0.04	35.9	478	LMXB, D
92	GS 1826−24	277.366	−23.789	8.48 ± 0.03	5.29 ± 0.03	230.1	705	LMXB, B
93	IGR J18325−0756	278.113	−7.937	0.53 ± 0.02	0.27 ± 0.03	15.8	708	?
94	SNR 021.5−00.9	278.383	−10.560	0.28 ± 0.02	0.26 ± 0.03	10.6	757	SNR
95	PKS 1830−211	278.417	−21.079	0.29 ± 0.03	0.29 ± 0.03	9.6	714	AGN
96	RX J1832−33	278.930	−32.980	1.39 ± 0.04	0.91 ± 0.04	30.4	479	LMXB, G, B
97	AX J1838.0−0655	279.523	−6.921	0.18 ± 0.02	0.20 ± 0.03	6.3	659	?
98	Ser X−1	279.996	5.038	1.26 ± 0.06	<0.32	20.5*	192	LMXB, B
99	Kes 73	280.318	−4.932	0.28 ± 0.03	0.34 ± 0.03	9.8	589	SNR, XP
100	Ginga 1843+00	281.412	0.891	0.33 ± 0.04	<0.24	8.2*	335	HMXB, XP
101	AX J1846.4−0258	281.600	−2.959	0.26 ± 0.03	0.26 ± 0.04	6.1	488	SNR, PWN, XP
102	IGR J18483−0311	282.075	−3.161	0.36 ± 0.03	<0.29	7.7	487	?
103	4U 1850−087	283.270	−8.705	0.56 ± 0.03	0.31 ± 0.03	13.2	618	LMXB, G, B
104	4U 1849−31	283.762	−31.154	0.93 ± 0.04	<0.33	12.0	349	CV
105	XTE J1855−026	283.873	−2.597	1.57 ± 0.03	0.62 ± 0.04	29.9	426	HMXB, XP
106	XTE J1901+014	285.460	1.464	0.43 ± 0.05	<0.39	7.9*	254	?, T, BHC
107	4U 1901+03	285.914	3.215	9.29 ± 0.07	0.84 ± 0.09	42.6	184	HMXB, T
108	4U 1907+097	287.401	9.843	2.40 ± 0.11	<0.56	6.8	54	HMXB, XP, T
109	4U 1909+07	287.699	7.598	2.12 ± 0.12	1.08 ± 0.14	14.2	72	HMXB
110	SS 433	287.950	4.990	2.52 ± 0.11	<1.02	13.5	109	HMXB
111	IGR J19140+098	288.512	9.888	1.06 ± 0.11	<0.59	9.5*	51	?
112	GRS 1915+105	288.796	10.951	31.08 ± 0.11	8.63 ± 0.13	144.9	48	LMXB, T, BHC
113	1916−053	289.720	−5.253	1.20 ± 0.04	<0.30	13.1	321	LMXB, B, D
114	RX J1940.2−1025	295.050	−10.383	0.35 ± 0.05	<0.27	7.3*	218	CV
115	KS 1947+300	297.390	30.213	3.43 ± 0.09	1.73 ± 0.11	26.8	66	HMXB, T
116	Cyg X-1	299.593	35.208	75.51 ± 0.09	66.37 ± 0.11	676.6	67	HMXB, BHC, U
117	EXO 2030+375	308.054	37.645	1.51 ± 0.09	0.74 ± 0.10	11.8	70	HMXB, XP, T
118	Cyg X-3	308.102	40.968	18.07 ± 0.08	5.68 ± 0.10	122.7	71	HMXB
119	SAX J2103.5+4545	315.899	45.757	4.65 ± 0.08	2.04 ± 0.10	41.6	70	HMXB, XP
120	IGR J21247+5058	321.175	50.980	0.51 ± 0.07	0.64 ± 0.10	6.5	70	?
121	1H 2140+433	325.687	43.577	0.71 ± 0.10	<0.45	7.0*	45	Dwarf nova
122	Cyg X-2	326.184	38.338	3.99 ± 0.18	<0.87	21.8*	24	LMXB, B, Z
123	4U 2206+543	331.993	54.527	1.87 ± 0.07	0.96 ± 0.10	17.1	69	HMXB

NOTE.—The following unidentified sources may have counterparts in the *ROSAT* Bright All-Sky Survey: 16, 19, 35, 50, 52, 54, 56, and 74.

[a] Significance in primary detection band (30–50 keV), or in the 20–40 keV band if marked with an asterisk.

[b] On-source exposure, adjusted for off-axis vignetting effects.

[c] Type identifiers: A = Atoll source, AGN = active galactic nucleus, B = burster (neutron star), BHC = black hole candidate, CV = cataclysmic variable, D = dipping source; G = globular cluster X-ray source, HMXB = high-mass X-ray binary, LMXB = low-mass X-ray binary, PSR = radio pulsar, PWN = pulsar wind nebula, SGR = soft gamma repeater, Sy1 = Seyfert 1 galaxy, Sy2 = Seyfert 2 galaxy, SNR = supernova remnant, T = transient, U = ultrasoft source, XP = X-ray pulsar, Z = Z-type source (neutron stars).

that any differences between the derived significance and the true significance are less than 1% at the detection threshold. It is clear that, notwithstanding all the approximations, a PL log N–log S emerges at higher significances with a PL slope of −0.76. This analysis allows us to estimate at what significance we would have 90% of the excesses coming from the true source population and 10% from the background variations (6.6 and 5.8 in mosaic significance units for the 20–40 and 30–50 keV maps, respectively).

Only sources present above 6 σ in the 30–50 keV band or above 7 σ in the 20–40 band (the higher threshold compensating for the higher image structure) were accepted. Those associated with image structures around the brightest sources (principally Sco X-1 and Crab) were removed manually.

4. RESULTS AND DISCUSSION

The *INTEGRAL*/IBIS survey program results, after the first year of core program data accumulation, have demonstrated that the instrument capability reaches a sensitivity of the order of 1 mcrab in the soft γ-ray band.

The 123 sources in the first catalog are listed in Table 1. Source locations were cross-correlated with the SIMBAD/NED database, taking as a positional uncertainty a circle with 3′

radius; furthermore, the positions were cross-checked with the HEASARC database to search for previous emission in the X-ray band above 10 keV. A simple classification by source type is provided in the table. In this first survey, we have detected (among others) 23 HMXBs, 53 LMXBs, five AGNs, and a further 28 sources not associated with any one type of object. Bright *ROSAT* All-Sky Survey sources are possible counterparts to a number of unidentified sources (see Table 1); more detailed correlation between *ROSAT* sources and IBIS sources will be presented elsewhere (in preparation).

The initial data analysis shows a soft γ-ray sky populated with discrete, mostly variable sources—several exhibiting transient behavior. The source distribution is currently only well defined in the Galactic center region (Lebrun et al. 2004); elsewhere the limited and varying exposure limits the analysis that can be made so far. The sources belong to all possible classes, being mainly galactic binaries containing a weakly magnetized neutron star. Others are pulsars (with and without SNRs) and a few are black hole candidates. Some of those binaries are heavily absorbed and show a Compton-thick envelope (Walter et al. 2003), suggesting a possible new class of high-energy emitters.

We acknowledge the following funding: in Italy, Italian Space Agency financial and programmatic support via contracts I/R/389/02 and I/R/041/02; in the UK, PPARC grant GR/2002/00446; and in France, we thank the CNES for support during ISGRI development and *INTEGRAL* data analysis.

REFERENCES

Bertin, E., & Arnouts, S. 1996, A&AS, 117, 393
Bodaghee, A., et al. 2004, in Proc. Fifth *INTEGRAL* Science Workshop (ESA SP-552; Noorwijk: ESA), in press
Courvoisier, T. J.-L., et al. 2003, A&A, 411, L53
Goldwurm, A., et al. 2003, A&A, 411, L223
Harmon, B. A., et al. 2002, ApJS, 138, 149
in 't Zand, J. J. M., et al. 2004, Nucl. Phys. B Suppl. Ser., in press
Jager, R., et al. 1997, A&AS, 125, 557
Lebrun, F., et al. 2003, A&A, 411, L141
———. 2004, Nature, 428, 293
Levine, A. M., et al. 1984, ApJS, 54, 581
Shaw, S. E., et al. 2004, A&A, in press
Sugizaki, M., Mitsuda, K., Kaneda, H., Matsuzaki, K., Yamauchi, S., & Koyama, K. 2001, ApJS, 134, 77
Terrier, R., et al. 2003, A&A, 411, L167
Ubertini, P., Bazzano, A., Cocchi, M., Heise, J., in 't Zand, M. J. J., Muller, M. J., Natalucci, L., & Smith, S. M. J. 1999, Astrophys. Lett. Commun., 38, 129
Ubertini, P., et al. 2003, A&A, 411, L131
Vargas, M., et al. 1996, in ASP Conf. 102, The Galactic Center, Fourth ESO/CTIO Workshop, ed. R. Gredel (San Francisco: ASP), 431
Walter, R., et al. 2003, A&A, 411, L427
Winkler, C., et al. 2003, A&A, 411, L1

Part III

Individual IGR Sources

Chapter 6

Multi-wavelength Observations of IGR Sources

The ISGRI surveys presented in Part II led to a number of new source discoveries. These new sources are dubbed IGR(s) for *INTEGRAL* Gamma-Ray source(s). The first IGR source, IGR 16318−4848 (Courvoisier et al. 2003b), underwent follow-up observations in the soft X-rays which showed that its spectrum features an extremely high column density ($N_{\rm H} \sim 10^{24}\,{\rm cm}^{-2}$). This can only be attributed to matter local to the source, since it is about 2 orders of magnitude greater than the absorption expected along the line of sight (Dickey & Lockman 1990).

Thereafter, many other IGRs were exposed as having large $N_{\rm H}$ values leading Walter et al. (2004b) and Kuulkers (2005) to label them as new members of the growing class of absorbed Galactic X-ray binaries. In order to produce such high levels of absorption, the vicinity of the compact primary (i.e. neutron star or black hole) must be dense with material. While a thick disk can sometimes suffice, the more likely scenario involves the compact object being deeply embedded in the radial stellar wind of a high-mass companion ($M \gtrsim 10\,M_{\odot}$) (Walter et al. 2006).

Absorption affects the spectrum $\lesssim$ 5–10 keV which is one reason why these sources eluded detection by previous X-ray missions. Photons emitted above 20 keV are energetic enough to penetrate obscuring matter along the line of sight. By operating in this enery range, ISGRI is able to reveal sources that are otherwise hidden behind both the shell of material around the source, and the dust and gas along the Galactic Plane. Therefore, deep, wide-field observations by *INTEGRAL* represent an ideal way to discover absorbed sources. However, follow-up X-ray monitoring by e.g. *XMM-Newton* is necessary to extend the source spectrum below 20 keV in order to detect an absorption, iron lines, a spectral break in the continuum, and to refine the position so that an optical/IR counterpart can be determined.

We studied IGR J16393−4643, IGR J16320−4751, IGR J17252−3616 and IGR J17497−2821 in detail using multi-wavelength observations. The first three are shown to be absorbed X-ray pulsars consisting of a slowly-rotating neutron star (pulse periods ~1 ks) accreting from the wind of a supergiant star. The last one, IGR J17497−2821, is a system comprised of a black hole and a low-mass star. The following chapters describe my contributions to the analyses of these 4 sources, and our main conclusions.

Chapter 7

IGR J16393−4643

IGR J16393−4643 was discovered in the X-ray band with *ASCA* and was listed as AX J163904−4642 (Sugizaki et al. 2001). Its flat power-law slope ($\Gamma = -0.01$), its absorption ($N_\mathrm{H} = 13^{+9}_{-7} \cdot 10^{22}\,\mathrm{cm}^{-2}$), its lack of radio emission, and its position in the galactic plane ($l = 337.99^\circ$ and $b = 0.07^\circ$) compelled Sugizaki et al. (2001) to classify it as a HMXB.

On April 21, 2003, we detected IGR J16393−4643 with ISGRI at an average flux of 0.85 cps in a 15–40 keV mosaic image created from the first GPS and GCDE observation period (revolutions 50–59). An announcement was made in the 1st ISGRI Catalog (Bird et al. 2004). Malizia et al. (2004) noted a possible association between IGR J16393−4643 and the unidentified *EGRET* source 3EG J1639−4702 (Hartman et al. 1999). Combi et al. (2004) discovered non-thermal radio emission within the 58″ *ASCA* error box. This suggests that IGR J16393−4643 is a dust-enshrouded microquasar (μQSO). The radio emission would be the signature of jets emanating from the vicinity of a black hole which is surrounded by a thick accretion disk. A μQSO scenario could also help justify the IBIS and *EGRET* association.

A follow-up observation of IGR J16393−4643 was obtained with *XMM-Newton*. The set of *INTEGRAL* and *XMM-Newton* data are introduced in Section 7.2, as are the refined X-ray positions that we used to locate the most likely counterpart at other wavelengths. Timing and spectral analyses are presented in Sections 7.3 and 7.4, respectively. Finally, we discuss the nature of IGR J16393−4643 and we offer our conclusions in Section 7.5.

7.1 Data & Analysis

7.1.1 ISGRI

Using the Archive Browse feature on the ISDC Web page, we selected all CP and public ScWs that had the source position from Bird et al. (2004) within 20° of the center of the ISGRI FOV. As of January 3, 2005, this sample spanned the first 244

Table 7.1: Journal of ISGRI observations of IGR J16393−4643. Listed for each SC revolution are the number of ScWs which had the source position within the FOV, the start time of the revolution, the effective exposure time on the source, and the average source off-axis angle. Revolutions which have less than 5 ScWs with the source on target are excluded.

Rev.	ScWs	start MJD	exp. ks	angle °	Rev.	ScWs	start MJD	exp. ks	angle °
		public data					core program		
30	21	52650.86	48.5	14.7	164	13	53052.23	24.7	14.2
32	8	52657.93	19.4	14.8	165	14	53054.43	26.0	13.2
37	94	52671.23	208.5	3.8	167	58	53061.24	108.5	9.5
38	42	52674.12	92.5	3.6	168	18	53063.10	32.7	10.8
46	37	52698.57	76.7	13.6	169	8	53066.48	14.4	18.2
47	90	52701.03	160.9	7.0	171	7	53072.18	13.2	18.2
49	49	52707.78	87.6	6.2	173	15	53078.14	27.0	9.3
50	60	52710.00	111.3	9.7	174	30	53081.06	54.2	9.3
51	44	52712.99	79.5	11.3	179	6	53097.31	10.7	15.2
52	53	52717.40	96.0	10.1	183	10	53107.98	18.0	15.6
53	18	52718.97	32.1	16.8	185	10	53114.69	18.0	15.6
54	59	52722.25	108.2	10.0	226	7	53236.57	17.6	10.6
55	44	52724.95	98.7	11.9	229	5	53245.82	11.0	7.3
57	34	52732.51	77.2	11.7	232	79	53254.49	143.3	9.3
58	16	52734.03	36.3	15.0	233	39	53257.99	77.0	9.2
60	50	52739.91	105.8	12.6	234	26	53260.35	49.5	13.1
61	12	52742.90	24.8	15.8	235	28	53263.35	54.2	10.3
63	7	52750.26	13.0	16.5	243	6	53289.53	10.8	16.2
100	113	52859.62	209.8	6.9	244	7	53290.47	12.7	17.1
101	15	52862.50	27.9	9.1					
103	61	52868.96	109.7	13.6					
105	12	52874.57	41.2	18.1					
106	8	52878.96	29.9	18.2					
107	8	52882.72	28.5	18.2					
108	5	52885.20	18.0	18.3					
116	64	52907.95	129.1	7.0					
118	83	52913.45	153.4	10.1					
119	16	52916.46	30.1	15.0					

revolutions (2,550 ScWs). Because the region of IGR J16393−4643 was regularly monitored by the ISGRI GPS, the total exposure time on the source was 4.4 Ms after 2 years. To minimize the number of potentially bad ScWs affecting the quality of the output mosaic, ScWs with exposure times less than 2 ks were excluded yielding a sample of ~1,500 ScWs.

Several versions of OSA were released during the course of this analysis. The large data set, and the demands it would place on computing power and on disk space, limited the number of times we could reanalyze all of the data with each renewed software package. Most of the analysis relied on OSA 4.2. When OSA 5.0 became available, it was an opportunity to test the OSA packages under similar conditions, and to redo some of the analysis with improved software. This was especially the case for the timing analysis, which is relatively easy to generate.

Analyses were performed on an observation group created from each ScW. In this way, if an analysis of a single ScW were to fail for any reason (usually due to a faulty pointing or an incorrect parameter setting), the other ScWs will still be analyzed since they are treated independently. The bad ScWs are reanalyzed when possible. Computational processes were distributed across a grid network of Linux-operated machines.

Version 20 of the ISDC General Reference Catalog (see Chapter 10) selected for the ~250 sources with `ISGRI_FLAG==1` (i.e. previously detected by ISGRI) served as the input source list. The catalog position was used to fit the source rather than allowing the software to find its best position. The analysis began with the correction phase and ended once it had created an image in the energy band specified (typically, 22.09–63.26 keV). Source fluxes were extracted for all catalog sources in the FOV that were detected with a significance above 3σ. Around 10 new sources were expected in the FOV, but any new source below 5σ was considered to be spurious. These settings were based on experience with the instrument and on the characteristics of the observed field.

A journal of ISGRI observations of IGR J16393−4643 is reported in Table 7.1. Given the large error radius on the source position, it is unrealistic to expect to distinguish the optical counterpart to IGR J16393−4643. For JEM-X, its smaller FOV means fewer ScWs that contain the source position with an acceptable off-axis angle. Furthermore, JEM-X has never detected IGR J16393−4643, and SPI is unable to resolve the source in such a crowded field. Hence, data from OMC, JEM-X, and SPI were not used.

The process described above was repeated for 22.09–40.28 keV. For the source spectrum, the analysis involved 5 energy bands: 22.09–25.92, 25.92–30.23, 30.23–40.28, 40.28–51.29, and 51.29–63.26 keV. These boundaries were chosen to be compatible with the energy bands of the ISGRI response files.

7.1.2 *XMM-Newton*

XMM-Newton (Jansen et al. 2001) observed IGR J16393−4643 on March 21, 2004, from 08:21:15 to 11:41:15 (UT) as part of proposal ID: 020638 (PI: R. Walter) which includes follow-up observations of IGR J16320−4751, IGR J17252−3616, and others (see Chapter 8). A detailed description of the procedure that was used for *XMM-Newton* data reduction of IGR J16393−4643 (as well as for IGR J17252−3616) can be found in the doctoral thesis of Juan Antonio Zurita Heras (2006). The Science Analysis System (SAS) 6.1.0 software was used to analyze background-subtracted data from the EPIC MOS(1-2) (Turner et al. 2001) and PN (Strüder et al. 2001) cameras. The effective exposure times were around 8.4, 8, and 7 ks for MOS-1, MOS-2, and PN, respectively.

The *XMM-Newton* observation corresponds to *INTEGRAL* revolution 175. In this revolution, there were 5 consecutive ISGRI pointings that had the source within the FOV and that were simultaneous to the *XMM-Newton* observation (ScWs: 017500590010–017500630010), but the data were private.

7.2 Imaging & Counterparts

Intensity, significance, variance, and exposure mosaic images were constructed from background-subtracted images of individual ISGRI pointings. The flux spread of the mosaic pixels was based on the statistical weight of each image, with a vignetting correction to account for distortions near the edge of the image.

Mosaic energy bands and timescales were tailored to answer specific questions. Broad-band mosaics are best for collecting as many photons as possible in a short time (∼100 ks). On the other hand, narrow-band mosaics that accumulate long periods of exposure (∼1 Ms) can be used to determine an average source spectrum.

Figure 7.1 presents the ISGRI intensity map of IGR J16393−4643 and its vicinity in the 20–40 keV band for revolutions 30–185. Using this image, we extracted a source location of R.A. (J2000) = $16^h39^m05^s$, and Dec. = $-46°42'16''$. The error radius is $26''$ which includes $12''$ due to systematic uncertainties. This position agrees with and improves on the X-ray positions offered by Bird et al. (2004) and Sugizaki et al. (2001) (see Table 7.2).

IGR J16393−4643 is clearly detected in images taken by EPIC. Figure 7.2 presents an image of IGR J16393−4643 from the MOS-1 camera. Furthermore, the source coincides with the updated ISGRI position and error circle from this analysis. The refined (J2000) X-ray position averaged from MOS and PN is R.A. = $16^h39^m05.41^s$, and Dec. = $-46°42'11.9''$, with an uncertainty of $4''$. This is the most precise X-ray position of IGR J16393−4643 to date (see Table 7.2).

Figure 7.3 shows that the *XMM-Newton* error circle for IGR J16393−4643 does not

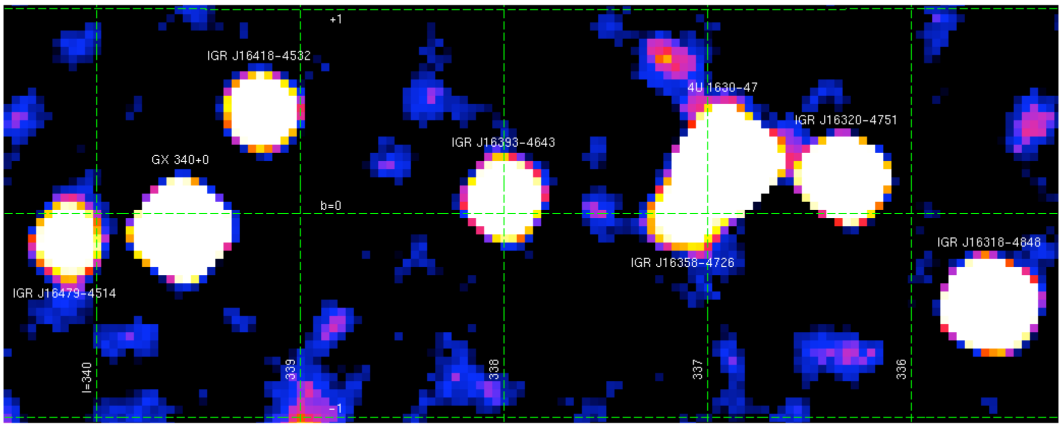

Figure *7.1: Intensity map of the region around IGR J16393−4643 in the 20–40 keV band accumulating ISGRI data from revolutions 30–185 for an effective exposure time of 670 ks.*

Table 7.2: The position and error radius of IGR J16393−4643 from various references.

Instrument	energy band keV	R.A. J2000	Dec. J2000	error ″	reference
ASCA	2–10	16 39 04	-46 42 47	58	Sugizaki et al. (2001)
INTEGRAL-ISGRI	20–40	16 39 02	-46 40 34	42	Bird et al. (2004)
INTEGRAL-ISGRI	20–40	16 39 05	-46 42 16	26	this work
XMM-Newton	0.1–12	16 39 05.41	-46 42 11.9	4	this work

intersect the error boxes of the radio source MOST J1639.0−4642 and of the far infrared source IRAS 16353−4636. These were the possible counterparts proposed by Combi et al. (2004) that led them to believe that IGR J16393−4643 is a microquasar. The tight *XMM-Newton* error circle excludes optical counterparts from the USNO-B1 catalog (Monet et al. 2003), radio sources from the Vizier database (Ochsenbein et al. 2000), and *ROSAT* sources (Voges et al. 1999). A single infrared source belonging to the Two Microns All-Sky Survey (2MASS: Cutri et al. 2003), 2MASS J16390535−4642137, is compatible with the *XMM-Newton* position.

7.3 Timing Analysis

7.3.1 Long-term Behavior

There are only a few pointings in which IGR J16393−4643 is detected above the 4σ level (see Fig. 7.4). The temporal behavior of the source was initially assessed by creating 4 broad-band (20–60 keV) mosaics which correspond to the 4 GPS observation periods. In each one, IGR J16393−4643 was detected with a significance above a conservative level of 6σ. This is a first indication that IGR J16393−4643

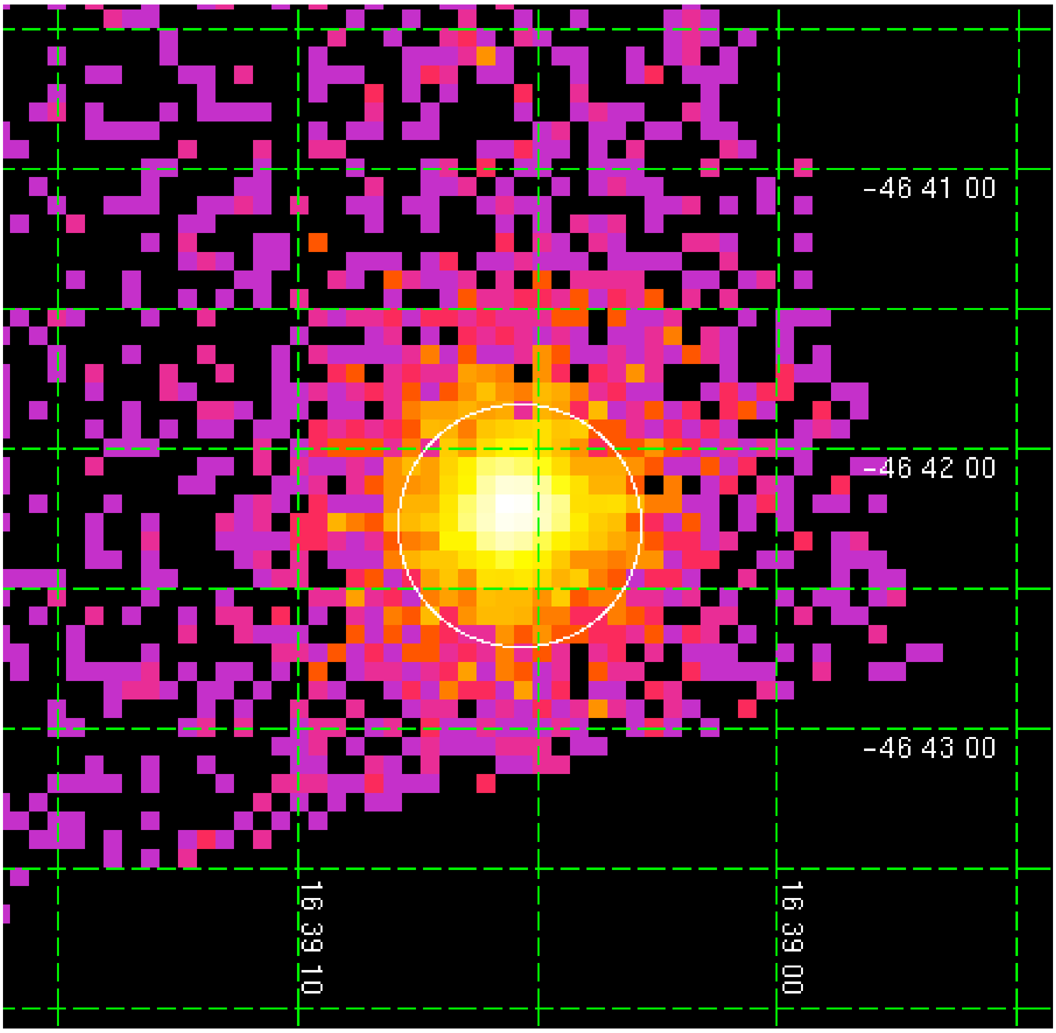

Figure *7.2: MOS-1 image of IGR J16393−4643 in the 0.15–12 keV energy range with an effective exposure time of 8.4 ks. The refined ISGRI error circle from our analysis is superimposed.*

is a persistent γ-ray source.

Mosaic images were then generated for each spacecraft revolution in the 20–60 and 60–100 keV bands. The OSA task `mosaic_spec` was used to extract the source flux and error, its significance, and the effective exposure time from each image. Whenever the source significance in a revolution mosaic was less than 4σ, an upper limit (3σ) was determined from the variance map of that revolution. Table 7.3 lists these results.

The persistence of IGR J16393−4643 in the 20–60 keV energy range is apparent in Figure 7.5. In each of the 4 GPS observation periods, there is at least 1 revolution in which the source was detected in the mosaic image. IGR J16393−4643

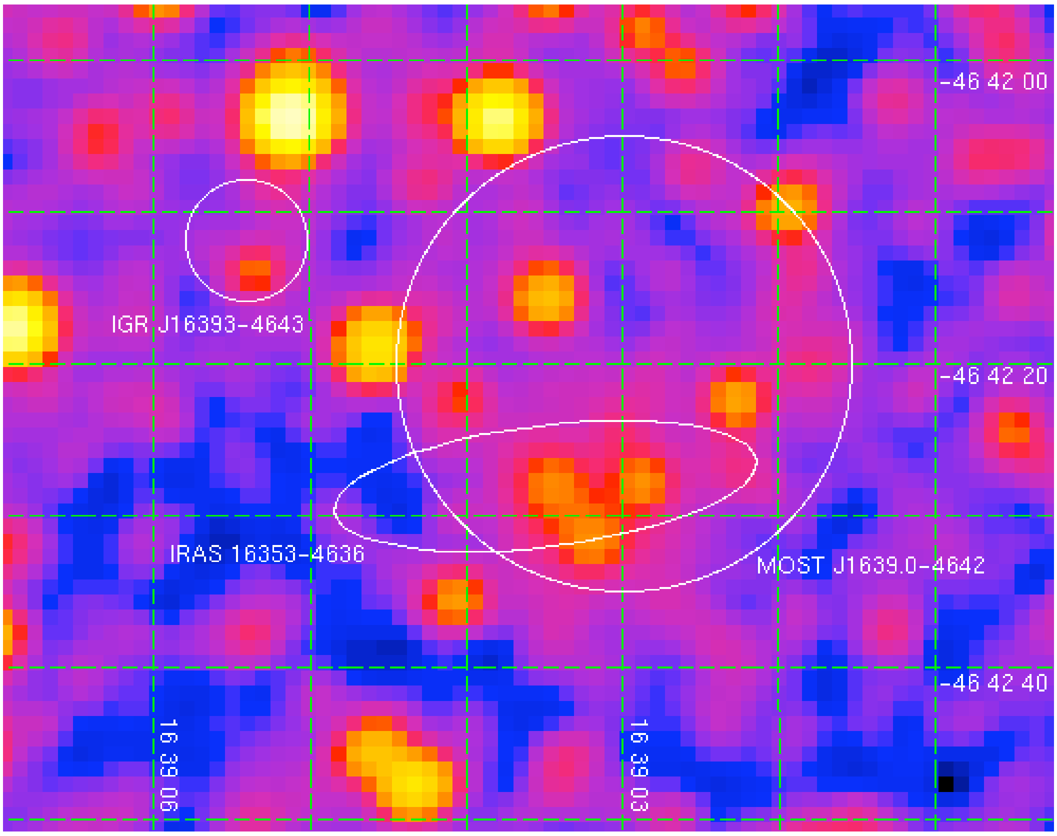

Figure *7.3: Image from 2MASS (Cutri et al. 2003) of the region around IGR J16393−4643 in the K_s band. The only infrared object inside the* XMM-Newton *error circle is 2MASS J16390535−4642137.*

presents strong variability as well. The highest flux registered in an individual 2 ks pointing of the 20–60 keV band was 4.3±0.6 cps, or ∼ 29 mCrab (MJD 52673.623–52673.641). Compared with the average count rate in revolution 100 (0.21±0.05 cps), the source flux varied by a factor larger than 20.

At higher energies (60–100 keV), the source was not detected above 4σ on any timescale (from a 2-ks pointing, to a revolution mosaic of ∼100 ks, to the full-data mosaic of ∼1 Ms).

7.3.2 Pulsations

Figure 7.6 shows the PN image of IGR J16393−4643 and the regions that were used to extract source and background light curves. The background region was chosen within the same detector chip as the source region, and at an equivalent distance from the detector edge. In these 1’-wide regions, single and double events with energies between 0.4 and 10 keV were collected in 3-s bins. The FTOOLS `lcmath` was then used to subtract the background, resulting in the light curve shown in

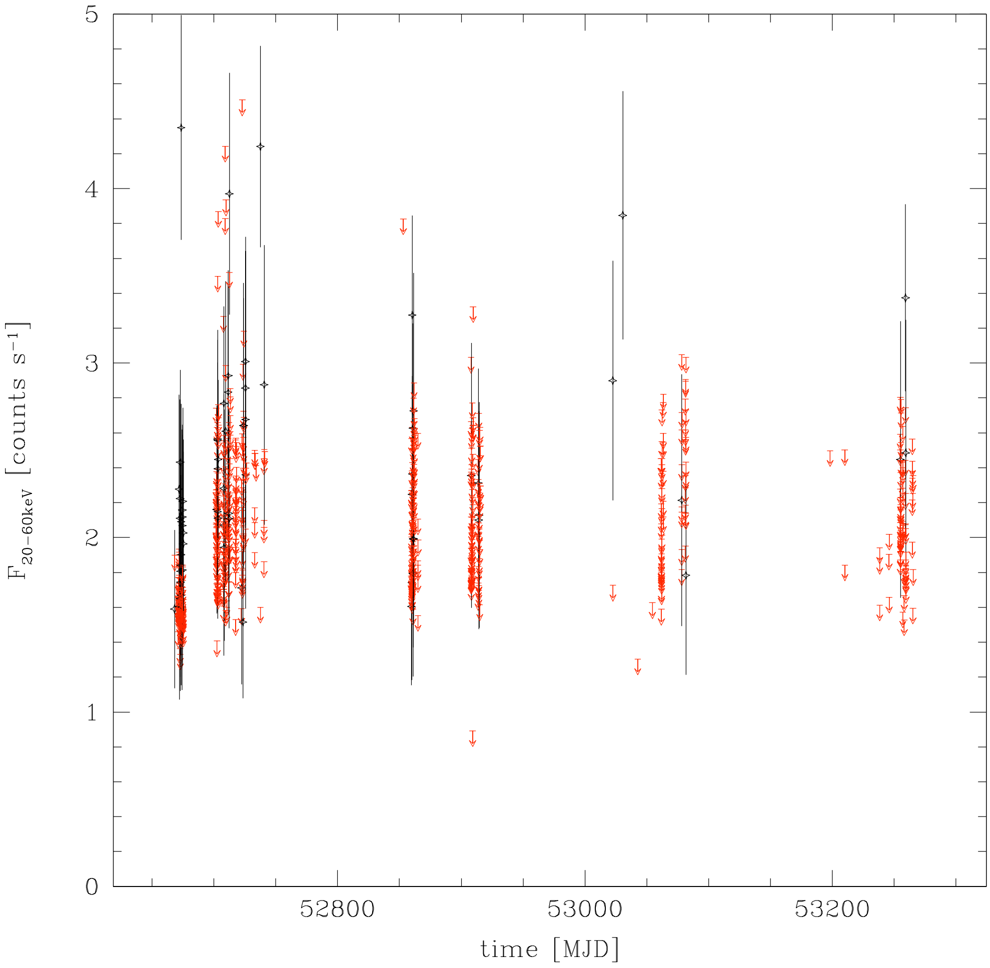

Figure *7.4: Light curve from ISGRI (20–60 keV) of IGR J16393−4643 where each point represents the flux from a single ScW. Upper limits (3σ) are provided when the source is not detected at the 4σ level.*

Fig. 7.7. Events with high background activity are excluded. This appears in the light curve as a source count rate of 0.

During the PN observation, the source count rate varied from 1 to 4 cps. Furthermore, the variations occured periodically and with structure in each cycle. By searching for modulations in the power spectrum (`powspec`) and in the χ^2 distribution (`efsearch`), we obtained a period of 912±5 s at a χ^2 of ~600. The pulse period and error were calculated using the procedure developed by Horne & Baliunas (1986) on Lomb-Scargle periodograms (see Fig. 7.8). An alternative procedure, the bootstrap method, returned a similar pulse period uncertainty. The large uncertainty on the pulse period is due to the short observation time which only covered 5 cycles. Two peaks are visible in the PN pulse profile folded with

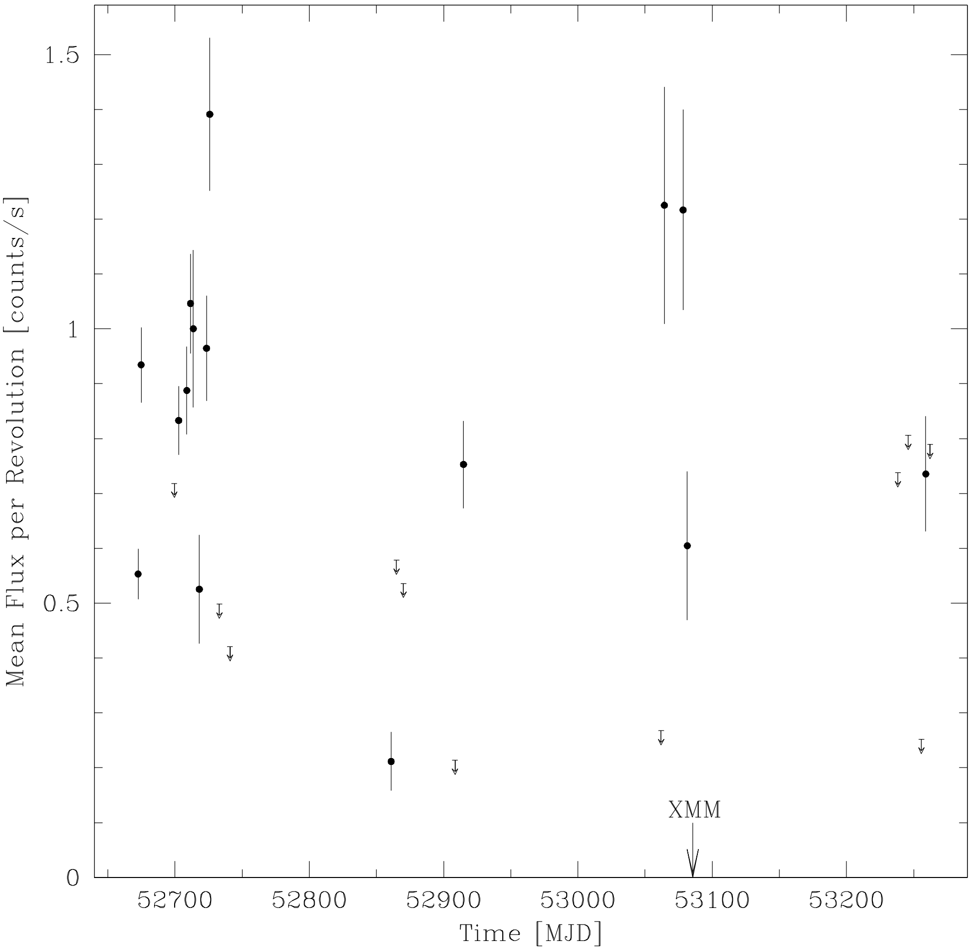

Figure *7.5: ISGRI light curve (20–60 keV) of IGR J16393−4643 where each point represents the flux averaged over 1 spacecraft revolution. Revolutions with less than 10 ks of effective exposure on the source, and those for which the source off-axis angles are larger than* 15° *are excluded. Upper limits (3σ) are provided when the source is not detected. The* XMM-Newton *observation occurred on MJD 53085.*

a period of 912 s as illustrated in Fig. 7.9 which indicates that both magnetic poles come into view during a cycle.

For a number cycle n, the ephemeris of IGR J16393−4643 is therefore:

$$\mathrm{MJD}\,T = \mathrm{MJD}\,53085.38738 + n \times (912\,\mathrm{s}/86,400) \tag{7.1}$$

To check whether the modulation affected the γ-rays, 100-s binned light curves were generated in the ISGRI 15–40 keV band by the task `iilight`. The light curves from revolutions 37–55 were merged because they represented a nearly-

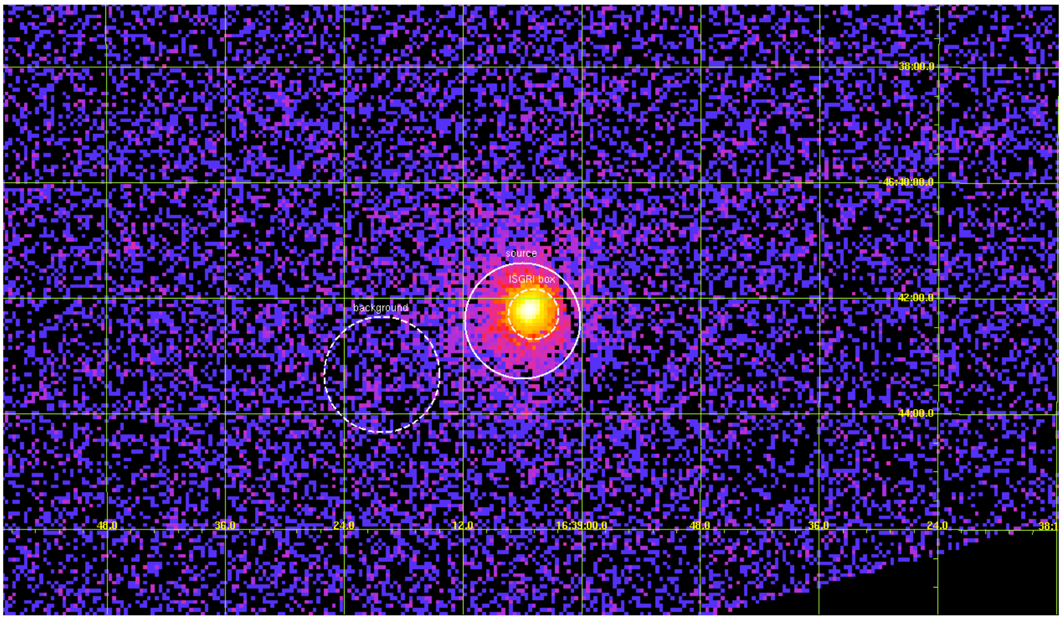

Figure *7.6: Image from PN with the 26" ISGRI error circle from this analysis, and the 1'-wide regions that served for the extraction of source and background light curves.*

continuous observation, and because the source was detected significantly in almost every revolution. A Lomb-Scargle periodogram of this light curve yielded a pulse period of 912.0±0.1 s. Here, the uncertainty is much lower than for PN owing to the fact that the combined observation covers around 100 cycles. The ISGRI periodogram is compatible with that of PN with a similar bimodal structure.

The modulation can be interpreted as the spin of the neutron star (NS) primary in IGR J16393−4643. A scenario involving a black hole primary (as in a μQSO) is henceforth rejected. The long spin period is typical of a NS with wind-driven accretion from a supergiant companion.

7.4 Spectral Analysis

7.4.1 Time-averaged Spectrum

Figure 7.10 presents the 0.4–50 keV spectrum of IGR J16393−4643 from EPIC and ISGRI data. A simple power law fit to the ISGRI 20–40 keV spectrum returned a relatively steep photon index ($\Gamma = 4.48^{+0.41}_{-0.31}$). An absorbed power law applied to the MOS and PN spectra gave a photon index of 1.02±0.09 with $N_\mathrm{H} = (31 \pm 1) \cdot 10^{22}\,\mathrm{cm}^{-2}$. Figure 7.11 focuses on the PN spectrum of IGR J16393−4643, in which we find a heavily-absorbed continuum below 4 keV, iron emission lines at 6.4 keV (Fe K_α) and at 7.1 keV (Fe K_β), a discontinuity in the continuum above 7.1 keV suggestive of an iron absorption edge, and an excess of soft emission between 0.5 and 2 keV.

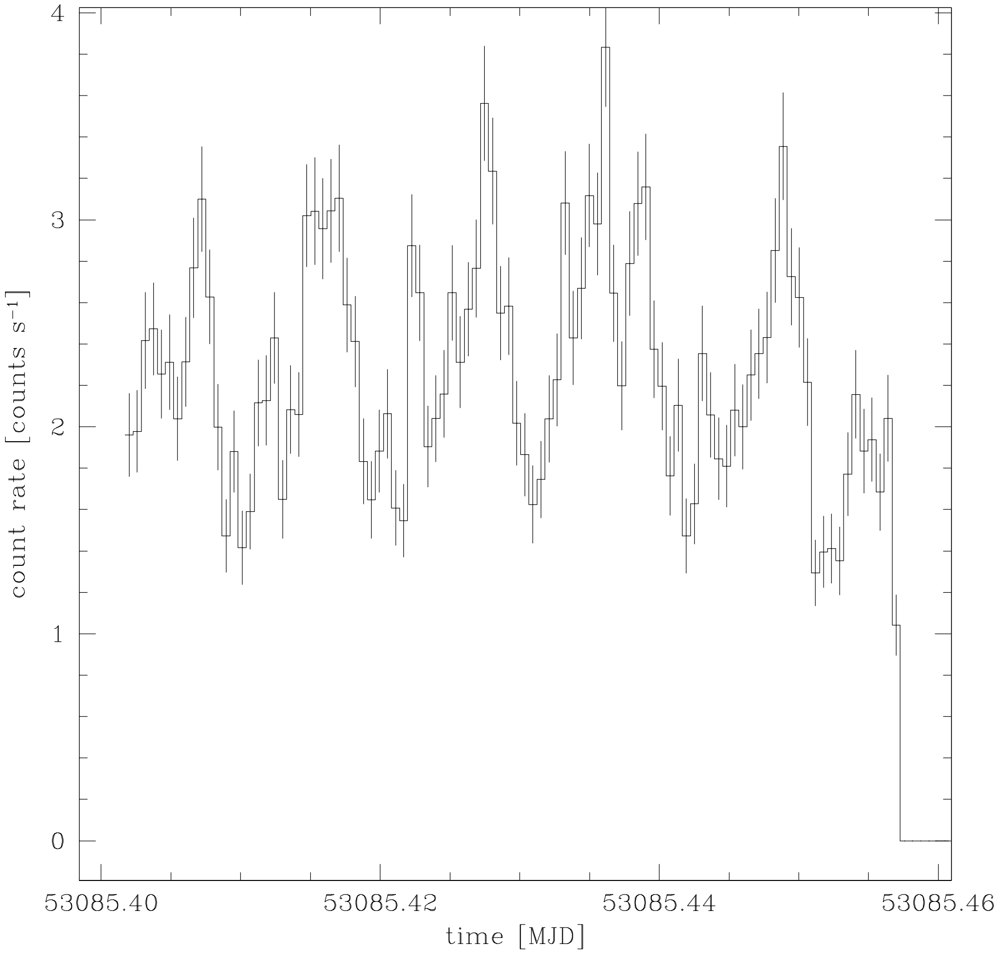

Figure *7.7: PN light curve for IGR J16393−4643 in the 2–10 keV energy range.*

The spectra from EPIC and ISGRI were fit with an absorbed power law, but this model left significant residuals in the hard X-rays. Recall that the EPIC photon index was smaller than the one observed for ISGRI alone indicating a spectral break. Such spectral shapes—a flat power law at low energies with a high-energy cutoff between 10–20 keV beyond which the slope steepens—are typical of X-ray pulsars (White et al. 1995).

Therefore, the combined EPIC and ISGRI spectra were fit with a broken power law (BP). The phenomenological BP model is usually interpreted physically as a Compton emission (CE) model (`comptt` within XSPEC). Both models were modified by Galactic absorption in the direction of the source, and an intrinsic absorption. Soft excess emission was represented by a blackbody that was affected by the Galactic absorption only. Two narrow Gaussians described the iron lines

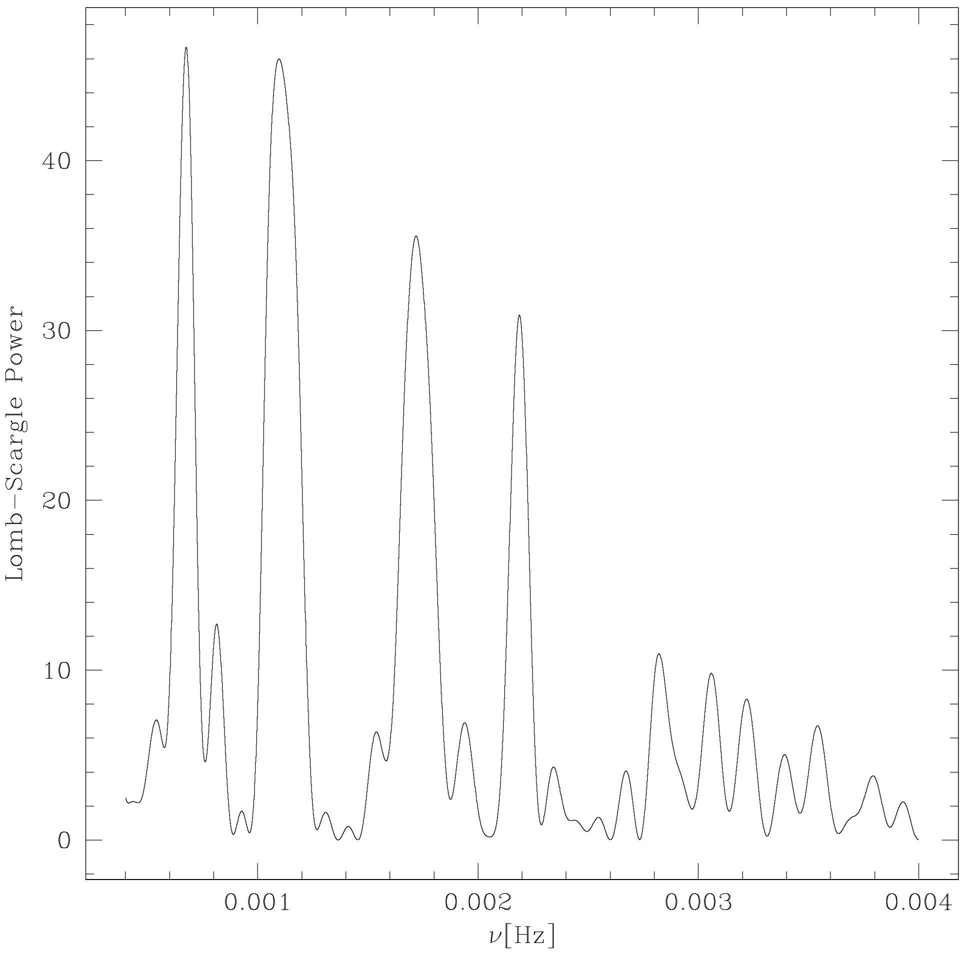

Figure *7.8: Lomb-Scargle periodogram for IGR J16393−4643 using the light curve from PN. The peak in the power density spectrum occurs at* $\nu \sim 0.0011$ *Hz or ~912 s.*

whose abundances ($Z_{\rm Fe}$) were left free. A constant (C_I) accounted for the asynchronous observations and for cross-calibration uncertainties.

Parameters from the various models are listed in Table 7.4. Note that the BP model required one more parameter than the the CP model and it could not constrain the break energy unless C_I was fixed at 1. The absorbed, integrated fluxes of IGR J16393−4643 (in units of 10^{-11} ergs cm^{-2} s^{-1}) were 4.4 in the 2–10 keV band, and 5.1 in the 20–60 keV band.

Overall, the time-averaged, broad-band spectral parameters of IGR J16393−4643 are reminiscent of other HMXBs where the NS accretes the radial wind of a SG companion.

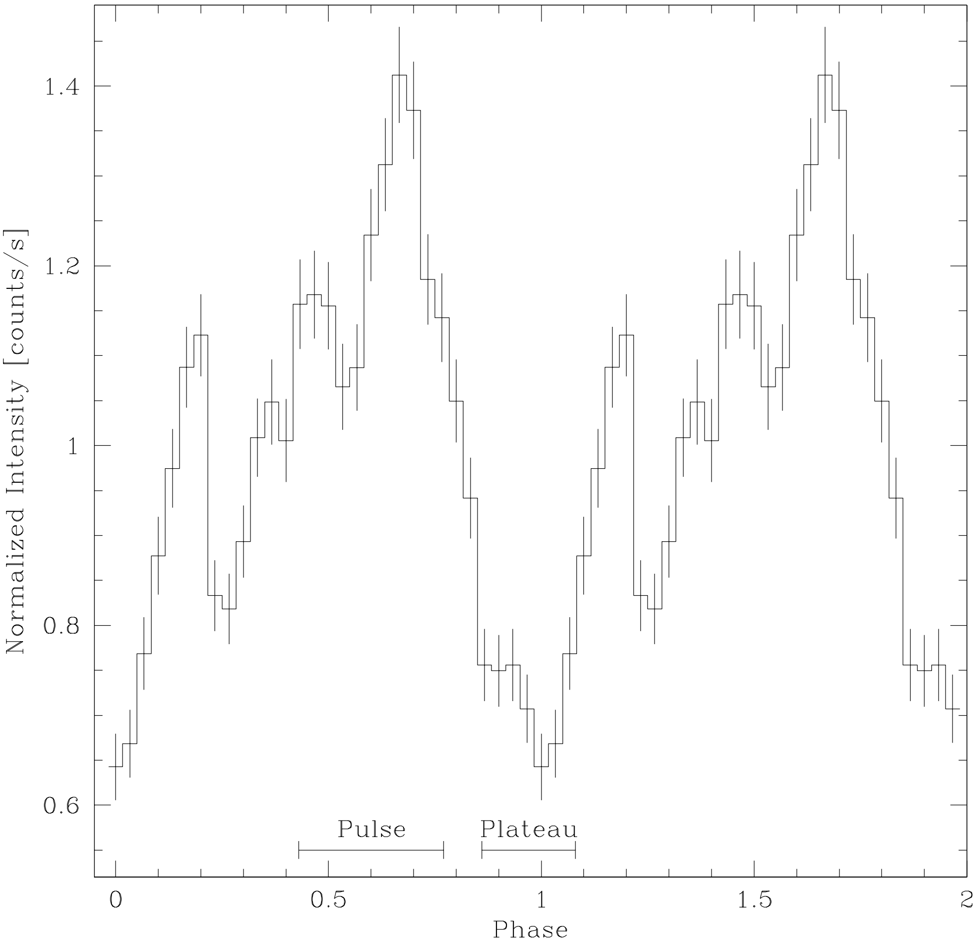

Figure *7.9: Folded PN light curve for a pulse period of 912 s beginning at MJD 53085.38738. The intervals indicate the pulse and plateau states of the phase-resolved spectrum.*

7.4.2 Phase-resolved Spectrum

To determine whether the pulsations affected the source spectrum, the PN spectra were binned according to two states: a pulse state around the primary peak in the folded light curve, and a plateau state (see Fig. 7.9). The pulsation changed the normalizations but did not modify the shape of the spectra nor its parameters, specifically the N_{H}, in any appreciable way.

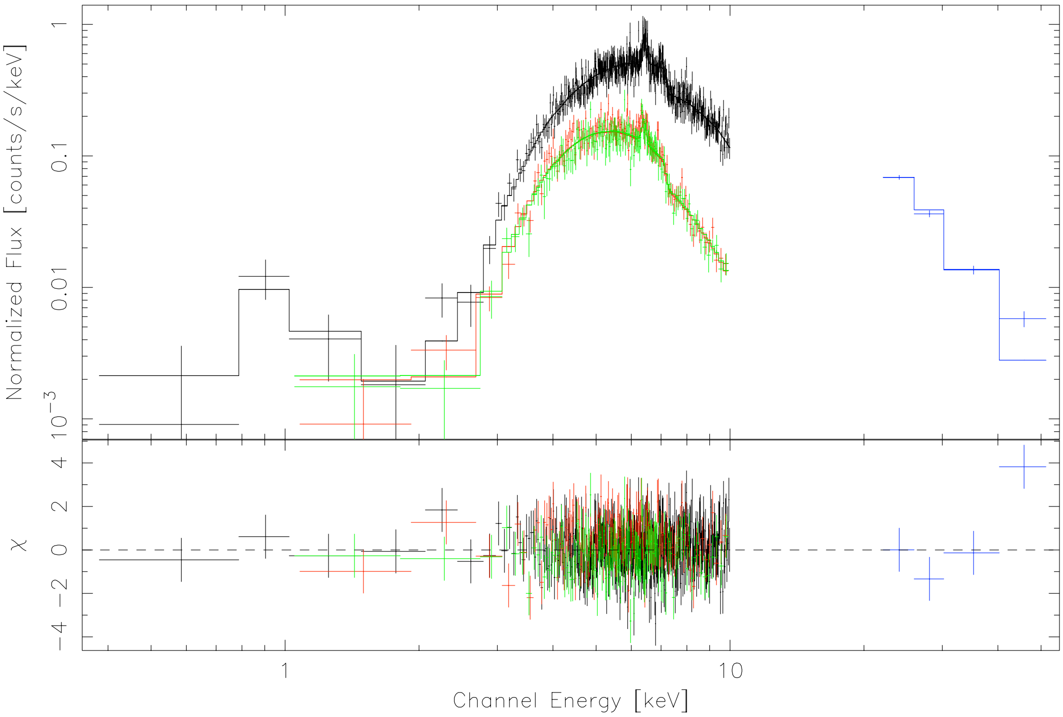

Figure *7.10: Photon spectrum of IGR J16393−4643 from PN (black), MOS-1 (green), MOS-2 (red), and ISGRI (blue), fit with the comptonized continuum model (CE).*

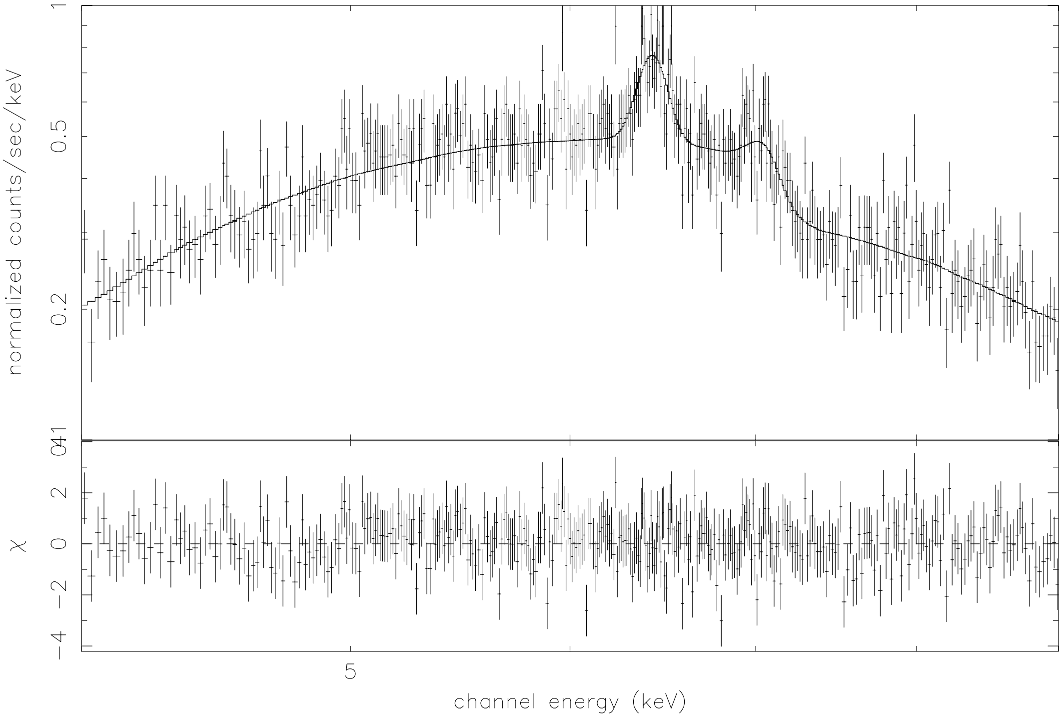

Figure *7.11: Spectrum of IGR J16393−4643 from PN data.*

7.5 Discussion

Observations of IGR J16393−4643 by *INTEGRAL* and *XMM-Newton* reveal a source that is highly-obscured, persistent in the 20–40 keV band, with significant variations in intensity. We discovered a pulsation period of 912 s.

Our *XMM-Newton* position for IGR J16393−4643 is incompatible with the position of any known radio source. The pulsation and the lack of radio emission invalidate the microquasar interpretation for the HMXB. Also, the chance association of the *EGRET* source with IGR J16393−4643 is strong given the high density of sources in the region. A single infrared candidate, 2MASS J16390535−4642137, lies within the *XMM-Newton* error circle of IGR J16393−4643.

The strong absorption ($N_{\mathrm{H}} = (25 \pm 2) \cdot 10^{22}\,\mathrm{cm}^{-2}$) is intrinsic since it is an order of magnitude larger than the Galactic absorption along the line of sight (Dickey & Lockman 1990). This absorption indicates the presence of optically-thick material surrounding the compact object, which is consistent with the detection of iron lines. These emission lines at 6.4 and 7.1 keV trace the quantity of matter in the shell that envelopes the neutron star. The lines are at the positions that would be expected from the fluorescence of cold neutral matter illuminated by continuum X-rays, and their equivalent widths are compatible with a spherical distribution of dense gas around the compact object (Matt 2002). There appears to be a soft excess flux which is probably caused by the scattering of X-rays in the stellar wind (Haberl & White 1990; Hickox et al. 2004).

High-energy spectral and timing characteristics of IGR J16393−4643 suggest a HMXB system consisting of a magnetized neutron star orbiting inside the dense stellar wind of an O or B supergiant companion. A Be stellar companion is unlikely given that such systems are usually transient. Infrared observations should confirm the supergiant nature of the optical counterpart. If this is the case, it will constitute another argument rejecting the *EGRET* association (Orellana & Romero 2005).

We could not find an orbital period of the order of a few days in the ISGRI light curves. However, after this analysis was published, *RXTE* observations of the source revealed an orbital period of ~ 3.7 d which constrains the mass of the companion to $\sim 7\,M_{\odot}$ further confirming its HMXB nature (Thompson et al. 2006).

INTEGRAL and *XMM-Newton* observations have helped us add IGR J16393−4643 to the growing class of obscured supergiant HMXB pulsars (see Chapter 8). So far, wind-accreting X-ray pulsars such as IGR J16393−4643 have been detected preferentially towards the Norma Arm region (Walter et al. 2004b, 2006). The increasing sample size that these objects represent should enable meaningful statistical studies to be performed (see Part IV). Understanding the nature of sources such as IGR J16393−4643 could shed light on the structure of stellar winds, provide constraints on the masses of neutron stars, and help to elucidate the evolution of Galactic X-ray binaries.

7.5.1 Scientific Article on IGR J16393−4643

The details of this research were published in A&A as Bodaghee et al. (2006), a copy of which is provided on the next few pages:

- Bodaghee A., Walter R., Zurita Heras J.A., Bird A.J., Courvoisier T.J.-L., Malizia A., Terrier R. & Ubertini P.
  IGR J16393−4643: a new heavily-obscured X-ray pulsar
  Astronomy & Astrophysics, Vol. 447-3, pp. 1027–1034, 2006

Table 7.3: Source flux value (20–60 keV), significance, and the effective exposure time from the mosaic image of each spacecraft revolution. Revolutions with exposure times less than 10 ks are excluded.

visibility period		exp.	flux	significance		off-axis angle
(rev.)	(MJD)	(ks)	(cps)	(σ_{20-60})	(σ_{60-100})	(°)
30	52652	43	0.38±0.04	1.0	0.0	14.6
32	52658	18	1.80±0.62	2.9	0.0	14.8
37	52672	204	0.55±0.05	12.1	1.4	3.8
38	52675	92	0.93±0.07	13.7	0.0	3.6
46	52699	72	<0.24	0.4	0.0	13.6
47	52703	153	0.83±0.06	13.3	0.3	7.0
49	52709	85	0.89±0.08	11.1	0.9	6.2
50	52712	104	1.05±0.09	11.6	0.0	9.5
51	52714	76	1.00±0.14	7.0	0.8	11.3
52	52718	93	0.53±0.10	5.3	0.0	10.1
54	52724	100	0.96±0.10	10.0	2.0	9.7
55	52726	96	1.39±0.14	10.0	0.0	11.9
57	52733	73	0.62±0.17	3.7	0.0	11.7
58	52735	32	1.12±0.33	3.4	0.0	15.0
60	52741	103	0.34±0.14	2.4	0.0	12.6
61	52744	18	0.99±0.76	1.3	0.0	15.8
100	52861	205	0.21±0.05	4.0	0.0	6.9
101	52865	18	0.45±0.19	2.3	0.0	7.5
103	52870	100	<0.18	0.0	0.0	13.6
105	52876	34	<1.97	0.4	3.2	18.1
106	52879	23	<3.12	0.7	0.6	18.2
116	52908	116	0.25±0.07	3.5	0.0	7.0
118	52915	146	0.75±0.08	9.4	0.0	10.0
119	52917	29	1.20±0.45	2.7	0.0	15.0
164	53052	24	<0.43	0.1	0.6	14.3
167	53062	106	0.26±0.09	2.9	0.0	9.4
168	53064	28	1.22±0.22	5.7	0.4	11.5
169	53067	14	4.33±2.53	1.7	0.0	18.2
173	53078	27	1.22±0.18	6.7	0.0	9.3
174	53081	53	0.60±0.14	4.5	0.0	9.3
183	53108	18	<0.57	0.6	0.0	15.6
226	53238	17	0.46±0.25	1.9	0.0	10.6
229	53246	11	<0.27	0.8	0.0	7.3
232	53255	14	0.25±0.08	3.0	0.3	9.3
233	53259	72	0.74±0.10	7.0	0.0	9.2
234	53262	45	1.03±0.03	3.9	0.0	13.1
243	53288	11	1.54±0.98	1.6	1.0	16.2
244	53291	11	2.94±1.32	2.2	0.1	17.2

Table 7.4: Parameters from a power law, a broken power law (BP), and a Compton emission (CE) model fit to the combined EPIC and ISGRI spectra of IGR J16393−4643. The models are modulated by Galactic absorption fixed at $2.2 \cdot 10^{22}\,\mathrm{cm}^{-2}$ (Dickey & Lockman 1990). The BP and CE models include an extra absorption component, a soft excess (F_{se}) which is represented by a fixed black-body temperature of $kT_b = 0.06\,\mathrm{keV}$, and fixed, narrow-width Gaussians for the iron lines. In the CE model, the initial photon temperature is held to $kT_i = 0.1\,\mathrm{keV}$, and the integrated fluxes are listed as observed (F_{2-10}) or unabsorbed (F^{UA}_{2-10}). Errors denote 90% confidence.

Parameter	Value	Unit
absorbed power law		
N_{H}	45.0±0.6	$10^{22}\,\mathrm{cm}^{-2}$
Γ	2.30±0.02	
χ^2_ν/dof	2.07/683	
BP model		
C_I	1 (fixed)	
N_{H}	26^{+2}_{-3}	$10^{22}\,\mathrm{cm}^{-2}$
Γ_1	$0.86^{+0.12}_{-0.22}$	
E_{break}	$16.7^{+0.8}_{-1.3}$	keV
Γ_2	4.6±0.4	
Z_{Fe}	$0.9^{+0.2}_{-0.1}$	$\mathrm{Z}_\odot$
$\mathrm{E}_{K\alpha}$	6.41±0.04	keV
$F_{K\alpha}$	1.2±0.2	$10^{-4}\,\mathrm{ph\,cm}^{-2}\,\mathrm{s}^{-1}$
$\mathrm{E}_{K\beta}$	7.1±0.1	keV
$F_{K\beta}$	<0.6	$10^{-4}\,\mathrm{ph\,cm}^{-2}\,\mathrm{s}^{-1}$
χ^2_ν/dof	0.96/675	
CE model		
C_I	0.8±0.2	
N_{H}	25±2	$10^{22}\,\mathrm{cm}^{-2}$
τ	9±1	
kT_{e}	4.4±0.3	keV
F_{2-10}	4.4	$10^{-11}\,\mathrm{ergs\,cm}^{-2}\,\mathrm{s}^{-1}$
F^{UA}_{2-10}	9.2	$10^{-11}\,\mathrm{ergs\,cm}^{-2}\,\mathrm{s}^{-1}$
F_{se}	7	$10^{-15}\,\mathrm{ergs\,cm}^{-2}\,\mathrm{s}^{-1}$
Z_{Fe}	$1.0^{+0.4}_{-0.2}$	$\mathrm{Z}_\odot$
$\mathrm{E}_{K\alpha}$	6.41±0.03	keV
$F_{K\alpha}$	1.1±0.2	$10^{-4}\,\mathrm{ph\,cm}^{-2}\,\mathrm{s}^{-1}$
$\mathrm{E}_{K\beta}$	7.1±0.1	keV
$F_{K\beta}$	<0.6	$10^{-4}\,\mathrm{ph\,cm}^{-2}\,\mathrm{s}^{-1}$
χ^2_ν/dof	0.95/676	

A&A 447, 1027–1034 (2006)
DOI: 10.1051/0004-6361:20053809

Astronomy
&
Astrophysics

IGR J16393−4643: a new heavily-obscured X-ray pulsar

A. Bodaghee[1,2], R. Walter[1,2], J. A. Zurita Heras[1,2], A. J. Bird[3], T. J.-L. Courvoisier[1,2], A. Malizia[4],
R. Terrier[5,6], and P. Ubertini[7]

[1] *INTEGRAL* Science Data Centre, Chemin d'Ecogia 16, 1290 Versoix, Switzerland
e-mail: `arash.bodaghee@obs.unige.ch`
[2] Observatoire de Genève, Chemin des Maillettes 51, 1290 Sauverny, Switzerland
[3] School of Physics and Astronomy, University of Southampton, Highfield, Southampton, SO17 1BJ, UK
[4] IASF/CNR, Via Gobetti 101, 40129 Bologna, Italy
[5] CEA-Saclay, DAPNIA/Service d'Astrophysique, 91191 Gif-sur-Yvette Cedex, France
[6] Fédération de recherche APC, Collège de France, 11 place Marcelin Berthelot, 75231 Paris, France
[7] IASF/CNR, Via Fosso del Cavaliere 100, 00133 Rome, Italy

Received 11 July 2005 / Accepted 27 September 2005

ABSTRACT

An analysis of the high-energy emission from IGR J16393−4643 (=AX J1639.0−4642) is presented using data from *INTEGRAL* and *XMM-Newton*. The source is persistent in the 20–40 keV band at an average flux of 5.1×10^{-11} erg cm^{-2} s^{-1}, with variations in intensity by at least an order of magnitude. A pulse period of 912.0±0.1 s was discovered in the *ISGRI* and *EPIC* light curves. The source spectrum is a strongly-absorbed ($N_{\rm H} = (2.5 \pm 0.2) \times 10^{23}$ cm^{-2}) power law that features a high-energy cutoff above 10 keV. Two iron emission lines at 6.4 and 7.1 keV, an iron absorption edge $\gtrsim$7.1 keV, and a soft excess emission of 7×10^{-15} erg cm^{-2} s^{-1} between 0.5–2 keV, are detected in the *EPIC* spectrum. The shape of the spectrum does not change with the pulse. Its persistence, pulsation, and spectrum place IGR J16393−4643 among the class of heavily-absorbed HMXBs. The improved position from *EPIC* is RA (J2000) = $16^{\rm h}39^{\rm m}05.4^{\rm s}$ and Dec = $-46°42'12''$ ($4''$ uncertainty) which is compatible with that of 2MASS J16390535−4642137.

Key words. gamma-rays: observations – X-rays: binaries – pulsars: individuals: IGR J16393−4643 – pulsars: individuals: AX J1639.0−4642

1. Introduction

The *INTEGRAL* core program (CP: Winkler et al. 2003) routinely devotes observation time to Galactic Plane Scans (GPS) and Galactic Centre Deep Exposures (GCDE). These numerous snapshots of the Milky Way can be assembled into mosaic images of long exposure time (∼1 Ms). This gamma-ray view of the galaxy, as collected by *ISGRI* (Ubertini et al. 2003; Lebrun et al. 2003), enabled Bird et al. (2004) to detect 123 sources at a significance above 6σ. Around 20 of these sources are of unknown origin. A good portion of these new sources probably belong to the class of heavily-absorbed High Mass X-ray Binaries (HMXBs) that are concentrated along the galactic plane and in the spiral arms.

High-Mass X-ray Binaries are composed of a compact object such as a neutron star or a black hole that orbits a massive stellar companion. Depending on the type of companion, known HMXBs can be divided into two groups (van Paradijs 1983). Most HMXBs classified by Liu et al. (2000) contain a Be star. These systems are usually transient sources with hard spectra. The compact object has a wide orbit which mostly keeps it away from the Be star and its disk. Outbursts in these systems are due primarily to the compact object approaching the star and accreting matter from the slow, dense stellar wind. The second group of HMXBs features an O or B supergiant star. The orbit of the compact object places it well within the stellar wind, so material from the supergiant can be fed directly to the compact object through Bondi accretion, or it can pass to the compact object via an accretion disk. The latter mechanism is typically found in bright X-ray binaries in which the Roche lobe overflow of gas from the OB star supersedes the flow of accreting matter. For less luminous binaries, the OB star does not fill its Roche lobe and the behaviour of the X-ray source is determined predominantly by the stellar wind. X-ray emission in supergiant HMXB systems is usually persistent, with flares stemming from inhomogeneities in the wind. Neutron stars with strong magnetic fields develop a hot spot for accretion which can result in a pulsation.

The number of persistent and heavily-absorbed HMXBs associated with supergiant companions has increased thanks to deep, wide-field observations by *INTEGRAL* combined with follow-up X-ray monitoring by *XMM-Newton* (Walter et al. 2003; Rodriguez et al. 2003; Hill et al. 2005; Lutovinov et al. 2005b). So far, these sources have been detected preferentially in the Norma Arm region (Walter et al. 2004) which features high formation rates of OB supergiant stars.

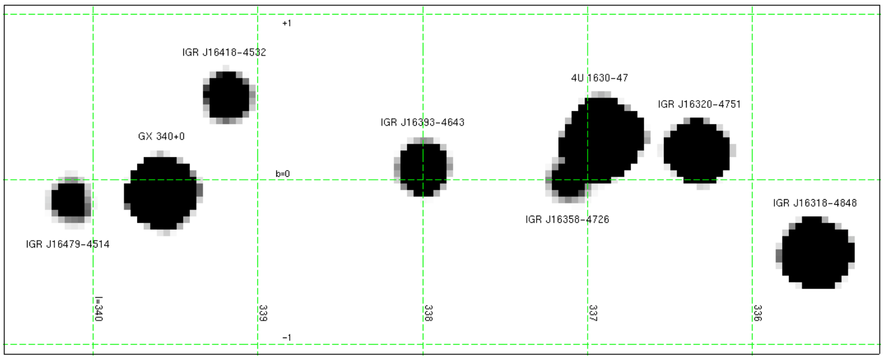

Fig. 1. Intensity map of the Norma Arm in the 20–40 keV band accumulating data from revolutions 30–185 for an effective exposure time of 670 ks. The image is in galactic coordinates and represents an area 2° tall by 5° wide. The galactic equator ($b = 0$) bisects the image horizontally. Neighboring sources from the catalog of Bird et al. (2004) are also shown.

It is there that *INTEGRAL* uncovered its first new source, IGR J16318−4848 (Walter et al. 2003). The Norma Arm also harbors IGR J16393−4643. This object was initially discovered in the X-ray band and listed as AX J163904−4642 in the *ASCA* Faint Source Catalog (Sugizaki et al. 2001). Its flat power-law slope, its absorption ($N_\mathrm{H} = 13^{+9}_{-7} \times 10^{22}\,\mathrm{cm}^{-2}$), its lack of radio emission, and its position in the galactic plane compelled the authors to classify it as a HMXB. A non-thermal radio counterpart was recently detected in the *ASCA* error box which suggests a dust-enshrouded microquasar interpretation for the HMXB (Combi et al. 2004), and would help explain the possible association with the unidentified *EGRET* source 3EG J1639−4702 (Hartman et al. 1999) noted by Malizia et al. (2004).

We detected IGR J16393−4643 in the *ISGRI* GPS data of the Norma Arm's first visibility period, and we obtained a follow-up observation with *XMM-Newton*. The set of *INTEGRAL* and *XMM-Newton* data are introduced in Sect. 2. In Sect. 3, the refined X-ray position is used to locate the most likely counterpart at other wavelengths. Timing and spectral analyses are presented in Sects. 4 and 5, respectively. Finally, we discuss the nature of the source and we offer our conclusions in Sect. 6.

2. Observations and data sets

2.1. INTEGRAL data and imaging

The *INTEGRAL* data consist of all CP pointings during revolutions 30–260, as well as pointings that were public by January 3, 2005, which had the source within the *ISGRI* field of view (FOV). To improve the quality of the output mosaic, pointings with exposure times below 1 ks were ignored. The resulting data set groups roughly 1500 pointings with an average exposure time of 2 ks each.

Version 4.2 of the *INTEGRAL* Offline Scientific Analysis (OSA) software was used to reduce raw data into images. Source extraction employed version 18 of the *INTEGRAL* General Reference Catalog (Ebisawa et al. 2003) selected for objects detected by *ISGRI*. These tools are available to the public through the *INTEGRAL* Science Data Centre (ISDC: Courvoisier et al. 2003).

Intensity, significance, variance, and exposure mosaic images were constructed from background-subtracted images of individual pointings. Figure 1 provides an example of an intensity map of IGR J16393−4643 and its vicinity in the 20–40 keV band from the pointings of revolutions 30 to 185. The effective exposure time is 670 ks after correcting for vignetting. Using this image, we extracted a source location of RA (J2000) = $16^\mathrm{h}39^\mathrm{m}05^\mathrm{s}$ and Dec = −46°42.3′ (26″ uncertainty) which agrees with and improves the *ISGRI* position of Bird et al. (2004). The mean flux (20–60 keV) of the source is 0.73 ± 0.02 counts per second (cps), or 4.9 mCrab, at a significance of 36σ.

2.2. XMM-Newton data and imaging

XMM-Newton (Jansen et al. 2001; Strüder et al. 2001; Turner et al. 2001) observed IGR J16393−4643 on March 21, 2004, from 08:21:15 to 11:41:15 (UT). We used the Science Analysis System (SAS) v. 6.1.0 software to analyse the data and to extract the *EPIC* spectrum. The data were screened for background variability by excluding time intervals in which the count rate above 10 keV was greater than a selected threshold (0.33 cps for *EPIC/MOS1*, 0.25 cps for *EPIC/MOS2*, and 2.4 cps for *EPIC/PN*). After screening, the effective exposure times were around 8.4, 8, and 7 ks for *EPIC/MOS1*, *EPIC/MOS2*, and *EPIC/PN*, respectively.

IGR J16393−4643 is clearly detected in images taken by *EPIC*. Figure 2 presents an image of IGR J16393−4643 from the *EPIC/MOS1* camera. Furthermore, the source coincides with the updated *ISGRI* position and error circle from this paper. The refined X-ray position averaged from *EPIC/MOS* and *EPIC/PN* is RA (J2000) = $16^\mathrm{h}39^\mathrm{m}05.4^\mathrm{s}$ and Dec = −46°42′12″ (4″ uncertainty).

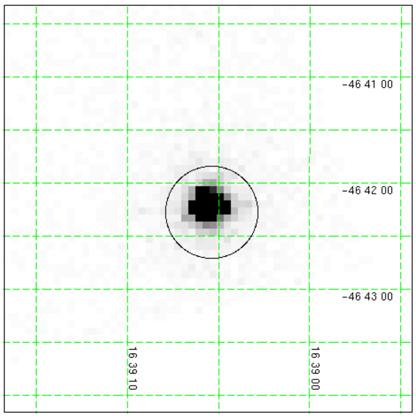

Fig. 2. *EPIC/MOS1* image of IGR J16393−4643 in the 0.15–12 keV energy range with an effective exposure time of 8.4 ks. The refined *ISGRI* error circle from this paper is superimposed.

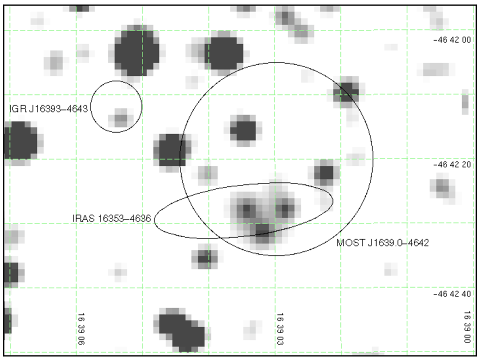

Fig. 3. Image from the 2MASS survey of the region around IGR J16393−4643 in the K_s band. The *XMM-Newton* error circle from this paper does not intersect the error boxes of the radio source MOST J1639.0−4642 and the far infrared source IRAS 16353−4636. The only infrared object inside the *XMM-Newton* error circle is 2MASS J16390535−4642137.

3. Counterparts

We searched for counterparts at other wavelengths and found a single infrared source belonging to the Two Microns All-Sky Survey (2MASS: Cutri et al. 2003) in the *XMM-Newton* error box. This potential counterpart, 2MASS J16390535−4642137, is located about 2″ away from the *XMM-Newton* position at RA (J2000) = $16^h39^m05.36^s$ and Dec = −46°42′13.7″ (0.06″ uncertainty). It appears in the J, H, and K_s bands with magnitudes of 14.63 ± 0.06, 13.32 ± 0.04, and 12.78 ± 0.04, respectively (95% confidence).

Figure 3 shows that the *XMM-Newton* position and error radius for IGR J16393−4643 do not intersect the error boxes of the radio source MOST J1639.0−4642 and the far infrared source IRAS 16353−4636, which are the possible counterparts proposed by Combi et al. (2004). The tight *XMM-Newton* error circle excludes optical counterparts from the USNO-B1 catalog (Monet et al. 2003), radio sources from the Vizier database (Ochsenbein et al. 2000), and *ROSAT* sources (Voges et al. 1999).

A possible association of IGR J16393−4643 with the *EGRET* source 3EG J1639−4702 (Hartman et al. 1999) has been proposed by Malizia et al. (2004). Another *ISGRI* source, IGR J16358−4726, and 4U 1630−47 are just outside the *EGRET* 95% error contour. In the 2° × 5° degree section of the Norma Arm presented in Fig. 1, the probability to observe a counterpart in the 0.56° error radius of the *EGRET* source is close to 1, so the coincidence with IGR J16393−4643 is probably a chance one.

4. Timing analysis

4.1. Long-term variability

Most *ISGRI* pointings have exposure times that are too brief for a significant detection. Therefore, a mosaic was prepared for each 3-day spacecraft revolution (from 30–244) in the 20–60 and 60–150 keV bands. We extracted the source flux, error, and significance by fitting a Gaussian with a fixed point spread function to the mosaic images. Upper limits (3σ), calculated from the variance maps, are provided when the source is not detected at the 4σ level in a mosaic image with an effective exposure time above 7 ks. There were no detections in mosaic images of the 60–150 keV band so its light curve is omitted.

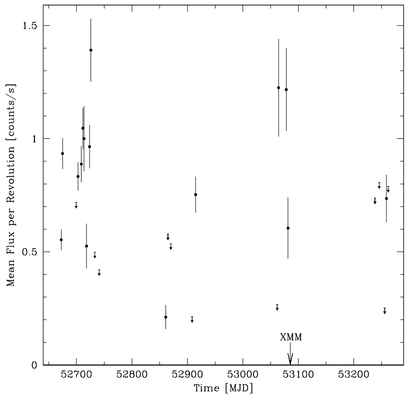

Fig. 4. *ISGRI* light curve (20–60 keV) of IGR J16393−4643 where each point represents the flux averaged over 1 spacecraft revolution. Upper limits (3σ) are provided when the source is not detected for an effective exposure time above 7 ks. The *XMM-Newton* observation (Fig. 5) occurred on MJD 53 085.

Figure 4 illustrates the persistence of IGR J16393−4643 in the 20–60 keV energy range. Table 1 collects the 15 revolutions in which the source is detected in the mosaic image with a significance above 4σ. The average flux in these mosaics is 0.86 cps (5.6 mCrab) with a cumulative exposure time of 1.5 Ms. The mean flux per revolution varies by a factor of at

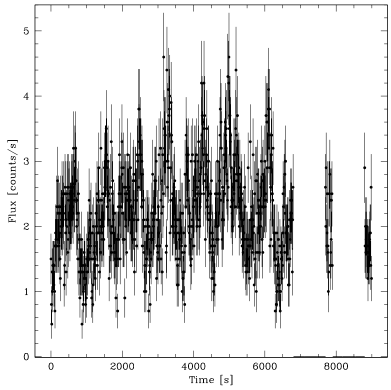

Fig. 5. *EPIC/PN* light curve for IGR J16393−4643 in the 2–10 keV energy range with a time resolution of 10 s. The observation starts at MJD 53 085.37516.

Table 1. Source flux value (20–60 keV), significance, average off-axis angle, and exposure time when IGR J16393−4643 is detected at the 4σ level in the mosaic image of a spacecraft revolution. The median MJD of the visibility period is also given in reference to Fig. 4.

Visibility period		Exp.	Flux	Sig.	Angle
[Rev.]	[MJD]	[ks]	[counts/s]	[σ]	[°]
37	52 672	204	0.55 ± 0.05	12.1	3.8
38	52 675	92	0.93 ± 0.07	13.7	3.6
47	52 703	153	0.83 ± 0.06	13.3	7.0
49	52 709	85	0.89 ± 0.08	11.1	6.2
50	52 712	104	1.05 ± 0.09	11.6	9.5
51	52 714	76	1.00 ± 0.14	7.0	11.3
52	52 718	93	0.53 ± 0.10	5.3	10.1
54	52 724	100	0.96 ± 0.10	10.0	9.7
55	52 726	96	1.39 ± 0.14	10.0	11.9
100	52 861	205	0.21 ± 0.05	4.0	6.9
118	52 915	146	0.75 ± 0.08	9.4	10.0
168	53 064	28	1.22 ± 0.22	5.7	11.5
173	53 078	27	1.22 ± 0.18	6.7	9.3
174	53 081	53	0.60 ± 0.14	4.5	9.3
233	53 259	72	0.74 ± 0.10	7.0	9.2

least 6 from 0.21 ± 0.05 counts per second (cps) or 1.4 mCrab in revolution 100 (205 ks), to 1.39 ± 0.14 cps (9.3 mCrab) in revolution 55 (96 ks). When the flux value during revolution 100 is compared to the highest flux registered in a single 2-ks pointing of the 20–60 keV band (4.3 ± 0.6 cps, or 29 mCrab, during MJD 52 673.623–52 673.641), we find that the source flux varies by a factor larger than 20.

4.2. Pulsations

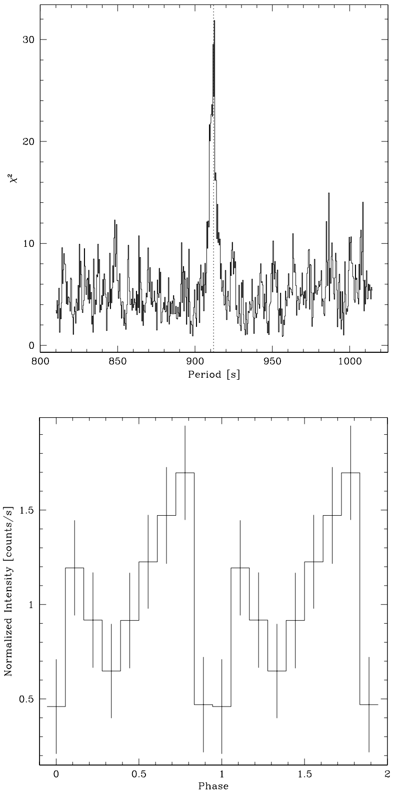

Fig. 6. *Top* **a)**: period search (χ^2 distribution) on the *ISGRI* light curve (15–40 keV) of revolution 38, centred at 912 s (vertical line), with 9 bins per period, and a resolution of 0.4 s. *Bottom* **b)**: pulse profile of the folded *ISGRI* light curve (15–40 keV) for a period of 912 s. The start time is MJD 52 674.53833.

During the *EPIC/PN* observation of 8 ks, the source count rate varied from 1 to 4 cps (Fig. 5). Furthermore, the variations occur periodically. By searching for modulations in the power spectrum and in the χ^2 distribution, we obtain a period of 912 ± 5 s at a χ^2 of ~600 for 30 bins per period (Fig. 7a). The pulse period is determined by the centre of a Gaussian fit to the χ^2 distribution, and the error is calculated using the procedure developed by Horne & Baliunas (1986) on Lomb-Scargle periodograms. The *EPIC/PN* pulse profile folded with a period of 912 s, illustrated in Fig. 7b, indicates a pulse fraction of 38 ± 5%.

For *ISGRI*, the pulse is best detected in the 100-s light curve of revolution 38 in the 15–40 keV band since this revolution has enough effective exposure time (50 ks) with low off-axis angles (~4°), and its light curve is free of gaps that hinder a periodicity search. Figure 6a presents the χ^2 distribution centered at 912 s, with 9 bins per period. The phase diagram is shown in Fig. 6b, and the pulse fraction is 57 ± 24%. We merged the 100-s light curves (15–30 keV) from revolutions 37–55, and derived a pulse period and error of 912.0 ± 0.1 s.

With respect to the pulse fractions, the amplitude does not change significantly as a function of energy. Both display

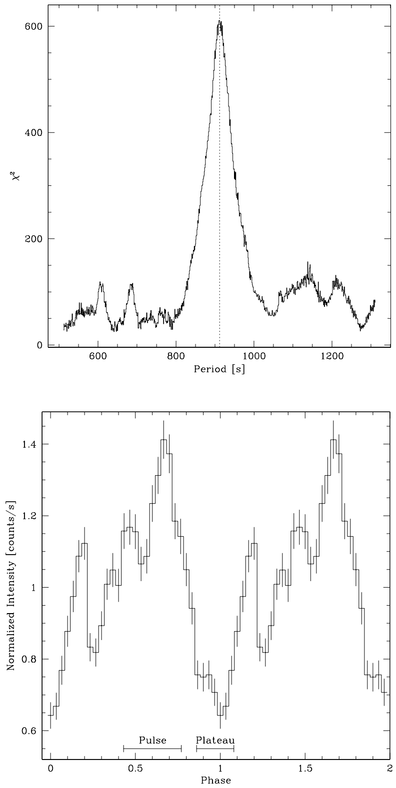

Fig. 7. *Top* **a)**: distribution of χ^2 for the *EPIC/PN* 2–10 keV light curve with 30 bins per period, a resolution of 1 s, and centred at 912 s (vertical line). *Bottom* **b)**: folded *EPIC/PN* light curve for a pulse period of 912 s beginning at MJD 53 085.38738. The intervals indicate the pulse and plateau states of the phase-resolved spectrum.

a jagged rise to a peak flux followed by a drop. There appear to be primary and secondary peaks in the pulse profiles of both instruments at phases of ~0.7 and ~0.2, respectively. Although the *ISGRI* and *EPIC* periods are derived from observations about 400 days apart, the period is not accurate enough to search for possible variations. In addition, the *ISGRI* light curves of revolutions that are nearly concurrent with the *EPIC* observation present low source significances which makes it difficult to search for a period.

There is an indication in the *EPIC* light curve (Fig. 5) that the source varies over timescales longer than the pulse period. At the beginning of the observation, the maximum of the pulse is about 3 cps. This maximum rises to 4 cps about 5 ks after the start time, and then decreases.

We did not detect an orbital period of the order of a few days in the combined *ISGRI* light curves (15–30 keV, 100-s resolution) of detected revolutions between 37 and 55.

5. Spectral analysis

5.1. Average spectrum

To extract an *ISGRI* spectrum, we created mosaics accumulating the data from revolutions 37–185 in the following energy bands; 22.09–25.92, 25.92–30.23, 30.23–40.28, 40.28–51.29, and 51.29–63.26 keV. These boundaries were chosen to conform with the current response matrices. The source is clearly detected up to 40 keV, so spectral bins at higher energies are ignored. A power law fit to the *ISGRI* spectrum returns a relatively steep photon index of 4.5±0.4 ($\chi^2_\nu = 0.32$).

Spectral extraction for *EPIC/PN*, *EPIC/MOS1*, and *EPIC/MOS2* relied on single and double events within a circle of radius 25″ centred on the source. To estimate the background, we made an event list from a circle of equal radius in the same detector and at an equivalent distance from the detector's edge. Channels were configured to collect 30 counts per bin. An absorbed power law fit to the *EPIC* spectra has a photon index of 1.0 ± 0.1 with a column density of $3.1 \pm 0.1 \times 10^{23}$ cm^{-2} ($\chi^2_\nu = 1.15$).

The *EPIC* spectrum is heavily-absorbed below 4 keV. Iron emission lines appear at 6.4 keV (Fe K$_\alpha$) and at 7.1 keV (Fe K$_\beta$). A discontinuity in the continuum above 7.1 keV suggests an iron absorption edge. There is an indication of an excess of soft emission between 0.5 and 2 keV. Including a soft blackbody component in an absorbed power law adjusted to the *EPIC* spectra decreases the χ^2 by 9 for 680 degrees of freedom (d.o.f.), or a 0.5% probability that this feature is due to chance. Using a partial covering absorption instead of a blackbody raises the χ^2 by 60 for the same dof (679). A partially-ionised absorber is also insufficient to model the soft excess.

Simply fitting an absorbed power law to the spectra from *EPIC* and *ISGRI* yields $N_{\rm H} \sim 4 \times 10^{23}$ cm^{-2} and $\Gamma \sim 2.3$, but the fit is poor ($\chi^2_\nu = 2.1$) with significant residuals in the hard X-rays. The *EPIC* photon index of 1.0 ± 0.1 is smaller than the one observed for *ISGRI* (4.5 ± 0.4) which indicates a spectral break. Such spectral shapes – a flat power law at low energies with a high-energy cutoff between 10–20 keV beyond which the slope steepens – are typical of X-ray pulsars (White et al. 1995).

We fit the combined *EPIC* and *ISGRI* spectra (Fig. 8) with a broken power law (BP), a power law with an exponential cutoff energy (CP), and a Compton emission (CE) model (`comptt` within Xspec). The models are modified by a galactic absorption in the direction of the source (fixed at 2.2×10^{22} cm^{-2}, Dickey & Lockman 1990), and an intrinsic photoelectric absorption with free iron abundances ($Z_{\rm Fe}$). Soft excess emission is represented by a blackbody (with a fixed temperature of $kT_{\rm b} = 0.06$ keV) that is affected by the galactic absorption only. Two narrow Gaussians (with widths fixed at 0) describe the iron lines. A constant (C_I) accounts for the asynchronous observations and for cross-calibration uncertainties.

The BP model (χ^2_ν/d.o.f. = 0.95/675) has photon indices of $\Gamma_1 = 0.9^{+0.1}_{-0.2}$ and $\Gamma_2 = 4.6^{+0.8}_{-0.3}$. However, the BP model does not constrain the break energy ($E_{\rm break}$ >17 keV) nor C_I because it requires one more parameter than the other models. The CP model (χ^2_ν/d.o.f. = 1.07/676) gives $\Gamma = 0.8 \pm 0.2$,

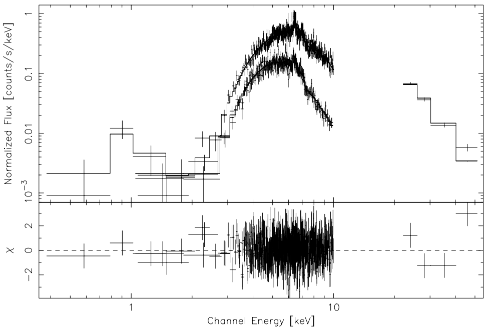

Fig. 8. Photon spectrum of IGR J16393−4643 from *EPIC/PN*, *EPIC/MOS1*, *EPIC/MOS2*, and *ISGRI*, fit with the comptonised continuum model (CE).

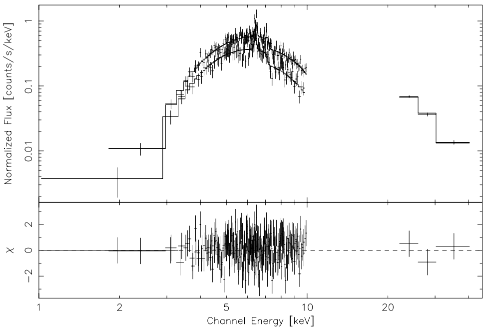

Fig. 9. Phase-resolved spectrum of IGR J16393−4643 from *EPIC/PN* during the pulse and plateau states. The *ISGRI* spectrum is included to constrain the CE model.

and a cutoff energy of $E_{\mathrm{cut}} = 10 \pm 1$ keV, but residuals remain at high energy because of the low cutoff temperature. In Lutovinov et al. (2005a), an absorbed cutoff power law fit to the combined *ASCA* and *ISGRI* spectra had a comparable cutoff energy of 11 ± 1 keV, but the photon index was poorly constrained ($\Gamma = 1.3 \pm 1.0$).

Parameters from the CE model (χ^2_ν/d.o.f. = 0.95/676) are listed in Table 2. The column density (N_{H}) is $(25 \pm 2) \times 10^{22}$ cm^{-2}. The comptonising medium has an electron temperature (kT_{e}) of 4.4 ± 0.3 keV with an optical depth (τ) of 9 ± 1. The Fe K$_\alpha$ line is at 6.41 ± 0.03 and has an equivalent width of 60 ± 30 eV when measured with respect to the unabsorbed continuum, while the energy of the Fe K$_\beta$ line is 7.1 ± 0.1 keV with an equivalent width of <120 eV. The detection of the K$_\beta$ line is marginal given the uncertainties and its F-test probability of 3%. However, the ratio of iron intensities ($F_{\mathrm{K}\beta}/F_{\mathrm{K}\alpha}$) is consistent with the value expected from the photoionisation of iron (Kaastra & Mewe 1993). The absorbed, integrated fluxes (in units of 10^{-11} erg cm^{-2} s^{-1}) are 4.4 in the 2–10 keV band, and 5.1 in the 20–60 keV band. The observed soft excess flux between 0.5 and 2 keV is 7×10^{-15} erg cm^{-2} s^{-1}. Since $C_I \sim 1$, the *EPIC* observation occurred during a period in which the source was in an average state.

5.2. Phase-resolved spectrum

The *EPIC/PN* spectra were binned according to two states: a pulse state around the primary peak in the folded light curve (phase 0.43–0.77 in Fig. 7b), and a plateau state (phases 0.00–0.07 and 0.87–1.00). Average count rates for the pulse and plateau states are almost a factor of 2 apart at ~1.2 and ~0.7, respectively. The CE model was applied to the phase-resolved *EPIC* spectra constrained with the *ISGRI* spectrum. Bins for the plateau gather 20 counts and bins for the pulse collect 40 counts per channel. The soft excess is not prominent in either spectrum so the blackbody component is omitted. This prevents an evaluation of the influence of the pulse on the soft excess. Table 2 reports parameters for the CE model fit to the phase-resolved spectra. The pulsation affects the normalisations but does not modify the shape of the spectra nor its parameters, specifically the N_{H}, in any appreciable way.

Table 2. Parameters from the Compton emission (CE) model fit to the spectra of *EPIC* and *ISGRI* combined. Also listed are the values of the CE model (without a blackbody) fit to the pulse and plateau states of the phase-resolved *EPIC/PN* spectra constrained with the *ISGRI* spectrum. The integrated fluxes are listed as observed (F_{2-10}) or unabsorbed (F^{UA}_{2-10}). Errors denote 90% confidence.

Parameter	CE	Pulse	Plateau	Unit
C_I	0.8 ± 0.2	0.6 ± 0.2	1.3 ± 0.7	
τ	9 ± 1	12^{+6}_{-2}	8^{+4}_{-2}	
kT_{e}	4.4 ± 0.3	4.4 ± 0.3	4.4 ± 0.4	keV
N_{H}	25 ± 2	23^{+2}_{-6}	24^{+3}_{-7}	10^{22} cm^{-2}
Z_{Fe}	$1.0^{+0.4}_{-0.2}$	$0.9^{+0.6}_{-0.3}$	$1.2^{+0.8}_{-0.6}$	$Z_\odot$
F_{2-10}	4.4	5.2	3.0	10^{-11} erg cm^{-2} s^{-1}
F^{UA}_{2-10}	9.2	9.8	6.7	10^{-11} erg cm^{-2} s^{-1}
$E_{\mathrm{K}\alpha}$	6.41 ± 0.03	6.44 ± 0.03	6.41 ± 0.04	keV
$F_{\mathrm{K}\alpha}$	1.1 ± 0.2	1.1 ± 0.4	0.8 ± 0.4	10^{-4} ph cm^{-2} s^{-1}
$E_{\mathrm{K}\beta}$	7.1 ± 0.1	7.1 ± 0.3	7.2 ± 0.3	keV
$F_{\mathrm{K}\beta}$	<0.62	<1.1	<1.3	10^{-4} ph cm^{-2} s^{-1}
χ^2_ν/d.o.f.	0.95/676	0.92/140	0.92/94	

6. Discussion

Observations of IGR J16393−4643 by *INTEGRAL* and *XMM-Newton* present a source that is highly-obscured and persistent, with an intensity varying by a factor larger than 20. The source has a pulsation period of 912.0 ± 0.1 s. These attributes, along with its spectral shape, its neutral iron lines, and its lack of radio emission, suggest a HMXB system consisting of a magnetised neutron star orbiting inside the dense stellar wind of a supergiant companion. In the 2–10 keV energy band, the unabsorbed flux of IGR J16393−4643 is

9.2×10^{-11} erg cm^{-2}s^{-1}. Assuming a luminosity of 1.2×10^{36} erg s^{-1}, which is typical for accretion-driven X-ray pulsars (Bildsten et al. 1997), the source is located approximately 10 kpc away.

The absorbing column density is large whenever the source is detected, whether by *ASCA* ($N_{\rm H} = 13^{+9}_{-7} \times 10^{22}$ cm^{-2}), or now with *INTEGRAL* and *XMM-Newton* ($N_{\rm H} = (25 \pm 2) \times 10^{22}$ cm^{-2}). The strong absorption below 5 keV is intrinsic since it is an order of magnitude larger than the galactic absorption along the line of sight ($N_{\rm H} = 2.2 \times 10^{22}$ cm^{-2}). The absorption does not vary with the pulsation, which means that it is not related to the accretion column, but it may change with the orbital phase. This absorption indicates the presence of optically-thick material surrounding the compact object, which is consistent with the detection of iron lines.

Emission lines at 6.4 and 7.1 keV trace the quantity of matter in the shell that envelopes the neutron star. These lines are at the positions that would be expected from the fluorescence of cold neutral matter illuminated by continuum X-rays, and their equivalent widths are compatible with a spherical distribution of dense gas around the compact object (Matt 2002). A Kα line at 6.41 ± 0.03 keV ($\gtrsim$1.925 Å) corresponds to an ionisation of at most Fe XVIII (House 1969), which does not constrain the distance between the ionising source and the inner surface of the ionised shell. Given the errors on the line equivalent widths, we can not determine whether the fluxes of the iron lines are modified by the pulse.

There appears to be a soft excess flux of 7×10^{-15} erg cm^{-2} s^{-1} that is best represented by a blackbody rather than with a partial covering or partially-ionised absorber. The scattering of X-rays by the stellar wind is the most likely explanation for the soft excess emission (Haberl & White 1990). To what extent the pulse affects the soft excess emission is still unknown as the soft excess flux is not prominent in the phase-resolved spectrum.

The *ASCA* Faint Source Catalog (Sugizaki et al. 2001) listed IGR J16393−4643 among the brightest objects in its catalog, but the uncertainty of the position and the heavy absorption prevented Sugizaki et al. (2001) from associating this source with an optical counterpart. Malizia et al. (2004) noted the possible association between IGR J16393−4643 and the unidentified *EGRET* source 3EG J1639−4702 (Hartman et al. 1999). Non-thermal radio emission was recently detected within the *ASCA* error box (Combi et al. 2004) which suggests a dust-enshrouded microquasar and could help justify the *IBIS* and *EGRET* association. However, the *XMM-Newton* position (RA (J2000) = $16^{\rm h}39^{\rm m}05.4^{\rm s}$, Dec = $-46°42'12''$, $4''$ uncertainty) is incompatible with the position of the radio source MOST J1639.0−4642, or any known radio source from the Vizier database. The pulsation and the lack of radio emission invalidate the microquasar interpretation for the HMXB. Also, the chance association of the *EGRET* source with IGR J16393−4643 is strong given the high density of sources in the region.

A single infrared candidate, 2MASS J16390535−4642137, lies within the *XMM-Newton* error circle of IGR J16393−4643. The high-energy spectral and timing characteristics of IGR J16393−4643 are reminiscent of other heavily-absorbed, wind-accreting X-ray pulsars with OB supergiant companions (Walter et al. 2004). A Be stellar companion is unlikely given that such systems are usually transient. Infrared observations should confirm the supergiant nature of the companion. If this is the case, it will constitute another argument rejecting the *EGRET* association (Orellana & Romero 2005).

Recently, combined *INTEGRAL* and *XMM-Newton* observations of the Norma Arm have revealed more pulsating X-ray binaries than were previously known. These objects have joined the ranks of what might be a new class of heavily-absorbed HMXBs that were previously undetected below 5 keV. The increasing sample size these objects represent should enable meaningful statistical studies to be performed. Understanding the nature of sources such as IGR J16393−4643 could shed light on the structure of stellar winds, provide constraints on the masses of neutron stars, and help elucidate the evolution of binaries.

Acknowledgements. The authors thank the anonymous referee for their prompt report which improved the paper. A. Bodaghee acknowledges J. Wendt, J. Rodriguez, A. Paizis, D. Willis, N. Produit and S. Paltani for their input and discussions. This research has made use of the SIMBAD database, operated at CDS, Strasbourg, France. This publication uses observations obtained with the ESA science missions *INTEGRAL* and *XMM-Newton*. The *INTEGRAL* and *XMM-Newton* instruments and data centres were directly funded by ESA member states and the USA (NASA).

References

Bildsten, L., Chakrabarty, D., Chiu, J., et al. 1997, ApJS, 113, 367
Bird, A. J., Barlow, E. J., Bassani, L., et al. 2004, ApJ, 607, L33
Combi, J. A., Ribó, M., Mirabel, I. F., & Sugizaki, M. 2004, A&A, 422, 1031
Courvoisier, T. J.-L., Walter, R., Beckmann, V., et al. 2003, A&A, 411, L53
Cutri, R. M., Skrutskie, M. F., van Dyk, S., et al. 2003, VizieR Online Data Catalog, 2246, 0
Dickey, J. M., & Lockman, F. J. 1990, ARA&A, 28, 215
Ebisawa, K., Bourban, G., Bodaghee, A., Mowlavi, N., & Courvoisier, T. J.-L. 2003, A&A, 411, L59
Haberl, F., & White, N. E. 1990, ApJ, 361, 225
Hartman, R. C., Bertsch, D. L., Bloom, S. D., et al. 1999, ApJS, 123, 79
Hill, A. B., Walter, R., Knigge, C., et al. 2005, A&A, 411, L53
Horne, J. H., & Baliunas, S. L. 1986, ApJ, 302, 757
House, L. L. 1969, ApJS, 18, 21
Jansen, F., Lumb, D., Altieri, B., et al. 2001, A&A, 365, L1
Kaastra, J. S., & Mewe, R. 1993, A&AS, 97, 443
Lebrun, F., Leray, J. P., Lavocat, P., et al. 2003, A&A, 411, L141
Liu, Q. Z., van Paradijs, J., & van den Heuvel, E. P. J. 2000, A&AS, 147, 25
Lutovinov, A., Revnivtsev, M., Gilfanov, et al. 2005a, A&A, 444, 821
Lutovinov, A., Rodriguez, J., Revnivtsev, M., & Shtykovskiy, P. 2005b, A&A, 433, L41
Malizia, A., Bassani, L., di Cocco, G., et al. 2004, The Astronomer's Telegram, 227, 1
Matt, G. 2002, MNRAS, 337, 147
Monet, D. G., Levine, S. E., Canzian, B., et al. 2003, AJ, 125, 984

Ochsenbein, F., Bauer, P., & Marcout, J. 2000, A&AS, 143, 23

Orellana, M., & Romero, G. E. 2005, Ap&SS, 297, 167

Rodriguez, J., Tomsick, J. A., Foschini, L., et al. 2003, A&A, 407, L41

Strüder, L., Briel, U., Dennerl, K., et al. 2001, A&A, 365, L18

Sugizaki, M., Mitsuda, K., Kaneda, H., et al. 2001, ApJS, 134, 77

Turner, M. J. L., Abbey, A., Arnaud, M., et al. 2001, A&A, 365, L27

Ubertini, P., Lebrun, F., Di Cocco, G., et al. 2003, A&A, 411, L131

van Paradijs, J. 1983, in Accretion-Driven Stellar X-ray Sources, 189

Voges, W., Aschenbach, B., Boller, T., et al. 1999, A&A, 349, 389

Walter, R., Rodriguez, J., Foschini, L., et al. 2003, A&A, 411, L427

Walter, R., Courvoisier, T. J.-L., Foschini, L., et al. 2004, in The INTEGRAL Universe, Proceedings of the Fifth INTEGRAL Workshop, 16–20 February 2004, Munich, Germany, ed. B. Battrick, Scientific ed. V. Schoenfelder, G. Lichti, & C. Winkler, ESA SP-552 (Noordwijk: ESA Publication Division), 417

White, N. E., Nagase, F., & Parmar, A. N. 1995, X-ray binaries Cambridge Astrophysics Series, ed. W. H. G. Lewin, J. Van Paradijs, & E. P. J. Van den Heuvel (Cambridge, MA: Cambridge University Press), 1

Winkler, C., Courvoisier, T. J.-L., Di Cocco, G., et al. 2003, A&A, 411, L1

Chapter 8
Other IGR Sources

After the multi-wavelength study of IGR J16393−4643, I contributed in varying capacities to the analyses of multi-wavelength observations of 3 other IGR sources: IGR J16320−4751, IGR J17252−3616, and IGR J17497−2821. I assisted Dr. Jerome Rodriguez with the spectral analysis of IGR J16320−4751 using the experience that I gained with the similar source IGR J16393−4643. I was involved with the early stages of the analysis of IGR J17252−3616, particularly the ISGRI imaging. For IGR J17497−2821, I was a co-investigator of the *RXTE* observation led by Dr. Rodriguez. The major results from our studies on these IGRs are discussed in the following sections.

8.1 IGR J16320−4751

Like IGR J16393−4643, IGR J16320−4751 (Tomsick et al. 2003) is another Norma Arm source that is actually the hard X-ray counterpart to an *ASCA* source: AX J1631.9−4752 (Sugizaki et al. 2001). in 't Zand et al. (2003) noticed that IGR J16320−4751 was present in archival data from the Wide-Field Camera aboard *BeppoSAX*, which means that the source has been emitting persistently for at least 8 years. A refined position from *XMM-Newton* excludes all but 2 potential infrared counterparts, leading Rodriguez et al. (2003) to conclude that the source is likely to be a HMXB hosting a NS. Confirmation of the NS came with the discovery of X-ray pulsations (pulse period ∼ 1300 s) in light curves from *XMM-Newton* and *ASCA* (Lutovinov et al. 2005b). Recent observations with *Swift* revealed a probable orbital period of ∼ 8.96 d (Corbet et al. 2005) suggesting that the stellar companion is an early-type supergiant.

We analyzed simultaneous *INTEGRAL* and *XMM-Newton* observations of IGR J16320−4751 that took place between August 19 and 20, 2004. The exposure times were ∼ 118 and ∼ 51 ks for ISGRI and EPIC, respectively. We improved the X-ray coordinates of the source to R.A. (J2000) = $16^{h}32^{m}01.9^{s}$ and Dec. = $-47°52'27''$ (∼ $3''$ uncertainty). This strongly suggests that the first of the 2 infrared counterpart candidates proposed in Rodriguez et al. (2003) is the genuine counterpart of IGR J16320−4751, since the second candidate is outside the

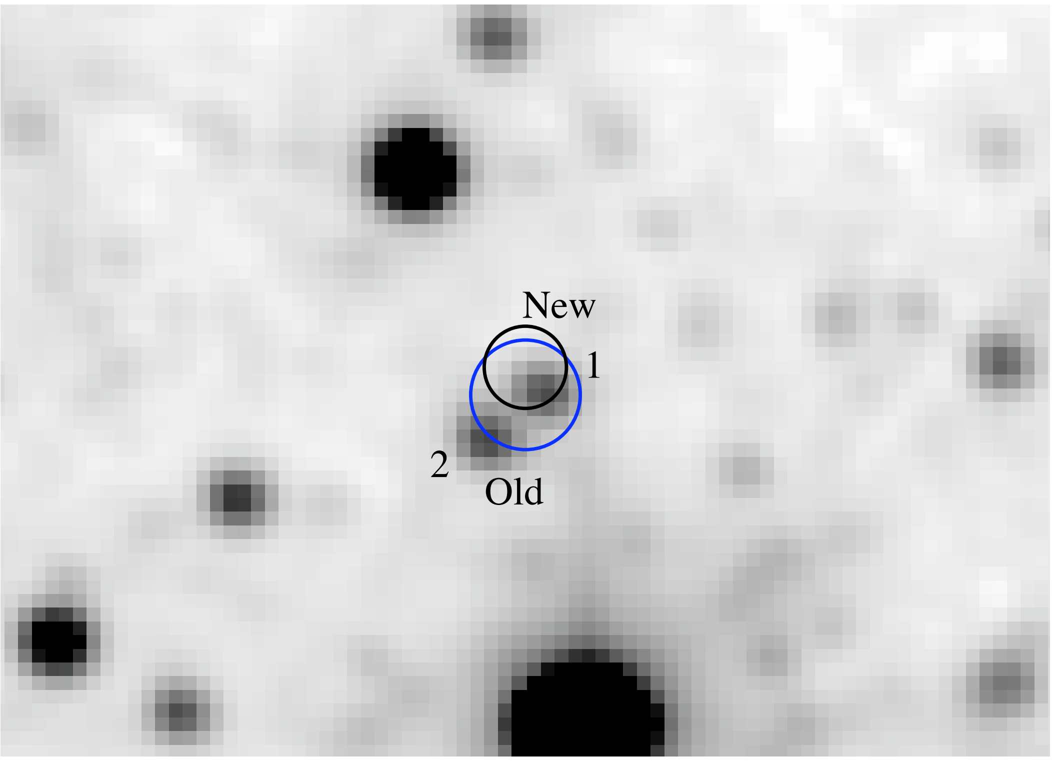

Figure *8.1: Image from 2MASS (Cutri et al. 2003) of the field around IGR J16320−4751. The large circle represents the* XMM-Newton *position given by Rodriguez et al. (2003), and the small circle represents the refined position from this analysis.*

90% error circle of the new X-ray position (see Fig. 8.1).

Figure 8.2 presents the light curves of IGR J16320−4751 as obtained by *INTEGRAL* and *XMM-Newton*. During our observations, the source showed a huge flare that was prominent in both light curves. We detected X-ray pulsations lasting ~ 1300 s in the *XMM-Newton* data, reaffirming the results of Lutovinov et al. (2005b). In addition, we were able to detect pulsations for the first time above 20 keV with ISGRI.

Source spectral data from *XMM-Newton* (0.6–12 keV) and *INTEGRAL* (20–80 keV) were split according to flaring and non-flaring epochs. The extension of the source spectrum up to 80 keV is unprecedented at this level of significance. Simply fitting the spectra with an absorbed power law leaves significant residuals at high energies. Adding a cutoff improves the fit as do the additions of a Gaussian representing an iron emission line at 6.4 keV, and an iron edge at 7 keV. The unabsorbed 2–10 and 20–100 keV fluxes (in 10^{-11} ergs cm^{-2} s^{-1}) are 9.2 and 23.3, respectively.

We obtained a good fit ($\chi^2_\nu = 1.15$ for 438 dof) to the spectrum by replacing the cutoff power law with a thermal Comptonization (CE) model (Titarchuk 1994) (see

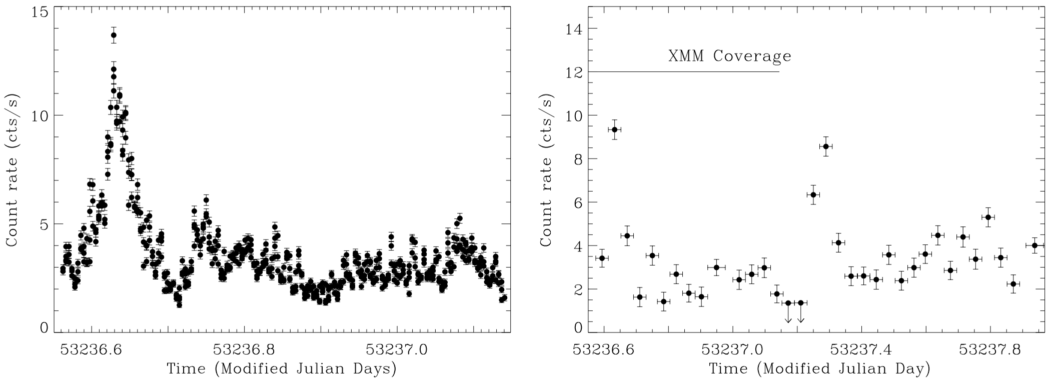

Figure *8.2: Light curves of IGR J16320−4751 from PN (left, 2–12 keV) and ISGRI (right, 20–60 keV). The time bin of the PN light curve is 100 s, while that of ISGRI is about 3200 s. Upper limits are given at the 3-σ level.*

Fig. 8.3). Table 8.1 reports the parameters from this model. Except for the normalization, which is related to the source flux, the spectral parameters do not change with the pulse.

This is the first time that an iron line has been detected for IGR J16320−4751. Iron emission lines are usually interpreted as being due to the fluorescence of iron in cold neutral matter surrounding the X-ray source. This suggests that accretion occurs in part through the wind, implying that the system is a HMXB.

A large excess below 2 keV is reminiscent of the soft excess emission found for e.g. IGR J16393−4643 (see Chapter 7). This soft excess was best modeled by a blackbody rather than by an ionized absorber that covers part of the X-ray source. A medium different from the Comptonizing cloud that produces the hard X-ray emission must be responsible for the soft excess given that the temperatures are clearly different and given that the pulse is not detected in the soft excess.

The soft excess is probably due to the reprocessing of hard X-rays in the stellar wind (Haberl & White 1990; Hickox et al. 2004). However, the origin of this emission depends on which object is being considered. Conservation of energy requires $F_{\mathrm{bb}} \lesssim \Delta F_{\mathrm{CE}}$, where F_{bb} is the unabsorbed bolometric flux of the blackbody, and ΔF_{CE} is the difference of the unabsorbed to the absorbed (~ bolometric) flux of the Comptonized component. For IGR J16320−4751, our fits returned $\Delta F_{\mathrm{CE}} \sim 0.4 \cdot 10^{-10}$ ergs cm^{-2} s^{-1} and $F_{\mathrm{bb}} \sim 2.2 \cdot 10^{-10}$ ergs cm^{-2} s^{-1}. This seems to invalidate thermal reprocessing as the origin of the soft excess in IGR J16320−4751, and favors other interpretations such as collisionally energized clouds.

During the flare, the column density decreased marginally, whereas the temperature of the injected photons and the temperature of the Comptonized electrons decreased significantly. The drop in temperature leads to a reduced optical depth

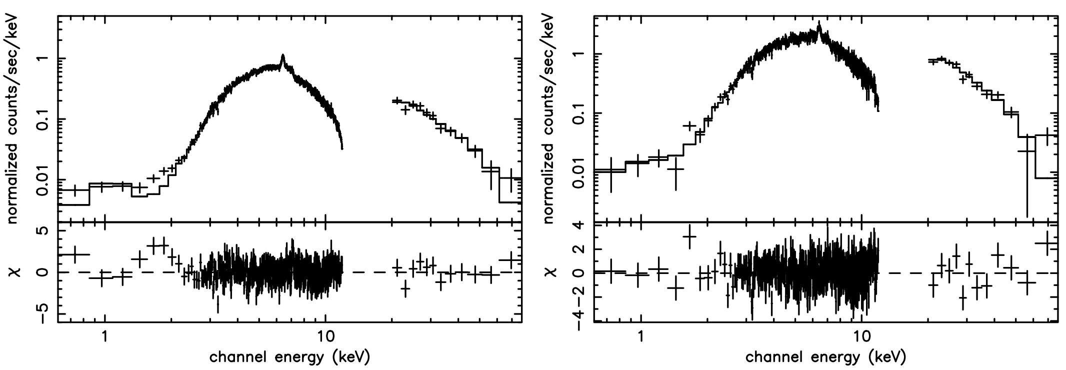

Figure *8.3: PN and ISGRI count spectra of IGR J16320−4751 during flaring (right) and non-flaring epochs (left) fit with the Comptonized emission (CE) model described in the text.*

Table 8.1: Parameters from a Comptonized emission (CE) model fit to the 0.6–80 keV EPIC and ISGRI spectra of IGR J16320−4751 during flaring and non-flaring epochs. $N_{\rm H}$ is the intrinsic absorption, τ is the optical depth of the Comptonizing medium, $kT_{\rm bb}$ is the blackbody temperature, $kT_{\rm i}$ is the temperature of the injected photons for Comptonization, $kT_{\rm e}$ is the electron temperature. The iron abundance ($\rm Z_{Fe}$) is given with respect to the Solar value, and the iron line is represented in the model by a Gaussian with an equivalent width of $\mathrm{EW}_{K\alpha}$ and centered at $\mathrm{E}_{K\alpha}$. Errors represent the 90% confidence level.

Parameter	Non-Flare	Flare	Unit
$N_{\rm H}$	$8.9^{+0.2}_{-0.7}$	$7.6^{+1.2}_{-1.4}$	$10^{22}\,\mathrm{cm}^{-2}$
τ	$4.9^{+0.5}_{-0.4}$	$9.8^{+1.2}_{-1.4}$	
$kT_{\rm i}$	$1.98^{+0.15}_{-0.10}$	$1.30^{+0.31}_{-0.24}$	keV
$kT_{\rm e}$	$8.0^{+1.0}_{-0.7}$	$6.5^{+0.4}_{-0.3}$	keV
$kT_{\rm bb}$	$0.075^{+0.024}_{-0.018}$	0.075 (fixed)	keV
$\rm Z_{Fe}$	1.8 ± 0.3	$2.2^{+0.9}_{-0.6}$	$\mathrm{Z}_\odot$
$\mathrm{E}_{K\alpha}$	6.411 ± 0.006	$6.419^{+0.014}_{-0.015}$	keV
$\mathrm{EW}_{K\alpha}$	100^{+24}_{-20}	112^{+42}_{-44}	eV

for the Comptonizing plasma, and a much more efficient Compton up-scattering during the flare. The flare was probably caused by inhomogeneities in the densities of the stellar wind. We estimate that the inner edge of the shell of material responsible for photoelectric absorption and iron fluorescence is situated some 0.07 AU from the X-ray source. This is compatible with the expected orbital radius, and is where density inhomogeneities are likely to be the strongest.

Our imaging, timing and spectral analyses of IGR J16320−4751 point towards it being another member of the class of X-ray pulsars with supergiant companions. Although we appear to know IGR J16320−4751 well, the source clearly deserves further research in order to clarify the origin of its soft excess emission, to better understand the reasons behind the unusually long spin period of its neutron star, and to confirm the recently proposed orbital period.

8.1.1 Scientific Article on IGR J16320−4751

This study was published as Rodriguez et al. (2006). A copy of the article is provided at the end of the chapter:

- Rodriguez J., Bodaghee A., Kaaret P., Tomsick J.A., Kuulkers E., Malaguti G., Petrucci P.-O., Cabanac C., Chernyakova M., Corbel S., Deluit S., Di Cocco G., Ebisawa K., Goldwurm A., Henri G., Lebrun F., Paizis A., Walter R. & Foschini L.
  INTEGRAL and XMM-Newton observations of the X-ray pulsar IGR J16320−4751/AX J1631.9−4752
  Monthly Notices of the Royal Astronomical Society, Vol. 366-1, pp. 274–282, 2006

8.2 IGR J17252−3616

The discovery of IGR J17252−3616 was reported along with 13 other hard X-ray sources that were detected in ISGRI mosaic images of the Galactic Center and Plane (Walter et al. 2004a). As with IGR J16393−4643 and IGR J16320−4751, there is evidence that IGR J17252−3616 was previously detected at lower energies. The *EXOSAT* source EXO 1722−363 was detected at a position that is incompatible with IGR J17252−3616 but with a large error circle (Warwick et al. 1988). *Ginga* observations showed a pulse period of $\sim 413.9 \pm 0.2$ s (Tawara et al. 1989), and set lower limits to the orbital period ($\lesssim 9$ d) and to the mass of the companion star ($\lesssim 15\,M_\odot$) (Takeuchi et al. 1990). An orbital period of 9.741 ± 0.004 d was confirmed by Corbet et al. (2005) which, when considered with other factors, led the authors to conclude that the source is an absorbed HMXB consisting of a NS that accretes from the wind of an early-type supergiant companion.

Because of its location near the Galactic Center, IGR J17252−3616 is regularly monitored by *INTEGRAL*. The ISGRI data set consists of core program and public observations from revolutions 37–244, for a total exposure time of 6.5 Ms. A follow-up observation lasting 11 ks was performed with *XMM-Newton* on March 21, 2004. The procedures for data extraction and analysis are similar to those of Bodaghee et al. (2006) (see Chapter 7).

The best ISGRI position of R.A. (2000) = $17^{\mathrm{h}}25^{\mathrm{m}}10^{\mathrm{s}}$ and Dec. = $-36^\circ 17' 18''$ ($23''$ uncertainty) was obtained from the 20–60 keV band mosaic image of revolution 106, where the source was detected at its highest average flux.

XMM-Newton provided us with the most precise X-ray position of the source to date: R.A. (2000) = $17^{\mathrm{h}}25^{\mathrm{m}}11.4^{\mathrm{s}}$ and Dec. = $-36^\circ 16' 58.6''$ ($4''$ uncertainty). The

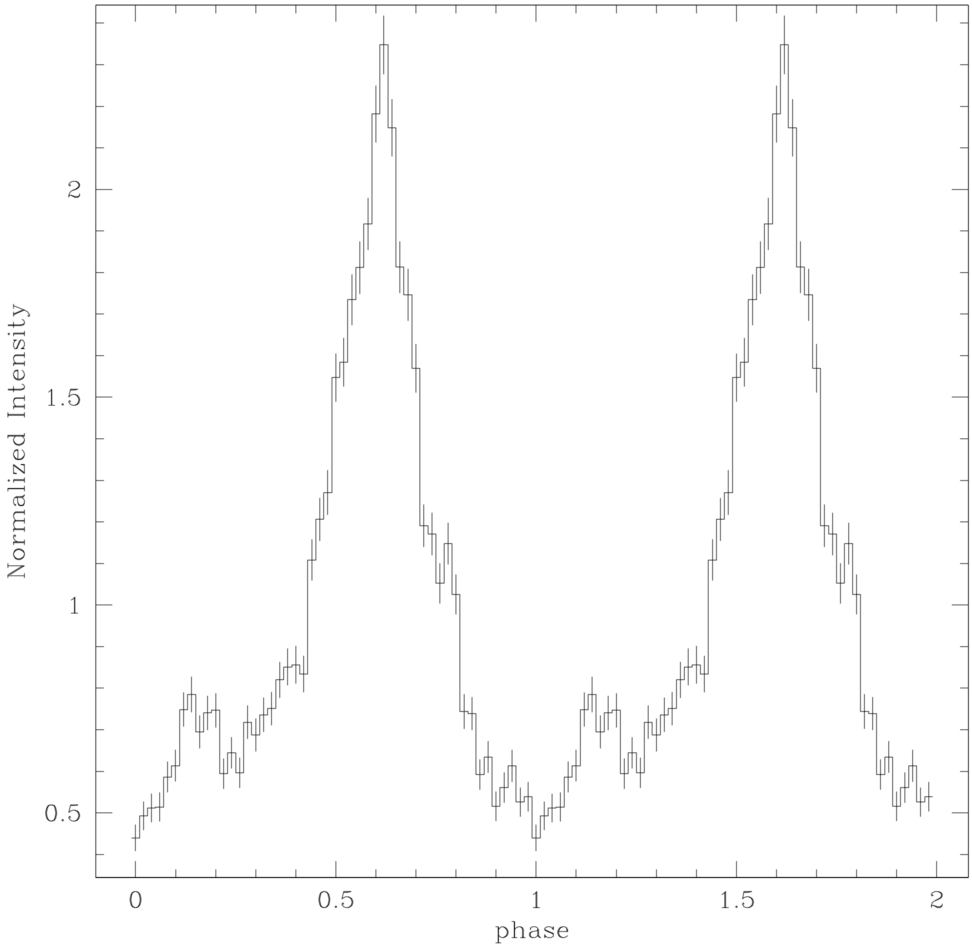

Figure *8.4: The 0.4–10 keV light curve of IGR J17252−3616 folded with a spin period of* ~ 414 *s.*

only infrared object within this new error circle is 2MASS J17251139−3616575 which is 1″ away. Even though the 4″ EPIC error box is 12′ from the position of the *EXOSAT* source EXO 1722−363 (with an error radius of 9′), the 2 sources are the same given the identical timing and spectral behavior attributed to them.

IGR J17252−3616 was detected in the ISGRI 20–60 keV mosaic image of almost every spacecraft revolution. This demonstrates the persistence of the emission from IGR J17252−3616 in the soft γ-rays. An orbital period of 9.72±0.09 d was detected in the long term ISGRI light curve. On shorter time scales, we found significant flares in the ISGRI data, and a periodic oscillation of ~ 414 s in both the ISGRI and EPIC data (see Fig. 8.4). The pulse and orbital periods are consistent with the results of Tawara et al. (1989) and Corbet et al. (2005). The constancy of the pulse period over 17 years suggests a wind-accreting neutron star. Its orbital and spin pe-

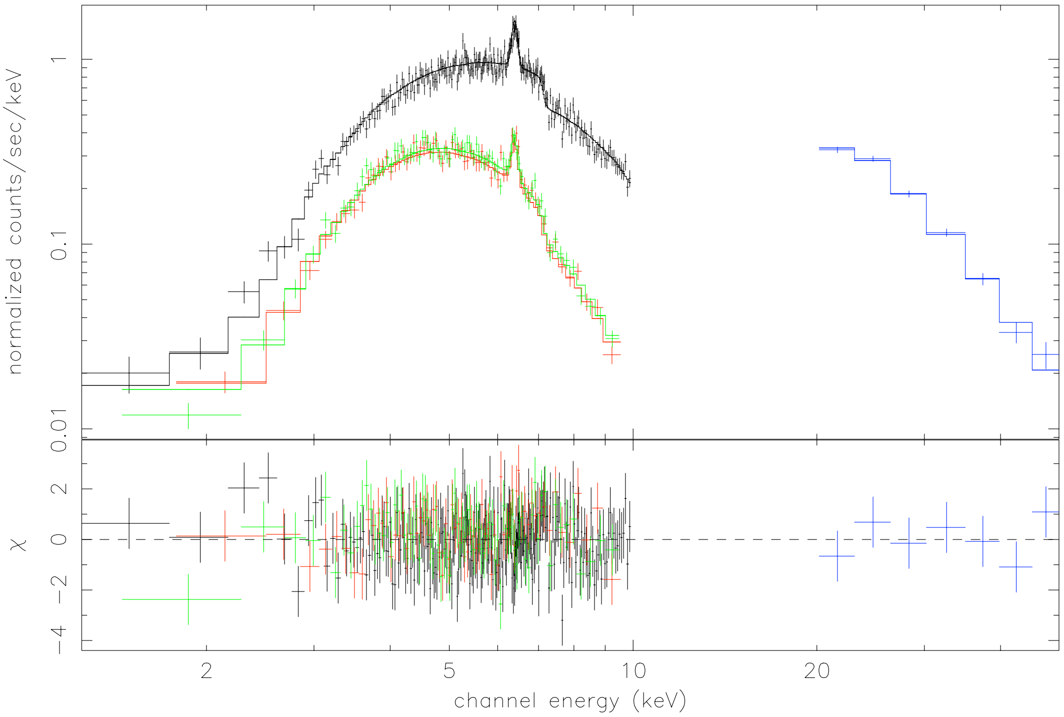

Figure *8.5: Average source spectra from PN and ISGRI of IGR J17252−3616. The continuous line represents the Comptonized emission (CE) model.*

riods place IGR J17252−3616 among other wind-fed systems in the Corbet (1986) diagram.

Figure 8.5 presents the combined EPIC and ISGRI 1–50 keV spectrum of IGR J17252−3616. The source spectrum is typical of wind-accreting X-ray pulsars in that it presents a soft excess emission, a large column density ($N_H = 15.3^{+1.1}_{-1.0} \cdot 10^{22}$ cm^{-2}), an iron line at 6.4 keV, a flat power law below 10 keV ($\Gamma \sim 0$) and a high-energy cutoff. A good fit ($\chi^2_\nu = 1.07$ for 376 dof) was achieved with either an absorbed cutoff power law (CP) or Comptonized emission (CE) model used for similar IGRs (e.g. Bodaghee et al. 2006; Rodriguez et al. 2006; Walter et al. 2006). The Comptonizing medium has an optical depth of $\tau = 7.8^{+0.6}_{-0.5}$, and an electron temperature of $kT_e = 5.5 \pm 0.2$. The pulsation only affects the normalization.

The evidence strongly favor IGR J17252−3616 being an absorbed HMXB composed of a neutron star accreting from the wind of a supergiant companion. This source, along with IGR J16320−4751 (Rodriguez et al. 2006) and IGR J16393−4643 (Bodaghee et al. 2006), represent an emerging class of absorbed Galactic binaries. Detections with *INTEGRAL* combined with pointed observations with *XMM-Newton* have helped to clarify their nature (Walter et al. 2006).

Details concerning the analysis of this source were published as Zurita Heras et al.

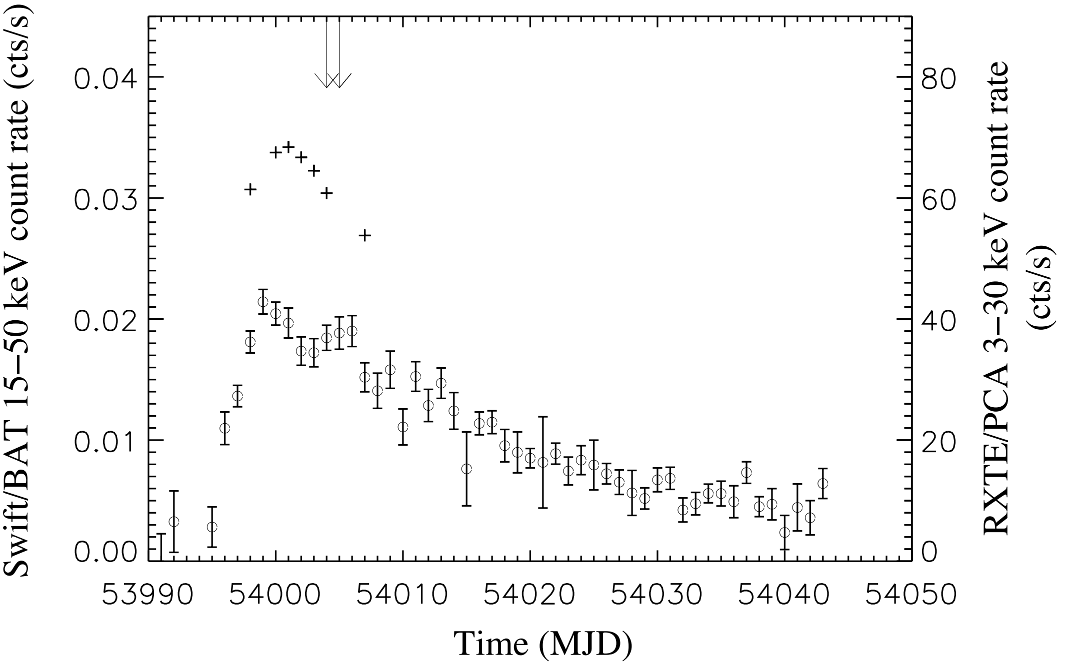

Figure *8.6: Light curves of IGR J17497−2821 during its outburst. Circles represent the 15–50 keV* Swift/*BAT data and crosses symbolize the 3–30 keV* RXTE/*PCA data. The vertical arrows represent the dates of our ATCA observations. One Crab* ~ 0.23 *cps and* ~ 1840 *cps for BAT and PCA, respectively.*

(2006):

- Zurita Heras J.A., de Cesare G., Walter R., Bodaghee A., Bélanger G., Courvoisier T.J.-L., Shaw S.E. & Stephen J.B.
  IGR J17252−3616: an accreting pulsar observed by INTEGRAL and XMM-Newton
  Astronomy & Astrophysics, Vol. 448-1, pp. 261–270, 2006

8.3 IGR J17497−2821

IGR J17497−2821 was discovered with ISGRI on Sept. 17, 2006, at Galactic coordinates $l = 0.97°$ and $b = -0.46°$ (Soldi et al. 2006). Assuming a distance of 8 kpc, given that the source is in the direction of the Galactic Center, Kuulkers et al. (2006) estimated an unabsorbed luminosity of ~ 10^{37} ergs s^{-1} for 2–100 keV. Its location and its luminosity indicate that IGR J17497−2821 is a new transient Galactic XRB. A preliminary spectral analysis of *INTEGRAL* data led Kuulkers et al. (2006) to further suggest the source was in a Low-Hard State (LHS) typical of BH and NS XRBs.

Follow-up observations with *Chandra* refined the X-ray position to R.A. (J2000)

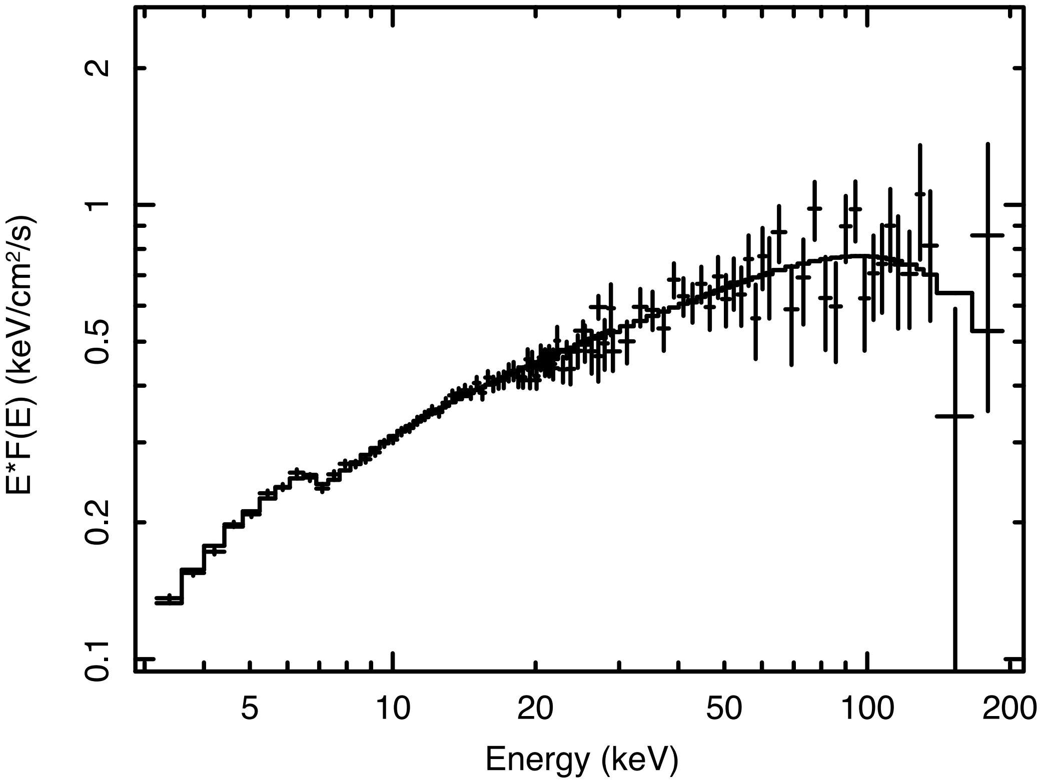

Figure *8.7: The 3–200 keV* RXTE *spectrum of Obs. 7. The best fit model is superimposed as a line.*

= $17^h49^m38.037^s$ and Dec. = $-28°21'17.37''$, with a 90% confidence circle radius of 0.6” (Paizis et al. 2007). This improved X-ray position enabled the likely optical/IR counterpart to be identified as a red K-type giant. Hence, IGR J17497−2821 is a LMXB.

A few days after the discovery of IGR J17497−2821, we triggered an *RXTE* ToO observation (P92016) as well as radio observations with the Australian Telescope Compact Array (ATCA).

Our *RXTE* program was divided into seven pointings during September 20–29, 2006. Roughly 12.3 hours of simultaneous observations were performed with ATCA at 4.80 GHz (6 cm) and 8.64 GHz (3.5 cm), with a continuum bandwidth of 128 MHz. Radio emission was not detected from IGR J17497−2821 with a 3σ upper limit of 0.21 mJy in 4.80 GHz and 8.64 GHz.

Figure 8.6 presents the 3–30 keV *RXTE*/PCA and 15–50 keV *Swift*/BAT light curves of IGR J17497−2821 during the outburst. As the figure shows, the *RXTE* observations were coincident with the peak of the outburst. Over a span of 5 days, the 15–50 keV BAT flux increased by a factor greater than 5.

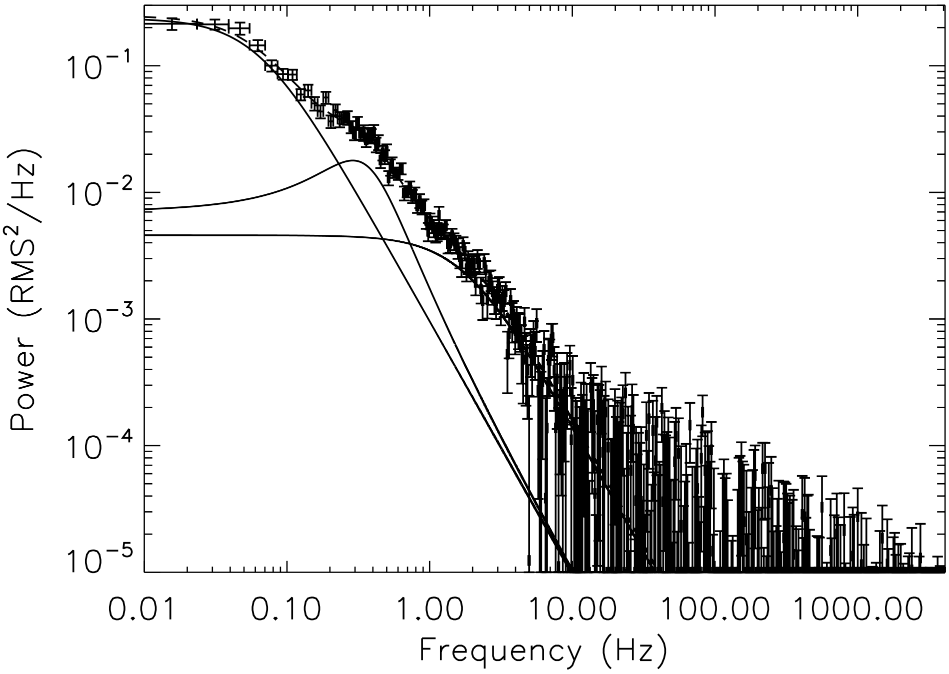

Figure *8.8: Noise-corrected PDS of IGR J17497−2821 from* RXTE. *The continuous lines represent 3 broad Lorentzians, and the dashed line is the best model.*

The power density spectra (PDS) from IGR J17497−2821 are typical of the LHS of XRBs (see Fig. 8.8). By themselves, the shapes of the PDS are not enough to distinguish between a NS or a BHC as the compact object (e.g. Lewin & van der Klis 2006). However, BHCs in the LHS are expected to have lower typical frequencies with no significant signals detected above ~ 50 Hz (Sunyaev & Revnivtsev 2000). Note that the accreting millisecond pulsar IGR J00291+5934 represents a recent exception.

We did not detect a significant signal $\gtrsim$10 Hz in the PDS of IGR J17497−2821 which suggests that the source is a BHC. The low break frequency of the first Lorentzian component (0.06 Hz) coupled with the high level of the flat-top noise also suggest a BH primary. In fact, none of the defining characteristics of NS systems were observed in IGR J17497−2821: there were no coherent pulsations, no kHz QPOs, and no X-ray bursts.

The model that best fits the photon spectrum of IGR J17497−2821 (Fig. 8.7) is a power law ($\Gamma \sim 1.57$) modified by interstellar absorption (Dickey & Lockman 1990) and a high-energy cutoff ($E_{\rm cut} \sim 50$ keV), which are all reminiscent of XRBs in the LHS. The high electron temperature ($kT_e \sim 40$ keV) and optical depth $\tau \sim 2$ derived from a thermal Comptonization model (Titarchuk 1994) suggest that the compact object is a BHC. An iron edge around 7 keV was first noticed in the *Suzaku* spectrum of the source (Itoh et al. 2006), and we were also able to detect this feature with *RXTE*.

Our *RXTE* and radio observations lead us to conclude that IGR J17497−2821 is a BHC in the LHS. For BHCs in the LHS, the correlation that typically occurs between X-rays and radio waves represents a unique opportunity to study a potential coupling of accretion (X-rays) and ejection (radio jets). However, a few objects such as IGR J17497−2821 might somehow be prevented from forming jets and/or emitting from them.

We can not predict when IGR J17497−2821 will experience its next outburst. If it occurs in the next few years, an armada of space telescopes and crews of scientists worldwide will be ready to observe and analyze any new behavior which could help shed light on the true nature of IGR J17497−2821.

Further details of the multi-wavelength analysis of IGR J17497−2821 can be found in Rodriguez et al. (2007):

- Rodriguez J., Cadolle Bel M., Tomsick J.A., Corbel S., Brocksopp C., Paizis A., Shaw S.E. & Bodaghee A.
  The discovery outburst of the X-ray transient IGR J17497−2821 observed with RXTE and ATCA
  ApJL, Vol. 655, pp. L97–L100, 2007

Mon. Not. R. Astron. Soc. **366,** 274–282 (2006) doi:10.1111/j.1365-2966.2005.09855.x

INTEGRAL and XMM–Newton observations of the X-ray pulsar IGR J16320−4751/AX J1631.9−4752

J. Rodriguez,[1,2,3]★ A. Bodaghee,[3,4] P. Kaaret,[5] J.A. Tomsick,[6] E. Kuulkers,[7] G. Malaguti,[8] P.-O. Petrucci,[9] C. Cabanac,[9] M. Chernyakova,[3] S. Corbel,[1,2] S. Deluit,[10] G. Di Cocco,[8] K. Ebisawa,[11] A. Goldwurm,[1,12] G. Henri,[9] F. Lebrun,[1,12] A. Paizis,[3,13] R. Walter[3,4] and L. Foschini[8]

[1] *CEA Saclay, DSM/DAPNIA/Service d'Astrophysique, 91191 Gif sur Yvette, France*
[2] *Unité mixte de recherche CEA/CNRS/Université Paris 7 UMR AIM/7158*
[3] *ISDC, Chemin d'Ecogia, 16, 1290 Versoix, Switzerland*
[4] *Observatoire de Genève, Chemin des Maillettes 51, 1290 Sauverny, Switzerland*
[5] *Department for Physics and Astronomy, University of Iowa, Iowa City, IA 52242, USA*
[6] *Center for Astrophysics and Space Science, University of California at San Diego, MS 0424, La Jolla, CA 92093 USA*
[7] *ISOC, ESA/ESAC, Urb. Villafranca del Castillo, PO Box 50727, 28080 Madrid, Spain*
[8] *INAF/IASF, Via Gobetti 101, 40129 Bologna, Italy*
[9] *Laboratoire d'Astrophysique de l'Obesrvatoire de Grenoble, BP 53X, 38041 Grenoble, France*
[10] *Centre d'Etude Spatiale des Rayonnements 9, avenue du Colonel Roche - Boite postale 4346 31028 Toulouse Cedex 4, France*
[11] *NASA Goddard Space Flight Center, Code 661, Greenbelt, MD 20771, USA*
[12] *Unité mixte de recherche APC, 11 place Berthelot 75005 Paris, France*
[13] *INAF/IASF sezione di Milano, Via Bassini 15, 20133 Milano, Italy*

Accepted 2005 November 10. Received 2005 November 9; in original form 2005 September 19

ABSTRACT

We report on observations of the X-ray pulsar IGR J16320−4751 (also known as AX J1631.9−4752) performed simultaneously with International Gamma-Ray Astrophysics Laboratory (*INTEGRAL*) and *XMM–Newton*. We refine the source position and identify the most likely infrared counterpart. Our simultaneous coverage allows us to confirm the presence of X-ray pulsations at ∼1300 s, that we detect above 20 keV with *INTEGRAL* for the first time. The pulse fraction is consistent with being constant with energy, which is compatible with a model of polar accretion by a pulsar. We study the spectral properties of IGR J16320−4751 during two major periods occurring during the simultaneous coverage with both satellites, namely a flare and a non-flare period. We detect the presence of a narrow 6.4 keV iron line in both periods. The presence of such a feature is typical of supergiant wind accretors such as Vela X-1 or GX 301−2. We inspect the spectral variations with respect to the pulse phase during the non-flare period, and show that the pulse is solely due to variations of the X-ray flux emitted by the source and not due to variations of the spectral parameters. Our results are therefore compatible with the source being a pulsar in a High Mass X-ray Binary. We detect a soft excess appearing in the spectra as a blackbody with a temperature of ∼0.07 keV. We discuss the origin of the X-ray emission in IGR J16320−4751: while the hard X-rays are likely the result of Compton emission produced in the close vicinity of the pulsar, based on energy argument we suggest that the soft excess is likely the emission by a collisionally energized cloud in which the compact object is embedded.

Key words: stars: neutron – pulsars: general – stars: individual: IGR J16320-4751, AX J1631.9-4752 – X-rays: binaries.

1 INTRODUCTION

The International Gamma-Ray Astrophysics Laboratory (*INTEGRAL*) was set up on 2002 October 17 (Winkler et al. 2003). Since then, through regular scans of our Galaxy and guest observers'

★E-mail: rodrigue@discovery.saclay.cea.fr

Table 1. Journal of the observations analysed in this paper.

Satellite	Revolution no	Date obs. Start day	Stop day	(MJD 53000)	Prop. Id	Total duration ($\times 10^3$ s)
INTEGRAL	226	2004 Aug 19	2004 Aug 20	236.57–237.94	0220014&0220007	∼118
XMM–Newton	860	2004 Aug 19	2004 Aug-20	236.55–237.14	0201700301	∼51

observations, about 75 new sources[1] have been discovered mainly with the IBIS telescope (Ubertini et al. 2003), thanks to its low-energy camera ISGRI (Lebrun et al. 2003). Because of its energy range (from 15 keV to ∼1 MeV), its high angular resolution (12 arcmin), good positional accuracy (down to ∼0.5 arcmin for bright sources) and its unprecedented sensitivity, between 20 and 200 keV, IBIS/ISGRI has helped us to answer the question of the origin of the hard X-ray background in the Galaxy (Lebrun et al. 2004). These capacities have helped us to discover many peculiar X-ray binaries characterized by a huge equivalent absorption column density ($N_{\rm H}$), as high as a few times 10^{24} cm^{-2} in IGR J16318−4848 (Matt & Guainazzi 2003; Walter et al. 2003), the first source discovered by *INTEGRAL*. Due to the high absorption, most of these sources were not detected during previous soft X-ray scans of the Galaxy [see e.g. Kuulkers (2005) for a review].

IGR J16320−4751 was detected on 2003 February 1 with ISGRI (Tomsick et al. 2003) as a hard X-ray source. The source was observed to vary significantly in the 15–40 keV energy range on time-scales of ∼1000 s, and was sometimes detected above 60 keV (Tomsick et al. 2003; Foschini et al. 2004). The inspection of the X-ray archives revealed that IGR J16320−4751 is the hard X-ray counterpart to AX J1631.9-4752, observed with *ASCA* in 1994 and 1997 (Sugizaki et al. 2001). The analysis of archival BeppoSAX-WFC data showed that this source was persistent for at least 8 yr (in't Zand et al. 2003). Soon after the discovery of IGR J16320−4751 by *INTEGRAL*, an *XMM–Newton* Target of Opportunity was triggered. This allowed us to obtain the most accurate X-ray position to date (Rodriguez et al. 2003), which in particular led to the identification of two possible infrared counterparts (Tomsick et al. 2003; Rodriguez et al. 2003) (hereafter source 1 and 2). From this analysis, we suggested that IGR J16320−4751 is probably a High Mass X-ray Binary (HMXB) hosting a neutron star (Rodriguez et al. 2003). This last point has been reinforced since the discovery of X-ray pulsations from this source in both *XMM–Newton* and *ASCA* observations (Lutovinov et al. 2005) with a pulse period of about 1300 s. Aharonian et al. (2005), reporting results of the survey of the inner regions of the Galaxy at very high energy with the High Energy Stereoscopic System (HESS), found a new source, HESS J1632−478, at a position coincident with IGR J16320−4751, but the authors suggest that this could be simply a chance coincidence. Very recently, Corbet et al. (2005) reported the discovery of strong modulations of the X-ray flux seen with Swift, that they interpreted as revealing the orbital period of the system. The period of 8.96 d that they find is compatible with the system containing an early-type supergiant (Corbet et al. 2005).

Here, we report on observations of IGR J16320−4751 performed simultaneously with *INTEGRAL* and *XMM–Newton* in 2004 August. The sequence of observations is introduced in the following section together with technical information concerning the data reduction. Section 3 of this paper describes the results which are commented and discussed in the last part of the paper.

2 OBSERVATIONS AND DATA REDUCTION

The journal of the observations can be found in Table 1. The *INTEGRAL* observation results from an amalgamation of the observation of IGR J16318−4848 (PI Kuulkers, programme no 0220007) with that of IGR J16320−4751 (PI Foschini, programme no 0220014). IGR J16320−4751, however, remained the on-axis target for this observation.

2.1 *INTEGRAL* Data Reduction

Our *INTEGRAL* observation was performed with the so-called hexagonal dithering pattern (Courvoisier et al. 2003), which consists of a sequence of seven pointings (called science windows, hereafter: SCW) following a hexagonal dithering on and around the position of the source. Being the on-axis target, IGR J16320−4751 is always in the fully coded field of view of the IBIS and SPI instruments, where the instrumental response is optimal. The *INTEGRAL* data were reduced using the Off-line Scientific Analysis (OSA) v 5.0, with specificities for each instrument described below.

The data from IBIS/ISGRI were first processed until the production of images in the 20–40 and 40–80 keV energy ranges, with the aim of identifying the most active sources in the field. From the results of this step, we produced a catalogue of active sources which was given as an input for a second run producing images in the 20–60 and 60–200 keV energy ranges. In the latter, we forced the extraction/cleaning of each of the catalogue sources in order to obtain the most reliable results for IGR J16320−4751 [see Goldwurm et al. (2003) for a detailed description of the IBIS software]. In order to check for the presence of the 1300-s X-ray pulsations in the IBIS range, we also produced light curves with a time bin of 250 s (with the OSA 5.0/II_LC_EXTRACT V2.4.3 module) in the same energy ranges.

We produced spectra using two alternative methods. The first method is to use the standard spectral extraction from the OSA pipeline. The second method uses the individual images produced in 20 energy bins to estimate the source count rate and build the spectrum as explained in Rodriguez et al. (2005). This second method can be used to crosscheck the results obtained with the standard spectral extraction. Comparison of the spectra obtained with the two methods showed no significant differences, we therefore used the spectra obtained with the standard procedure in our spectral fits. We used the standard response matrices provided with OSA 5.0, i.e. ISGR_ARF_RSP_0010.FITS and ISGR_RMF_GRP_0016.FITS, the latter rebinned to 20 spectral channels.

The source is not spontaneously detected by the JEM-X detector. We tentatively forced the extraction of science products at the position of IGR J16320−4751, but a rapid comparison with the *XMM–Newton* data showed that the JEM-X products were very likely to be contaminated by the nearby black hole candidate 4U 1630−47 that was in a bright soft state outburst at the time of the observation (Tomsick et al. 2005). These data were not considered further. We did not use the data from the spectrometer SPI because the

---

[1] An updated list of all *INTEGRAL* sources can be found at http://isdc.unige.ch/∼rodrigue/html/igrsources.html.

$2\overset{\circ}{.}5$ angular resolution did not allow to discriminate the emission of IGR J16320−4751 from that of e.g. 4U 1630−47 (the angular separation between the two sources is ~40 arcmin), or IGR J16318−4848 (~55 arcmin).

2.2 *XMM–Newton* data reduction

The *XMM–Newton* data were reduced with the Science Analysis System (SAS) v6.1.0. Event lists for EPIC MOS (Turner et al. 2001) and EPIC PN (Strüder et al. 2001) cameras were obtained after processing the Observation Data Files with EMCHAIN and EPCHAIN. During the processing, the data were screened by rejecting periods of high background, and by filtering the bad pixels. The EPIC MOS were both operating in timing mode allowing one to obtain light curves from the central chip with 1.5-ms resolution. The EPIC PN was operating in full frame mode, allowing light curves with a time resolution as high as 73.4 ms to be obtained. For the PN camera, we extracted the spectra and light curves from a 35-arcsec radius circle centred on the source, while background products were extracted from a 60-arcsec circular region free of sources (from the same chip).

Because of the operating mode of the MOS cameras, no background estimate can be obtained from the central chip where the source lies. A 'quick look' at the lateral MOS chips shows that the background remained negligible during the whole observation. The latter could therefore be neglected in the analysis of the MOS data. MOS light curves were hence extracted from the central chip of both cameras. For the three EPIC cameras, light curves were extracted in different energy ranges (2–12, 0.6–2, 2–5, 5–8, 8–12 keV) with the highest time resolution achievable. Barycentric correction was applied to all light curves. The MOS light curves were then summed using the FTOOLS LCMATH.

A redistribution response matrix and an ancillary response file for the PN spectral products were generated with RMFGEN and ARFGEN. The resulting spectrum was fitted in XSPEC v11.3.1 (Arnaud 1996) simultaneously with the spectrum obtained with *INTEGRAL*/ISGRI.

3 RESULTS

3.1 Refining of the X-ray position

Given the long exposure time (Table 1) and the high flux from the source, we tried to obtain a better estimate on the position in order to possibly discriminate between the two candidate counterparts (Rodriguez et al. 2003). For this purpose, we used the EDETECT_CHAIN task after having extracted PN images in five energy ranges. The latter were further rebinned so that an image pixel had a physical size of 4.4 arcmin. The best position obtained with this method is $\mathrm{RA}_{J2000} = 248\overset{\circ}{.}0077$ and $\mathrm{Dec.}_{\mathrm{J2000}} = -47\overset{\circ}{.}8742$ with a nominal uncertainty of ~4 arcmin. This is about 1.9 arcmin from the position reported by Rodriguez et al. (2003). To cross check, we re-analysed the 2003 *XMM–Newton* observation with the latest calibration files available, and using the same EDETECT_CHAIN in the same energy ranges. As explained in Rodriguez et al. (2003), only MOS data are available, and the data need to be filtered for soft proton flares. The best position we obtained is $\mathrm{RA}_{\mathrm{J2000}} = 248.0081^{\circ}$ and $\mathrm{Dec.}_{\mathrm{J2000}} = -47\overset{\circ}{.}8741$. We can therefore refine the X-ray position to $\mathrm{RA}_{\mathrm{J2000}} = 16^{\mathrm{h}}32^{\mathrm{m}}01\overset{\mathrm{s}}{.}9$ $\mathrm{Dec.}_{\mathrm{J2000}} = -47^{\circ}52'27''$ with an uncertainty of ~3 arcmin at 90 per cent confidence. This new position more strongly suggests that the source labelled as no 1 in Fig. 1 is the genuine counterpart of IGR J16320−4751, since source 2 is now outside the 90 per cent error box on the X-ray position.

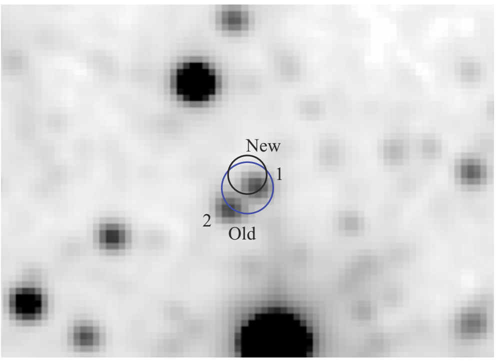

Figure 1. 2MASS K_S 1.3 × 0.9 arcsec^2 image of the field around IGR J16320−4751. The two circles respectively represent the *XMM–Newton* position given in Rodriguez et al. (2003, large circle), and the refined position discussed in the text. Infrared sources 1 and 2 are the candidate counterparts.

We compared the X-ray source positions for high significance sources (likelihood ⩾200) with infrared sources from the Two Micron All Sky Survey (2MASS) catalogue. We found a match within 0.4 arcsec between the *XMM–Newton* source at $\mathrm{RA}_{\mathrm{J2000}} = 16^{\mathrm{h}}32^{\mathrm{m}}12\overset{\mathrm{s}}{.}306$, $\mathrm{Dec.}_{\mathrm{J2000}} = -47^{\circ}44'59\overset{''}{.}32$ and a bright 2MASS source with a K magnitude of 9.3 located at $\mathrm{RA}_{\mathrm{J2000}} = 16^{\mathrm{h}}32^{\mathrm{m}}12\overset{\mathrm{s}}{.}339$ and $\mathrm{Dec.}_{\mathrm{J2000}} = -47^{\circ}44'59\overset{''}{.}45$. We found a second close match between the *XMM–Newton* source at $\mathrm{RA}_{\mathrm{J2000}} = 16^{\mathrm{h}}31^{\mathrm{m}}35\overset{\mathrm{s}}{.}642$, $\mathrm{Dec.}_{\mathrm{J200}} = -47^{\circ}51'27\overset{''}{.}42$ and a bright 2MASS source with a K magnitude of 9.3 located at $\mathrm{RA}_{\mathrm{J2000}} = 16^{\mathrm{h}}31^{\mathrm{m}}35\overset{\mathrm{s}}{.}634$, $\mathrm{Dec.}_{\mathrm{J2000}} = -47^{\circ}51'27\overset{''}{.}89$. Allowing a 1-arcsec error circle for the *XMM–Newton* source, and taking into account the surface density of *XMM–Newton* sources and 2MASS sources at appropriate magnitude limits, we find that the chance probability of occurrence of these X-ray/IR source coincidences is 0.3 per cent. This increases our confidence that the astrometry of the X-ray is correct and that we have identified the correct infrared (IR) counterpart to IGR J16320−4751.

3.2 Timing analysis

The light curves of IGR J16320−4751 obtained in different energy ranges with the different instruments are presented in Fig. 2. As already reported, IGR J16320−4751 is a variable source on various time-scales, from seconds–minutes (Rodriguez et al. 2003; Fig. 2) to days–months (e.g. Foschini et al. 2004). During our observations, the source shows a prominent flare around MJD 53236.6, visible in both light curves (Fig. 2). A second similar flare is visible in the ISGRI 20–60 keV light curve around MJD 53237.3. Unfortunately, our *XMM–Newton* observation does not cover this period.

We used the EPIC cameras to study the pulsations of IGR J16320−4751 already reported in Lutovinov et al. (2005). We performed a period search on the MOS and PN light curves using the XRONOS tool EFSEARCH. Because the source is highly absorbed (Rodriguez et al. 2003), and in order to improve the detection of the pulsation we restricted our period search to the 2–12 keV range for all EPIC cameras. The Lomb–Scargle of the PN 2–12 keV light curve is reported in Fig. 3.

A very prominent peak is visible with both PN and MOS detectors. Fitting the peak with Gaussian profiles led to best values of 1303.8 ± 0.9 s ($7.669 \pm 0.005 \times 10^{-4}$ Hz) and 1302.0 ± 1.1 s (7.680 ±

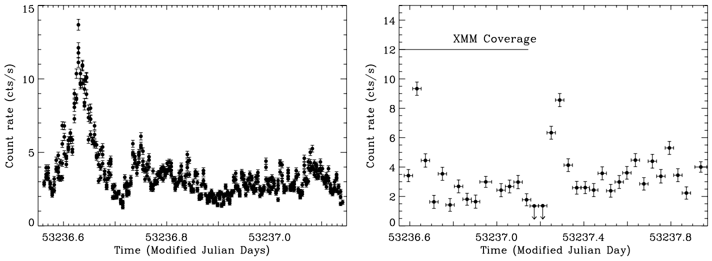

Figure 2. Left-hand side: the 2–12 keV *XMM–Newton*/PN light curve of IGR J16320−4751. Right-hand side: the 20–60 keV *INTEGRAL*/ISGRI light curve of IGR J16320−4751. Note that the two data sets have different lengths, and the light curves have different time resolutions. The time bin of the *XMM–Newton* light curve is 100 s, while that of *INTEGRAL*/ISGRI is about 3200 s (length of a SCW). Upper limits are given at the 3σ level.

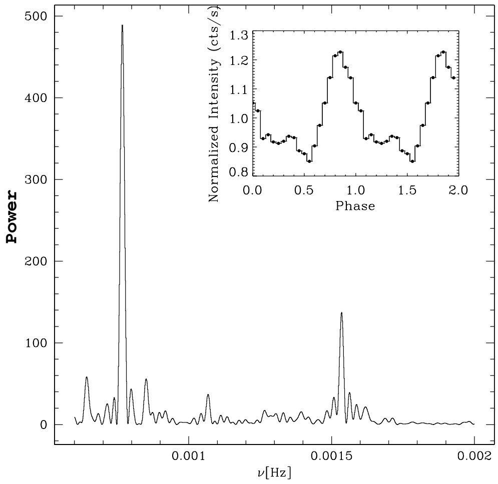

Figure 3. Lomb–Scargle periodogram of the 2–12 keV PN light curve. The insert shows the pulse profile of the 2–12 keV light curve obtained by folding the PN light curve at a period of 1303 s.

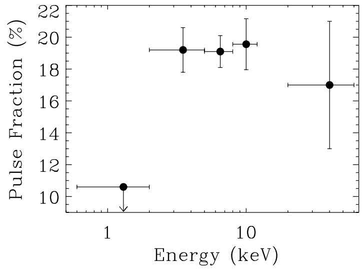

Figure 4. Energy dependence of the pulse fraction, obtained after folding the *XMM–Newton* and *INTEGRAL* light curves. The upper limit at low energy is given at the 3σ level.

0.006 × 10^{-4} Hz) for MOS and PN, respectively. The errors are calculated from the periodograms using the method developed by Horne & Baliunas (1986). These values are in complete agreement with the best value reported by Lutovinov et al. (2005), therefore confirming the identification of the pulsation at ~1300 s. A fainter peak is found at a period half that of the main feature (Fig. 3) that identifies it as a first harmonic of the pulse period. We then folded the PN light curve with a period of 1303 s (the mean of the PN and MOS values). The folded light curve is shown in Fig. 3 (insert). The pulse fraction (defined as $P = \frac{I_{\max}-I_{\min}}{I_{\max}+I_{\min}}$, where $I_{\max}$ and $I_{\min}$ respectively represent the intensities at the maximum and the minimum of the pulse profile) is 18.11 ± 0.7 per cent between 2 and 12 keV for the main pulse. The pulsation is also visible in the ISGRI 20–60 keV light curve. Folding the light curve at a period of 1303 s leads to a pulse fraction between 20 and 60 keV of 17 ± 4 per cent. We produced light curves in several energy ranges and folded them with a period of 1303 s in order to study the energetic dependence of the pulse fraction. As can be seen in Fig. 4 apart from the possible non-detection of pulsations below 2 keV, the pulse amplitude is compatible with being flat from 2 to 60 keV. The reported upper limit below 2 keV is 10.5 per cent.

3.3 Spectral analysis

In order to avoid mixing different spectral properties together, we separated the observation in two different time regions, the first corresponding to the first flare (where we isolated ~3.6 ks), and the second corresponding to the end of the simultaneous coverage by *XMM–Newton* and *INTEGRAL*, i.e. the last ~30 ks of the *XMM–Newton* observation. The spectra were fitted between 0.6 and 12 keV (*XMM–Newton*), and 20 and 80 keV (*INTEGRAL*). No relative normalization constant was included in any of the fits.

3.3.1 Spectral analysis of the non-flaring period

Several models were tested in the course of the analysis starting first with phenomenological models. A single absorbed power law leads to a poor reduced χ^2 (in the remaining of the paper χ^2_ν stands for reduced χ^2). In fact, a large deviation is seen at high energy, indicative of a high energy cut-off. Replacing the single (absorbed) power law by a power law with a high energy cut-off improves the fit, although the χ^2_ν is still poor, and high residuals are found around 6.4 keV. We obtain a relatively acceptable fit with a model consisting of an absorbed power law with a high energy cut-off, and a Gaussian emission line at ~6.4 keV. The χ^2_ν is 1.48 for 441 degrees of freedom (d.o.f.). This value and some remaining significant residuals indicate that an improvement is achievable. This is particularly true below

Table 2. Best-fitting parameters obtained from the fit to the 0.6–12 and 20–80 keV *XMM–Newton* and *INTEGRAL* flare and non-flare spectra with the simple phenomenological model consisting of an absorbed power law with a high energy cut-off, a Gaussian and an iron edge. Errors and limits are given at the 90 per cent confidence level.

Spectra	$N_{\rm H}$ ($\times 10^{22}$ cm^{-2})	Cut-off energy (keV)	e-folding (keV)	Γ	Line (centroid) (keV)	Line width (keV)	Line eq. width (eV)	Edge (keV)	Max τ
Non-flare	$15.5^{+0.1}_{-0.6}$	7.1 ± 0.4	$13.4^{+0.7}_{-0.9}$	$0.24^{+0.02}_{-0.12}$	$6.409^{+0.027}_{-0.005}$	<0.03	100^{+20}_{-14}	7.21 ± 0.04	0.14 ± 0.04
Flare	11.5 ± 0.5	$11.4^{+0.9}_{-0.5}$	10.1 ± 0.7	$0.28^{+0.07}_{-0.03}$	6.419 ± 0.014	$0.046^{+0.025}_{-0.029}$	116^{+39}_{-37}	$7.3^{+0.3}_{-0.1}$	$0.15^{+0.02}_{-0.05}$

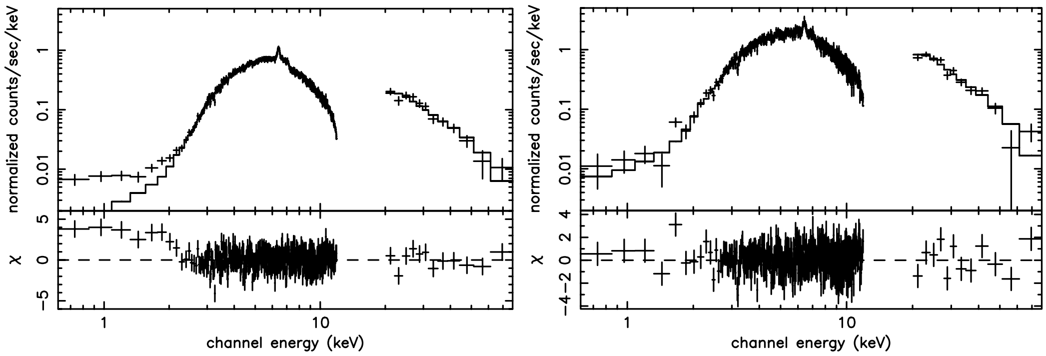

Figure 5. *XMM–Newton*/PN and *INTEGRAL*/ISGRI count spectra. Left-hand side: non-flare spectra. Right-hand side: Flare spectra. In both the cases, the continuous line represents the best-fitting model (EDGE*WABS*HIGHECUT*(POWERLAW+GAUSS), see the text for the details of the fitting). Note that the same vertical scale is used for both the cases.

2 keV, where a significant excess is detected, and around 7 keV. To account for the latter, we included an iron edge in the model. The fit is significantly improved with $\chi^2_\nu = 1.20$ (for 439 d.o.f.). The best-fitting parameters are reported in Table 2 (all errors on the spectral parameters are given at the 90 per cent confidence level). The 2–10 keV unabsorbed flux is 9.22×10^{-11} erg cm^{-2} s^{-1}, and the 20–100 keV flux is 2.33×10^{-10} erg cm^{-2} s^{-1}.

The large excess still visible below 2 keV (Fig. 5) seems to be reminiscent of several of the so-called highly absorbed sources detected by *INTEGRAL* (e.g. IGR J17252−3616; Zurita et al. 2005, IGR J16393−4643, Bodaghee et al. 2005), and has been seen in other X-ray Binaries containing pulsars (e.g. Hickox, Narayan & Kallman 2004). In order to try to understand its origin, we fitted the spectra with different types of absorption. The first one ($N_{\rm H_{ext}}$) corresponds to the absorption on the line of sight by the Galaxy and was modelled with the PHABS model in XSPEC, while the second ($N_{\rm H}$) is modelled by photoelectric absorption with variable abundance cross-sections. All the abundances were frozen to the solar values except that of iron given the presence of an emission line and an absorption edge in the simple model presented earlier. The soft excess is modelled by a blackbody emission. The spectral model is PHABS*(BBODY+VPHABS*HIGHECUT*(POWERLAW+GAUSS)) in the XSPEC terminology. The value of the interstellar absorption ($N_{\rm H_{ext}}$) was fixed to the value obtained from Dickey & Lockman (1990) in the direction of the source, i.e. $N_{\rm H_{ext}} = 2.1 \times 10^{22}$ cm^{-2} while the abundances of elements are set to solar values. The fit is good with $\chi^2_\nu = 1.13$ (438 d.o.f.). The intrinsic absorption is $11.8^{+0.5}_{-0.4} \times 10^{22}$ cm^{-2}, the blackbody temperature is $0.07^{+0.04}_{-0.01}$ keV and the iron abundance is $Z_{\rm Fe} = 1.50^{+0.25}_{-0.15}\ Z_\odot$. The other parameters are compatible with those returned from the previous fit. The (extrapolated) 0.01–10 keV unabsorbed flux of the blackbody (soft excess) is 3.7×10^{-10} erg cm^{-2} s^{-1}, while the 0.01–100 keV unabsorbed flux of the power-law component is $\sim 4.7 \times 10^{-10}$ erg cm^{-2} s^{-1}.

Since a cut-off power law is usually interpreted as a signature for thermal Comptonization, we replaced the phenomenological model by a more physical model of Comptonization (COMPTT, Titarchuk 1994). The choice of this model is also dictated by the fact that it gave a good representation of the *XMM–Newton* spectrum of a previous observation Rodriguez et al. (2003), although the lack of high energy data had prevented us from obtaining a good constraint on the temperature of the electrons. A simple absorbed COMPTT model (plus a Gaussian) represents the data rather well ($\chi^2_\nu = 1.54$ for 442 d.o.f.), although the soft excess and an iron edge are here again clearly visible. We therefore fitted the data with a model consisting of an (externally) absorbed blackbody plus intrinsically absorbed Comptonization (all abundances are set to solar values except the iron density of the local (vphabs) absorption that was left as a free parameter) and a Gaussian line (PHABS(BBODY+VPHABS(COMPTT+GAUSS)) in XSPEC). Similar to the previous case, $N_{\rm H_{ext}}$ is frozen to the Galactic value along the line of sight. We obtain a good representation of the spectrum with $\chi^2_\nu = 1.15$ for 438 d.o.f. The best-fitting parameters are reported in Table 3, while the '$\nu - F_\nu$' spectrum is presented in Fig. 6. The blackbody (unabsorbed) bolometric flux is 2.2×10^{-10} erg cm^{-2} s^{-1}, while the 0.01–100 keV unabsorbed (i.e. external plus intrinsic absorption corrected) COMPTT flux is 4.4×10^{-10} erg cm^{-2} s^{-1}.

We also tried an alternative model involving partial covering by an ionized absorber (PCFABS in XSPEC). When leaving the disc temperature free to vary, non-realistic values are obtained for its normalization. We then froze $kT_{\rm bb}$ to the best value obtained with

Table 3. Best-fitting parameters obtained from the fit to the 0.6–12 and 20–80 keV *XMM–Newton* and *INTEGRAL* flare and non-flare spectra with the physical models involving thermal Comptonization. $N_{\rm H}$ is the absorption intrinsic to the source, $kT_{\rm bb}$ represents the temperature of the soft excess, kT_{inj} represents the temperature of the injected photon for Comptonization and $kT_{\rm e}$ is the temperature of the Comptonizing cloud. Errors represent the 90 per cent confidence level.

Spectra	$N_{\rm H}$ ($\times 10^{22}$ cm^{-2})	$Z_{\rm Fe}$ $Z_\odot$	$kT_{\rm bb}$ (keV)	kT_{inj} (keV)	$kT_{\rm e}$ (keV)	τ_ρ	Line (centroid) (keV)	Line width (keV)	Line e.q. width (eV)
Non-Flare	$8.9^{+0.2}_{-0.7}$	$1.83^{+0.30}_{-0.26}$	$0.075^{+0.024}_{-0.018}$	$1.98^{+0.15}_{-0.10}$	$8.0^{+1.0}_{-0.7}$	$4.9^{+0.5}_{-0.4}$	6.411 ± 0.006	<0.03	100^{+24}_{-20}
Flare	$7.6^{+1.2}_{-1.4}$	$2.2^{+0.9}_{-0.6}$	0.075 *frozen*	$1.30^{+0.31}_{-0.24}$	$6.5^{+0.4}_{-0.3}$	$9.8^{+1.2}_{-1.4}$	$6.419^{+0.014}_{-0.015}$	0.04 ± 0.02	112^{+42}_{-44}

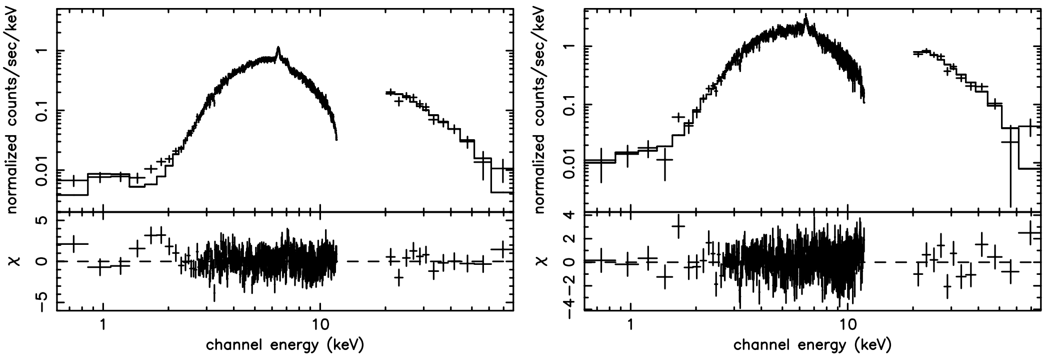

Figure 6. *XMM–Newton*/PN and *INTEGRAL*/ISGRI unfolded spectra. Left-hand side: non-flare spectra. Right-hand side: flare spectra. In both the cases, the continuous line represents the best-fitting model (PHABS*(BBODY+VPHABS*(COMPTT+GAUSS)), see the text for the details of the fitting). Individual components are also represented. Note that the same vertical scale is used for both the cases.

Table 4. Best-fitting parameters from the thermal Comptonization model, modified by a partial-covering absorber applied to the 0.6–12 and 20–80 keV *XMM–Newton* and *INTEGRAL* flare and non-flare spectra. Errors and limits denote the 90 per cent confidence level. In both the cases, the blackbody temperature of the soft excess is frozen to 0.075 keV.

Spectra	$N_{\rm H}$ ($\times 10^{22}$ cm^{-2})	kT_{inj} (keV)	$kT_{\rm e}$ (keV)	τ_ρ	Covering fraction per cent
Non-flare	12.2 ± 0.6	$1.5^{+0.05}_{-0.11}$	$7.0^{+0.5}_{-0.4}$	6.4 ± 0.7	$98.4^{+0.3}_{-0.7}$
Flare	$9.2^{+1.1}_{-1.3}$	1.0 ± 0.2	6.6 ± 0.2	$9.9^{+0.5}_{-0.7}$	$98.0^{+1.8}_{-0.5}$

the other models, i.e. 0.075 keV. The fit is good with $\chi^2_\nu = 1.17$ for 444 d.o.f. The spectral parameters are compatible with those obtained with the previous model except that the intrinsic absorption is slightly higher here (Table 4). Note that the fit indicates that the central source is almost completely covered by the absorber.

3.3.2 The initial flare

We started to fit the spectra with the best (first) phenomenological model obtained in the previous case, namely an absorbed power law with a high energy cut-off, a Gaussian line and an iron edge. The χ^2_ν is 1.06 for 439 d.o.f. The best-fitting parameters are reported in Table 2, while the spectra are shown in Fig. 5 with those of the non-flare period. The 2–10 keV unabsorbed flux is 2.39×10^{-10} erg cm^{-2} s^{-1}, and the 20–100 keV flux is 4.20×10^{-10} erg cm^{-2} s^{-1}. It is interesting to note that no soft excess is obvious here, while the value of $N_{\rm H}$ has significantly decreased. It is possible that the soft excess is still present, although at a level compatible with the emission from the source (Fig. 5). This could then affect the results of the fits, in particular the value of the absorption. In order to compare with the non-flare period, we fitted the data with the same types of models. We first started with the PHABS*(BBODY+VPHABS*HIGHECUT*(POWERLAW+GAUSS)) model, fixing $N_{\rm H_{ext}}$ to the Galactic value along the line of sight. Given the presence of an iron edge in the simple previous fit, we also left the iron abundance free to vary. As one could expect, the parameters of the blackbody are poorly constrained, and the values of the parameters are close to those found without the inclusion of the blackbody. In a second run, we fixed the blackbody temperature to the value found during the non-flare period (0.07 keV, with the phenomenological model). A good fit is achieved with $\chi^2_\nu = 1.06$ (439 d.o.f). The value of the intrinsic absorption is still lower than in the non-flare case with $N_{\rm H} = 7.8^{+0.9}_{-0.8} \times 10^{22}$ cm^{-2}. The cut-off energy is now $16.2^{+1.6}_{-1.7}$ keV, while the folding energy is $11.8^{+1.2}_{-1.1}$ keV. The iron abundance is quite higher (although compatible within the errors) than in the non-flare case with $Z_{\rm Fe} = 1.97^{+0.64}_{-0.52}$. The other parameters are compatible with those obtained with the simple model. We also allowed the temperature of the blackbody to vary while fixing

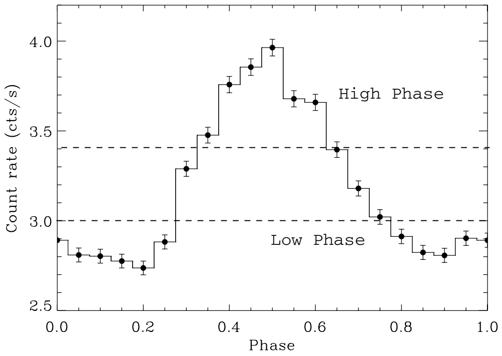

Figure 7. Phase diagram of the non-flare period. Only one cycle is represented. The horizontal lines represent the limit above (respectively below) which the high phase (resp. low phase) PN spectrum has been extracted.

the value of the intrinsic absorption to that found during the non-flare period (11.8 × 10^{22} cm^{-2}). In this case, however, non-credible parameters are obtained for the blackbody.

Replacing the phenomenological model by a COMPTT also leads to a good representation of the spectra with $\chi^2_\nu = 1.07$ for 438 d.o.f. In a first fit, the blackbody parameters are left free to vary. We obtain an upper limit on the temperature of 0.11 keV (90 per cent confidence), but the normalization is poorly constrained. We therefore froze the temperature to the best value obtained during the non-flare period (0.075 keV) and refitted the spectra. The χ^2_ν is 1.07 for 439 d.o.f. The best-fitting parameters are almost identical to those obtained when $kT_{\rm bb}$ is free to vary, and are reported in Table 3. Contrary to the phenomenological case, the $N_{\rm H}$ value obtained is marginally compatible with the value obtained from the fit to the non-flare period.

As in the non-flare case, we replaced the previous model by a model involving partial covering. Here again, to fit the soft excess well, a blackbody component is required. Since no constraints are obtained on the blackbody parameters if the blackbody temperature is left free to vary, we froze the latter to 0.075 keV. The fit is good with $\chi^2_\nu = 1.11$ for 442 d.o.f., and the best-fitting parameters are reported in Table 4.

3.4 Phase resolved spectroscopy

To study the dependence of the spectrum along the phase, we extracted PN spectra from the non-flare period in the low part of the phase diagram (hereafter low phase) and from the high part of the phase diagram (hereafter high phase) as illustrated in Fig. 7, i.e. the high phase corresponds to the time when the count rate is higher than 3.4 cts s^{-1}, while the low phase corresponds to the time when the count rate is lower than 3 cts s^{-1}. The origin of the phase is taken here as the start of the non-flare period, which we consider as the start of the good time intervals for the phase resolved spectroscopy. The shift of the phase diagram of Fig. 7 as compared to that of Fig. 3 is simply due to the fact that the origin of the phase in the former is equal to the beginning of the entire observation. Also in Fig. 7, the vertical axis is 'real' mean counts per second rather than normalized ones as it is the case in Fig. 3.

We focus on the 2–12 keV energy range, since the 0.6–2 keV does not show the presence of the pulsation with a rather constraining 3σ upper limit of 10.5 per cent. We fitted the spectra directly with the PHABS(VPHABS(COMPTT+GAUSS)) model. The Galactic absorption ($N_{\rm H_{ext}}$) was again fixed to 2.1 × 10^{22} cm^{-2}. Since we only consider the *XMM–Newton* spectra here, no constraint can be obtained for the temperature of the Comptonizing electrons. We therefore fixed $kT_{\rm e}$ to the value obtained during the fit to the entire non-flare spectra, i.e. 7.8 keV. In both the cases, the fits are good with $\chi^2_\nu = 1.18$ and $\chi^2_\nu = 1.01$ (422 d.o.f.) for the low and high phases, respectively. The best-fitting parameters are reported in Table 5.

It is obvious from Table 5 that the spectral parameters of both the high and the low phase are completely compatible. The only change is clearly related to a change of the source flux. Although the errors on the line equivalent width may indicate that this parameter does not evolve with the pulse, it is interesting to note the possible decrease of this parameter by ~30 per cent between the low and high phase. This may suggest that the iron is unpulsed.

4 DISCUSSION

We report here on the analysis of simultaneous *XMM–Newton* and *INTEGRAL* observations of the enigmatic source IGR J16320−4751. We focus on the time of strict simultaneous coverage by both satellites. We detect very significant X-ray pulsations at a period of around 1300 s confirming previous findings (Lutovinov et al. 2005). The pulsation is seen in the *INTEGRAL*/ISGRI light curve above 20 keV. Apart from the non-detection of the pulsation below 2 keV, no particular dependence of the pulse amplitude with the energy is seen. When studying the phase-dependent *XMM–Newton* spectra of the source (in the non-flare) period, we observe no particular spectral differences between the high-phase and low-phase spectra. In particular, the intrinsic absorption, temperature of seed photons for Comptonization and plasma optical depth remain relatively constant. This is compatible with a model of polar accretion by a pulsar. The modulation of the X-ray flux is due to the misalignment of the pulsar spin axis and the pulsar magnetic axis. When the pulsar magnetic axis points towards us, the X-ray flux we detect is enhanced. The pulse period would then be the spin period as already suggested by Lutovinov et al. (2005). The weak amplitude of the pulse (as compared to other absorbed source as e.g. IGR J16393−4643; Bodaghee et al. 2005)

Table 5. Best-fitting parameters obtained from the fit to the 2–12 keV high and low phase PN spectra, with the PHABS(VPHABS(COMPTT+GAUSS)) model. Errors are given at the 90 per cent level.

Spectra	$N_{\rm H}$ ($\times 10^{22}$ cm^{-2})	$Z_{\rm Fe}$ $Z_\odot$	kT_{inj} (keV)	τ_ρ (keV)	Fe centroid (keV)	E.q. width (eV)	2-10 unabs. Flux ($\times 10^{-10}$ erg cm^{-2} s^{-1})
Low phase	$9.2^{+0.4}_{-0.8}$	1.7 ± 0.3	$1.93^{+0.17}_{-0.11}$	$5.1^{+0.4}_{-0.6}$	6.411 ± 0.006	104^{+20}_{-17}	0.86
High phase	9.4 ± 1.4	$1.8^{+0.3}_{-0.5}$	1.9 ± 0.3	$4.8^{+1.0}_{-1.5}$	6.44 ± 0.02	72^{+38}_{-31}	1.04

may indicate that the spin axis and the magnetic axis are not highly misaligned, or simply that the angle of the pulsar equator with the line of sight is quite low. The constancy of the pulse amplitude above 20 keV indicates that the Comptonized component is also pulsed. This shows that Comptonization occurs very close to the site of production of the soft photons.

Using two independent *XMM–Newton* observations, we could refine the X-ray position to the source. This allowed us to further suggest that the infrared source labelled as no 1 in Rodriguez et al. (2003), and in Fig. 1 here, was the most likely counterpart to IGR J16320−4751. As discussed in Rodriguez et al. (2003), the magnitudes of this object could be indicative of some infrared excess possibly due to circumstellar matter, either a hot plasma or some dust.

We provide for the first time a spectral analysis of IGR J16320−4751 up to 80 keV, with significant detection by *INTEGRAL*/ISGRI. The hard X-ray spectrum of the source is indicative of a high energy cut-off, whose parameters cannot be constrained when focusing on the soft X-rays only (Rodriguez et al. 2003). The main emission mechanism in the source seems to be Compton up-scattering of soft X-ray photons by a hotter plasma. The spectral parameters we obtained either with phenomenological fits (Table 2) or more physical fits to the data are similar to those obtained for several HMXB (e.g. 4U 1700−37; Boroson et al. 2003). If we assume that the source is associated with the Norma arm located between 5 and 10 kpc from the Sun, with a tangent at 8 kpc, we can estimate its bolometric luminosity. During the non-flare period, the extrapolated bolometric flux of the source is 4.12×10^{-10} erg cm^{-2} s^{-1}. This leads to a luminosity of 3.15×10^{36} erg s^{-1} at 8 kpc, and 1.23×10^{36} (resp. 4.92×10^{36}) for a distance of 5 (resp. 10) kpc. We note that this estimate of the luminosity is compatible with the typical ionizing luminosity of accretion driven X-ray (1.2×10^{36} erg s^{-1}) pulsars suggested by Bildsten et al. (1997).

Our spectral analysis allowed us to reveal the presence of a soft excess that may be indicative of an additional medium. This soft excess is well fitted with a blackbody with temperature quite low and found around 0.07 keV. Such a soft excess seems to be commonly observed in X-ray binaries (Hickox et al. 2004), and some other highly absorbed *INTEGRAL* sources (Bodaghee et al. 2005; Walter et al. 2005; Zurita et al. 2005). This soft excess can have different origins from one system to another (Hickox et al. 2004). It could be, for example, the signature of thermal reprocessing of the harder X-rays produced by the accretion of material on to the pulsar either by the inner boundary of an optically thick accretion disc or by an optically thin diffuse cloud. Whatever is the exact origin of the medium responsible for the soft excess, the fact that the temperature of the soft excess is different than that of the seed photon for Comptonization rules out a model where this medium would be contained in the Comptonizing cloud. It seems difficult to consider that this medium could be the Comptonizing medium giving birth to the hard X-ray emission. Given that the Comptonized component shows the pulsation with an amplitude similar to that of the soft X-rays, it is very likely that Comptonization occurs in the close vicinity of the pulsar, the seed photons being then probably emitted by the hot surface of the compact object, and the up-scattered pulsed Comptonized component emitted by the channelled accretion flow.

Given the high quality of our data and the long exposure time, we detect for the first time a narrow iron line in IGR J16320−4751. This kind of feature is again reminiscent in many HMXB, and is also detected in most of the highly absorbed sources unveiled by *INTEGRAL*, the extreme case being IGR J16318−4848 (Matt & Guainazzi 2003; Walter et al. 2003, 2004; Kuulkers 2005). The presence of a narrow fluorescence line, as in e.g. Vela X-1, GX 301−2, 4U 1700−37, or even Cen X-3 (e.g. Boroson et al. 2003; Wojdowski et al. 2003), is usually interpreted as fluorescence of iron in a wind or circumstellar matter. This indicates that accretion occurs (at least partly) through a wind. This points towards a high mass companion in IGR J16320−4751 rather than a low mass one. The value of the centroid obtained during the fit to the non-flare spectra corresponds to Fe xiii (House 1969). We can estimate the distance R between the irradiating source and the inner radius of the fluorescent shell using $\xi = L/(\rho \times R^2)$, with L the luminosity of the source, ρ the density of the gas and ξ the ionization parameter. From fig. 5 of Kallman et al. (2004), we can estimate $\log(\xi) < 2$ therefore $\xi < 100$. Knowing that $\rho \times R = N_{\mathrm{H}}$, we obtain

$$R > \frac{L}{N_{\mathrm{H}} \times \xi} = 10^{11}\,\mathrm{cm} \sim 0.07\,\mathrm{au}$$

using the value of the luminosity found assuming a distance of 5 kpc, i.e. 1.23×10^{36} erg s^{-1}, and $R > 0.18$ au (resp. 0.28 au) for a distance of 8 (resp. 10) kpc. The inner edge of the fluorescent shell seems therefore quite far from the inner accretion flow which is again compatible with the presence of an additional medium responsible for the soft excess. It is interesting to note that when leaving the iron abundance free to vary, it tends to values greater than the solar abundance [using the values of the abundance of Anders & Grevesse (1989)]. This could be indicative of the iron origin and the cloud itself since both seem linked. Iron could have been produced by the evolution of the protopulsar in IGR J16320−4751.

Given the fact that in all the energy ranges the pulse fraction is roughly constant, it is very probable that the non-detection of the pulsation below 2 keV indicates that the X-ray flux below 2 keV, and consequently the soft excess, does not pulsate. As discussed in Hickox et al. (2004), this clearly rules out the accretion column as the origin of the soft excess. This property would suggest that the soft excess is either the emission by a collisionally energized cloud or simply the reprocessing of the hard X-rays by a diffuse cloud. In the latter case, it seems quite natural to think that the absorbing material is the cloud itself. Because of the energy conservation, $F_{\mathrm{bb}} \lesssim \Delta F_{\mathrm{comptt}}$ where F_{bb} is the unabsorbed bolometric flux of the blackbody and $\Delta F_{\mathrm{comptt}}$ the difference of the unabsorbed to the absorbed (∼bolometric) flux of the Comptonized component. In the non-flare case (when the blackbody components are well constrained), our fits lead to $\Delta F_{\mathrm{comptt}} \sim 0.4 \times 10^{10}$ erg cm^{-2} s^{-1}. The unabsorbed bolometric flux of the blackbody component is 2.2×10^{-10} erg cm^{-2} s^{-1}. Hence, the origin of the blackbody emission cannot be due to reprocessing of the hard X-rays. The soft excess would rather be the signature of a collisionally energized cloud.

We also studied the spectral properties of the source during a flare period and compared it to the non-flare period. Although a strict comparison is rendered delicate by the presence of the soft excess which is very poorly constrained during the flare, it seems that the change during the flare is accompanied by a slight decrease of the absorption column density, while the injected temperature of the photons for Comptonization and that of the Comptonizing electrons decreases significantly. Given the degeneracy of those two parameters, the contour plots of τ versus kT_{e} are reported in Fig. 8 for both periods. This plot shows that the evolution of the Comptonizing plasma optical depth and temperature is genuine. The ratio of the $y(\propto kT_{\mathrm{e}}\tau^2$, e.g. Titarchuk 1994) parameters between the flare and

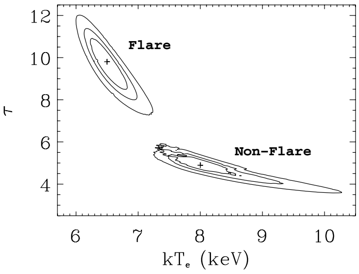

Figure 8. Error contour for the optical depth τ versus the electron temperature kT_e from the fit with the COMPTT model and the absorption with variable abundances. The crosses mark the location of the best values, while the contour are the 68, 90 and 99 per cent confidence region.

non-flare spectra is $y_{\mathrm{noflare}}/y_{\mathrm{flare}} = 0.30$, indicating a much more efficient Compton up-scattering in the case of the flare period. The short time-scale on which the flare occurs is more compatible with free-falling phenomena, rather than phenomena occurring in an accretion disc where times are of the order of the viscous time-scale. This argument again points to radial accretion in IGR J16320−4751, therefore further suggesting that the system is a HMXB.

We note that in order to test other possibilities and explain the soft excess, a model involving partial covering was tested in the course of the analysis. However, although it can lead to good results, it has to be noted that this model requires the addition of the blackbody to account for the soft excess. The result of the fits indicates that the covering of the central source of X-ray is quite high and close in both cases to its maximum value. The high values of the covering fraction would tend to confirm a picture in which the X-ray source is embedded in a dense material responsible for the soft X-ray. The fact that this covering fraction undergoes few variations between the flare and the non-flare periods seems to suggest that the flare is not caused by a huge geometrical change of this medium. This does not exclude that the flare is powered by inhomogeneities in the density of the stellar wind close to the neutron star. As the size of the region responsible for the absorption and fluorescence is of the order of the orbital radius, this is where such inhomogeneities in the wind are in fact expected. The evolution of the absorbing column density in the model involving partial covering would tend to be in agreement with a picture, where variations of the local wind density are responsible for both the variations of the column density and of the hard X-ray flux. Clearly, more observations on this and other highly absorbed sources will shed light on the origin of the soft excess in accreting X-ray pulsars.

ACKNOWLEDGMENTS

JR is specially grateful to J. Zurita for his great help with the timing analysis. JR acknowledges G. Bélanger, M. Cadolle-Bel, T. Courvoisier, A. Lutovinov, G. Palumbo and M. Revnivtsev for useful discussions on various aspects of the work and analysis presented here. The authors thank the anonymous referee for his/her very useful comments. This work is based on observations with *INTEGRAL*, an ESA mission with instruments and science data centre funded by ESA member states (especially the PI countries: Denmark, France, Germany, Italy, Switzerland, Spain), Czech Republic and Poland, and with the participation of Russia and the USA, and observations obtained with *XMM–Newton*, an ESA science mission with instruments and contributions directly funded by ESA member states and NASA.

REFERENCES

Aharonian et al. (the HESS collaboration), 2005, ApJ, in press (astro-ph/0510397)
Anders E., Grevesse N., 1989, GeCoA, 53, 197
Arnaud K. A., 1996, in Jacoby G. H., Barne J., eds, ASP Conf. Ser. Vol. 101, Astronomical Data Analysis Software an Systems V. Astron. Soc. Pac., San Francisco, p. 17
Bodaghee A., Walter R., Zurita, Heras J. A., Bird A. J., Courvoisier T. J.-L., Malizia A., Terrier R., Ubertini P., 2005, A&A, in press (astro-ph/0510112)
Bilsten L. et al., 1997, ApJS, 113, 367
Boroson B., Vrtilek S. D., Kallman T., Corcoran M., 2003, ApJ, 592, 516
Corbet R. et al., 2005, Atel, 649
Courvoisier T. J.-C. et al., 2003, A&A, 411, L53
Dickey J. M., Lockman F. J., 1990, ARA&A, 28, 215
Foschini L., Tomsick J. A., Rodriguez J., Walter R., Goldwurm A., Corbel S., Kaaret P., 2004 in Schönfelder V., Lichti G., Winkler C., eds, Proc. V *INTEGRAL* Workshop: The *INTEGRAL* Universe. ESA-SP552, p. 247
Goldwurm A. et al., 2003, A&A, 411, L223
Hickox R. C., Narayan R., Kallman T. R., 2004, ApJ, 614, 881
Horne J. H., Baliunas S. L., 1986, ApJ, 302, 757
House L. L., 1969, ApJS, 18, 21
in't Zand J. J. M., Ubertini P., Capitanio F., Del Santo M., 2003, IAUC, 8077
Kallman T. R., Palmeri P., Bautista M. A., Mendoza C., Krolik J. H., 2004, ApJS, 155, 675
Kuulkers E., 2005, in Antonelli L. A. et al., eds, Interacting Binaries: Accretion, Evolution and Outcomes. AIP, New York, in press (astro-ph/0504625)
Lebrun F. et al., 2003, A&A, 411, L141
Lebrun F. et al., 2004, Nat, 428, 293
Lutovinov A. A., Rodriguez J., Revnivtsev M., Shtykovskiy P., 2005, A&A, 433, L41.
Matt G., Guainazzi M., 2003, MNRAS, 343, L13.
Rodriguez J., Tomsick J. A., Foschini L., Walter R., Goldwurm A., Corbel S., Kaaret P., 2003, A&A, 407, L41
Rodriguez J., Cabanac C., Hannikainen D. C., Beckmann V., Shaw S. E., Schultz J., 2005, A&A, 432, 235
Strüder L. et al., 2001, A&A, 365, L18
Sugizaki M., Mitsuda K., Kaneda H., Matsuzaki K., Yamauchi S., Koyama K., 2001, ApJS, 134, 77
Tomsick J. A., Rodriguez J., Foschini L., Walter R., Goldwurm A., 2003, IAUC, 8096
Tomsick J. A., Corbel S., Goldwurm A., Kaaret P., 2005 ApJ, 630, 413
Titarchuk L., 1994, ApJ, 434, 570
Turner M. et al., 2001, A&A, 365, L27
Ubertini P. et al., 2003, A&A, 411, L131
Walter R. et al., 2003, A&A, 411, L427
Walter, R. et al., 2004, in Schönfelder V., Lichti G., Winkler C., eds, Proc. V *INTEGRAL* Workshop: The *INTEGRAL* Universe. ESA-SP552, p. 417
Walter R. et al., 2005, A&A, submitted
Winkler C. et al., 2003, A&A, 411, L1
Wojdowski P. S., Liedahl D. A., Sako M., Kahn S. M., Paerels F., 2003, ApJ, 582, 959
Zurita J., De Cesare G., Walter R., Bodaghee A., Belanger G., Courvoisier T. J.-L., Shaw S. E., Stephen J. B., 2005, A&A, in press (astro-ph/0511115)

This paper has been typeset from a TEX/LATEX file prepared by the author.

Part IV

Global Properties of IGR Sources

Chapter 9
Introduction

The 4 years of *INTEGRAL*-IBIS/ISGRI observations in the hard X to soft γ-ray band (20–100 keV) have led to the detection of $\sim$ 300 previously-known sources, and the discovery of $\sim$ 200 sources that were previously unknown at these energies. As we discussed in Part II, most of these sources were detected by creating long-exposure mosaic images of the Galactic Plane and Center (e.g. Bird et al. 2006).

In Part III, we used multi-wavelength observations to show that a few of these IGRs host X-ray pulsars. Their persistent emission, their long pulsation periods, and their large column densities suggest that these systems are likely to be SG HMXBs. These kinds of systems are still a minority compared to Be HMXBs, but *INTEGRAL* is expanding their ranks.

During the IAU Symposium in Dublin titled "Populations of High-Energy Sources in Galaxies," I became motivated to study the population of IGRs, particularly, the growing class of SG HMXBs. During the next year, I scanned the literature and catalogued a few of the relevant parameters of these sources, as well as the parameters of all sources detected by ISGRI. Given the sometimes rapid pace of discovery, it was important to stay informed of any new announcements, and to document every reference. To this end, two of the tools that we used were the ISDC General Reference Catalog (GRC: Ebisawa et al. 2003) (see Chapter 10) and the IGR Sources Page (see Chapter 11).

The study of the parameters of different classes of sources detected by ISGRI represents a natural progression from my initial tasks of finding new sources in mosaic images, the subsequent studies which revealed that some of the the new sources are absorbed X-ray pulsars, and the constant maintenance of the GRC which helps us to discriminate between new and known sources to begin with.

While it was being put together, the need for such a catalog became evident. There were numerous catalogs in the literature pertaining to *INTEGRAL* sources, but most were restricted to a specific class of source. For example, Beckmann et al. (2006a) focused on AGN, while Lutovinov et al. (2005a) treated HMXBs, and Barlow et al. (2006) catalogued CVs. Multi-class surveys such as Bird et al. (2007) only provided positions and fluxes without information about the column density, modulations, distances, etc.

The intention was to synthesize the most important paramaters of all sources detected by ISGRI. These parameters would then serve in the study of populations of high-energy sources by testing various correlations expected from theoretical predictions, and by investigating where the new and previously-known sources detected by ISGRI fit in the parameter space of high-energy objects.

An article discussing the main results of this research was published in A&A as Bodaghee et al. (2007). The key steps of the analysis are presented along with a copy of the article at the end of the chapter.

Chapter 10

The ISDC General Reference Catalog

One of the initial steps of *INTEGRAL* data analysis, either with IQLA or with OSA, involves building a list of sources that are in a given FOV. Knowing which sources are in the FOV is a prerequisite for the deconvolution of raw shadowgrams into clean images and mosaics. An up-to-date X/γ-ray source catalog is also needed to compare with these results from IQLA and OSA, in order to discover γ-ray sources and to monitor sources that are known to vary.

The ISDC General Reference Catalog (GRC) is the master list of all known high-energy sources of relevance to *INTEGRAL*. By definition, the GRC contains all objects that have been brighter than $\sim$ 1 mCrab in the spectral domain covered by *INTEGRAL*, namely between $\sim$ 1 keV and $\sim$ 10 MeV.

10.1 The Pre-launch Catalog

Prior to the launch of *INTEGRAL*, the information available for known high-energy sources had to be grouped together. Objects in the original pre-launch GRC (c.f. Master's Thesis of Gérald Bourban) were compiled from the following references:

- Macomb & Gehrels gamma-ray sources catalog
- Liu's LMXB and HMXB catalogs
- The 4th Uhuru catalog
- Van Paradji's X-ray Binaries catalog
- HEAO1 A4 catalog
- BATSE observations of Piccinotti's sample of AGN
- Tartarus reduced AGN data

Each source in the GRC has a name, a position, and a Spectral Energy Distribution (SED) model with parameters such as column density, photon index, and normalization. In most cases, a default SED model was assigned according to the source type. The normalization can be adjusted to reflect *INTEGRAL* observations. The format of the models and parameters follows the conventions of XSPEC (Arnaud 1996; `http://xspec.gsfc.nasa.gov`):

powerlaw : photon power law, typically due to synchrotron radiation

$$S(E) = A(\frac{E}{E_{\rm o}})^{\Gamma} \tag{10.1}$$

cutoff : power law with a high energy exponential cutoff

$$S(E) = A(\frac{E}{E_{\rm o}})^{\Gamma} \cdot e^{(\frac{-E}{E_{\rm cut}})} \tag{10.2}$$

bknpower : broken power law

$$S(E < E_{\rm break}) = A(\frac{E}{E_{\rm o}})^{\Gamma_1} \tag{10.3}$$

$$S(E \geq E_{\rm break}) = A \cdot E_{\rm break}^{(\Gamma_2-\Gamma_1)} \cdot (\frac{E}{E_{\rm o}})^{\Gamma_2} \tag{10.4}$$

wabs : photo-electric absorption using Wisconsin cross sections

$$m(E) = e^{-N_{\rm H}\cdot\sigma(E)} \tag{10.5}$$

highecut : high energy exponential cutoff

$$m(E < E_{\rm cut}) = 1 \tag{10.6}$$

$$m(E \geq E_{\rm cut}) = e^{(\frac{E_{\rm cut}-E}{E_{\rm fold}})} \tag{10.7}$$

E	energy [keV]
$E_{\rm o}$	reference energy [keV] (1 keV in XSPEC)
$E_{\rm cut}$	exponential cutoff energy [keV]
$E_{\rm fold}$	exponential folding energy [keV]
$E_{\rm break}$	break energy [keV]
Γ_1	photon index for $E < E_{\rm break}$
Γ_2	photon index for $E \geq E_{\rm break}$
$N_{\rm H}$	column density of hydrogen [10^{22} cm^{-2}]
$S(E)$	monochromatic flux at energy E [ph cm^{-2} s^{-1}]
$A = S(E_{\rm o})$	normalization ($\frac{F_{\rm obs}}{F_{\rm comp}}$) at 1 keV [ph cm^{-2} s^{-1} keV^{-1}]
$m(E)$	multiplicative flux coefficient of $S(E)$ at energy E
$\sigma(E)$	photo-electric cross section (excluding Thompson scattering)

These models are used to reproduce the expected source count rates for JEM-X (3–10 and 10–30 keV) and for ISGRI (20–40 and 40–80 keV) using the latest detector response matrices. Count rates are merely symbolic since it is unlikely that a default model can represent the broad range of possible SEDs of sources within a class. Nevertheless, source count rates in the GRC are precise enough for IQLA which focuses on highly significant variations in the source flux (a factor of 10 or more compared with quiescent emission).

Therefore, the pre-launch GRC gave the status of our knowledge of high-energy sources. In most cases, this understanding relied on the interpolation and the extrapolation of very few measurements.

10.2 A Revised Catalog & New Formats

The original set of codes for creating the GRC (written by G. Bourban and Dr. Ken Ebisawa) managed to patch together multiple catalog files with drastically different styles. This apparent flexibility was actually a drawback. Because the style files that created the initial GRC employed different naming conventions, some sources were repeated under different names, and others had names that were not recognized by SIMBAD or in an ADS query. This hampers efforts to find references for these sources. In addition, making changes to the GRC was a tedious procedure.

When responsibility for the GRC was transferred to me, the catalog was reviewed entirely so that the names, positions, and classifications of sources could be checked against references from SIMBAD. I was assisted during this review by Drs. Nami Mowlavi and K. Ebisawa, and by Professor Thierry J.-L. Courvoisier.

After the removal of duplicated and false sources, each of the remaining sources was assigned a more SIMBAD-friendly name corresponding to what we judged to be the most popular name in high-energy astrophysics. Aliases (from SIMBAD) are listed in the comments section. Moreover, each source was issued the most accurate position available, an error and a reference. This cleaned version of the GRC was published as Ebisawa et al. (2003) (see Section 10.3.1).

While IQLA and OSA rely on the FITS format of the GRC, formats in HTML and TeX are provided as extra diagnostic tools. For example, each source in the HTML file (Fig. 10.2) has a name that hyper-links directly to the relevant page in SIMBAD and a position that links to the reference in ADS. The TeX file is easily compiled to produce hard copies of the GRC. All versions and formats of the GRC can be retrieved online (http://isdc.unige.ch/Data/cat).

10.3 Outlook

New versions of the catalog need to be made regularly so that the latest source discoveries, new detections of known sources, or position updates can be included.

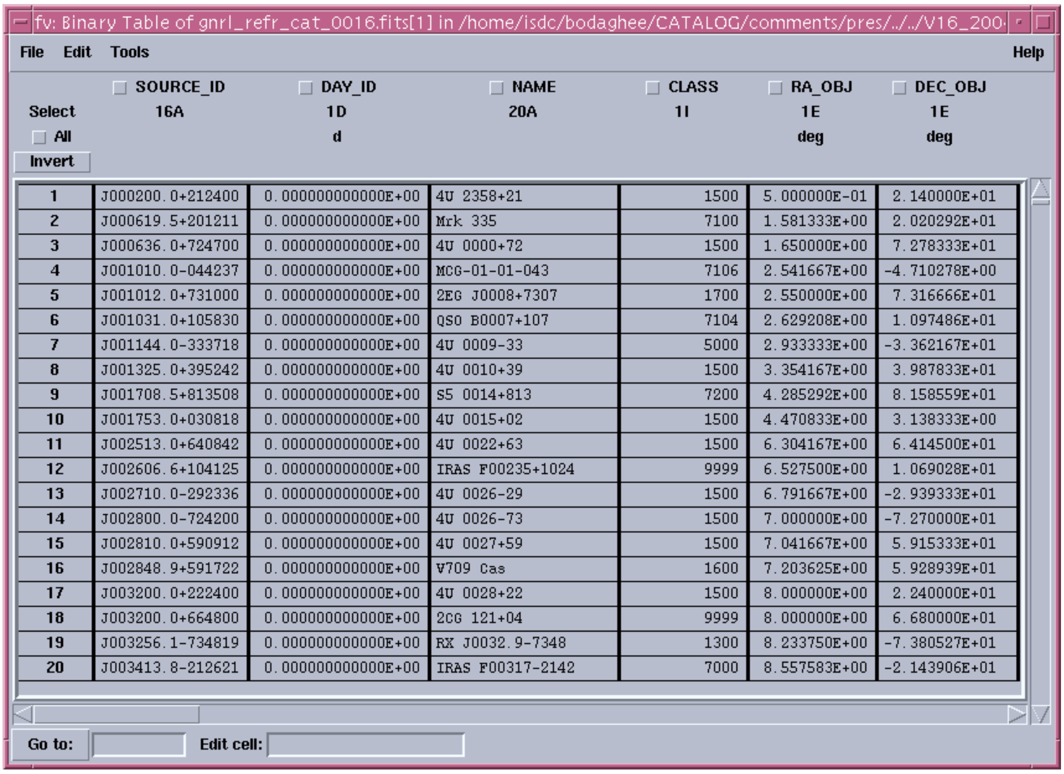

	☐ SOURCE_ID	☐ DAY_ID	☐ NAME	☐ CLASS	☐ RA_OBJ	☐ DEC_OBJ
	16A	1D	20A	1I	1E	1E
		d			deg	deg
1	J000200.0+212400	0.000000000000E+00	4U 2358+21	1500	5.000000E-01	2.140000E+01
2	J000619.5+201211	0.000000000000E+00	Mrk 335	7100	1.581333E+00	2.020292E+01
3	J000636.0+724700	0.000000000000E+00	4U 0000+72	1500	1.650000E+00	7.278333E+01
4	J001010.0-044237	0.000000000000E+00	MCG-01-01-043	7106	2.541667E+00	-4.710278E+00
5	J001012.0+731000	0.000000000000E+00	2EG J0008+7307	1700	2.550000E+00	7.316666E+01
6	J001031.0+105830	0.000000000000E+00	QSO B0007+107	7104	2.629208E+00	1.097486E+01
7	J001144.0-333718	0.000000000000E+00	4U 0009-33	5000	2.933333E+00	-3.362167E+01
8	J001325.0+395242	0.000000000000E+00	4U 0010+39	1500	3.354167E+00	3.987833E+01
9	J001708.5+813508	0.000000000000E+00	S5 0014+813	7200	4.285292E+00	8.158559E+01
10	J001753.0+030818	0.000000000000E+00	4U 0015+02	1500	4.470833E+00	3.138333E+00
11	J002513.0+640842	0.000000000000E+00	4U 0022+63	1500	6.304167E+00	6.414500E+01
12	J002606.6+104125	0.000000000000E+00	IRAS F00235+1024	9999	6.527500E+00	1.069028E+01
13	J002710.0-292336	0.000000000000E+00	4U 0026-29	1500	6.791667E+00	-2.939333E+01
14	J002800.0-724200	0.000000000000E+00	4U 0026-73	1500	7.000000E+00	-7.270000E+01
15	J002810.0+590912	0.000000000000E+00	4U 0027+59	1500	7.041667E+00	5.915333E+01
16	J002848.9+591722	0.000000000000E+00	V709 Cas	1600	7.203625E+00	5.928939E+01
17	J003200.0+222400	0.000000000000E+00	4U 0028+22	1500	8.000000E+00	2.240000E+01
18	J003200.0+664800	0.000000000000E+00	2CG 121+04	9999	8.000000E+00	6.680000E+01
19	J003256.1-734819	0.000000000000E+00	RX J0032.9-7348	1300	8.233750E+00	-7.380527E+01
20	J003413.8-212621	0.000000000000E+00	IRAS F00317-2142	7000	8.557583E+00	-2.143906E+01

Figure *10.1: The General Reference Catalog in the FITS format used by OSA.*

New software was written to streamline the procedure for generating the GRC (see Appendix). With this software, the *ASCA* catalogs (Sugizaki et al. 2001; Sakano et al. 2002), the IBIS surveys (Bird et al. 2004; Revnivtsev et al. 2004; Bird et al. 2006, 2007), and source detections from other references could be easily incorporated. During the last 3 years, any new information published about sources in the GRC had to be monitored, the scripts that create the GRC were altered to accomodate new functionalities, and the latest versions of the GRC were regularly delivered to the ISDC Archive. All modifications to the GRC are recorded in a log file. Each source is devoted a section documenting its discovery and/or detection, and the references for the various flags and parameters listed in the GRC.

Among the major changes to the GRC in the last few years has been the addition of instrument-specific flags that inform the user which sources have been detected by an *INTEGRAL* instrument. A flag is switched from 0 to 1 whenever a detection is announced in a peer-reviewed journal, a proceeding, on astro-ph, in an ATel or in an IAUC. Scientists working on public data from IQLA, and scientists from the *INTEGRAL* instrument teams (e.g. Drs. Peter Kretschmar and Jérôme Chenevez from JEM-X, or Dr. Volker Beckmann for SPI) can also notify me of the need to change a flag.

The need for detection flags grew from our attempts at cleaning mosaic images. We found that one of the best ways to quickly improve the quality of the output mosaic image was to use a catalog that included only those sources in our FOV that we expected to detect. Allowing the source extraction step of OSA to try to fit all sources in the FOV, regardless of whether they were detected, increased the level of the background as a whole, and it created local clusters of negative pixels wherever the source extraction program expected to find a catalogued source.

Unfortunately, the rigidity of (0;1) has become apparent now that so many of the sources flagged for ISGRI flag are in fact transient. They are rarely detectable and so they should not be considered unless one were studying these specific sources in a carefully selected data set. Yet since they are flagged, OSA processes them anyway leading to systematics in the images.

There have been times when I have been asked to switch off the flag of a source with a confirmed detection because it was located near another known source and so was interfering in the data analysis of the region. For the busy Galactic Center, it was decided that only sources from Bélanger et al. (2004) should be flagged. While the user is able to switch flags off in a personal copy of the GRC when the evidence from imaging favors it, my belief is that in turning flags off in the GRC we lose some information about the source. Even though the source was detected in the past by ISGRI, the GRC would show otherwise. In another case, two IGR sources (IGR J18159-3353 and IGR J20188+3647) that were recently announced by Sguera et al. (2006) and added to the GRC with an ISGRI flag of 1, were later contested independently in private communications from R. Walter and J. Chenevez.

There should be at least 4 values for the flag:

$0 \equiv$ not detected

$1 \equiv$ detected, persistent

$2 \equiv$ detected, transient

$3 \equiv$ detection in doubt

Persistent sources are those that are usually detected ($\gtrsim 4\sigma$) in a mosaic image of a single spacecraft revolution, with frequent and significant detections at the ScW level. Transient sources appear sporadically, i.e. in the mosaics of a few revolutions, if any, with rare detections at the ScW level. Transients can also include the exceptional case of a dim but persistent source located near a bright persistent source. Both IQLA and OSA would only consider a flag value of 1. The user can adjust the flags to suit the needs of their specific data set. Similar values for the detection flags were submitted as a software change request, but the proposal was rejected without an explanation.

With its 1,655 sources, Version 27 of the GRC is among the most complete high-energy catalogs available. Future maintenance of the GRC will still require being attentive to any publications or announcements. Further improvements can be

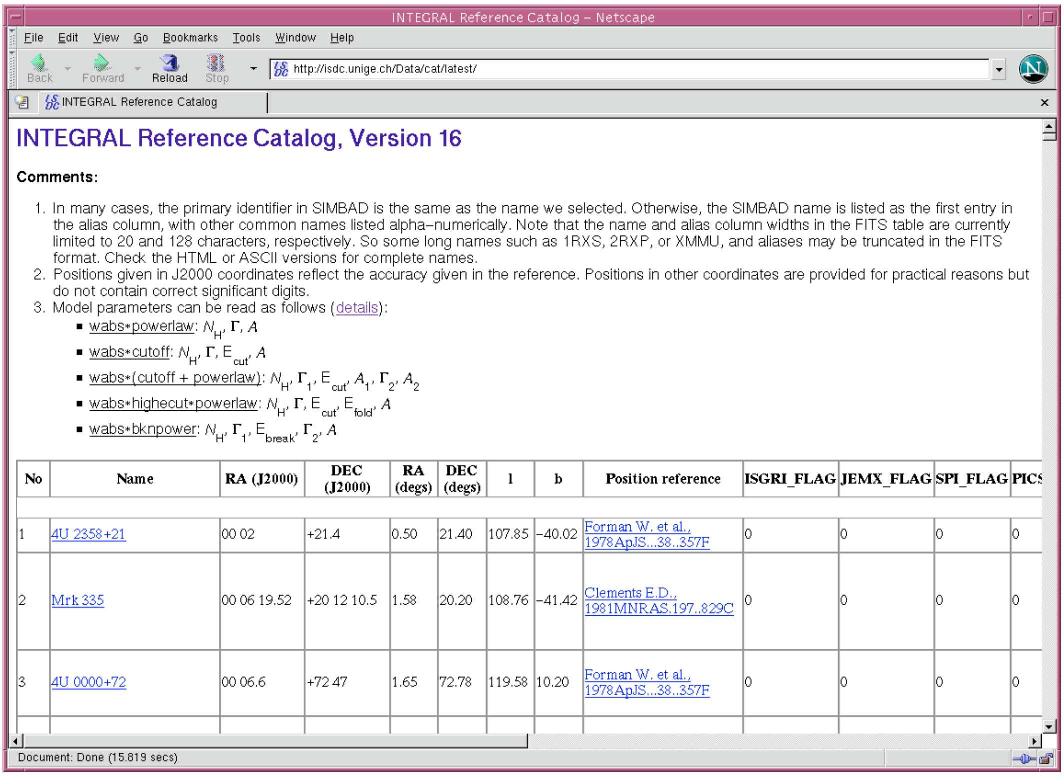

INTEGRAL Reference Catalog, Version 16

Comments:

1. In many cases, the primary identifier in SIMBAD is the same as the name we selected. Otherwise, the SIMBAD name is listed as the first entry in the alias column, with other common names listed alpha–numerically. Note that the name and alias column widths in the FITS table are currently limited to 20 and 128 characters, respectively. So some long names such as 1RXS, 2RXP, or XMMU, and aliases may be truncated in the FITS format. Check the HTML or ASCII versions for complete names.
2. Positions given in J2000 coordinates reflect the accuracy given in the reference. Positions in other coordinates are provided for practical reasons but do not contain correct significant digits.
3. Model parameters can be read as follows (details):
    - wabs∗powerlaw: N_H, Γ, A
    - wabs∗cutoff: N_H, Γ, E_{cut}, A
    - wabs∗(cutoff + powerlaw): N_H, Γ_1, E_{cut}, A_1, Γ_2, A_2
    - wabs∗highecut∗powerlaw: N_H, Γ, E_{cut}, E_{fold}, A
    - wabs∗bknpower: N_H, Γ_1, E_{break}, Γ_2, A

No	Name	RA (J2000)	DEC (J2000)	RA (degs)	DEC (degs)	l	b	Position reference	ISGRI_FLAG	JEMX_FLAG	SPI_FLAG	PICS
1	4U 2358+21	00 02	+21.4	0.50	21.40	107.85	−40.02	Forman W. et al., 1978ApJS...38..357F	0	0	0	0
2	Mrk 335	00 06 19.52	+20 12 10.5	1.58	20.20	108.76	−41.42	Clements E.D., 1981MNRAS.197..829C	0	0	0	0
3	4U 0000+72	00 06.6	+72 47	1.65	72.78	119.58	10.20	Forman W. et al., 1978ApJS...38..357F	0	0	0	0

Figure *10.2: The HTML version of the General Reference Catalog.*

made by replacing the expected count rates derived from the SEDs with the more realistic average count rates from *INTEGRAL* archive results. A first step in this direction was taken by making the 10 brightest sources in the GRC identical (in count rate and order) to the 10 brighest sources in Bird et al. (2006).

Another improvement that was proposed over 3 years ago and that remains unresolved is to increase the possible length of source names. Currently, the template of the FITS format limits the number of characters in the name column to 20, and truncates the rest. While this was fine for earlier missions, we are in an era in which *XMM-Newton* and *Chandra* are finding sources with such precision that the names (composed of the prefix XMMU or CXOU, a space, and the R.A. and Dec.) are longer than 20 characters. Sources from the *Rosat* X-ray survey (1RXS) also have more than 20 characters. The omission of the last characters of a name causes problems for hyper-links in the HTML version, and it hampers efforts to find references for the source. Also, since the GRC is expected to serve as a reference for other missions (e.g. *Swift* and *Suzaku*), altering the official source name would introduce confusion. More than a year ago, all OSA and IQLA programs that were prone to being affected by an increase in characters from 20 to e.g. 30 were identified. Regrettably, there has been no other progress since then.

10.3.1 Scientific Article on the GRC

A fully-revised GRC with pre-launch values was published as (Ebisawa et al. 2003) in the A&A special issue devoted to *INTEGRAL* science:

Ebisawa K., Bourban G., Bodaghee A., Mowlavi N. & Courvoisier T.J.-L.
High-energy sources before INTEGRAL: The INTEGRAL Reference Catalog
Astronomy & Astrophysics, Vol. 411, pp. L59–L62, 2003

A&A 411, L59–L62 (2003)
DOI: 10.1051/0004-6361:20031336

Astronomy & Astrophysics

High-energy sources before INTEGRAL

INTEGRAL reference catalog*

K. Ebisawa[1,2,]**, G. Bourban[3], A. Bodaghee[1,3], N. Mowlavi[1,3], and T. J.-L. Courvoisier[1,3]

[1] INTEGRAL Science Data Center, Chemin d'Écogia 16, 1290 Versoix, Switzerland
[2] code 662, NASA/GSFC, Greenbelt, 20771 Maryland, USA
[3] Observatory of Geneva, 51 chemin des Maillettes, 1290 Sauverny, Switzerland

Received 9 July 2003 / Accepted 1 September 2003

Abstract. We describe the INTEGRAL reference catalog which classifies previously known bright X-ray and gamma-ray sources before the launch of INTEGRAL. These sources are, or have been at least once, brighter than ~1 mCrab above 3 keV, and are expected to be detected by INTEGRAL. This catalog is being used in the INTEGRAL *Quick Look Analysis* to discover new sources or significantly variable sources. We compiled several published X-ray and gamma-ray catalogs, and surveyed recent publications for new sources. Consequently, there are 1122 sources in our INTEGRAL reference catalog. In addition to the source positions, we show an approximate spectral model and expected flux for each source, based on which we derive expected INTEGRAL counting rates. Assuming the default instrument performances and at least $\sim 10^5$ s exposure time for any part of the sky, we expect that INTEGRAL will detect at least ~700 sources below 10 keV and ~400 sources above 20 keV over the mission life.

Key words. INTEGRAL – X-ray sources – gamma-ray sources – catalog

1. Introduction

One of the main purposes of the INTEGRAL mission is to discover new X-ray/gamma-ray sources, and also to monitor significantly variable sources. When new or transient sources are detected, INTEGRAL is expected to give prompt announcements to the worldwide astronomical community. Near real-time monitoring of the INTEGRAL data, i.e., *Quick Look Analysis* (QLA), is carried out at the INTEGRAL Science Data Center (ISDC; Courvoisier et al. 2003a). To this end, we need a reliable X-ray/gamma-ray source catalog with which INTEGRAL QLA results can be compared.

Many X-ray/gamma-ray source catalogs have already been published. To make the *INTEGRAL Reference Catalog*, which we describe in the current paper, we searched the literature, took several high-energy catalogs, combined them and selected sources to suit our needs. Note that the INTEGRAL Reference Catalog is continuously updated for the QLA purpose by incorporating new sources discovered by INTEGRAL and other high-energy satellites. In this paper, we describe all the sources included in the INTEGRAL Reference Catalog at the end of June 2003, *except* those sources discovered by INTEGRAL.

All the sources in the INTEGRAL Reference Catalog are shown in Fig. 1 in Galactic coordinates. Size and color of the symbol indicate approximate fluxes and spectral hardness.

2. Method of selecting sources

The idea behind the INTEGRAL Reference Catalog is to put all sources which are *possibly* detected and identified by INTEGRAL. Corresponding to the expected sensitivity and energy range of INTEGRAL, we select sources that are, or have been at least once, brighter than ~1 mCrab in any energy band from 3 keV to 8000 MeV (energy range covered with JEMX, IBIS and SPI). Thus, for example, historic X-ray novae are included even if they are expected in quiescence when observed with INTEGRAL, since these sources *may* be detected when brightened. In addition, we include all the EGRET sources in Macomb & Gehrels (1999) even if they have never been detected in the INTEGRAL energy band.

We took all the sources in the following catalogs.

- High-mass X-ray binary catalog by Liu et al. (2000).
- Low-mass X-ray binary catalog by Liu et al. (2001).
- Gamma-ray sources catalog by Macomb & Gehrels (1999).
- The 4th Uhuru catalog by Forman et al. (1978).
- HEAO1 A4 catalog by Levine et al. (1984).
- BATSE observation of the Piccinotti's sample AGNs.

Send offprint requests to: K. Ebisawa,
e-mail: `ebisawa@obs.unige.ch`

[*] The Catalog is available in electronic form at the CDS via anonymous ftp to `cdsarc.u-strasbg.fr (130.79.128.5)` or via `http://cdsweb.u-strasbg.fr/cgi-bin/qcat?/A+A/411/L59`

[**] Universities Space Research Association.

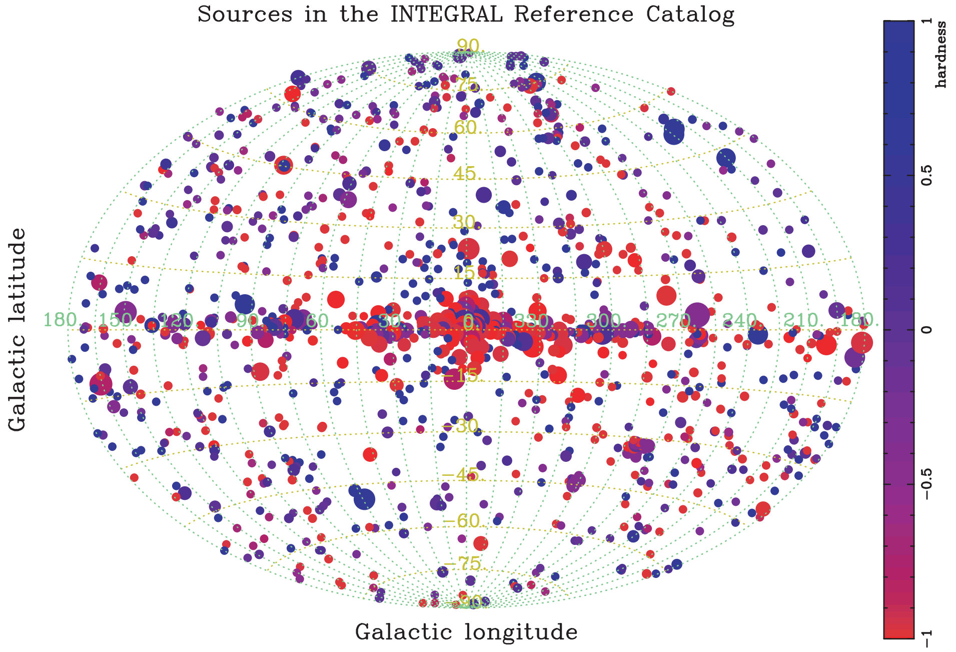

Fig. 1. All the sources included in the INTEGRAL reference catalog. Size and color of the symbols indicate approximate source brightness and spectral hardness, respectively. Symbol size is logarithmically proportional to the total JEMX + ISGRI counting rates. The hardenss is defined as $H - S/H + S$, where H is the total ISGRI counting rates (20–200 keV) and S is the soft-band (3–10 keV) JEMX counting rates.

- ASCA AGN data from the Tartarus database (`http:// tartarus.gsfc.nasa.gov`).
- IAUC circulars until June 30, 2003.

3. Information included in the catalog

The INTEGRAL Reference Catalog is published in electronic form and available at `http://cdsweb.u-strasbg.fr/cgi-bin/qcat?J/A+A/411/L59`. It is an ASCII file written in the LaTeX tabular form, so that readers can run LaTeX and easily print. Since column entries are formatted with fixed-width columns, the file is legible even in the original ASCII format.

The catalog is also available in the html version and FITS version from the ISDC web-site (`http://isdc.unige.ch`). The FITS version of the catalog is used in the actual QLA operation and INTEGRAL data analysis. In the html version, the source name and the position reference is hyper-linked to its corresponding page in SIMBAD and ADS, respectively.

The following is an explanation of each column in the catalog:

- *Catalog source number*
- *Source name*:
  Often there are two or more names commonly used for the same source. We take the name which we consider most popular in high-energy astrophysics and is also used as a SIMBAD source identifier. Thus, users can directly put the source name into the SIMBAD query box.
- *Right Ascension and Declination in J2000 coordinates*:
  These are given in "hh mm ss.s" and "deg arcmin arcsec" format, respectively. In most cases, positions are taken from SIMBAD. From time to time, however, we found and adopted a more recent position determination than SIMBAD. Accuracy depends on individual sources, which is reflected in the representation of the source positions. For example, an Uhuru source 4U 1130−14 has the source position (11 33, −14.9), namely, no accuracy of arcseconds in Uhuru.
- *Galactic coordinates*
- *Reference for the position determination*:
  This is for readers who need to know the position accuracy and/or position determination method. Often SIMBAD gives the source position reference as well as the position itself, in which case we take both. Otherwise, we searched for proper references by ourselves.
- *Spectral Model and Model Parameters*:
  We put a "typical" spectral model and model parameters, including the model normalization. We follow the XSPEC (Arnaud 1996; `http://xspec.gsfc.nasa.gov`) format for definition of the models and model parameters. See Sect. 4 for details.
- *Energy fluxes*:
  Energy fluxes are in ergs s^{-1} cm^{-2} and are calculated from the assumed spectral models for several energy bands. We take typical JEMX soft and hard energy bands

Table 1. Default spectral models adopted for different categories of sources. See XSPEC manual (Arnaud 1996; `http://xspec.gsfc.nasa.gov`) for precise descriptions of the spectral models.

Source category	model	N_H (10^{22} cm^{-2})	Γ1	Γ2	E_{cut} [keV]	E_{fold} or E_{break}† [keV]
X-ray binaries						
LMXB	wabs*cutoff	1.0	1.7	–	5	–
LMXB with hard-tail	wabs*(cutoff+powerlaw)	1.0	1.7	2.5	10	–
HMXB	wabs*highecut*powerlaw	1.0	1.0	–	10	15
AGN						
Seyfert 1	wabs*cutoff	1.0	1.7	–	100	–
Seyfert 2I	wabs*cutoff	10.0	1.7	–	100	–
Blazar	wabs*cutoff	1.0	1.7	–	100	–
Quasar	wabs*cutoff	1.0	1.7	–	100	–
Clusters of Galaxies	wabs*cutoff	1.0	1.7	–	10	–
Unidentified						
X-ray sources	wabs*cutoff	1.0	1.7	–	10	–
COMPTEL sources	wabs*bknpower	100	−1.5	2.1	–	1000
EGRET sources	wabs*bknpower	100	−1.5	2.1	–	10 000

†E_{fold} for highecut model and E_{break} for bknpower model.

(3–10 keV and 10–30 keV), and ISGRI soft and hard bands (20–60 keV and 60–200 keV).

- *JEMX, ISGRI counting rates*:
  Using the nominal detector responses, expected JEMX and ISGRI counting rates are calculated for the soft and hard energy bands indicated above. In the actual QLA operation, JEMX and ISGRI source counting rates are measured in these energy bands to compare with the catalog. The following calibration files, most recent ones in July 2003 (but still based on pre-launch calibration), are used in this calculation: `jmx2_rmf_grp_0003.fits` for JEMX and `isgr_rmf_grp_0005.fits` and `isgr_arf_rsp_0002.fits` for ISGRI.
  After the launch of INTEGRAL, the pre-launch estimate of the JEMX effective area was revealed to be overestimated by a factor of ~2 (P. Kretschmar, private communication). Therefore, we divided the JEMX counting rates calculated using the aforementioned responses by a factor of two. This prescription has been confirmed to be valid from simultaneous INTEGRAL–XTE observations of 3C 273 (Courvoisier et al. 2003b) and Cyg X-1 (Pottschmidt et al. 2003).
  For ISGRI, actual observations of Crab pulsar ane other sources confirmed that the pre-launch estimate of the effective area was more or less correct (within ~20 % or so).
- *Name aliases*:
  Since there are many varieties of sources, we do not have a consistent rule to decide which aliases to choose. However, we try to put at least one alias directly related to high-energy satellites and/or catalogs. For example, "4U" for 4th Uhuru catalog (Forman et al. 1978), and "2EG" for second EGRET source catalog (Thompson et al. 1995).
- *Comment on the nature of the source*:
  Such as low-mass X-ray binaries, high-mass X-ray binaries, Seyfert-1 galaxy, etc.

4. Method to determine the spectral models and fluxes

Except for a small number of sources which are known to be invariable, it is hardly possible to put a single "typical" spectral model for each source to represent its energy spectrum from 3 keV to 8000 keV, In practice, however, we only require *rough* estimates of the source fluxes for the INTEGRAL QLA operation, in which we want to detect only the very significant flux variations of more than a factor ~10 with JEMX and ISGRI in 3 to 200 keV. This means that the requirement of the flux estimate in our catalog can be as loose as a factor ~10 in 3 to 200 keV, which we believe is more or less achieved.

The published catalogs we use provide source fluxes in a very inhomogeneous set of energy bands and units. In order to use this information in our catalog, it is essential to harmonize the available data in the published catalogs. For isolated pulsars (including the Crab pulsar) which are known to be invariable and well approximated with power-law spectra, we adopt the known power-law slopes and normalizations. For other sources, we take a typical spectral model to describe the emission for a class of sources (Table 1), and adjusted only the normalization of the model for each source using the published data. We use the spectral models that are appropriate for the most probable state of any given source (for example, "low" state for Cyg X-1). For X-ray novae, on the other hand, we use the published fluxes obtained when the source is bright. Often there are two or more flux measurements for a given source in the same state; in such a case we adopt the average normalization which best fits all the available measurements.

5. Discussion

In Fig. 2, we show $\log N - \log S$ curves of the sources in our catalog in 3–10 keV and 20–60 keV, as well as corresponding JEMX and ISGRI counting rates and sensitivities.

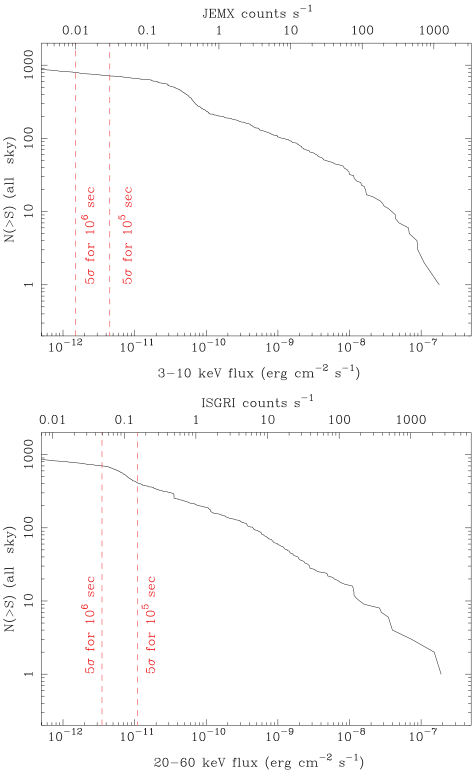

Fig. 2. The $\log N - \log S$ curves of the sources in our catalog and JEMX and ISGRI sensitivities in the energy bands which are most sensitive and used for Quick Look Analysis (3–10 keV for JEMX and 20–60 keV for ISGRI). JEMX and ISGRI counting rates for corresponding energy fluxes are also indicated.

The sensitivities are calculated based on the pre-launch estimates available in the IBIS and JEMX Observer's Manual, Issue 1.

Thanks to the large field of view and dithering strategy, INTEGRAL observations cover vast regions of the sky (IBIS bottom-to-bottom field of view is 29° × 29°). Thus the entire sky is expected to be covered during the INTEGRAL mission life, at least with $\sim 10^5$ s, which is a standard exposure time. For the Galactic plane region, at least 10^6 s of exposure is expected because of the Galactic center and plane survey core programs. In Fig. 2, we show 5 σ detection limits for 10^5 and 10^6 s exposures, respectively. Since our catalog is not complete, we see flattening of the $\log N - \log S$ curves at around the INTEGRAL detection limit, more conspicuously in JEMX. In any case, our catalog includes ~700 and ~400 sources, respectively, which are brighter than the JEMX and ISGRI sensitivities with 10^5 s exposure. We may expect to detect still more sources, which may be transient, or dim persistent sources because of the incompleteness of the catalog. Also, initial operation of ISGRI has already detected several heavily absorbed, transient Galactic sources (e.g, IGR J16318−4848 see Walter et al. 2003 and references therein), which may not have been noticed previously below ~10 keV, but may be discovered with INTEGRAL.

Note that our catalog was made by combining observations of many different instruments; not a single satellite has observed so many sources above 20 keV. One of the main purposes of INTEGRAL is to create a homogeneous and most complete high-energy source catalog above 20 keV.

Acknowledgements. We acknowledge all the INTEGRAL team members who gave comments to improve early versions of the INTEGRAL reference catalog. This research has made use of the SIMBAD database operated at CDS (Strasbourg, France), NASA's Astrophysics Data System Service, the High Energy Astrophysics Science Archive Research Center (HEASARC) provided by NASA's Goddard Space Flight Center, and the TARTARUS database supported by Jane Turner and Kirpal Nandra under NASA grants NAG5-7385 and NAG5-7067. We thank Dr. Peter Kretschmar for the information on the latest JEMX effective area calibration.

References

Arnaud, K. A. 1996, Astronomical Data Analysis Software and Systems V, ed. G. Jacoby, & J. Barnes, ASP Conf. Ser., 17, 101
Courvoisier, T. J.-L., Walter, R. Beckmann, V., et al. 2003a, A&A, 411, L53
Courvoisier, T. J.-L., Beckmann, V., Bourban, G., et al. 2003b, A&A, 411, L343
Forman, W., Jones, C., Cominsky, L., et al. 1978, ApJS, 182, 489
Macomb, D. J., & Gehrels, N. 1999, ApJS, 120, 335
Levine, A. M., Lang, F. L., Lewin, W. H. G., et al. ApJS, 54, 581
Liu, Q. Z., van Paradijs, J., & van den Heuvel, E. P. J. 2000, A&AS, 147, 25
Liu, Q. Z., van Paradijs, J., & van den Heuvel, E. P. J. 2001, A&A, 368, 1021
Malizia, A., Bassani, L., Zhang, S. N., et al. 1999, ApJ, 519, 637
Pottschmidt, K., Wilms, J., Chernyakova, M., et al. 2003, A&A, 411, L383
Thompson, D. J., Bertsch, D. L., Dingus, B. L., et al. 1995, ApJS, 101, 259
Walter, R., Rodriguez, J, Foschini, L., et al. 2003, A&A, 411, L427

Chapter 11

The IGR Sources Page

Many IGR source discoveries are followed by a flurry of publications as scientists race to observe and analyze the objects with other instruments. Along with the GRC described in the last chapter, the IGR Sources Page is another tool that I used to keep track of the most important information about high-energy sources. Developed initially by J. Rodriguez, the IGR Sources Page is a Web database that caters specifically to astronomers interested in IGRs:

`http://isdc.unige.ch/~rodrigue/html/igrsources.html`

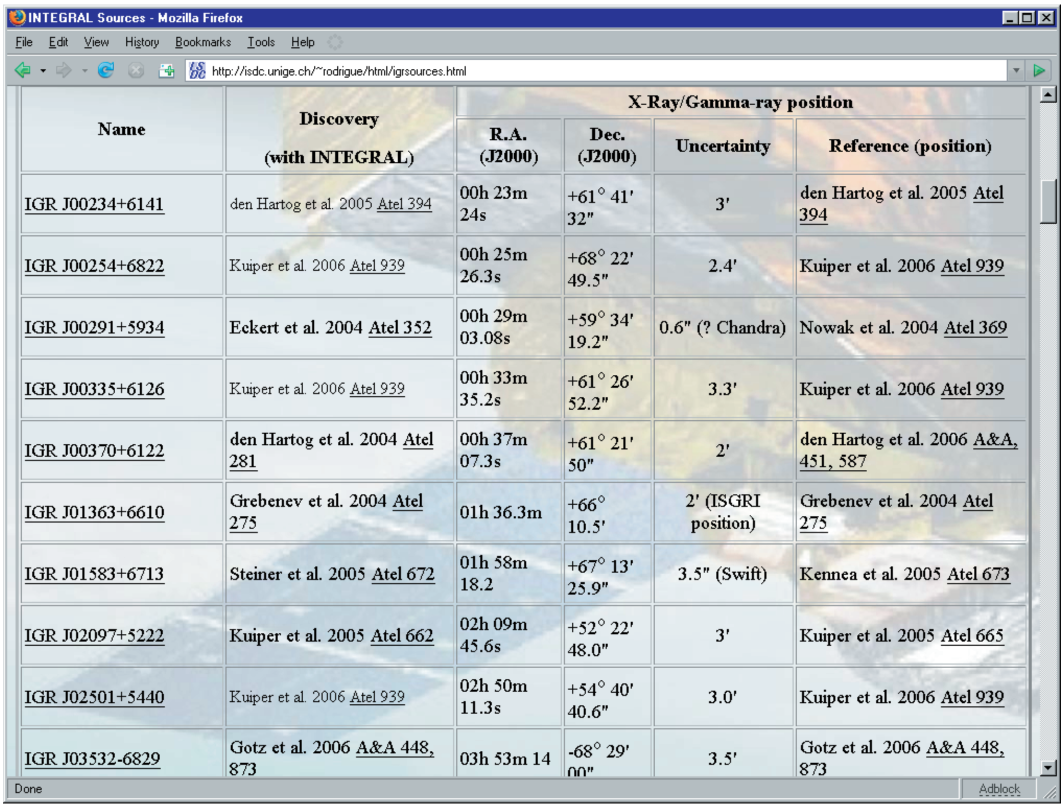

Name	Discovery (with INTEGRAL)	X-Ray/Gamma-ray position			
		R.A. (J2000)	Dec. (J2000)	Uncertainty	Reference (position)
IGR J00234+6141	den Hartog et al. 2005 Atel 394	00h 23m 24s	+61° 41' 32"	3'	den Hartog et al. 2005 Atel 394
IGR J00254+6822	Kuiper et al. 2006 Atel 939	00h 25m 26.3s	+68° 22' 49.5"	2.4'	Kuiper et al. 2006 Atel 939
IGR J00291+5934	Eckert et al. 2004 Atel 352	00h 29m 03.08s	+59° 34' 19.2"	0.6" (? Chandra)	Nowak et al. 2004 Atel 369
IGR J00335+6126	Kuiper et al. 2006 Atel 939	00h 33m 35.2s	+61° 26' 52.2"	3.3'	Kuiper et al. 2006 Atel 939
IGR J00370+6122	den Hartog et al. 2004 Atel 281	00h 37m 07.3s	+61° 21' 50"	2'	den Hartog et al. 2006 A&A, 451, 587
IGR J01363+6610	Grebenev et al. 2004 Atel 275	01h 36.3m	+66° 10.5'	2' (ISGRI position)	Grebenev et al. 2004 Atel 275
IGR J01583+6713	Steiner et al. 2005 Atel 672	01h 58m 18.2	+67° 13' 25.9"	3.5" (Swift)	Kennea et al. 2005 Atel 673
IGR J02097+5222	Kuiper et al. 2005 Atel 662	02h 09m 45.6s	+52° 22' 48.0"	3'	Kuiper et al. 2005 Atel 665
IGR J02501+5440	Kuiper et al. 2006 Atel 939	02h 50m 11.3s	+54° 40' 40.6"	3.0'	Kuiper et al. 2006 Atel 939
IGR J03532-6829	Gotz et al. 2006 A&A 448, 873	03h 53m 14	-68° 29' 00"	3.5'	Gotz et al. 2006 A&A 448, 873

Figure *11.1: The IGR Sources Page on the World Wide Web.*

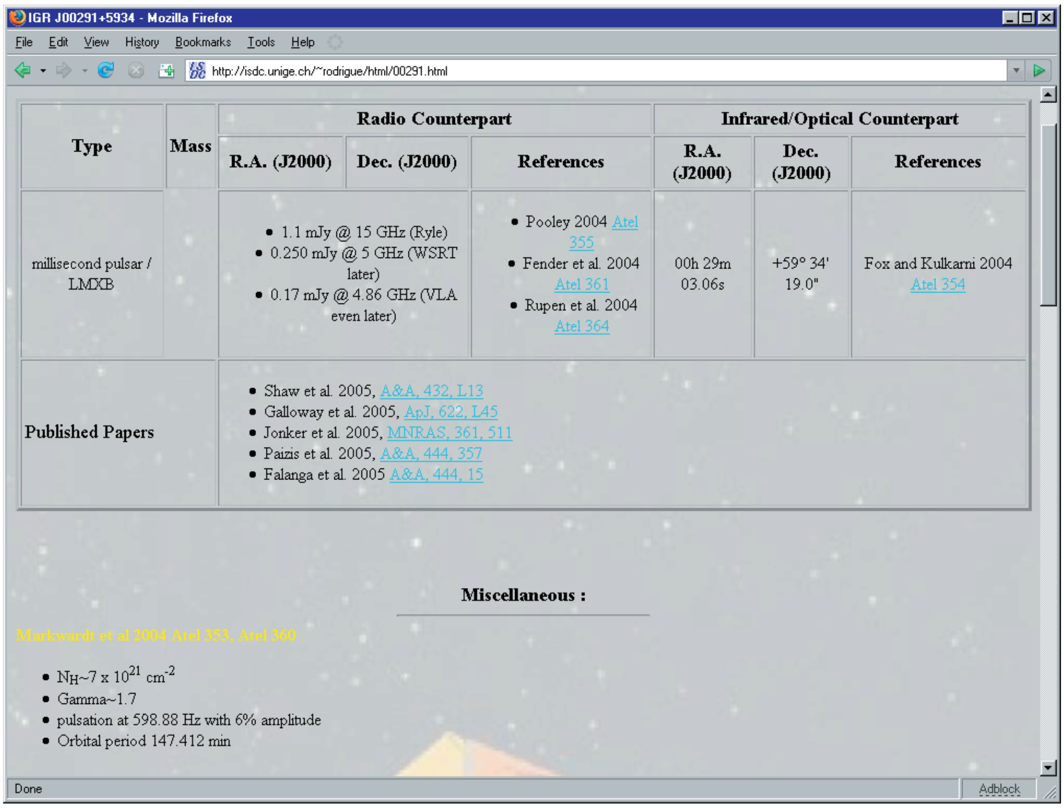

Type	Mass	Radio Counterpart			Infrared/Optical Counterpart		
		R.A. (J2000)	Dec. (J2000)	References	R.A. (J2000)	Dec. (J2000)	References
millisecond pulsar / LMXB		• 1.1 mJy @ 15 GHz (Ryle) • 0.250 mJy @ 5 GHz (WSRT later) • 0.17 mJy @ 4.86 GHz (VLA even later)		• Pooley 2004 Atel 355 • Fender et al. 2004 Atel 361 • Rupen et al. 2004 Atel 364	00h 29m 03.06s	+59° 34' 19.0"	Fox and Kulkarni 2004 Atel 354
Published Papers		• Shaw et al. 2005, A&A, 432, L13 • Galloway et al. 2005, ApJ, 622, L45 • Jonker et al. 2005, MNRAS, 361, 511 • Paizis et al. 2005, A&A, 444, 357 • Falanga et al. 2005 A&A, 444, 15					

Miscellaneous :

Markwardt et al 2004 Atel 353, Atel 360 :

- N_H~7 x 10^{21} cm^{-2}
- Gamma~1.7
- pulsation at 598.88 Hz with 6% amplitude
- Orbital period 147.412 min

Figure *11.2: Web page of IGR J00291+5934.*

Figure 11.1 presents the main page which lists each IGR along with its most accurate X-ray position, and references for the discovery and for the position. The name of each source links to its corresponding page which features published parameters, radio/optical/IR counterparts, and all references. Figure 11.2 presents the page dedicated to the accreting millisecond pulsar IGR J00291+5934. The IGR Sources Page is updated as soon as new information is published in an Astronomer's Telegram, an IAUC, astro-ph, or in a peer-reviewed journal.

The goal is to gather in a single place all that is known about IGRs, and to notify the community about new results. Astronomers who wish to perform follow-up observations of IGRs must be informed quickly in case of a new source announcement, or when an IGR source undergoes an outburst. Therefore, whenever new information about a source is available, an E-mail circular is sent to astronomers who have asked to be included on the mailing list. The circular summarizes the key results and conclusions of each publication or ATel.

During the week-long IAU Symposium in Dublin, J. Rodriguez and I agreed that I should help him write the IGR circulars and help maintain the IGR Sources Page. This made sense given that I was embarking on a review of the literature for all sources detected by ISGRI, which implies staying informed of any new developments during construction of the ISGRI source parameter catalog. Furthermore, as a recipient of the circular, each IGR mail that I received meant that I had to determine whether the new information was worthy of inclusion in the GRC and/or in the ISGRI source parameter catalog. It was clear that uniting our efforts made us more efficient. Tangential benefits for me were the exposure to the *INTEGRAL* community, and the experience of isolating the key points from the chatter and summarizing the pertinent facts of a long-winded article.

Chapter 12

A Catalog of ISGRI Source Parameters

Version 27 of the GRC contains 499 sources detected by ISGRI (i.e. `ISGRI_FLAG==1`) until December 1, 2006. The names and positions of these sources were queried to the SIMBAD and ADS servers for references that could provide any of the following parameters: position and error radius, classification, column density (N_{H}), spin period, orbital period, and distance (or redshift).

Arcsecond X-ray positions were favored when available (i.e. from Chandra, Swift or XMM) as well as radio/IR/optical positions of confirmed counterparts. Source classifications reflect the concensus opinion in the literature. Column densities originate from models that best fits a recent X-ray spectrum. Bear in mind that column densities can vary based on the type of system and on its configuration during the observation. It was not always clear whether the listed N_{H} assumed a Galactic component, so for comparison, I included the expected line-of-sight N_{H} from Dickey & Lockman (1990).

Table 12.1 lists the major source populations detected by ISGRI that are either new (≡ IGRs) or that were previously known. For a number of reasons, *INTEGRAL* has not discovered many LMXBs. They are generally not too absorbed, so a fair number of LMXBs should, in principle, already be known thanks to previous soft X-ray surveys such as RXTE/ASM. Because the companions to LMXBs are usually fainter in the optical/IR wavelengths, this makes it more difficult to identify an IGR source as a LMXB. An additional problem is that the transient nature of many LMXBs might have contributed to preventing a follow-up observation that would help determine a counterpart.

The exposure map that can be seen in Fig. 12.1 was created by accumulating all public pointings in revolutions 30–484 (UTC: 11/1/2003–1/10/2006). There are clear exposure biases that are not easy to account for given that the sample contains sources that were detected serendipitously with only 10 ks of exposure, as well as sources that need several hundred ks of exposure for detection. A more precise analysis would require a normalization with respect to the exposure map,

Table 12.1: The number of sources from each of the major classes detected by ISGRI are listed for new (≡ IGRs) and previously-known sources. Miscellaneous sources are Galactic objects that are not X-ray binaries (e.g. CVs, SNRs, AXPs, etc.).

	IGRs	previously known	total
HMXBs	32 (15%)	46 (16%)	78 (16%)
LMXBs	6 (3%)	76 (27%)	82 (16%)
Miscellaneous	15 (7%)	32 (11%)	47 (9%)
Extragalactic	50 (23%)	113 (40%)	163 (33%)
Unclassified	111 (52%)	18 (6%)	129 (26%)
total	214	285	499

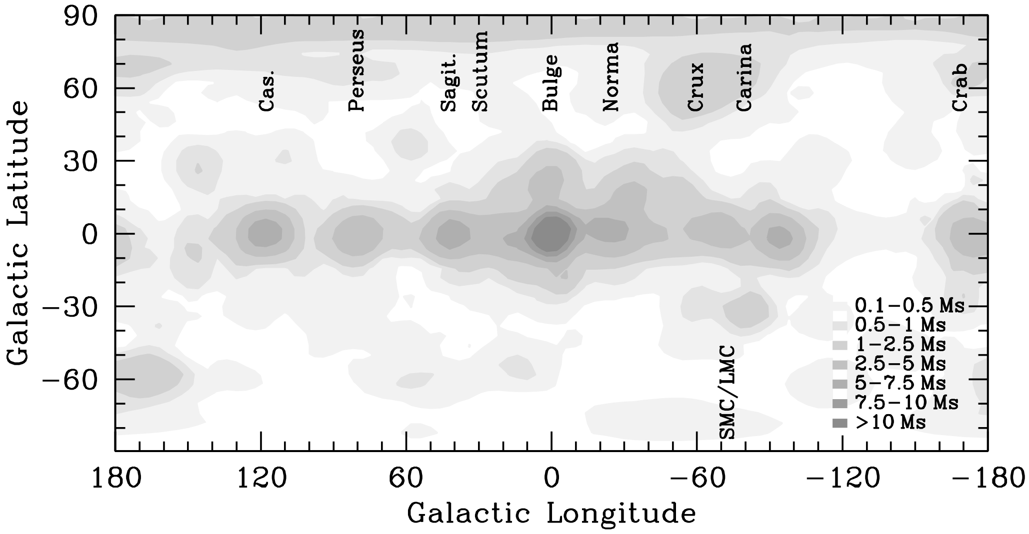

Figure *12.1: The exposure map is presented for public data in revs. 30–484.*

and possibly a correction for the expected spatial distribution. For example, even if the exposure map were homogenous, one would not expect to find a homogenous spatial distribution of Galactic binaries. Extragalactic sources, on the other hand, would be distributed evenly for a homogenous exposure map, with a spatial correction accounting for the volume distribution of AGN (e.g. Beckmann et al. 2006b).

Table 12 represents what we know about sources detected by ISGRI to date. This table serves as the basis for the source distributions presented in the following chapters.

Table 12.2: The parameters of sources detected by ISGRI.

Name	R.A.	Dec.	Error	l	b	$N_{\rm H}$	Spin	Orbit	Distance	Type	Ref.
	(J2000)		(min)	(deg)		(10^{22} cm^{-2})	(s)	(d)	(kpc or z)		
IGR J00040+7020	00 04 01	+70 20 10	3.8	118.930	7.834	–	–	–	–	Unclassified (AGN?)	1
IGR J00234+6141	00 22 54	+61 42 22	4.8	119.557	−0.978	–	570	–	0.3	CV (IP)	1,2,3
IGR J00245+6251	00 24 28	+62 50 35	2.3	119.860	0.132	–	–	–	–	GRB	1
4U 0022+63	00 25 17	+64 09 32	3.6	120.086	1.432	–	–	–	2.83(79)	SNR	1,4
IGR J00254+6822	00 25 26	+68 22 50	2.3	120.529	5.630	–	–	–	–	Unclassified (Sey-2?)	5
V709 Cas	00 28 48.87	+59 17 21.8	0.017	120.042	−3.455	0.8±0.4	312.746(3)	0.2225(2)	0.230(20)	CV (DQ Her)	6,7,8,9
IGR J00291+5934	00 29 03.08	+59 34 19.2	0.01	120.096	−3.176	$0.43^{+0.07}_{-0.05}$	0.0016698(1)	0.1023622(4)	$5.1^{+0.3}_{-0.4}$	LMXB (P, T)	10,11,12,13,14
IGR J00335+6126	00 33 35	+61 26 52	3.3	120.800	−1.350	–	–	–	–	Unclassified	5
1ES 0033+59.5	00 35 52.63	+59 50 04.6	0.017	120.976	−2.978	0.36±0.08	–	–	0.086	BL Lac	15,16
IGR J00370+6122	00 37 09.63	+61 21 36.5	0.002	121.221	−1.464	13±6	–	15.670(4)	3	HMXB (SG)	17,18,19,20
Mrk 348	00 48 47.14	+31 57 25.1	0.017	122.276	−30.911	∼30	–	–	0.0154	Sey-2	21,22,23
RX J0053.8−7226	00 53 55.0	−72 26 47	0.167	302.669	−44.681	0.23±0.11	46.63(4)	137.4(4)	65	HMXB (Be, P, T, in SMC)	24,25,26,27
gam Cas	00 56 42.53	+60 43 00.3	0.002	123.577	−2.148	0.3±0.1	–	203.59(29)	0.19	HMXB (Be)	17,28,29,30
SMC X−1	01 17 05.09	−73 26 36.0	0.002	300.415	−43.559	0.255±0.009	0.7071801(44)	3.8921(4)	65	HMXB (SG, P, E)	19,31,32
3A 0114+650	01 18 02.70	+65 17 29.8	0.002	125.710	2.563	–	9700	11.588(3)	7.0(3.2)	HMXB (P)	17,33,34,35
H 0115+634	01 18 31.9	+63 44 24	0.017	125.924	1.026	1.74±0.18	3.614690(2)	24.31535(5)	8(1)	HMXB (Be, P, T)	24,36,37,38
NGC 526	01 23 54.2	−35 03 55	0.017	263.758	−79.459	1.6±0.2	–	–	0.0192	Sey-1.5	39,40,41
IGR J01363+6610	01 36 05	+66 09 58	3.7	127.427	3.685	–	–	–	2	HMXB (Be, T)	1,42
ESO 297−18	01 38 37.18	−40 00 40.7	0.017	268.727	−73.829	–	–	–	0.0252	Sey-2	43,44
4U 0142+614	01 46 22.41	+61 45 03.2	0.017	129.384	−0.431	0.96±0.02	8.6882(2)	–	2.7	AXP	30,45,46
RX J0146.9+6121	01 47 00.17	+61 21 23.7	0.034	129.541	−0.800	1.2±0.3	1404.2	–	2.5	HMXB (Be, P, T?)	24,47,48
IGR J01528−0326	01 53 01	−03 26 28	4	157.442	−62.114	–	–	–	0.01691	Sey-2	1,49
IGR J01583+6713	01 58 18.2	+67 13 26	0.058	129.352	5.189	∼10	–	–	6.4	HMXB (Be, T)	3,50,51
NGC 788	02 01 06.45	−06 48 55.9	0.017	165.254	−63.805	21±0.5	–	–	0.0136	Sey-2	16,22,52
IGR J02097+5222	02 09 46	+52 22 48	3	134.876	−8.666	–	–	–	0.0492	Sey-1	44,53
SWIFT J0216.3+5128	02 16 33	+51 25 52	5	136.183	−9.238	–	–	–	–	Sey-2	1
Mrk 1040	02 28 14.59	+31 18 39.4	0.017	146.115	−27.166	∼0.067	–	–	[0.016338(314)]	Sey-1.5	54,55,56
IGR J02343+3229	02 34.3	+32 29	2	146.869	−25.563	–	–	–	0.01574	Sey-2	49
NGC 985	02 34 37.77	−08 47 15.4	0.017	180.836	−59.490	$0.6^{+0.5}_{-0.2}$	–	–	[0.04274(5)]	Sey-1	57,58,59
GT 0236+610	02 40 31.67	+61 13 45.6	0.017	135.675	1.086	0.60±0.05	–	26.52(4)	2.5	HMXB (Be, muQSO)	17,30,60,61
NGC 1052	02 41 04.80	−08 15 20.8	0.017	182.019	−57.925	$0.041^{+0.16}_{-0.020}$	–	–	[0.004930(87)]	Sey-2	56,62,63
RBS 345	02 42 16	+05 31 48	5.5	166.437	−47.759	–	–	–	0.069	Sey-1	1,64
NGC 1068	02 42 40.83	−00 00 48.4	0.017	172.104	−51.934	∼0.1	–	–	[0.003786(33)]	Sey-2	54,56,65
QSO B0241+62	02 44 57.70	+62 28 06.5	0.017	135.636	2.430	1.5±0.3	–	–	[0.04456(51)]	Sey-1	16,56,66
IGR J02501+5440	02 50 11	+54 40 41	3	139.619	−4.300	–	–	–	–	Unclassified (AGN?)	5

Table 12.2: continued.

Name	R.A.	Dec.	Error	l	b	N_H	Spin	Orbit	Distance	Type	Ref.
	(J2000)		(’)	(deg)		(10^{22} cm^{-2})	(s)	(d)	(kpc or [z])		
MCG−02−08−014	02 52 23.3	−08 30 38	0.017	185.556	−55.885	–	–	–	[0.016758(13)]	Sey-2	56,67
NGC 1142	02 55 12.32	−00 11 01.7	0.017	175.876	−49.889	~45	–	–	[0.028847(47)]	Sey-2	22,54,68
QSO B0309+411	03 13 01.962	+41 20 01.18	0.017	149.577	−14.098	–	–	–	0.136	Sey-1	62,69
IGR J03184−0014	03 18 24	−00 13 44	4	181.762	−45.644	–	–	–	–	QSO	1
NGC 1275	03 19 48.16	+41 30 42.1	0.017	150.576	−13.261	1.5±0.7	–	–	0.017559	Sey-2	16,62
1H 0323+342	03 24 41.161	+34 10 45.86	0.017	155.727	−18.757	~0.1	–	–	0.062	Sey-1	22,70,71
GK Per	03 31 11.82	+43 54 16.8	0.017	150.955	−10.104	17.54±0.29	351.34	2.00	0.420	CV (IP)	6,9,72
IGR J03334+3718	03 33 18.8	+37 18 11	0.017	155.275	−15.202	–	–	–	0.05471	Sey-1	73
NGC 1365	03 33 36.5	−36 08 17	0.017	237.952	−54.598	44±8	–	–	0.005559	Sey-1.8	40,56,74
EXO 0331+530	03 34 59.9	+53 10 23	0.017	146.052	−2.194	1.10±0.07	4.3751(2)	34.25(10)	7.5(1.5)	HMXB (Be, P, QPO, T)	24,75,76,77,78
IGR J03532−6829	03 53 14	−68 28 59	3.6	282.738	−40.784	–	–	–	0.087	BL Lac	1,3
X Per	03 55 23.08	+31 02 45.0	0.002	163.081	−17.136	0.129±0.028	837.8(1)	250.3(6)	0.700(300)	HMXB (Be, P)	17,19,79,80,81
3C 111	04 18 21.28	+38 01 35.8	0.017	161.676	−8.820	~0.9	–	–	0.0485	Sey-1	16,82
UGC 3142	04 43 46.89	+28 58 19.0	0.017	172.089	−10.996	–	–	–	[0.02183(19)]	Sey-1	54,56
LEDA 168563	04 52 04.7	+49 32 45	0.017	157.252	3.419	–	–	–	0.029	Sey-1	56,83
ESO 33−2	04 55 59.6	−75 32 26	0.017	287.767	−33.285	~0.1	–	–	[0.01843(46)]	Sey-2	22,56,84
IGR J05007−7047	05 00 46.08	−70 44 36.0	0.01	282.167	−34.525	1.0±0.2	–	–	50	HMXB (in LMC)	85,86
IGR J05053−7343	05 05 19	−73 42 58	3.6	285.463	−33.309	–	–	–	–	Unclassified (T)	1
4U 0517+17	05 10 45.5	+16 29 55	0.017	186.114	−13.499	~0.1	–	–	0.017879	Sey-1.5	22,87,88
Ark 120	05 16 11.48	−00 09 00.6	0.017	201.695	−21.132	–	–	–	0.033687	Sey-1	54,74
SGR 0526−66	05 26 00.89	−66 04 36.3	0.01	276.087	−33.246	0.54±0.02	8.0470(2)	–	–	SGR (P)	89
IGR J05270−6631	05 27 01	−66 30 40	4.4	276.585	−33.088	–	–	–	–	Unclassified	1
EXO 053109−6609.2	05 31 13.3	−66 07 05	0.067	276.058	−32.718	$0.69^{+0.07}_{-0.13}$	13.66817(1)	25.4	50	HMXB (Be, P, T, in LMC)	90,91
IGR J05319−6601	05 31.9	−66 02	3.5	275.949	−32.659	–	–	–	–	Unclassified (T)	92
LMC X−4	05 32 49.79	−66 22 13.8	0.017	276.335	−32.529	~0.055	13.503(1)	1.40841(2)	55	HMXB (SG, P)	93,94,95
Crab	05 34 31.97	+22 00 52.1	0.017	184.558	−5.784	0.260±0.001	0.0335(1)	–	2	SNR (PWN)	96,97,98,99
IGR J05346−5759	05 34.6	−58 00	3.5	266.390	−32.811	–	–	–	–	Unclassified (T, CV?)	92
1A 0535+262	05 38 54.57	+26 18 56.8	0.017	181.445	−2.644	$0.65^{+0.25}_{-0.12}$	104	111.0(4)	$2^{+0.4}_{-0.7}$	HMXB (Be, P, T)	17,24,100,101
LMC X−1	05 39 38.7	−69 44 36	0.05	280.203	−31.516	0.46±0.02	–	3.9081(15)	55	HMXB (SG, BHC)	24,102,103,104
PSR B0540−69.3	05 40 07.72	−69 20 05.1	0.017	279.721	−31.520	0.43±0.02	0.0504988(1)	–	55	Unclassified (P, in LMC)	31,105,106
BY Cam	05 42 48.90	+60 51 31.8	0.017	151.833	15.690	~0.001	11960.2(2)	0.139759(3)	0.190	CV (AM Her)	6,9,107,108
MCG+08−11−011	05 54 53.63	+46 26 21.8	0.017	165.731	10.407	$0.183^{+0.006}_{-0.003}$	–	–	0.020484	Sey-1.5	16,54,109
IRAS 05589+2828	06 02 09.7	+28 28 17	0.017	182.238	2.892	–	–	–	0.0330	Sey-1	22,110
SWIFT J0601.9−8636	06 05 39.1	−86 37 52	0.082	299.201	−27.747	–	–	–	[0.006(1)]	AGN (Sey-2?)	111,112
IGR J06074+2205	06 07.4	+22 05	2	188.392	0.798	–	–	–	1	HMXB (Be)	3,113

Table 12.2: continued.

Name	R.A.	Dec.	Error	l	b	N_H	Spin	Orbit	Distance	Type	Ref.
	(J2000)		(’)	(deg)		(10^{22} cm^{-2})	(s)	(d)	(kpc or [z])		
PKS 0611−663	06 11 43.20	−66 24 30.0	0.017	276.241	−28.639	0.048±0.011	–	–	–	AGN	114,115
Mrk 3	06 15 36.31	+71 02 14.9	0.017	143.296	22.719	127^{+24}_{-22}	–	–	[0.01344(31)]	Sey-2	54,56,116
H 0614+091	06 17 07.3	+09 08 13	0.017	200.877	−3.364	0.37±0.02	0.0030(2)	–	$2.2^{+0.8}_{-0.7}$	LMXB (P, QPO, B, A)	117,118,119,120
IGR J06239−6052	06 23 55	−60 53 53	4.9	270.195	−26.761	–	–	–	–	Unclassified (T, AGN?)	1
IGR J06253+7334	06 25 22	+73 36 07	5.2	140.832	24.137	–	1187.3(1)	0.1965(2)	0.5	CV (IP)	1,9,121
IGR J06292+4858	06 29 12	+48 58 26	5	165.939	16.703	–	–	–	–	Unclassified	1
PKS 0637−752	06 35 46.51	−75 16 16.8	0.002	286.368	−27.158	0.035±0.005	–	–	0.651	Sey-1	62,122
Mrk 6	06 52 12.32	+74 25 36.8	0.017	140.328	26.107	$1.94^{+0.09}_{-0.14}$	–	–	[0.01868(83)]	Sey-1.5	54,56,123
LEDA 96373	07 26 26.3	−35 54 21	0.017	248.767	−9.076	–	–	–	[0.029624(544)]	Sey-2	56
IGR J07295−1329	07 29 30	−13 09 29	5.4	228.966	2.262	–	–	–	–	Unclassified	1
IGR J07437−5137	07 43 41	−51 37 01	5	264.477	−13.447	–	–	–	–	Unclassified	1
EXO 0748−676	07 48 33.8	−67 45 09	0.017	279.978	−19.811	8^{+5}_{-3}	–	0.1593375(6)	$8.0^{+1.1}_{-1.2}$	LMXB (B, D, T)	19,117,124,125
IGR J07506−1547	07 50 35	−15 47 17	1.7	233.770	5.423	–	–	–	–	Unclassified (T)	126
IGR J07565−4139	07 56 19.62	−41 37 42.1	0.01	256.656	−6.723	1.1±0.2	–	–	[0.021(1)]	Sey-2	85,86
IGR J07597−3842	07 59 41.819	−38 43 56.03	0.002	254.495	−4.679	~0.05	–	–	[0.040(1)]	Sey-1.2	86,127
ESO 209−12	08 01 57.6	−49 46 42	0.017	264.253	−10.026	~0.1	–	–	[0.03959(58)]	Sey-1.5	22,56
IGR J08023−6954	08 02.3	−69 55	3	282.616	−19.589	–	–	–	–	Unclassified (T)	128
PG 0804+761	08 10 58.66	+76 02 42.5	0.017	138.279	31.033	0.023±0.011	–	–	0.100	Sey-1	122,129
Vela Pulsar	08 35 20.66	−45 10 35.2	0.017	263.552	−2.787	0.033±0.003	0.0893	–	$0.294^{+0.076}_{-0.050}$	SNR (PWN)	62,130,131
Ginga 0836−429	08 37 23.6	−42 54 02	0.167	261.954	−1.124	2.2±0.3	–	–	10.0	LMXB (B, T)	30,117,132
Fairall 1146	08 38 30.7	−35 59 35	0.017	256.585	3.230	~0.1	–	–	[0.0318(3)]	Sey-1.5	22,56
IGR J08408−4503	08 40 47.97	−45 03 29.8	0.09	264.041	−1.950	–	–	–	3	HMXB (SG, SFXT)	133
QSO B0836+710	08 41 24.37	+70 53 42.2	0.017	143.541	34.426	$1.1^{+1.6}_{-0.8}$	–	–	2.172	Blazar	21,62,134
Vela X−1	09 02 06.86	−40 33 16.9	0.017	263.058	3.930	$5.6^{+0.3}_{-0.2}$	283.2(1)	8.965(4)	1.9(2)	HMXB (SG, P, E)	17,19,135,136,137
IGR J09025−6814	09 02 27	−68 14 06	5.1	284.169	−14.178	–	–	–	–	Unclassified (T)	1
IGR J09026−4812	09 02 40	−48 12 58	2.3	268.866	−1.072	–	–	–	–	Unclassified	126
IGR J09103−3741	09 10 18	−37 40 30	5.2	261.972	7.035	–	–	–	–	Unclassified (T)	1
SWIFT J0917.2−6221	09 16 09.41	−62 19 29.5	0.017	280.612	−9.195	~1	–	–	[0.05715(21)]	Sey-1	56,138,139
EXMS B0918−549E	09 20 05	−55 08 35	0.9	275.771	−3.837	–	–	–	–	Unclassified (T)	126
H 0918−549	09 20 26.95	−55 12 24.7	0.01	275.853	−3.845	0.24±0.03	–	–	$5.0^{+0.8}_{-0.7}$	LMXB (B, QPO)	125,140
Mrk 110	09 25 12.87	+52 17 10.5	0.017	165.011	44.364	0.019±0.001	–	–	[0.035398(510)]	Sey-1 (NL)	55,56,57
IGR J09253+6929	09 25 17	+69 29 17	4.7	143.423	38.392	–	–	–	–	Unclassified	1
IGR J09446−2636	09 44.6	−26 36	3	259.106	19.968	~0.1	–	–	0.1425	Sey-1	22
1RXS J094436.5−263353	09 44 36.50	−26 33 53.0	0.017	259.081	19.995	~0.1	–	–	0.0492	Sey-1	22,141
4U 0937−12	09 45 42.05	−14 19 35.0	0.017	249.706	28.781	$0.85^{+0.05}_{-0.04}$	–	–	[0.007710(13)]	Sey-2	40,52,68

Table 12.2: continued.

Name	R.A. (J2000)	Dec. (J2000)	Error (')	l (deg)	b (deg)	N_H (10^{22} cm^{-2})	Spin (s)	Orbit (d)	Distance (kpc or [z])	Type	Ref.
IGR J09469−4603	09 46 53	−46 02 46	4.8	272.736	5.726	–	–	–	–	Unclassified	1
MCG−05−23−016	09 47 40.2	−30 56 54	0.017	262.744	17.234	1.80±0.23	–	–	[0.00823(16)]	Sey-2	56,142,143
IGR J09485−4726	09 48 29	−47 25 37	4.9	273.838	4.843	–	–	–	–	Unclassified	1
IGR J09523−6231	09 52 17	−62 30 58	3.9	283.832	−6.490	–	–	–	–	Unclassified	1
IGR J10043−8702	10 04.3	−87 02	3.4	300.753	−24.899	–	–	–	–	Unclassified (T)	144
GRO J1008−57	10 09 46	−58 17 32	0.017	282.998	−1.822	0.86±0.03	93.57(9)	248.9(5)	5	HMXB (Be, P, T)	24,30,103,145
SWIFT J1009.3−4250	10 09 48.3	−42 48 44	0.083	273.979	10.792	~100	–	–	0.03355	Sey-2	146
IGR J10101−5654	10 10 11.866	−56 55 32.06	0.002	282.257	−0.672	–	–	–	–	HMXB (T)	86
IGR J10109−5746	10 11 02.95	−57 48 13.9	0.017	282.855	−1.325	–	–	–	–	Symbiotic Star	147
IGR J10147−6354	10 14 42	−63 53 31	5	286.695	−6.078	–	–	–	–	Unclassified	1
NGC 3227	10 23 30.62	+19 51 53.7	0.017	216.992	55.445	6.8±0.3	–	–	0.003827	Sey-1.5	54,65,148
IGR J10252−6829	10 25 00.49	−68 27 27.3	0.01	290.112	−9.311	–	–	–	–	Unclassified (T)	85
NGC 3281	10 31 52.06	−34 51 13.3	0.017	273.007	19.783	151^{+20}_{-19}	–	–	[0.011475(87)]	Sey-2	56,149,150
4U 1036−56	10 37 33.8	−56 47 58	0.017	285.350	1.431	4.6±0.4	860(2)	–	5.0	HMXB (Be, P, T)	30,141,151
SWIFT J1038.8−4942	10 38 45.0	−49 46 55	0.055	282.049	7.633	$1^{+2}_{-0.7}$	–	–	[0.060(1)]	Sey-1.5	112,139
IGR J10404−4625	10 40 23	−46 24 58	1.5	280.617	10.700	~1	–	–	[0.0240(6)]	Sey-2	56,126,152
IGR J10448−5945	10 44 47	−59 45 18	5.2	287.599	−0.708	–	–	–	–	Unclassified	1
IGR J10500−6410	10 50.1	−64 10	4	290.181	−4.341	–	–	–	–	Unclassified (T)	144
IGR J11085−5100	11 08 50.48	−51 02 32.8	0.01	286.954	8.619	–	–	–	–	Unclassified (T)	85
IGR J11098−6457	11 09 46	−64 56 46	5.5	292.432	−4.168	–	–	–	–	Unclassified	1
IGR J11114−6723	11 11 25	−67 23 31	1.7	293.521	−6.366	–	–	–	–	Unclassified (T)	126
IGR J11187−5438	11 18 42	−54 37 59	4	289.690	5.837	–	–	–	–	Unclassified	1
Cen X−3	11 21 15.78	−60 37 22.7	0.017	292.091	0.337	1.95±0.03	4.81423(1)	2.0871384(1)	10(1)	HMXB (SG, P, E)	93,153,154,155
IGR J11215−5952	11 21 46.9	−59 51 42	0.083	291.893	1.075	11±3	195(10)	–	6.2	HMXB (SG, P, SFXT)	152,156,157,158
IGR J11305−6256	11 31 06	−62 56 20	1.2	293.941	−1.478	–	–	–	3	HMXB (Be, T)	1,152
IGR J11321−5311	11 32.1	−53 11	2	291.087	7.854	–	–	–	–	Unclassified (T, BHC?)	159
IGR J11366−6002	11 36 38	−60 02 02	4.9	293.713	1.492	–	–	–	–	Unclassified (AGN?)	1
NGC 3783	11 39 01.78	−37 44 18.7	0.017	287.456	22.948	1.8±0.3	–	–	[0.00965(67)]	Sey-1	56,149,160
EXMS B1136−650	11 39 29	−65 24 18	3.2	295.533	−3.572	–	–	–	–	RS CVn Star (T)	1
IGR J11435−6109	11 44 00.4	−61 07 16	1.4	294.880	0.692	9±2	161.76(1)	52.46(6)	–	HMXB (Be, P, T)	161,162
1E 1145.1−6141	11 47 28.6	−61 57 14	0.017	295.490	−0.010	~3.3	296.573(2)	14.365(2)	8.5(1.5)	HMXB (SG, P)	24,163
H 1145−619	11 48 00.02	−62 12 24.9	0.017	295.611	−0.240	$2.6^{+0.4}_{-0.2}$	292.4	187.5	3.1(5)	HMXB (Be, P, T)	17,24,164,165
IGR J12026−5349	12 02 47.63	−53 50 07.7	0.01	295.714	8.353	2.2±0.3	–	–	[0.028(1)]	Sey-2	85,86
NGC 4051	12 03 09.63	+44 31 53.2	0.017	148.883	70.085	0.3±0.1	–	–	0.002336	Sey-1.5	54,65,166
NGC 4138	12 09 29.87	+43 41 06.0	0.017	147.305	71.404	8±1	–	–	[0.00296(13)]	Sey-1.9	54,56,65

Table 12.2: continued.

Name	R.A.	Dec.	Error	l	b	N_H	Spin	Orbit	Distance	Type	Ref.
	(J2000)		(')	(deg)		(10^{22} cm^{-2})	(s)	(d)	(kpc or [z])		
NGC 4151	12 10 32.73	+39 24 19.6	0.017	155.077	75.064	7.5±0.1	–	–	[0.003262(67)]	Sey-1.5	54,56,65
NGC 4180	12 13 02.97	+07 02 17.8	0.017	276.792	67.940	–	–	–	[0.00690(21)]	AGN	54,56
EXMS B1210−645	12 13 05.28	−64 53 49	4.9	298.877	−2.328	–	–	–	–	Unclassified (T)	1
Was 49	12 14 17.81	+29 31 43.4	0.017	194.392	81.485	~10	–	–	0.064	Sey-2	71,167,168
Mrk 766	12 18 26.63	+29 48 45.6	0.017	190.681	82.271	~0.8	–	–	[0.012662(364)]	Sey-1.5	54,56,166
NGC 4258	12 18 57.54	+47 18 14.3	0.101	138.320	68.842	8.7±0.3	–	–	[0.001541(90)]	Sey-1.9	54,56,65
4C 04.42	12 22 22.55	+04 13 15.8	0.017	284.819	66.066	~0.1	–	–	[0.965001(207)]	Blazar	55,56,62
Mrk 50	12 23 24.14	+02 40 44.8	0.017	286.393	64.647	~0.018	–	–	[0.023196(277)]	Sey-1	55,56,169
NGC 4388	12 25 46.93	+12 39 43.3	0.017	279.124	74.336	27±2	–	–	[0.008426(57)]	Sey-2	54,56,65
NGC 4395	12 25 48.93	+33 32 47.8	0.017	162.095	81.533	5.3±0.3	–	–	0.001064	Sey-1.8	54,65,166
GX 301−2	12 26 37.6	−62 46 14	0.05	300.098	−0.035	50±10	679.5(5)	41.59(6)	4.1	HMXB (P, F, T)	19,24,170,171
XSS J12270−4859	12 28 02	−48 53 35	4.3	298.974	13.799	–	–	–	–	CV (IP)	1
3C 273	12 29 06.69	+02 03 08.6	0.017	289.951	64.360	$0.090^{+0.003}_{-0.005}$	–	–	0.15834	QSO	17,134,166
IGR J12349−6434	12 34 54.7	−64 33 56	0.1	301.158	−1.751	–	–	–	–	Symbiotic Star	172
NGC 4507	12 35 36.55	−39 54 33.3	0.017	299.639	22.861	29±2	–	–	[0.01177(14)]	Sey-2	16,56,149
SWIFT J1238.9−2720	12 38 54.5	−27 18 28	0.06	299.514	35.481	10^{+22}_{-7}	–	–	[0.025208(117)]	Sey-2	39,139
IGR J12391−1612	12 39 06.29	−16 10 47.1	0.01	298.621	46.589	1.9±0.3	–	–	0.0367	Sey-2	85
NGC 4593	12 39 39.43	−05 20 39.3	0.017	297.483	57.403	0.023±0.003	–	–	0.009	Sey-1	16,173,174
IGR J12415−5750	12 41 25.8	−57 50 03	0.017	301.595	5.012	~0.11	–	–	[0.0242(3)]	Sey-2	56,127,175
1H 1249−637	12 42 50.266	−63 03 31.05	0.017	301.958	−0.203	1.38±0.30	–	–	0.300(50)	HMXB (Be)	17,176,177
PKS 1241−399	12 44 29.34	−40 12 46.4	0.017	301.495	22.639	–	–	–	0.191	QSO	178
3A 1246−588	12 49 39.61	−59 05 13.3	0.005	302.703	3.784	0.29±0.09	–	–	5	LMXB (T)	179,180
ESO 323−32	12 53 20.35	−41 38 13.8	0.017	303.313	21.233	–	–	–	[0.015941(147)]	Sey-1	56,181
3C 279	12 56 11.17	−05 47 21.5	0.017	305.104	57.062	~0.02	–	–	0.53620	Blazar	16,62,166
1H 1254−690	12 57 37.2	−69 17 21	0.017	303.482	−6.424	0.31±0.01	–	0.163890(3)	13(3)	LMXB (B, D)	103,117,182,183
Coma Cluster	12 59 48.7	+27 58 50	0.017	58.079	87.958	0.0094±0.0009	–	–	0.0231	Cluster of Galaxies	166,184,185
IGR J13000+2529	13 00.0	+25 29	3	352.806	87.473	–	–	–	–	AGN	16
IGR J13020−6359	13 01 58.8	−63 58 10	0.05	304.088	−1.121	2.48±0.07	704.2(1.1)	–	5.5(1.5)	HMXB (Be, P)	186
Mrk 783	13 02 58.841	+16 24 27.46	0.017	317.527	78.951	0.046±0.014	–	–	0.067	Sey-1.5	55,57,71
IGR J13038+5348	13 03 59.39	+53 47 30.2	0.017	118.814	63.236	–	–	–	0.02988	Sey-1	73,187
NGC 4945	13 05 26.1	−49 28 15	0.017	305.268	13.337	425±25	–	–	[0.001908(60)]	Sey-2	56,188
IGR J13057+2036	13 05 42.56	+20 34 51.7	0.017	330.166	82.686	–	–	–	–	AGN	189
ESO 323−77	13 06 26.6	−40 24 50	0.017	306.020	22.368	55±33	–	–	[0.014904(73)]	Sey-1.2	16,56,84
IGR J13091+1137	13 09 05.60	+11 38 02.9	0.01	318.764	73.961	90±10	–	–	[0.02520(9)]	Sey-2	56,85
IGR J13109−5552	13 10 44	−55 51 47	3.4	305.657	6.907	–	–	–	–	Unclassified (AGN?)	1

Table 12.2: continued.

Name	R.A. (J2000)	Dec. (J2000)	Error (')	l (deg)	b (deg)	N_H (10^{22} cm^{-2})	Spin (s)	Orbit (d)	Distance (kpc or [z])	Type	Ref.
NGC 5033	13 13 27.59	+36 35 36.9	0.017	98.057	79.448	~0.03	–	–	0.002919	Sey-1.9	54,65,166
IGR J13149+4422	13 15 15.73	+44 24 27	0.017	108.998	72.071	–	–	–	0.036698	Sey-2	190,191
IGR J13186−6257	13 18 36	−62 56 46	3.8	306.015	−0.237	–	–	–	–	Unclassified	1
Cen A	13 25 27.62	−43 01 08.8	0.017	309.516	19.417	10.0±0.6	–	–	0.00183	Sey-2	62,166,192
4U 1323−62	13 26 36.1	−62 08 10	0.017	307.028	0.456	2.42±0.14	–	0.1222(2)	15(5)	LMXB (B, D)	117,193,194
ESO 383−18	13 33 26.30	−34 00 58.7	0.017	312.787	28.050	–	–	–	0.0124	Sey-2	22,195
1RXS J133447.5+371100	13 34 47.808	+37 10 56.69	0.002	83.323	76.407	–	–	18.692	–	RS CVn	17,196
MCG−06−30−015	13 35 53.8	−34 17 44	0.017	313.292	27.680	0.03±0.01	–	–	[0.00789(16)]	Sey-1.2	56,197,198
NGC 5252	13 38 16.00	+04 32 32.5	0.017	331.299	64.803	$0.68^{+0.16}_{-0.07}$	–	–	[0.022219(884)]	Sey-2	40,54,56
Mrk 268	13 41 11.14	+30 22 41.2	0.017	52.467	78.630	–	–	–	[0.040408(804)]	Sey-2	56,167
4U 1344−60	13 47 32	−60 36 36	1	309.764	1.515	2.64±0.07	–	–	[0.012(1)]	Sey-1.5	1,166,199
IC 4329A	13 49 19.29	−30 18 34.4	0.017	317.496	30.920	0.42±0.02	–	–	[0.01602(15)]	Sey-1.2	16,56,149
IGR J14003−6326	14 00 37	−63 26 49	3.9	310.572	−1.606	–	–	–	–	Unclassified	1
V834 Cen	14 09 07.46	−45 17 17.1	0.017	316.979	15.454	1.03±0.39	–	0.07042	0.080	CV (DQ Her)	6,9,200
Circinus Galaxy	14 13 08.90	−65 20 27.0	0.017	311.324	−3.809	430^{+40}_{-70}	–	–	[0.00142(8)]	Sey-2	56,201,202
NGC 5506	14 13 14.87	−03 12 27.0	0.017	339.150	53.810	$3.42^{+0.24}_{-0.14}$	–	–	[0.00607(13)]	Sey-2	56,57,203
IGR J14175−4641	14 17 03.662	−46 41 41.19	0.002	317.862	13.680	–	–	–	[0.076(1)]	Sey-2	86
NGC 5548	14 17 59.65	+25 08 13.4	0.017	31.962	70.495	0.5±0.1	–	–	0.01676	Sey-1.5	54,204,205
RHS 39	14 19 22.2	−26 38 41	0.017	326.227	32.219	~0.05	–	–	[0.02224(17)]	Sey-1	16,56,64
IGR J14298−6715	14 29 21	−67 15 36	4.3	312.203	−6.168	–	–	–	–	Unclassified	1
IGR J14319−3315	14 31 57	−33 14 42	4.8	326.018	25.081	–	–	–	–	Unclassified	1
IGR J14331−6112	14 33 26	−61 12 14	3.7	314.901	−0.725	–	–	–	–	Unclassified	1
IGR J14471−6414	14 46 21	−64 17 38	4.6	314.998	−4.148	–	–	–	–	Unclassified	1
IGR J14471−6319	14 47 14.881	−63 17 19.24	0.002	315.521	−3.283	–	–	–	[0.038(1)]	Sey-2	86
IGR J14492−5535	14 49 13	−55 34 44	1.5	319.097	3.552	$10.1^{+6.3}_{-4.3}$	–	–	–	AGN	126,127
IGR J14515−5542	14 51 33.131	−55 40 38.40	0.002	319.350	3.318	~0.1	–	–	[0.018(1)]	Sey-2	22,86
IGR J14532−6356	14 53 14.88	−63 55 37	5.3	315.837	−4.151	–	–	–	–	Unclassified (T)	1
IGR J14536−5522	14 53 41.055	−55 21 38.74	0.002	319.763	3.465	–	–	–	0.190	CV (AM Her)	86
IGR J14552−5133	14 55 17.8	−51 34 17	0.017	321.716	6.726	~0.1	–	–	[0.016(1)]	Sey-1 (NL)	22,86
IGR J14579−4308	14 57 43.1	−43 07 48	0.017	326.120	13.984	–	–	–	[0.016261(150)]	Sey-2	84,206
IGR J15094−6649	15 09 26.013	−66 49 23.29	0.002	315.925	−7.499	–	–	–	0.140	CV (IP)	86
PSR B1509−58	15 13 54.6	−59 08 15	0.017	320.318	−1.162	0.82±0.03	0.1507477(1)	–	5.2(1.4)	SNR (PWN)	141,207,208,209
ESO 328−36	15 14 47.0	−40 21 31	0.017	330.405	14.745	–	–	–	0.0237	Sey-1	44,84
IGR J15161−3827	15 16 09	−38 26 53	5.3	331.711	16.206	–	–	–	–	Unclassified (AGN?)	1
Cir X−1	15 20 40.9	−57 10 01	0.017	322.118	0.037	1.6±0.1	–	16.55(1)	$9.2^{+1.3}_{-1.4}$	LMXB (B, A, T)	19,117,125,210

Table 12.2: continued.

Name	R.A.	Dec. (J2000)	Error (')	l	b (deg)	N_H (10^{22} cm^{-2})	Spin (s)	Orbit (d)	Distance (kpc or [z])	Type	Ref.
IGR J15283−4443	15 28.4	−44 44	3	330.056	9.715	–	–	–	–	Unclassified (T)	144
IGR J15359−5750	15 35 52	−57 49 55	1.3	323.431	−1.660	–	–	–	–	Unclassified	126
H 1538−522	15 42 23.3	−52 23 10	0.017	327.419	2.164	1.63±0.04	526.854(13)	3.7284(3)	6.4(1.0)	HMXB (SG, P, E)	19,24,211,212,213
XTE J1543−568	15 44 02	−56 42 43	4.2	324.985	−1.421	1.3±0.1	27.12156(59)	75.56(25)	10.0	HMXB (Be, P, T)	1,30,214
4U 1543−624	15 47 54.69	−62 34 05.4	0.01	321.757	−6.336	$0.31^{+0.02}_{-0.06}$	–	0.01264(7)	7	LMXB (NS?)	140,215,216
IGR J15479−4529	15 48 14.5	−45 28 45	0.15	332.439	7.022	9.5±0.8	693.01(6)	0.411(1)	0.69(15)	CV (IP)	217,218,219
NGC 5995	15 48 24.95	−13 45 28.0	0.017	354.960	30.719	–	–	–	[0.025091(357)]	Sey-2	56,220
XTE J1550−564	15 50 58.7	−56 28 36	0.034	325.882	−1.827	$0.88^{+0.12}_{-0.09}$	–	1.5420(10)	5.3(2.3)	LMXB (BHC, T)	125,221,222,223
IGR J15529−5029	15 52 56	−50 29 24	3.9	329.886	2.634	–	–	–	–	Unclassified	1
IGR J15539−6142	15 53 21	−61 40 16	3.9	322.822	−6.041	–	–	–	–	Unclassified (AGN?)	1
1H 1556−605	16 01 02.3	−60 44 18	0.017	324.139	−5.932	$0.30^{+0.01}_{-0.02}$	–	0.3807(3)	4.0	LMXB	30,117,215,224
IGR J16024−6107	16 02 26	−61 07 26	4.7	324.011	−6.333	–	–	–	–	Unclassified (AGN?)	1
IGR J16056−6110	16 05 35	−61 10 16	5	324.264	−6.622	–	–	–	–	AGN	1
IGR J16119−6036	16 11 51.4	−60 37 55	0.017	325.196	−6.744	~0.1	–	–	[0.015818(257)]	Sey-1	22,56,225
H 1608−522	16 12 43.0	−52 25 23	0.017	330.926	−0.850	1.28±0.06	–	0.5370(15)	3.3(5)	LMXB (B, T, A)	117,125,226,227
IGR J16167−4957	16 16 37.74	−49 58 44.5	0.01	333.056	0.496	$0.5^{+0.3}_{-0.2}$	–	–	0.170	CV (IP)	86,228
PSR J1617−5055	16 17 29.3	−50 55 13.2	0.017	332.499	−0.275	$1.6^{+2.4}_{-1.0}$	0.0693618(1)	–	3.3	Radio P	229,230,231,232
2E 1613.5−5053	16 17 36.3	−51 02 25	0.004	332.429	−0.374	$3.1^{+4.3}_{-2.1}$	21492^{+1692}_{-1584}	–	$0.7^{+3.8}_{-0.8}$	LMXB (P)	230,233,234
IGR J16185−5928	16 18 36.441	−59 27 17.36	0.002	326.630	−6.485	–	–	–	[0.035(1)]	Sey-1 (NL)	86
IGR J16194−2810	16 19 26	−28 09 36	1.5	349.076	15.539	–	–	–	–	AGN	126
IGR J16195−4945	16 19 32.20	−49 44 30.7	0.01	333.557	0.339	7^{+5}_{-3}	–	–	–	HMXB (SG, SFXT?)	228
Sco X−1	16 19 55.07	−15 38 24.8	0.002	359.094	23.784	2.37±0.5	–	0.78893(10)	2.8(3)	LMXB (QPO, Z)	125,235,236,237
IGR J16207−5129	16 20 46.26	−51 30 06.0	0.01	332.459	−1.050	$3.7^{+1.4}_{-1.2}$	–	–	4.6	HMXB (SG)	86,228
IGR J16248−4603	16 24 50	−46 02 35	4.7	336.804	2.322	–	–	–	–	Unclassified (T)	1
SWIFT J1626.6−5156	16 26 36.2	−51 56 33	0.058	332.780	−2.003	0.94±0.10	15.37682(5)	–	–	Unclassified (P, T, Be-HMXB?, LMXB?)	238,239
H 1624−490	16 28 02.83	−49 11 54.6	0.01	334.915	−0.263	$7.4^{+0.4}_{-0.2}$	–	0.86990(2)	15	LMXB (D)	19,240,241,242
IGR J16283−4838	16 28 10.7	−48 38 55	0.083	335.327	0.102	17^{+5}_{-4}	–	–	–	HMXB (T, NS?)	243,244
IGR J16287−5021	16 28 42	−50 20 38	4.4	334.161	−1.132	–	–	–	–	Unclassified	1
IGR J16316−4028	16 31.6	−40 28	3	341.700	5.281	–	–	–	–	Unclassified (T)	245
IGR J16318−4848	16 31 48.6	−48 49 00	0.067	335.617	−0.448	193±11	–	–	3.6(2.6)	HMXB	246,247,248
IGR J16320−4751	16 32 01.9	−47 52 27	0.05	336.330	0.169	$11.8^{+0.5}_{-0.4}$	1303.8(9)	8.96(1)	–	HMXB (SG, P)	249,250
4U 1626−67	16 32 16.8	−67 27 43	0.017	321.788	−13.092	0.11±0.02	7.66794(4)	0.028846(2)	9.0	LMXB (P)	30,117,251,252,253
IGR J16328−4726	16 32 46	−47 26 13	4.5	336.734	0.377	–	–	–	–	Unclassified (T)	1
4U 1630−47	16 34 00.4	−47 23 39	0.017	336.908	0.252	$11.03^{+0.28}_{-0.21}$	–	–	4.0	LMXB (BHC, D, T)	30,117,254

Table 12.2: continued.

Name	R.A.	Dec. (J2000)	Error (')	l	b (deg)	N_H (10^{22} cm^{-2})	Spin (s)	Orbit (d)	Distance (kpc or [z])	Type	Ref.
IGR J16351−5806	16 35 13.7	−58 04 48	0.017	329.128	−7.096	–	–	–	[0.009113(284)]	Sey-2	56
IGR J16358−4726	16 35 53.8	−47 25 41.1	0.01	337.099	−0.007	27.9±0.9	5871.3(3.5)	–	–	HMXB (P, T, LMXB?)	255,256
IGR J16377−6423	16 38 16.1	−64 20 50	0.017	324.604	−11.511	–	–	–	0.051	Cluster of Galaxies	257,258
IGR J16385−2057	16 38 30	−20 56 38	4.1	357.709	17.011	–	–	–	–	AGN	1
IGR J16393−4643	16 39 05.4	−46 42 12	0.067	338.002	0.075	25±2	911.3(1)	3.6875(6)	–	HMXB (SG, P)	259,260
H 1636−536	16 40 55.5	−53 45 05	0.017	332.915	−4.818	0.42±0.03	0.0017(1)	0.158048(2)	6.0(5)	LMXB (B, P, QPO, A)	103,117,261,262,263
IGR J16418−4532	16 41 51.0	−45 32 25	0.067	339.189	0.489	10.0±1.2	1246(100)	3.753(4)	–	HMXB (SG, P, E, SFXT?)	247,264
IGR J16426+6536	16 42 37	+65 35 38	4.5	96.716	37.678	–	–	–	–	Unclassified (T)	1
GX 340+0	16 45 47.7	−45 36 40	0.017	339.588	−0.079	3.9±0.4	–	–	11.0	LMXB (QPO, Z)	30,117,261
IGR J16460+0849	16 45 57	+08 49 05	5.2	26.297	31.853	–	–	–	–	Unclassified	1
IGR J16465−4507	16 46 35.5	−45 07 04	0.067	340.054	0.135	60±10	227(5)	–	12.5	HMXB (SG, P, T)	247,265
IGR J16479−4514	16 48 06.6	−45 12 08	0.067	340.163	−0.124	7.7±1.7	–	–	–	HMXB (SFXT?)	247
IGR J16482−3036	16 48 10	−30 35 35	1.1	351.432	9.231	$0.13^{+0.05}_{-0.13}$	–	–	[0.0313(6)]	Sey-1	126,127,152
IGR J16493−4348	16 49 26.92	−43 49 08.96	0.01	341.375	0.583	~10	–	–	–	Unclassified (HMXB?, LMXB?)	266,267
PSR J1649−4349	16 49 32	−43 50 08	0.62	341.372	0.561	–	0.8707116(1)	–	5.6	Radio P	268,269
IGR J16500−3307	16 50 01	−33 06 58	1.2	349.709	7.330	–	–	–	–	Unclassified	126
ESO 138−1	16 51 20.0	−59 14 02	0.017	329.609	−9.439	~150	–	–	0.009	Sey-2	16,56
NGC 6221	16 52 46.6	−59 12 59	0.017	329.740	−9.573	1.1±0.1	–	–	[0.00475(20)]	Sey-2	16,56
NGC 6240	16 52 58.97	+02 24 01.7	0.017	20.729	27.290	137±2	–	–	[0.024323(210)]	Sey-2	54,56,270
Mrk 501	16 53 52.22	+39 45 36.6	0.017	63.600	38.859	0.013±0.001	–	–	[0.033640(83)]	Blazar	56,62,271
GRO J1655−40	16 54 00.14	−39 50 44.9	0.002	344.982	2.456	$0.58^{+0.02}_{-0.01}$	–	2.621(7)	3.2(2)	LMXB (BHC, QPO, D, T)	103,117,125,272
IGR J16558−5203	16 56 05.618	−52 03 40.87	0.002	335.688	−5.492	~0.011	–	–	[0.054(1)]	Sey-1.2	86,127
SWIFT J1656.3−3302	16 56 16.56	−33 02 09.3	0.062	350.599	6.358	$0.390^{+0.17}_{-0.017}$	–	–	–	Unclassified (AGN?)	273
Her X−1	16 57 49.83	+35 20 32.6	0.017	58.149	37.523	$0.00019^{+0.00013}_{-0.00011}$	1.2377291(2)	1.70015(9)	6.6(4)	LMXB (P, E)	19,274,275,276,277
AX J1700.2−4220	17 00 18	−42 20.4	0.96	343.771	−0.027	$0.16^{+1.06}_{-0.16}$	–	–	–	HMXB (Be?)	278
OAO 1657−415	17 00 48.90	−41 39 21.6	0.008	344.369	0.319	12.0±0.4	37.348186(1)	10.44809(30)	7.1(1.3)	HMXB (SG, P, E)	279,280,281,282,283
IGR J17008−6425	17 00 49	−64 25 30	4.5	326.085	−13.473	–	–	–	–	Unclassified	1
XTE J1701−462	17 00 58.46	−46 11 08.6	0.002	340.813	−2.488	2.7±0.1	–	–	–	LMXB (QPO, T, Z)	284,285
GX 339−4	17 02 49.5	−48 47 23	0.017	338.939	−4.327	0.39±0.01	–	1.7563(3)	10^{+5}_{-4}	LMXB (BHC, QPO, T)	103,117,286,287
4U 1700−377	17 03 56.77	−37 50 38.9	0.017	347.754	2.173	12.7±0.3	–	3.4116(1)	1.9	HMXB (SG)	17,288,289,290
GX 349+2	17 05 44.5	−36 25 23	0.017	349.104	2.748	$0.673^{+0.048}_{-0.013}$	–	0.910(17)	9.2	LMXB (QPO, Z)	30,291,292,293
H 1702−429	17 06 15.31	−43 02 08.7	0.01	343.887	−1.318	~0.9	–	–	6.2(9)	LMXB (B, QPO, A)	125,240,294
H 1705−250	17 08 14.6	−25 05 29	0.034	358.587	9.057	~0.3	–	0.5213(13)	8.6(2)	LMXB (BHC, QPO, T)	117,125,295,296
IGR J17088−4008	17 08 49.0	−40 09 10	0.017	346.481	0.028	1.48±0.04	11.0017(4)	–	5	AXP	141,297
4U 1705−32	17 08 54.27	−32 19 57.1	0.01	352.780	4.672	0.40±0.10	–	–	13(2)	LMXB (B)	298

Table 12.2: continued.

Name	R.A.	Dec.	Error	l	b	N_H	Spin	Orbit	Distance	Type	Ref.
	(J2000)		(')		(deg)	(10^{22} cm^{-2})	(s)	(d)	(kpc or [z])		
H 1705−440	17 08 54.47	−44 06 07.4	0.008	343.321	−2.342	1.42±0.06	–	–	8.4(1.2)	LMXB (B, A)	125,299
IGR J17091−3624	17 09 07	−36 24 25	0.5	349.524	2.214	~5	–	–	0.8	LMXB (BHC, muQSO, T)	1,300,301
XTE J1709−267	17 09 30.4	−26 39 19.9	0.01	357.473	7.912	0.44±0.02	–	–	10	LMXB (B, T)	30,302
IGR J17098−3628	17 09 45.9	−36 27 57	0.083	349.554	2.075	~1	–	–	–	BHC (T)	303
XTE J1710−281	17 10 12.3	−28 07 54	0.017	356.357	6.922	–	–	0.137	17.3(2.5)	LMXB (B, T)	117,125,304
4U 1708−40	17 12 23.83	−40 50 34.0	0.01	346.329	−0.929	3.3±0.5	–	–	–	LMXB (B)	305
Oph Cluster	17 12 26	−23 21 47	0.6	0.575	9.279	$0.20^{+0.09}_{-0.07}$	–	–	0.028	Cluster of Galaxies	126,306,307
SAX J1712.6−3739	17 12 34	−37 38.6	0.1	348.935	0.928	~1	–	–	6.9(1)	LMXB (B, T)	117,125,308
V2400 Oph	17 12 36.45	−24 14 44.6	0.017	359.867	8.739	4.3±1.7	927	0.1425	0.5	CV (DQ Her)	9,309,310,311,312
XTE J1716−389	17 15 46	−38 50 06	1.1	348.336	−0.279	10±5	–	–	–	HMXB (SG)	126,313
NGC 6300	17 16 59.2	−62 49 11	0.017	328.492	−14.051	29±2	–	–	[0.003706(50)]	Sey-2	16,56,84
IGR J17195−4100	17 19 35.88	−41 00 53.6	0.01	346.979	−2.137	$0.08^{+0.13}_{-0.08}$	–	–	0.110	CV (IP)	86,228
XTE J1720−318	17 19 54	−31 44 56	0.5	354.615	3.117	1.24±0.02	–	–	10	LMXB (BHC, T)	126,314,315
IGR J17200−3116	17 20 05.913	−31 16 59.65	0.002	355.022	3.347	–	–	–	–	HMXB (T)	86
IGR J17204−3554	17 20 25	−35 54 00	0.8	351.267	0.658	12±1	–	–	–	AGN	126,316
IGR J17252−3616	17 25 11.4	−36 16 59	0.067	351.497	−0.354	$15.3^{+1.1}_{-1.0}$	414.8(5)	9.741(4)	–	HMXB (SG, P, E)	317,318
IGR J17254−3257	17 25 25.5	−32 57 18	0.233	354.280	1.472	–	–	–	–	LMXB (B)	217
IGR J17269−4737	17 26 49.30	−47 38 25.5	0.002	342.203	−6.923	0.47±0.01	–	–	–	Unclassified (T, BHC?)	319,320
4U 1722−30	17 27 33.2	−30 48 07	0.017	356.320	2.298	0.78±0.05	–	–	$9.5^{+2.5}_{-2.0}$	LMXB (B, A)	117,321
IGR J17285−2922	17 28 41	−29 22 55	1.2	357.639	2.881	–	–	–	–	Unclassified (T, BHC?)	126
IGR J17303−0601	17 30 21.5	−05 59 34	0.116	17.929	15.013	–	127.99991(5)	0.6426(1)	–	CV (IP)	217,322
IGR J17314−2854	17 31 25	−28 53 42	3.2	358.375	2.650	–	–	–	–	Unclassified (T)	1
3A 1728−169	17 31 44.2	−16 57 42	0.017	8.513	9.038	0.19±0.01	–	0.174727(3)	4.4	LMXB (A)	30,103,117,323
GX 354−0	17 31 57.4	−33 50 05	0.017	354.302	−0.150	2.66±0.07	0.0028(1)	–	5.3(8)	LMXB (P, B, QPO, A)	117,125,324,325
V2487 Oph	17 31 59.8	−19 13 56	0.017	6.604	7.775	~0.4	–	–	–	CV (N)	309,326
GX 1+4	17 32 02.16	−24 44 44.0	0.017	1.937	4.795	2.30±0.04	138.170(1)	1160.8(12.4)	4.5	LMXB (P)	30,327,328,329
QSO B1730−130	17 33 02.71	−13 04 49.5	0.017	12.032	10.811	–	–	–	[0.90200(23)]	QSO	56,62
IGR J17331−2406	17 33 13	−24 09 22	1.8	2.580	4.888	–	–	–	–	Unclassified (T)	1
4U 1730−335	17 33 24.1	−33 23 16	0.017	354.841	−0.158	1.5±0.3	–	–	$8.8^{+3.3}_{-2.4}$	LMXB (B, T)	117,321
IGR J17348−2045	17 34 48	−20 45 00	4.3	5.666	6.407	–	–	–	–	Unclassified (T)	1
IGR J17354−3255	17 35 21	−32 56 13	2.2	355.441	−0.256	–	–	–	–	Unclassified	1
IGR J17364−2711	17 36.5	−27 12	2	0.409	2.626	–	–	–	–	Unclassified (T)	330
GRS 1734−292	17 37 28.35	−29 08 02.5	0.002	358.891	1.407	$1.05^{+0.58}_{-0.64}$	–	–	[0.0214(5)]	Sey-1	331,332
IGR J17379−3747	17 37 54	−37 46 59	5.3	351.630	−3.298	–	–	–	–	Unclassified (T)	1
SLX 1735−269	17 38 17.12	−26 59 38.6	0.01	0.796	2.400	1.70±0.05	–	–	8.5	LMXB (B)	30,305

Table 12.2: continued.

Name	R.A. (J2000)	Dec. (J2000)	Error (')	l (deg)	b (deg)	N_H (10^{22} cm^{-2})	Spin (s)	Orbit (d)	Distance (kpc or [z])	Type	Ref.
4U 1735−444	17 38 58.3	−44 27 00	0.017	346.054	−6.994	0.34±0.02	–	0.1939(2)	9.4(1.4)	LMXB (B, A)	117,125,242,333
IGR J17391−3021	17 39 11.58	−30 20 37.6	0.002	358.068	0.445	3.2±0.3	–	–	$2.3^{+0.6}_{-0.5}$	HMXB (SG, SFXT)	334,335,336
AX J1739.3−2923	17 39 19	−29 23.9	0.96	358.882	0.926	$1.8^{+6.0}_{-0.1}$	–	–	–	Unclassified	335
XTE J1739−285	17 39 53.95	−28 29 46.8	0.002	359.714	1.298	–	–	–	12	LMXB (B, NS, T)	284,337
IGR J17404−3655	17 40 27	−36 54 47	3.5	352.638	−3.266	–	–	–	–	Unclassified	1
SLX 1737−282	17 40 39	−28 17 48	0.35	359.971	1.264	2.0±0.1	–	–	6.5(1.5)	LMXB (B, T)	268,335,338
IGR J17407−2808	17 40 41.2	−28 08 50	0.266	0.102	1.336	–	–	–	–	Unclassified (T, SFXT?)	339
IGR J17418−1212	17 41 51	−12 11 46	1.1	13.926	9.425	~0.1	–	–	[0.0372(1)]	Sey-1	22,126,340
IGR J17419−2802	17 41 56.0	−28 01 54.5	0.058	0.345	1.164	1.4±0.3	–	–	–	Unclassified (T)	341,342
IGR J17426−0258	17 42 35	−02 57 47	4.3	22.202	13.854	–	–	–	–	Unclassified (T)	1
XTE J1743−363	17 43 00.0	−36 20 41	0.017	353.392	−3.402	–	–	–	–	Unclassified (T)	343
1E 1740.7−2942	17 43 54.83	−29 44 42.6	0.002	359.116	−0.106	$11.8^{+2.3}_{-1.9}$	–	12.73(5)	8.5	LMXB (BHC, T)	344,345,346,347
IGR J17445−2747	17 44 32	−27 46 59	1.5	0.859	0.806	–	–	–	–	Unclassified (T)	126
IGR J17448−3232	17 44 55	−32 33 00	2.2	356.837	−1.755	–	–	–	–	Unclassified	1
KS 1741−293	17 44 56	−29 21 07	0.6	359.567	−0.089	20.3±1.7	–	–	–	LMXB (B, T)	117,335
IGR J17456−2901	17 45 40.04	−29 00 28.1	0.017	359.944	−0.046	$7.81^{+0.02}_{-0.04}$	–	–	8.5	BHC	348,349
1A 1742−294	17 46 05.5	−29 30 55	0.017	359.559	−0.389	6.6±0.1	–	–	$8.1^{+1.1}_{-1.2}$	LMXB (B, T)	125,278,339
IGR J17461−2853	17 46 06	−28 52 55	0.6	0.101	−0.061	–	–	–	–	Unclassified (Mol. Cloud?)	1
IGR J17461−2204	17 46 08	−22 03 32	3.7	5.939	3.475	–	–	–	–	Unclassified	1
IGR J17464−3213	17 46 16	−32 13 59	0.2	357.256	−1.834	~2.3	–	–	10.4(2.9)	LMXB (BHC, QPO, T, muQSO?)	1,350,351
1E 1743.1−2843	17 46 21.0	−28 43 44	0.025	0.260	−0.029	20.2±0.4	–	–	8	LMXB	352
1RXS J174607.8−213333	17 46.4	−21 33	0.2	6.408	3.685	–	–	–	–	Unclassified (T)	353
1A 1743−288	17 47 02.60	−28 52 58.9	0.002	0.207	−0.238	7.2±1.6	–	–	7.5(1.3)	LMXB (B, T)	354,355,356
IGR J17472+0701	17 47 11	+07 01 05	5.3	31.942	17.466	–	–	–	–	Unclassified	1
IGR J17475−2822	17 47 17	−28 26 42	0.7	0.609	−0.057	8±2	–	–	8.5	Mol. Cloud	126,357
IGR J17473−2721	17 47 18.06	−27 20 38.9	0.013	1.553	0.510	5.2±0.4	–	–	–	Unclassified (T)	358,359
SLX 1744−299	17 47 26	−30 01 14	0.17	359.278	−0.900	4.3±0.1	–	–	–	LMXB (B)	268,335
IGR J17476−2253	17 47 37	−22 53 13	1.8	5.407	2.754	–	–	–	–	Unclassified (AGN?, QSO?)	1
GX 3+1	17 47 56.0	−26 33 49	0.05	2.294	0.794	$1.59^{+0.07}_{-0.12}$	–	–	$5.0^{+0.8}_{-0.7}$	LMXB (B, QPO, A)	117,360
1A 1744−361	17 48 19.22	−36 07 16.6	0.017	354.140	−4.204	~0.79	0.002	0.0067(15)	9	LMXB (P, B, QPO, D, T)	361,362
IGR J17487−3124	17 48 41	−31 22 55	3	358.251	−1.833	–	–	–	–	Unclassified	1
H 1745−203	17 48 53.5	−20 22 02	1	7.724	3.795	0.47±0.07	–	–	$8.4^{+1.5}_{-1.3}$	LMXB (T)	117,321
IGR J17488−3253	17 48 55.129	−32 54 52.15	0.002	356.961	−2.664	$0.22^{+0.07}_{-0.05}$	–	–	[0.020(1)]	Sey-1	86,127
AX J1749.1−2733	17 49 09	−27 33.2	0.96	1.586	0.051	25^{+57}_{-21}	–	–	–	Unclassified (T, HMXB?, SFXT?)	335
AX J1749.2−2725	17 49 10.1	−27 25 16	1	1.701	0.116	$15.4^{+9.6}_{-4.5}$	220.38(20)	–	–	HMXB (P, T)	24,335,363

Table 12.2: continued.

Name	R.A.	Dec.	Error	l	b	N_H	Spin	Orbit	Distance	Type	Ref.
	(J2000)		(')	(deg)		(10^{22} cm^{-2})	(s)	(d)	(kpc or [z])		
IGR J17497−2821	17 49 38.04	−28 21 17.4	0.017	0.953	−0.453	4.2±0.1	–	–	–	LMXB (BHC, T)	364
SLX 1746−331	17 49 50.6	−33 11 55	0.583	356.816	−2.976	~0.4	–	–	–	LMXB (BHC, T)	117,305
1H 1746−370	17 50 12.7	−37 03 08	0.017	353.531	−5.005	$0.20^{+0.25}_{-0.06}$	–	0.215137(7)	$11.0^{+0.9}_{-0.8}$	LMXB (B, A)	103,117,321,365
IGR J17507−2647	17 50 42	−26 47 31	2.6	2.416	0.146	–	–	–	–	Unclassified	1
IGR J17507−2856	17 50 43	−28 56 28	2.2	0.572	−0.957	–	–	–	–	Unclassified (T)	1
GRS 1747−312	17 50 45.5	−31 17 32	0.017	358.555	−2.168	1.39±0.08	–	0.5149803(1)	$9.5^{+3.3}_{-2.5}$	LMXB (T)	117,321,365,366
IGR J17513−2011	17 51 13.623	−20 12 14.58	0.002	8.145	3.407	–	–	–	[0.047(1)]	Sey-1.9	86
1RXS J175113.3−201214	17 51 25	−20 12 07	0.77	8.169	3.370	–	–	–	–	Unclassified (T)	268
IGR J17515−1533	17 51 32	−15 32 38	4.8	12.214	5.704	–	–	–	–	Unclassified (T)	1
SWIFT J1753.5−0127	17 53 28.26	−01 27 06.1	0.008	24.898	12.186	0.20±0.04	–	–	–	LMXB (BHC, QPO, T)	367,368
IGR J17536−2339	17 53.6	−23 39	4	5.454	1.183	–	–	–	–	Unclassified (T, SFXT?)	369
IGR J17541−2252	17 54.1	−22 52	4	6.188	1.481	–	–	–	–	Unclassified (T, SFXT?)	369
IGR J17544−2619	17 54 25.28	−26 19 52.6	0.01	3.236	−0.336	1.8±0.3	–	–	3.2(1.0)	HMXB (SG, SFXT)	247,370,371
IGR J17586−2129	17 58 38	−21 19 37	3.3	8.047	1.346	–	–	–	–	Unclassified	1
IGR J17597−2201	17 59 45.7	−22 01 39	0.067	7.570	0.770	4.5±0.7	–	–	7.5(2.5)	LMXB (B, D)	247,372
GX 5−1	18 01 08.2	−25 04 45	0.05	5.077	−1.019	2.2±0.2	–	–	7.2	LMXB (Z)	30,117,261
GRS 1758−258	18 01 12.7	−25 44 26	0.017	4.511	−1.361	$1.81^{+0.08}_{-0.05}$	–	18.45(1)	8.5	LMXB (BHC)	30,117,346,373
GX 9+1	18 01 32.3	−20 31 44	0.05	9.077	1.154	0.8±0.1	–	–	4.4(1.3)	LMXB (A)	117,374
IGR J18027−2016	18 02 42.0	−20 17 18	0.067	9.420	1.036	9.1±0.5	139.61(4)	4.5696(9)	–	HMXB (SG, P)	247,375
IGR J18027−1455	18 02 47.375	−14 54 54.78	0.001	14.114	3.659	~19	–	–	[0.034(1)]	Sey-1	166,376
IGR J18048−1455	18 04 38.96	−14 56 47.3	0.01	14.307	3.252	–	–	–	–	HMXB	73
XTE J1807−294	18 06 59.8	−29 24 30	0.017	1.935	−4.273	$0.56^{+0.02}_{-0.01}$	0.0052459(1)	0.0278292(3)	5.5(2.5)	LMXB (P, QPO, T)	377,378
SGR 1806−20	18 08 39.32	−20 24 39.5	0.008	9.996	−0.242	6.6±0.2	7.5604(8)	–	$15.1^{+1.8}_{-1.3}$	SGR (P)	379,380,381,382
PSR J1811−1926	18 11 29.22	−19 25 27.6	0.01	11.181	−0.348	$2.22^{+0.78}_{-0.57}$	0.0646732(1)	–	5	SNR (PWN)	383,384,385,386
IGR J18134−1636	18 13 24	−16 35 53	3.8	13.879	0.610	–	–	–	–	Unclassified	1
IGR J18135−1751	18 13 27	−17 50 56	1.1	12.787	0.001	$5.15^{+1.70}_{-1.24}$	–	–	4	SNR (PWN?)	126,387,388
GX 13+1	18 14 31.55	−17 09 26.7	0.017	13.517	0.106	3.2±0.2	–	24.065(18)	7(1)	LMXB (B, QPO, A)	93,389,390,391
4U 1812−12	18 15 06.18	−12 05 47.1	0.01	18.033	2.398	1.1±0.2	–	–	4.0(6)	LMXB (B)	125,305
IGR J18159−3353	18 15.9	−33 53	4	358.865	−8.054	–	–	–	–	Unclassified (T, SFXT?)	392
GX 17+2	18 16 01.4	−14 02 11	0.017	16.432	1.278	$2.00^{+0.05}_{-0.03}$	–	–	$14.0^{+2.0}_{-2.1}$	LMXB (B, QPO, Z)	117,125,393
IGR J18173−2509	18 17 19	−25 09 04	2.2	6.784	−4.261	–	–	–	–	Unclassified	1
XTE J1817−330	18 17 43.53	−33 01 07.5	0.004	359.817	−7.996	$0.092^{+0.005}_{-0.004}$	–	–	2.5(1.5)	BHC (QPO, T)	394,395,396
XTE J1818−245	18 18 24.8	−24 32 15	0.116	7.444	−4.192	–	–	–	–	BHC (T)	397
SAX J1818.6−1703	18 18 37.89	−17 02 47.9	0.01	14.080	−0.704	6.0±0.7	–	–	–	HMXB (SG, SFXT)	398
IGR J18193−2542	18 19 17	−25 42 11	1.5	6.503	−4.912	–	–	–	–	Unclassified (T)	126

Table 12.2: continued.

Name	R.A.	Dec.	Error	l	b	N_H	Spin	Orbit	Distance	Type	Ref.
	(J2000)		(’)	(deg)		$(10^{22}\ \mathrm{cm}^{-2})$	(s)	(d)	(kpc or [z])		
AX J1820.5−1434	18 20 29.5	−14 34 24	0.5	16.472	0.070	9.8±1.7	152.26(4)	–	8.2(3.5)	HMXB (Be, P, T)	24,399
IGR J18214−1318	18 21 22	−13 18 29	0.9	17.688	0.479	–	–	–	–	Unclassified (T)	126
1RXS J182129.0−131641	18 21 29.0	−13 16 41	0.433	17.728	0.468	–	–	–	–	Unclassified (T)	400
H 1820−303	18 23 40.48	−30 21 40.1	0.001	2.788	−7.913	0.160±0.003	–	0.0079284(1)	7.6(4)	LMXB (B, A)	103,321,401
IGR J18244−5622	18 24 15	−56 21 47	5	338.441	−18.741	12±2	–	–	[0.017(1)]	Sey-2	1,86,402
IGR J18246−1425	18 24 39	−14 25 05	4.4	17.081	−0.746	–	–	–	–	Unclassified (T)	1
IGR J18249−3243	18 24 56.66	−32 42 59.8	0.002	0.782	−9.212	–	–	–	–	AGN	403
H 1822−000	18 25 22.02	−00 00 43.0	0.01	29.939	5.793	0.97±0.18	–	–	3.6	LMXB	30,404
IGR J18256−1035	18 25 37	−10 35 13	1.5	20.579	0.835	–	–	–	–	Unclassified	126
3A 1822−371	18 25 46.8	−37 06 19	0.017	356.850	−11.291	$0.123^{+0.016}_{-0.014}$	0.5931(1)	0.23	2.5(5)	LMXB (P, D)	117,405,406,407,408
IGR J18259−0706	18 25 56	−07 06 22	2	23.697	2.388	–	–	–	–	Unclassified (T, AGN?)	126
1RXS J182557.5−071021	18 25 57.5	−07 10 21	0.184	23.641	2.352	–	–	–	–	Unclassified (T)	141
RX J1826.2−1450	18 26 15.034	−14 50 53.59	0.002	16.882	−1.289	$0.72^{+0.03}_{-0.05}$	–	3.90603(17)	2.5(1)	HMXB (SG, muQSO)	409,410,411
Ginga 1826−24	18 29 28.2	−23 47 29	0.034	9.277	−6.085	$0.429^{+0.021}_{-0.019}$	–	0.088	7.5(5)	LMXB (BHC, B)	291,412,413,414
AX J1830.6−1002	18 30 39	−10 02.7	0.96	21.634	−0.009	$3.07^{+3.42}_{-2.60}$	–	–	–	Unclassified	278
IGR J18308−1232	18 30 47	−12 31 55	3.3	19.445	−1.189	–	–	–	–	Unclassified	1
IGR J18325−0756	18 32 28	−07 56 24	0.7	23.708	0.567	–	–	–	–	Unclassified (T)	126
SNR 021.5−00.9	18 33 35	−10 33 29	0.7	21.513	−0.886	2.1±0.1	0.0618657(1)	–	4.7(4)	SNR (PWN)	126,415,416
PKS 1830−211	18 33 39.89	−21 03 39.8	0.002	12.166	−5.712	$1.94^{+0.28}_{-0.25}$	–	–	2.507	Blazar	122,417,418
3C 382	18 35 03.390	+32 41 46.86	0.002	61.305	17.446	~0.88	–	–	[0.058137(577)]	Sey-1	56,70,419
XB 1832−330	18 35 44.0	−32 58 55	0.017	1.540	−11.368	0.85±0.15	–	0.0303(4)	9.6(4)	LMXB (B, T)	117,420,421
AX J1838.0−0655	18 38 02	−06 54 14	0.8	25.263	−0.181	6.7±1.3	–	–	–	SNR (PWN?)	126,422
ESO 103−35	18 38 20.3	−65 25 41	0.017	329.778	−23.175	$18.8^{+2.16}_{-1.12}$	–	–	[0.01325(18)]	Sey-2	56,84,332
Ser X−1	18 39 57.5	+05 02 09	0.017	36.118	4.842	0.50±0.03	–	–	11.1(1.6)	LMXB (B)	117,125,360
PSR J1840+13	18 40 09	+13 31 58	0.1	43.800	8.586	–	0.472331(1)	–	3.4	Radio P	423
IGR J18406−0539	18 40.6	−05 39	3	26.670	−0.173	–	–	–	1.1	HMXB (Be, muQSO?)	424
IGR J18410−0535	18 41 00.54	−05 35 46.8	0.01	26.764	−0.239	6.1±1.0	4.7394(8)	–	–	HMXB (Be, P, SFXT)	425,426
PSR B1841−04	18 41 19.34	−04 56 11.2	0.005	27.387	−0.007	$2.54^{+0.15}_{-0.13}$	11.766684(5)	–	$6.8^{+0.7}_{-0.8}$	AXP	427,428,429,430
AX J1841.3−0455	18 41 19.34	−04 56 11.2	0.015	27.387	−0.007	$2.54^{+0.15}_{-0.13}$	11.766684(6)	–	6.75(75)	AXP	427,428,429,430
3C 390.3	18 42 08.990	+79 46 17.13	0.017	111.438	27.074	1.3±0.2	–	–	[0.056159(464)]	Sey-1	56,62,134
IGR J18450−0435	18 45 01.9	−04 33 58	0.07	28.139	−0.659	2.3±0.7	–	–	3.6	HMXB (SG, SFXT)	431,432
Ginga 1843+009	18 45 37	+00 51 54	0.6	33.038	1.690	2.30±0.13	29.477(1)	–	12.5(2.5)	HMXB (Be, P, T)	1,433,434
PSR J1846−0258	18 46 24.5	−02 58 28	0.017	29.712	−0.238	3.96±0.08	0.3248636(1)	–	19	SNR (PWN)	435,436,437,438
IGR J18483−0311	18 48 15	−03 10 08	0.7	29.748	−0.736	–	–	18.55(3)	–	Unclassified (T)	103,126
3A 1845−024	18 48 17.7	−02 25 13	0.017	30.420	−0.405	25±10	94.8	242.18(1)	10.0	HMXB (Be, P, T)	24,30,103,439

Table 12.2: continued.

Name	R.A.	Dec.	Error	l	b	N_H	Spin	Orbit	Distance	Type	Ref.
	(J2000)		(')	(deg)		(10^{22} cm^{-2})	(s)	(d)	(kpc or [z])		
IGR J18485−0047	18 48 28	−00 46 44	3.4	31.900	0.306	–	–	–	–	Unclassified	1
IGR J18490−0000	18 49 04	−00 01 30	1.4	32.639	0.516	–	–	–	–	Unclassified	126
3A 1850−087	18 53 04.86	−08 42 20.4	0.01	25.355	−4.320	0.42±0.04	–	0.01417	8.2(6)	LMXB (B)	321,404
IGR J18539+0727	18 53 54	+07 27 29	0.9	39.854	2.849	1.5±0.4	–	–	–	BHC (T)	126,440
V1223 Sgr	18 55 02.24	−31 09 48.5	0.017	4.958	−14.355	3.7±0.1	745.506	0.140244	$0.527^{+0.054}_{-0.043}$	CV (DQ Her)	6,311,312,441
XTE J1855−026	18 55 31.3	−02 36 24	0.017	31.076	−2.096	14.7±0.6	360.741(2)	6.0752(8)	10	HMXB (SG, P, T)	19,30,442,443
IGR J18559+1535	18 56 00.0	+15 38 13	0.017	47.411	6.076	~0.1	–	–	[0.0838(2)]	Sey-1	22,444,445
XTE J1858+034	18 58 43	+03 26 20	0.3	36.822	−0.049	~6	221.0(5)	–	–	HMXB (Be, P, QPO, T)	1,446,447
HETE J1900.1−2455	19 00 09.77	−24 54 04.3	0.002	11.325	−12.869	0.16±0.04	0.0027(1)	0.0578155(1)	5	LMXB (P, B, T)	448,449,450,451
XTE J1901+014	19 01 41.0	+01 26 18	0.017	35.381	−1.623	–	–	–	–	Unclassified (T, BHC?)	217
4U 1901+03	19 03 37.1	+03 11 31	0.017	37.162	−1.250	–	2.7626530(1)	22.5827(2)	–	HMXB (Be, P, T)	452,453
IGR J19048−1240	19 04 49	−12 39 40	4.2	23.082	−8.662	–	–	–	–	Unclassified (T)	1
SGR 1900+14	19 07 14.33	+09 19 20.1	0.002	43.021	0.766	$2.6^{+0.9}_{-0.7}$	5.18019(2)	–	13.5(1.5)	SGR (P)	454,455,456
XTE J1908+094	19 08 53.08	+09 23 04.9	0.004	43.263	0.434	2.50±0.16	–	–	2(1)	LMXB (BHC, QPO, T)	457,458,459
H 1907+097	19 09 37.9	+09 49 49	0.017	43.744	0.476	2.81±0.04	441.0932(3)	8.3753(1)	5	HMXB (SG, P, T)	24,460,461,462,463
AX J1910.7+0917	19 10 47	+09 17.1	0.96	43.391	−0.028	$2.63^{+1.37}_{-1.03}$	–	–	–	Unclassified	278
4U 1909+07	19 10 48	+07 35 46	0.4	41.895	−0.812	24.3±0.2	604.684(1)	4.4005(4)	7(3)	HMXB (SG, P)	1,19,464,465
Aql X−1	19 11 16.0	+00 35 06	0.017	35.718	−4.143	0.36±0.02	–	0.7904(8)	$5.2^{+0.7}_{-0.8}$	LMXB (B, T, A)	117,125,466,467
SS 433	19 11 49.56	+04 58 57.6	0.002	39.694	−2.245	0.907±0.002	–	13.075(17)	5.5(2)	HMXB (SG, BHC, muQSO)	103,403,468,469
IGR J19140+0951	19 14 04.23	+09 52 58.3	0.01	44.296	−0.469	10±3	–	13.558(4)	–	HMXB (SG)	470,471
GRS 1915+105	19 15 11.6	+10 56 44	0.017	45.366	−0.219	1.98±0.02	–	33.5(1.5)	11^{+1}_{-4}	LMXB (BHC, QPO, T)	125,291,472,473
4U 1916−053	19 18 47.78	−05 14 11.2	0.017	31.359	−8.463	0.69±0.02	–	0.0347297(1)	8.8(1.3)	LMXB (B, D)	19,93,125,474
SWIFT J1922.7−1716	19 22 37.0	−17 17 03	0.053	20.683	−14.521	0.15±0.02	–	–	8(3)	Unclassified (T, NS LMXB?, BHC?)	139,475
1RXS J192450.8−291437	19 24 51.056	−29 14 30.12	0.002	9.344	−19.607	0.088±0.006	–	–	[0.352000(33)]	BL Lac	56,62,476
IGR J19267+1325	19 26 41	+13 25 30	3.7	48.874	−1.532	–	–	–	–	Unclassified	1
IGR J19284+0107	19 28 24	+01 07 08	1.3	38.177	−7.700	–	–	–	–	Unclassified (T)	126
IGR J19308+0530	19 30 46	+05 30 07	1.4	42.359	−6.175	–	–	–	–	Unclassified (T)	126
1H 1934−063	19 37 33.1	−06 13 05	0.017	32.591	−13.074	~0.1	–	–	0.01059	Sey-1	22,477,478
IGR J19378−0617	19 37 39	−06 13 05	4.4	32.602	−13.096	–	–	–	–	Sey-1	1
RX J1940.2−1025	19 40 11.47	−10 25 25.1	0.002	28.984	−15.503	8±2	12146.5(3)	0.140235(5)	0.230	CV (AM Her)	6,9,479,480
IGR J19405−3016	19 40 29	−30 15 58	5.4	9.549	−23.146	–	–	–	–	AGN	1
NGC 6814	19 42 40.4	−10 19 24	0.017	29.351	−16.011	~0.05	–	–	0.00520	Sey-1.5	16,56,166
IGR J19443+2117	19 44 17	+21 17 13	4.9	57.787	−1.374	–	–	–	–	Unclassified	1
IGR J19473+4452	19 47 19.37	+44 49 42.4	0.01	78.642	9.734	11±1	–	–	[0.0532(2)]	Sey-2	85,445
IGR J19487+5120	19 48 44	+51 20 10	4.4	84.593	12.620	–	–	–	–	Unclassified (T)	1

Table 12.2: continued.

Name	R.A. (J2000)	Dec. (J2000)	Error (')	l (deg)	b (deg)	N_H (10^{22} cm^{-2})	Spin (s)	Orbit (d)	Distance (kpc or [z])	Type	Ref.
KS 1947+300	19 49 35.6	+30 12 31	0.017	66.099	2.083	0.43±0.03	18.70969(5)	40.415(10)	9.5(1.1)	HMXB (Be, P, T)	24,481,482,483
3C 403	19 52 14.80	+02 30 28.0	0.017	42.262	−12.310	45^{+7}_{-6}	–	–	0.059	Sey-2	403,484,485
3A 1954+319	19 55 42.272	+32 05 48.82	0.011	68.392	1.927	28±2	18300(200)	–	1.7	LMXB (P, Symb, T)	486,487
Cyg X−1	19 58 21.68	+35 12 05.8	0.017	71.335	3.067	0.621±0.022	–	5.6008(7)	2.10(25)	HMXB (SG, BHC, muQSO)	17,19,488,489
QSO B1957+405	19 59 28.36	+40 44 01.9	0.002	76.190	5.755	38±8	–	–	[0.05615(16)]	Sey-2	16,56,66
IGR J20006+3210	20 00 21.9	+32 11 23	0.017	68.986	1.134	–	–	–	–	HMXB (T)	73
SWIFT J2000.6+3210	20 00 21.9	+32 11 22	0.06	68.986	1.134	$1^{+2.2}_{-0.7}$	–	–	–	HMXB (Be)	139
ESO 399−20	20 06 57.2	−34 32 54	0.017	6.749	−29.721	$0.048^{+0.044}_{-0.036}$	–	–	0.024951	Sey-1 (NL)	84,490,491
IGR J20187+4041	20 18 38.55	+40 41 00.4	0.07	78.114	2.671	$6.1^{+3.2}_{-2.2}$	–	–	–	AGN (Blazar?)	492
IGR J20188+3647	20 18.8	+36 48	3.4	74.920	0.460	–	–	–	–	Unclassified (T, SFXT?)	392
IGR J20286+2544	20 28 35.1	+25 44 01	0.017	67.005	−7.572	$42.3^{+19.5}_{-28.5}$	–	–	0.013	Sey-2	3,56,127
EXO 2030+375	20 32 15.2	+37 38 15	0.034	77.152	−1.242	2.6±0.3	41.691798(16)	46.0214(5)	7.1(2)	HMXB (Be, P, T)	221,493,494,495
Cyg X−3	20 32 25.78	+40 57 27.9	0.017	79.845	0.700	8.5±0.1	–	0.1996907(7)	9.0	HMXB (SG, BHC, muQSO)	19,30,496,497
4C 74.26	20 42 37.180	+75 08 02.52	0.002	108.998	19.527	0.189±0.005	–	–	[0.103999(23)]	QSO	56,498,499
SAX J2103.5+4545	21 03 35.71	+45 45 05.5	0.002	87.130	−0.685	3.8±0.1	355(3)	12.673(4)	3.2(8)	HMXB (Be, P, T)	19,500,501,502
IGR J21117+3427	21 11.8	+34 28	3.5	79.788	−9.425	–	–	–	–	Unclassified (T, SFXT?)	392
S5 2116+81	21 14 00.50	+82 04 47.1	0.058	115.978	22.344	0.098±0.021	–	–	0.084	Sey-1	271,503
IGR J21178+5139	21 17.8	+51 39	3	93.039	1.629	–	–	–	–	AGN	16
V2069 Cyg	21 23 44.83	+42 18 02.2	0.017	87.122	−5.686	–	–	0.311683(2)	1.65	CV (IP)	6,9,504
IGR J21247+5058	21 24 41	+50 58 19	1	93.321	0.389	~0.1	–	–	0.020	Sey-1	1,16,22
IGR J21272+4241	21 27 10	+42 41 31	5.5	87.850	−5.848	–	–	–	–	Unclassified	1
IGR J21277+5656	21 27 44.95	+56 56 39.7	0.017	97.803	4.368	~0.1	–	–	[0.0144(2)]	Sey-1	22,93,445
SWIFT J2127.4+5654	21 27 45.4	+56 56 35	0.056	97.802	4.367	$1^{+2.2}_{-0.7}$	–	–	0.0147	Sey-1 (NL)	139,505
IGR J21335+5105	21 33 30	+51 05 31	1.2	94.410	−0.476	–	570.823(13)	0.2997(7)	1.4	CV (IP)	9,126,506
IGR J21347+4737	21 34 42	+47 37 12	4.5	92.207	−3.169	–	–	–	–	Unclassified	1
RX J2135.9+4728	21 35 54.38	+47 28 28.3	0.313	92.260	−3.413	–	–	–	–	Sey-1	507
SS Cyg	21 42 42.80	+43 35 09.9	0.002	90.559	−7.111	~0.050	–	0.2751	$0.166^{+0.014}_{-0.012}$	CV (DN)	9,147,508,509
Cyg X−2	21 44 41.2	+38 19 18	0.017	87.328	−11.316	0.19±0.05	–	9.8444(3)	$13.4^{+1.9}_{-2.0}$	LMXB (B, Z)	117,125,510,511
NGC 7172	22 02 01.70	−31 52 18.0	0.017	15.126	−53.065	$10.18^{+0.80}_{-0.78}$	–	–	[0.008616(47)]	Sey-2	56,512,513
BL Lac	22 02 43.29	+42 16 40.0	0.017	92.590	−10.441	0.30±0.03	–	–	0.0688	BL Lac	62,485,514
3A 2206+543	22 07 56.24	+54 31 06.4	0.002	100.603	−1.106	$0.88^{+0.21}_{-0.19}$	–	9.5591(7)	2.6	HMXB (Be)	515,516,517,518
FO Aqr	22 17 55.43	−08 21 04.6	0.017	53.000	−49.158	32±4	1254.451(1)	0.2020596(1)	0.575(36)	CV (IP)	6,311,312,519,520
IGR J22234−4116	22 23 24	−41 15 43	5.3	358.238	−56.610	–	–	–	–	Unclassified	1
IGR J22292+6647	22 29 11	+66 47 17	4.8	109.558	7.685	–	–	–	–	Radio Galaxy	1

Table 12.2: continued.

Name	R.A. (J2000)	Dec. (J2000)	Error (')	l (deg)	b (deg)	N_H (10^{22} cm^{-2})	Spin (s)	Orbit (d)	Distance (kpc or [z])	Type	Ref.
NGC 7314	22 35 46.06	−26 03 01.7	0.017	27.135	−59.742	$0.122^{+0.009}_{-0.014}$	–	–	[0.004790(117)]	Sey-1.9	40,56,149
Mrk 915	22 36 46.50	−12 32 42.6	0.017	51.058	−55.294	–	–	–	[0.024043(130)]	Sey-1	56,173
3C 454.3	22 53 57.75	+16 08 53.6	0.017	86.111	−38.184	$0.5^{+0.5}_{-0.4}$	–	–	[0.85900(17)]	Blazar	56,62,134
1H 2251−179	22 54 05.88	−17 34 55.3	0.002	46.197	−61.326	$0.237^{+0.028}_{-0.015}$	–	–	0.06398	Sey-1	122,166,521
NGC 7469	23 03 15.75	+08 52 25.9	0.017	83.099	−45.467	0.061±0.002	–	–	0.01639	Sey-1.2	54,55,522
MCG−02−58−022	23 04 43.48	−08 41 08.6	0.017	64.092	−58.758	$0.034^{+0.012}_{-0.001}$	–	–	[0.047156(300)]	Sey-1.5	56,122,523
IGR J23130+8608	23 13 03	+86 07 59	4.8	121.177	23.601	–	–	–	–	Unclassified	1
NGC 7603	23 18 56.61	+00 14 36.5	0.017	80.067	−54.740	0.045±0.006	–	–	[0.029297(237)]	Sey-1.5	54,55,56
Cas A	23 23 27.94	+58 48 42.4	0.01	111.742	−2.135	1.25±0.03	–	–	$3.4^{+0.3}_{-0.1}$	SNR	524,525
IGR J23308+7120	23 30 47	+71 20 10	4.5	116.511	9.477	–	–	–	–	Unclassified (AGN?)	1
IGR J23524+5842	23 52 27	+58 42 00	4	115.320	−3.297	–	–	–	–	Unclassified	1

Name: One commonly used name for the source
R.A.: Right Ascension (J2000) in *hh mm ss.ss*
Dec.: Declination in *dd mm ss.ss*
Error: Error radius in arcminutes
l: Galactic longitude in degrees
b: Galactic latitude in degrees
N_H: Column density in 10^{22} cm^{-2}
Spin: Spin period in seconds
Orbit: Orbital period in days
Distance: Distance in kpc for galactic sources (including LMC/SMC), or redshift for extragalactic sources (in brackets)
Type: A (atoll), AGN (active galactic nucleus), AXP (anomalous X-ray pulsar), B (burster), Be (Be star), BHC (black hole candidate), CV (cataclysmic variable), E (eclipsing), D (dipping), DN (dwarf nova), F (flaring), GRS (gamma-ray source), HMXB (high-mass X-ray binary), IP (intermediate polar), LMXB (low-mass X-ray binary), Mol. Cloud (molecular cloud), muQSO (micro-quasar), N (nova), P (pulsar), PWN (pulsar wind nebula), QPO (quasi-periodic oscillations), QSO (quasar), RP (radio pulsar), Sey (Seyfert galaxy), SFXT (supergiant fast X-ray transient), SG (OB supergiant), SGR (soft gamma repeater), SNR (supernova remnant), Symb (symbiotic star), T (transient), Z (Z-track)
References: References for the listed parameters

[1] Bird A.J., Malizia A., Bazzano A., et al., 2007, ApJS, 170, 175

[2] Bikmaev I.F., Revnivtsev M.G., Burenin R.A., & Sunyaev R.A., 2006, AstL, 32, 588

[3] Masetti N., Bassani L., Bazzano A., et al., 2006, A&A, 455, 11

[4] Ruiz-Lapuente P., 2004, ApJ, 612, 357

[5] Kuiper L., Hartog P.R.D., & Hermsen W., 2006, ATel, 939, 1

[6] Downes R., Webbink R.F., & Shara M.M., 1997, PASP, 109, 345

[7] de Martino D., Matt G., Mukai K., et al., 2001, A&A, 377, 499

[8] Bonnet-Bidaud J.M., Mouchet M., de Martino D., et al., 2001, A&A, 374, 1003

[9] Barlow E.J., Knigge C., Bird A.J., et al., 2006, MNRAS, 372, 224

[10] Nowak M.A., Paizis A., Wilms J., et al., 2004, ATel, 369, 1

[11] Paizis A., Nowak M.A., Wilms J., et al., 2005, A&A, 444, 357

[12] Burderi L., di Salvo T., Riggio A., et al., 2006, ChJAS, 6, 192

[13] Galloway D.K., Markwardt C.B., Morgan E.H., et al., 2005, ApJL, 622, L45

[14] Falanga M., Kuiper L., Poutanen J., et al., 2005, A&A, 444, 15

[15] Laurent-Muehleisen S.A., Kollgaard R.I., Ryan P.J., et al., 1997, A&AS, 122, 235

[16] Bassani L., Molina M., Malizia A., et al., 2006, ApJL, 636, L65

[17] Perryman M.A.C., Lindegren L., Kovalevsky J., et al., 1997, A&A, 323, L49

[18] den Hartog P.R., Hermsen W., Kuiper L., et al., 2006, A&A, 451, 587

[19] Wen L., Levine A.M., Corbet R.H.D., & Bradt H.V., 2006, ApJS, 163, 372

[20] Negueruela I. & Reig P., 2004, ATel, 285, 1

[21] Snellen I.A.G., McMahon R.G., Hook I.M., & Browne I.W.A., 2002, MNRAS, 329, 700

[22] Sazonov S., Revnivtsev M., Krivonos R., et al., 2007, A&A, 462, 57

[23] Yu P.-C. & Hwang C.-Y., 2005, ApJ, 631, 720

[24] Liu Q.Z., van Paradijs J., & van den Heuvel E.P.J., 2000, A&AS, 147, 25

[25] Buckley D.A.H., Coe M.J., Stevens J.B., et al., 2001, MNRAS, 320, 281

[26] Corbet R., Marshall F.E., Lochner J.C., et al., 1998, IAU Circ., 6803, 1

[27] Galache J.L., Corbet R.H.D., Coe M.J., et al., 2005, ATel, 674, 1

[28] Smith M.A., Cohen D.H., Gu M.F., et al., 2004, ApJ, 600, 972

[29] Harmanec P., Habuda P., Štefl S., et al., 2000, A&A, 364, L85

[30] Grimm H.-J., Gilfanov M., & Sunyaev R., 2002, A&A, 391, 923

[31] Massey P., 2002, ApJS, 141, 81

[32] Naik S. & Paul B., 2004, A&A, 418, 655

[33] Corbet R.H.D., Finley J.P., & Peele A.G., 1999, ApJ, 511, 876

[34] Crampton D., Hutchings J.B., & Cowley A.P., 1985, ApJ, 299, 839

[35] Reig P., Chakrabarty D., Coe M.J., et al., 1996, A&A, 311, 879

[36] Campana S., Gastaldello F., Stella L., et al., 2001, ApJ, 561, 924

[37] Tamura K., Tsunemi H., Kitamoto S., et al., 1992, ApJ, 389, 676

[38] Negueruela I. & Okazaki A.T., 2001, A&A, 369, 108

[39] da Costa L.N., Willmer C.N.A., Pellegrini P.S., et al., 1998, AJ, 116, 1

[40] Risaliti G., 2002, A&A, 386, 379

[41] Polletta M., Bassani L., Malaguti G., et al., 1996, ApJS, 106, 399

[42] Reig P., Negueruela I., Papamastorakis G., et al., 2005, A&A, 440, 637

[43] Loveday J., 1996, MNRAS, 278, 1025

[44] Hewitt A. & Burbidge G., 1991, ApJS, 75, 297

[45] Hulleman F., van Kerkwijk M.H., & Kulkarni S.R., 2004, A&A, 416, 1037

[46] Göhler E., Wilms J., & Staubert R., 2005, A&A, 433, 1079

[47] Pigulski A., Kopacki G., & Kołaczkowski Z., 2001, A&A, 376, 144

[48] Mereghetti S., Tiengo A., Israel G.L., & Stella L., 2000, A&A, 354, 567

[49] Burenin R., Mescheryakov A., Sazonov S., et al., 2006, ATel, 883, 1

[50] Den Hartog P.R., Kuiper L., Hermsen W., et al., 2005, ATel, 394, 1

[51] Kennea J.A., Racusin J.L., Burrows D.N., et al., 2005, ATel, 673, 1

[52] Argyle R.W. & Eldridge P., 1990, MNRAS, 243, 504

[53] Kuiper L., Hermsen W., in 't Zand J., & den Hartog P.R., 2005, ATel, 665, 1

[54] Cotton W.D., Condon J.J., & Arbizzani E., 1999, ApJS, 125, 409

[55] Pfefferkorn F., Boller T., & Rafanelli P., 2001, A&A, 368, 797

[56] Paturel G. & Petit C., 2002, LEDA (2002), 0

[57] Clements E.D., 1981, MNRAS, 197, 829

[58] Krongold Y., Nicastro F., Elvis M., et al., 2005, ApJ, 620, 165

[59] Arribas S., Mediavilla E., del Burgo C., & García-Lorenzo B., 1999, ApJ, 511, 680

[60] Leahy D.A., Harrison F.A., & Yoshida A., 1997, ApJ, 475, 823

[61] Taylor A.R. & Gregory P.C., 1982, ApJ, 255, 210

[62] Ma C., Arias E.F., Eubanks T.M., et al., 1998, AJ, 116, 516

[63] Weaver K.A., Wilson A.S., Henkel C., & Braatz J.A., 1999, ApJ, 520, 130

[64] Fischer J.-U., Hasinger G., Schwope A.D., et al., 1998, AN, 319, 347

[65] Cappi M., Panessa F., Bassani L., et al., 2006, A&A, 446, 459

[66] Titov O.A., 2004, ARep, 48, 941

[67] Karachentsev I.D., Karachentseva V.E., Kudrya Y.N., et al., 1999, Bull. Special Astrophys.Obs., 47, 5

[68] Keel W.C., 1996, ApJS, 106, 27

[69] Ishwara-Chandra C.H. & Saikia D.J., 1999, MNRAS, 309, 100

[70] Beasley A.J., Gordon D., Peck A.B., et al., 2002, ApJS, 141, 13

[71] Enya K., Yoshii Y., Kobayashi Y., et al., 2002, ApJS, 141, 23

[72] Vrielmann S., Ness J.-U., & Schmitt J.H.M.M., 2005, A&A, 439, 287

[73] Burenin R., Mescheryakov A., Revnivtsev M., et al., 2006, ATel, 880, 1

[74] Lawrence A., Rowan-Robinson M., Ellis R.S., et al., 1999, MNRAS, 308, 897

[75] Unger S.J., Norton A.J., Coe M.J., & Lehto H.J., 1992, MNRAS, 256, 725

[76] Kreykenbohm I., Mowlavi N., Produit N., et al., 2005, A&A, 433, L45

[77] Stella L., White N.E., Davelaar J., et al., 1985, ApJL, 288, L45

[78] Negueruela I., Roche P., Fabregat J., & Coe M.J., 1999, MNRAS, 307, 695

[79] di Salvo T., Burderi L., Robba N.R., & Guainazzi M., 1998, ApJ, 509, 897

[80] Delgado-Martí, H., Levine A.M., Pfahl E., & Rappaport S.A., 2001, ApJ, 546, 455

[81] Lyubimkov L.S., Rostopchin S.I., Roche P., & Tarasov A.E., 1997, MNRAS, 286, 549

[82] Fomalont E.B., Frey S., Paragi Z., et al., 2000, ApJS, 131, 95

[83] Motch C., Guillout P., Haberl F., et al., 1998, A&AS, 132, 341

[84] Lauberts A., 1982, ESO/Uppsala survey of the ESO(B) atlas (Garching: European Southern Observatory (ESO), 1982)

[85] Sazonov S., Churazov E., Revnivtsev M., Vikhlinin A., & Sunyaev R., 2005, A&A, 444, L37

[86] Masetti N., Morelli L., Palazzi E., et al., 2006, A&A, 459, 21

[87] Remillard R.A., Bradt H.V.D., Brissenden R.J.V., et al., 1993, AJ, 105, 2079

[88] Takata T., Yamada T., Saito M., Chamaraux P., & Kazes I., 1994, A&AS, 104, 529

[89] Kulkarni S.R., Kaplan D.L., Marshall H.L., et al., 2003, ApJ, 585, 948

[90] Haberl F., Dennerl K., & Pietsch W., 2003, A&A, 406, 471

[91] Dennerl K., Haberl F., & Pietsch W., 1995, IAU Circ., 6184, 2

[92] Götz D., Mereghetti S., Merlini D., et al., 2006, A&A, 448, 873

[93] Fuhrmeister B. & Schmitt J.H.M.M., 2003, A&A, 403, 247

[94] Naik S. & Paul B., 2002, JApA, 23, 27

[95] Levine A.M., Rappaport S.A., & Zojcheski G., 2000, ApJ, 541, 194

[96] Han J.L. & Tian W.W., 1999, A&AS, 136, 571

[97] Kirsch M.G.F., Schönherr G., Kendziorra E., et al., 2006, A&A, 453, 173

[98] Lyne A.G., Pritchard R.S., & Graham-Smith F., 1993, MNRAS, 265, 1003

[99] Trimble V., 1973, PASP, 85, 579

[100] Mukherjee U. & Paul B., 2005, A&A, 431, 667

[101] Steele I.A., Negueruela I., Coe M.J., & Roche P., 1998, MNRAS, 297, L5

[102] Cui W., Feng Y.X., Zhang S.N., et al., 2002, ApJ, 576, 357

[103] Levine A.M. & Corbet R., 2006, ATel, 940, 1

[104] Haardt F., Galli M.R., Treves A., et al., 2001, ApJS, 133, 187

[105] Hirayama M., Nagase F., Endo T., et al., 2002, MNRAS, 333, 603

[106] Livingstone M.A., Kaspi V.M., & Gavriil F.P., 2005, ApJ, 633, 1095

[107] Ramsay G. & Cropper M., 2002, MNRAS, 334, 805

[108] Pavlenko E.P., 2006, Astrophysics, 49, 105

[109] Matt G., Bianchi S., de Rosa A., et al., 2006, A&A, 445, 451

[110] Helou G. & Walker D.W., eds. 1988, IRAS catalogs and atlases. Volume 7: The small scale structure catalog

[111] Kennea J.A., Markwardt C.B., Tueller J., et al., 2005, ATel, 677, 1

[112] Morelli L., Masetti N., Bassani L., et al., 2006, ATel, 785, 1

[113] Chenevez J., Budtz-Jorgensen C., Lund N., et al., 2004, ATel, 223, 1

[114] Mauch T., Murphy T., Buttery H.J., et al., 2003, MNRAS, 342, 1117

[115] Brinkmann W. & Siebert J., 1994, A&A, 285, 812

[116] Cappi M., Bassani L., Comastri A., et al., 1999, A&A, 344, 857

[117] Liu Q.Z., van Paradijs J., & van den Heuvel E.P.J., 2001, A&A, 368, 1021

[118] Piraino S., Santangelo A., Ford E.C., & Kaaret P., 1999, A&A, 349, L77

[119] Ford E., Kaaret P., Tavani M., et al., 1997, ApJL, 475, L123

[120] Paerels F., Brinkman A.C., van der Meer R.L.J., et al., 2001, ApJ, 546, 338

[121] Araujo-Betancor S., Gänsicke B.T., Hagen H.-J., et al., 2003, A&A, 406, 213

[122] Barkhouse W.A. & Hall P.B., 2001, AJ, 121, 2843

[123] Malizia A., Bassani L., Capalbi M., et al., 2003, A&A, 406, 105

[124] Sidoli L., Parmar A.N., & Oosterbroek T., 2005, A&A, 429, 291

[125] Jonker P.G. & Nelemans G., 2004, MNRAS, 354, 355

[126] Bird A.J., Barlow E.J., Bassani L., et al., 2006, ApJ, 636, 765

[127] Landi R., Malizia A., Bassani L., et al., 2006, astro-ph/0610358

[128] Revnivtsev M.G., Sazonov S.Y., Molkov S.V., et al., 2006, AstL, 32, 145

[129] Porquet D., Reeves J.N., O'Brien P., & Brinkmann W., 2004, A&A, 422, 85

[130] Pavlov G.G., Zavlin V.E., Sanwal D., et al., 2001, ApJL, 552, L129

[131] Caraveo P.A., De Luca A., Mignani R.P., & Bignami G.F., 2001, ApJ, 561, 930

[132] Belloni T., Hasinger G., Pietsch W., et al., 1993, A&A, 271, 487

[133] Kennea J.A. & Campana S., 2006, ATel, 818, 1

[134] Grandi P., Malaguti G., & Fiocchi M., 2006, ApJ, 642, 113

[135] Orlandini M., dal Fiume D., Frontera F., et al., 1998, A&A, 332, 121

[136] Kreykenbohm I., Coburn W., Wilms J., et al., 2002, A&A, 395, 129

[137] Sadakane K., Hirata R., Jugaku J., et al., 1985, ApJ, 288, 284

[138] Kirhakos S., Strauss M.A., Yahil A., et al., 1991, AJ, 102, 1933

[139] Tueller J., Barthelmy S., Burrows D., et al., 2005, ATel, 669, 1

[140] Juett A.M. & Chakrabarty D., 2003, ApJ, 599, 498

[141] Voges W., Aschenbach B., Boller T., et al., 1999, A&A, 349, 389

[142] Pineda F. & Schnopper H.W., 1978, IAU Circ., 3190, 3

[143] Balestra I., Bianchi S., & Matt G., 2004, A&A, 415, 437

[144] Paizis A., Gotz D., Sidoli L., et al., 2006, ATel, 865, 1

[145] Shrader C.R., Sutaria F.K., Singh K.P., & Macomb D.J., 1999, ApJ, 512, 920

[146] Ajello M., Greiner J., Küpcü Yoldas A., et al., 2006, ATel, 864, 1

[147] Zacharias N. Urban S.E. Zacharias M.I. et al., 2003, VizieR Online Data Catalog, 1289

[148] Ho L.C., Filippenko A.V., & Sargent W.L., 1995, ApJS, 98, 477

[149] Veron-Cetty M.-P. & Veron P., 1996, A Catalogue of quasars and active nuclei (ESO Scientific Report, Garching: European Southern Observatory (ESO), 1996, 7th ed.)

[150] Vignali C. & Comastri A., 2002, A&A, 381, 834

[151] Reig P. & Roche P., 1999, MNRAS, 306, 100

[152] Masetti N., Pretorius M.L., Palazzi E., et al., 2006, A&A, 449, 1139

[153] Burderi L., Di Salvo T., Robba N.R., et al., 2000, ApJ, 530, 429

[154] Nagase F., Corbet R.H.D., Day C.S.R., et al., 1992, ApJ, 396, 147

[155] Hutchings J.B., Cowley A.P., Crampton D., et al., 1979, ApJ, 229, 1079

[156] Steeghs D., Torres M.A.P., & Jonker P.G., 2006, ATel, 768, 1

[157] Smith D.M., Bezayiff N., & Negueruela I., 2006, ATel, 773, 1

[158] Sidoli L., Paizis A., & Mereghetti S., 2006, A&A, 450, L9

[159] Krivonos R., Molkov S., Revnivtsev M., et al., 2005, ATel, 545, 1

[160] De Rosa A., Piro L., Fiore F., et al., 2002, A&A, 387, 838

[161] in 't Zand J. & Heise J., 2004, ATel, 362, 1

[162] Corbet R.H.D. & Remillard R., 2005, ATel, 377, 1

[163] Ray P.S. & Chakrabarty D., 2002, ApJ, 581, 1293

[164] Cook M.C. & Warwick R.S., 1987, MNRAS, 227, 661

[165] Stevens J.B., Reig P., Coe M.J., et al., 1997, MNRAS, 288, 988

[166] Beckmann V., Gehrels N., Shrader C.R., & Soldi S., 2006, ApJ, 638, 642

[167] Becker R.H., White R.L., & Helfand D.J., 1995, ApJ, 450, 559

[168] Risaliti G., Gilli R., Maiolino R., & Salvati M., 2000, A&A, 357, 13

[169] Li J. & Jin W., 1996, A&AS, 120, 201

[170] La Barbera A., Segreto A., Santangelo A., et al., 2005, A&A, 438, 617

[171] Leahy D.A., 2002, A&A, 391, 219

[172] Tueller J., Gehrels N., Mushotzky R.F., et al., 2005, ATel, 591, 1

[173] Clements E.D., 1983, MNRAS, 204, 811

[174] Guainazzi M., Perola G.C., Matt G., et al., 1999, A&A, 346, 407

[175] Fairall A.P., Woudt P.A., & Kraan-Korteweg R.C., 1998, A&AS, 127, 463

[176] Torrejón J.M. & Orr A., 2001, A&A, 377, 148

[177] Perryman M.A.C. & ESA., 1997, The HIPPARCOS and TYCHO catalogues. Astrometric and photometric star catalogues derived from the ESA HIPPARCOS Space Astrometry Mission (Publisher: Noordwijk, Netherlands: ESA Publications Division, 1997, Series: ESA SP Series vol no: 1200, ISBN: 9290923997 (set))

[178] Jackson C.A., Wall J.V., Shaver P.A., et al., 2002, A&A, 386, 97

[179] Bassa C.G., Jonker P.G., in 't Zand J.J.M., & Verbunt F., 2006, A&A, 446, L17

[180] Boller T., Haberl F., Voges W., Piro L., & Heise J., 1997, IAU Circ., 6546, 1

[181] Jerjen H. & Dressler A., 1997, A&AS, 124, 1

[182] Boirin L. & Parmar A.N., 2003, A&A, 407, 1079

[183] in 't Zand J.J.M., Kuulkers E., Verbunt F., et al., 2003, A&A, 411, L487

[184] Mahdavi A. & Geller M.J., 2001, ApJL, 554, L129

[185] Arnaud M., Aghanim N., Gastaud R., et al., 2001, A&A, 365, L67

[186] Chernyakova M., Lutovinov A., Rodriguez J., & Revnivtsev M., 2005, MNRAS, 364, 455

[187] Bicay M.D., Stepanian J.A., Chavushyan V.H., et al., 2000, A&AS, 147, 169

[188] Done C., Madejski G.M., Życki P.T., & Greenhill L.J., 2003, ApJ, 588, 763

[189] Odewahn S.C. & Aldering G., 1996, Private Communication, 1

[190] Palumbo G.G.C., et al., 1988, in Accurate positions of Zwicky galaxies (1988), 0–+

[191] Nilson P., 1973, Nova Acta Regiae Soc.Sci.Upsaliensis Ser.V, 0

[192] Evans D.A., Kraft R.P., Worrall D.M., et al., 2004, ApJ, 612, 786

[193] Church M.J., Reed D., Dotani T., Bałucińska-Church M., & Smale A.P., 2005, MNRAS, 359, 1336

[194] Parmar A.N., Gottwald M., van der Klis M., & van Paradijs J., 1989, ApJ, 338, 1024

[195] Kaldare R., Colless M., Raychaudhury S., & Peterson B.A., 2003, MNRAS, 339, 652

[196] Demircan O., Eker Z., Karataş Y., & Bilir S., 2006, MNRAS, 366, 1511

[197] Willmer C.N.A., Maia M.A.G., Mendes S.O., et al., 1999, AJ, 118, 1131

[198] Papadakis I.E., Kazanas D., & Akylas A., 2005, ApJ, 631, 727

[199] Piconcelli E., Sánchez-Portal M., Guainazzi M., et al., 2006, A&A, 453, 839

[200] Imamura J.N., Steiman-Cameron T.Y., & Wolff M.T., 2000, PASP, 112, 18

[201] Wright A.E., Griffith M.R., Hunt A.J., et al., 1996, ApJS, 103, 145

[202] Matt G., Guainazzi M., Maiolino R., et al., 1999, A&A, 341, L39

[203] Bianchi S., Balestra I., Matt G., et al., 2003, A&A, 402, 141

[204] Nicastro F., Piro L., De Rosa A., et al., 2000, ApJ, 536, 718

[205] Crenshaw D.M. & Kraemer S.B., 1999, ApJ, 521, 572

[206] West R.M., Surdej J., Schuster H.-E., et al., 1981, A&AS, 46, 57

[207] DeLaney T., Gaensler B.M., Arons J., & Pivovaroff M.J., 2006, ApJ, 640, 929

[208] Livingstone M.A., Kaspi V.M., Gavriil F.P., & Manchester R.N., 2005, ApJ, 619, 1046

[209] Gaensler B.M., Brazier K.T.S., Manchester R.N., et al., 1999, MNRAS, 305,

724

[210] Iaria R., Di Salvo T., Burderi L., & Robba N.R., 2001, ApJ, 561, 321

[211] Robba N.R., Burderi L., Di Salvo T., et al., 2001, ApJ, 562, 950

[212] Baykal A., Inam S.Ç., & Beklen E., 2006, A&A, 453, 1037

[213] Reynolds A.P., Bell S.A., & Hilditch R.W., 1992, MNRAS, 256, 631

[214] in 't Zand J.J.M., Corbet R.H.D., & Marshall F.E., 2001, ApJL, 553, L165

[215] Farinelli R., Frontera F., Masetti N., et al., 2003, A&A, 402, 1021

[216] Wang Z. & Chakrabarty D., 2004, ApJL, 616, L139

[217] Stephen J.B., Bassani L., Molina M., et al., 2005, A&A, 432, L49

[218] Haberl F., Motch C., & Zickgraf F.-J., 2002, A&A, 387, 201

[219] de Martino D., Bonnet-Bidaud J.-M., Mouchet M., et al., 2006, A&A, 449, 1151

[220] Klemola A.R., Jones B.F., & Hanson R.B., 1987, AJ, 94, 501

[221] Kazarovets E.V., Samus N.N., & Durlevich O.V., 2001, IBVS, 5135, 1

[222] Corbel S., Tomsick J.A., & Kaaret P., 2006, ApJ, 636, 971

[223] Orosz J.A., Groot P.J., van der Klis M., et al., 2002, ApJ, 568, 845

[224] Smale A.P., 1991, PASP, 103, 636

[225] Woudt P.A. & Kraan-Korteweg R.C., 2001, A&A, 380, 441

[226] Greco M.V., Miller J.M., & Steeghs D., 2006, ATel, 858, 1

[227] Wachter S., Hoard D.W., Bailyn C.D., et al., 2002, ApJ, 568, 901

[228] Tomsick J.A., Chaty S., Rodriguez J., et al., 2006, ApJ, 647, 1309

[229] Kaspi V.M., Crawford F., Manchester R.N., et al., 1998, ApJL, 503, L161

[230] Gotthelf E.V., Petre R., & Hwang U., 1997, ApJL, 487, L175

[231] Torii K., Gotthelf E.V., Vasisht G., et al., 2000, ApJL, 534, L71

[232] Caswell J.L., Murray J.D., Roger R.S., et al., 1975, A&A, 45, 239

[233] Garmire G.P., Pavlov G.G., Garmire A.B., & Zavlin V.E., 2000, IAU Circ., 7350, 2

[234] Reynoso E.M., Green A.J., Johnston S., et al., 2004, PASA, 21, 82

[235] McNamara B.J., Harrison T.E., Zavala R.T., et al., 2003, AJ, 125, 1437

[236] Bradshaw C.F., Geldzahler B.J., & Fomalont E.B., 2003, ApJ, 592, 486

[237] Vanderlinde K.W., Levine A.M., & Rappaport S.A., 2003, PASP, 115, 739

[238] Campana S., Belloni T., Homan J., et al., 2006, ATel, 688, 1

[239] Markwardt C.B. & Swank J.H., 2005, ATel, 679, 1

[240] Wachter S., Wellhouse J.W., Patel S.K., et al., 2005, ApJ, 621, 393

[241] Parmar A.N., Oosterbroek T., Boirin L., & Lumb D., 2002, A&A, 386, 910

[242] Christian D.J. & Swank J.H., 1997, ApJS, 109, 177

[243] Kennea J.A., Burrows D.N., Nousek J.A., et al., 2005, ATel, 459, 1

[244] Beckmann V., Kennea J.A., Markwardt C., et al., 2005, ApJ, 631, 506

[245] Rodriguez J. & Goldwurm A., 2003, ATel, 201, 1

[246] Schartel N., Ehle M., Breitfellner M., et al., 2003, IAU Circ., 8072, 3

[247] Walter R., Zurita Heras J.A., Bassani L., et al., 2006, A&A, 453, 133

[248] Filliatre P. & Chaty S., 2004, ApJ, 616, 469

[249] Rodriguez J., Bodaghee A., Kaaret P., et al., 2006, MNRAS, 366, 274

[250] Corbet R., Barbier L., Barthelmy S., et al., 2005, ATel, 649, 1

[251] Orlandini M., Fiume D.D., Frontera F., et al., 1998, ApJL, 500, L163

[252] Owens A., Oosterbroek T., & Parmar A.N., 1997, A&A, 324, L9

[253] Middleditch J., Mason K.O., Nelson J.E., & White N.E., 1981, ApJ, 244, 1001

[254] Tomsick J.A., Corbel S., Goldwurm A., & Kaaret P., 2005, ApJ, 630, 413

[255] Kouveliotou C., Patel S., Tennant A., et al., 2003, IAU Circ., 8109, 2

[256] Patel S.K., Zurita Heras J.A., Del Santo M., et al., 2007, ApJ, 657, 994

[257] Ebeling H., Mullis C.R., & Tully R.B., 2002, ApJ, 580, 774

[258] McHardy I.M., Lawrence A., Pye J.P., & Pounds K.A., 1981, MNRAS, 197, 893

[259] Bodaghee A., Walter R., Zurita Heras J.A., et al., 2006, A&A, 447, 1027

[260] Thompson T.W.J., Tomsick J.A., Rothschild R.E., et al., 2006, ApJ, 649, 373

[261] Vrtilek S.D., McClintock J.E., Seward F.D., et al., 1991, ApJS, 76, 1127

[262] Strohmayer T.E. & Markwardt C.B., 2002, ApJ, 577, 337

[263] Galloway D.K., Psaltis D., Muno M.P., & Chakrabarty D., 2006, ApJ, 639, 1033

[264] Corbet R., Barbier L., Barthelmy S., et al., 2006, ATel, 779, 1

[265] Smith D.M., 2004, ATel, 338, 1

[266] Kuiper L., Jonker P., Hermsen W., & O’Brien K., 2005, ATel, 654, 1

[267] Markwardt C.B., Swank J.H., & Smith E., 2005, ATel, 465, 1

[268] Ebisawa K., Bourban G., Bodaghee A., et al., 2003, A&A, 411, L59

[269] Manchester R.N., Lyne A.G., Camilo F., et al., 2001, MNRAS, 328, 17

[270] Netzer H., Lemze D., Kaspi S., et al., 2005, ApJ, 629, 739

[271] Donato D., Sambruna R.M., & Gliozzi M., 2005, A&A, 433, 1163

[272] Brocksopp C., McGowan K.E., Krimm H., et al., 2006, MNRAS, 365, 1203

[273] Tueller J., Markwardt C., Ajello M., et al., 2006, ATel, 835, 1

[274] Kinnunen T. & Skiff B.A., 2000, IBVS, 4863, 1

[275] Oosterbroek T., Parmar A.N., Dal Fiume D., et al., 2000, A&A, 353, 575

[276] Kuster M., Wilms J., Staubert R., et al., 2005, A&A, 443, 753

[277] Reynolds A.P., Quaintrell H., Still M.D., et al., 1997, MNRAS, 288, 43

[278] Sugizaki M., Mitsuda K., Kaneda H., et al., 2001, ApJS, 134, 77

[279] Chakrabarty D., Wang Z., Juett A.M., et al., 2002, ApJ, 573, 789

[280] Orlandini M., dal Fiume D., del Sordo S., et al., 1999, A&A, 349, L9

[281] Baykal A., 2000, MNRAS, 313, 637

[282] Chakrabarty D., Grunsfeld J.M., Prince T.A., et al., 1993, ApJL, 403, L33

[283] Audley M.D., Nagase F., Mitsuda K., et al., 2006, MNRAS, 367, 1147

[284] Krauss M.I., Juett A.M., Chakrabarty D., et al., 2006, ATel, 777, 1

[285] Kennea J.A., Marshall F.E., Steeghs D., et al., 2006, ATel, 704, 1

[286] Miller J.M., Raymond J., Fabian A.C., et al., 2004, ApJ, 601, 450

[287] Hynes R.I., Steeghs D., Casares J., et al., 2004, ApJ, 609, 317

[288] Boroson B., Vrtilek S.D., Kallman T., & Corcoran M., 2003, ApJ, 592, 516

[289] Hong J. & Hailey C.J., 2004, ApJ, 600, 743

[290] Ankay A., Kaper L., de Bruijne J.H.J., et al., 2001, A&A, 370, 170

[291] Kazarovets E.V., Samus N.N., & Durlevich O.V., 2000, IBVS, 4870, 1

[292] Iaria R., Di Salvo T., Robba N.R., et al., 2004, ApJ, 600, 358

[293] Wachter S. & Margon B., 1996, AJ, 112, 2684

[294] Oosterbroek T., Penninx W., van der Klis M., et al., 1991, A&A, 250, 389

[295] Asai K., Dotani T., Hoshi R., et al., 1998, PASJ, 50, 611

[296] Remillard R.A., Orosz J.A., McClintock J.E., & Bailyn C.D., 1996, ApJ, 459, 226

[297] Rea N., Oosterbroek T., Zane S., et al., 2005, MNRAS, 361, 710

[298] in 't Zand J.J.M., Cornelisse R., & Méndez M., 2005, A&A, 440, 287

[299] Di Salvo T., Iaria R., Méndez M., et al., 2005, ApJL, 623, L121

[300] in 't Zand J.J.M., Heise J., Lowes P., & Ubertini P., 2003, ATel, 160, 1

[301] Negueruela I. & Schurch M., 2007, A&A, 461, 631

[302] Jonker P.G., Méndez M., Nelemans G., et al., 2003, MNRAS, 341, 823

[303] Kennea J.A., Burrows D.N., Nousek J.A., et al., 2005, ATel, 476, 1

[304] Ritter H. & Kolb U., 2003, A&A, 404, 301

[305] Wilson C.A., Patel S.K., Kouveliotou C., et al., 2003, ApJ, 596, 1220

[306] Edge A.C. & Stewart G.C., 1991, MNRAS, 252, 414

[307] Nevalainen J., Oosterbroek T., Bonamente M., & Colafrancesco S., 2004, ApJ, 608, 166

[308] Cocchi M., Bazzano A., Natalucci L., et al., 2001, Mem. Soc. Astron. Italiana, 72, 757

[309] Downes R.A., Webbink R.F., Shara M.M., et al., 2001, PASP, 113, 764

[310] de Martino D., Matt G., Belloni T., et al., 2004, A&A, 415, 1009

[311] Norton A.J., Wynn G.A., & Somerscales R.V., 2004, ApJ, 614, 349

[312] Suleimanov V., Revnivtsev M., & Ritter H., 2005, A&A, 435, 191

[313] Cornelisse R., Charles P.A., & Robertson C., 2006, MNRAS, 366, 918

[314] Cadolle Bel M., Rodriguez J., Sizun P., et al., 2004, A&A, 426, 659

[315] Nagata T., Kato D., Baba D., et al., 2003, PASJ, 55, L73

[316] Bykov A.M., Krassilchtchikov A.M., Uvarov Y.A., et al., 2006, A&A, 449, 917

[317] Zurita Heras J.A., de Cesare G., Walter R., et al., 2006, A&A, 448, 261

[318] Corbet R.H.D., Markwardt C.B., & Swank J.H., 2005, ApJ, 633, 377

[319] Steeghs D., Torres M.A.P., Koviak K., et al., 2005, ATel, 629, 1

[320] Kennea J.A., Burrows D.N., Chester M., et al., 2005, ATel, 632, 1

[321] Kuulkers E., den Hartog P.R., in 't Zand J.J.M., et al., 2003, A&A, 399, 663

[322] Gänsicke B.T., Marsh T.R., Edge A., et al., 2005, MNRAS, 361, 141

[323] Church M.J. & Balucińska-Church M., 2001, A&A, 369, 915

[324] D'Aí, A., di Salvo T., Iaria R., et al., 2006, A&A, 448, 817

[325] Strohmayer T.E., Zhang W., Swank J.H., et al., 1996, ApJL, 469, L9

[326] Hernanz M. & Sala G., 2002, Science, 298, 393

[327] Munari U. & Zwitter T., 2002, A&A, 383, 188

[328] Paul B., Dotani T., Nagase F., et al., 2005, ApJ, 627, 915

[329] Hinkle K.H., Fekel F.C., Joyce R.R., et al., 2006, ApJ, 641, 479

[330] Chelovekov I.V., Grebenev S.A., & Sunyaev R.A., 2006, AstL, 32, 456

[331] Marti J., Mirabel I.F., Chaty S., & Rodriguez L.F., 1998, A&A, 330, 72

[332] Molina M., Malizia A., Bassani L., et al., 2006, MNRAS, 371, 821

[333] Corbet R.H.D., Thorstensen J.R., Charles P.A., et al., 1986, MNRAS, 222, 15P

[334] Smith D.M., Heindl W.A., Markwardt C.B., et al., 2006, ApJ, 638, 974

[335] Sakano M., Koyama K., Murakami H., et al., 2002, ApJS, 138, 19

[336] Negueruela I., Smith D.M., Harrison T.E., & Torrejón J.M., 2006, ApJ, 638, 982

[337] Torres M.A.P., Steeghs D., Garcia M.R., et al., 2006, ATel, 784, 1

[338] in 't Zand J.J.M., Verbunt F., Kuulkers E., et al., 2002, A&A, 389, L43

[339] Sidoli L., Belloni T., & Mereghetti S., 2001, A&A, 368, 835

[340] Torres M.A.P., Garcia M.R., McClintock J.E., et al., 2004, ATel, 264, 1

[341] Kong A.K.H., 2006, ATel, 745, 1

[342] Kennea J.A., Burrows D.N., Nousek J., & Gehrels N., 2005, ATel, 617, 1

[343] Rupen M.P., Dhawan V., & Mioduszewski A.J., 2004, ATel, 335, 1

[344] Martí, J., Mirabel I.F., Chaty S., & Rodríguez L.F., 2000, A&A, 363, 184

[345] Gallo E. & Fender R.P., 2002, MNRAS, 337, 869

[346] Smith D.M., Heindl W.A., & Swank J.H., 2002, ApJL, 578, L129

[347] White N.E. & van Paradijs J., 1996, ApJL, 473, L25

[348] Reid M.J. & Brunthaler A., 2004, ApJ, 616, 872

[349] Bélanger G., Goldwurm A., Renaud M., et al., 2006, ApJ, 636, 275

[350] Miller J.M., Raymond J., Homan J., et al., 2006, ApJ, 646, 394

[351] Corbel S., Kaaret P., Fender R.P., et al., 2005, ApJ, 632, 504

[352] Porquet D., Rodriguez J., Corbel S., et al., 2003, A&A, 406, 299

[353] Revnivtsev M.G., Sunyaev R.A., Varshalovich D.A., et al., 2004, AstL, 30,

382

[354] Wijnands R., Miller J.M., & Wang Q.D., 2002, ApJ, 579, 422

[355] Kong A.K.H., Wijnands R., & Homan J., 2005, ATel, 641, 1

[356] Werner N., in 't Zand J.J.M., Natalucci L., et al., 2004, A&A, 416, 311

[357] Revnivtsev M.G., Churazov E.M., Sazonov S.Y., et al., 2004, A&A, 425, L49

[358] Juett A.M., Kaplan D.L., Chakrabarty D., et al., 2005, ATel, 521, 1

[359] Kennea J.A., Burrows D.N., Markwardt C., & Gehrels N., 2005, ATel, 500, 1

[360] Oosterbroek T., Barret D., Guainazzi M., & Ford E.C., 2001, A&A, 366, 138

[361] McClintock J., Murray S., Garcia M., & Jonker P., 2003, ATel, 205, 1

[362] Bhattacharyya S., Strohmayer T.E., Markwardt C.B., & Swank J.H., 2006, ApJL, 639, L31

[363] Torii K., Kinugasa K., Katayama K., et al., 1998, ApJ, 508, 854

[364] Paizis A., Nowak M.A., Rodriguez J., et al., 2006, ATel, 907, 1

[365] Sidoli L., Parmar A.N., Oosterbroek T., et al., 2001, A&A, 368, 451

[366] in 't Zand J.J.M., Hulleman F., Markwardt C.B., et al., 2003, A&A, 406, 233

[367] Still M., 2005, ATel, 555, 1

[368] Morris D.C., Burrows D.N., Racusin J., et al., 2005, ATel, 552, 1

[369] Türler M., Shaw S.E., Kuulkers E., et al., 2006, ATel, 790, 1

[370] in 't Zand J.J.M., 2005, A&A, 441, L1

[371] Pellizza L.J., Chaty S., & Negueruela I., 2006, A&A, 455, 653

[372] Lutovinov A., Revnivtsev M., Molkov S., & Sunyaev R., 2005, A&A, 430, 997

[373] Sidoli L. & Mereghetti S., 2002, A&A, 388, 293

[374] Iaria R., di Salvo T., Robba N.R., et al., 2005, A&A, 439, 575

[375] Hill A.B., Walter R., Knigge C., et al., 2005, A&A, 439, 255

[376] Combi J.A., Ribó M., Martí J., & Chaty S., 2006, A&A, 458, 761

[377] Markwardt C.B., Juda M., & Swank J.H., 2003, IAU Circ., 8095, 2

[378] Falanga M., Bonnet-Bidaud J.M., Poutanen J., et al., 2005, A&A, 436, 647

[379] Kaplan D.L., Fox D.W., Kulkarni S.R., et al., 2002, ApJ, 564, 935

[380] Molkov S., Hurley K., Sunyaev R., et al., 2005, A&A, 433, L13

[381] Tiengo A., Esposito P., Mereghetti S., et al., 2005, A&A, 440, L63

[382] Corbel S. & Eikenberry S.S., 2004, A&A, 419, 191

[383] Kaspi V.M., Roberts M.E., Vasisht G., et al., 2001, ApJ, 560, 371

[384] Roberts M.S.E., Tam C.R., Kaspi V.M., et al., 2003, ApJ, 588, 992

[385] Torii K., Tsunemi H., Dotani T., et al., 1999, ApJL, 523, L69

[386] Gotthelf E.V., 2003, ApJ, 591, 361

[387] Ubertini P., Bassani L., Malizia A., et al., 2005, ApJL, 629, L109

[388] Brogan C.L., Gaensler B.M., Gelfand J.D., et al., 2005, ApJL, 629, L105

[389] Ueda Y., Murakami H., Yamaoka K., et al., 2004, ApJ, 609, 325

[390] Corbet R.H.D., 2003, ApJ, 595, 1086

[391] Bandyopadhyay R.M., Shahbaz T., Charles P.A., & Naylor T., 1999, MNRAS, 306, 417

[392] Sguera V., Bird A.J., Dean A.J., et al., 2006, ATel, 873, 1

[393] Farinelli R., Frontera F., Zdziarski A.A., et al., 2005, A&A, 434, 25

[394] Dhawan M.P.R.V. & Mioduszewski A.J., 2006, ATel, 721, 1

[395] Miller J.M., Homan J., Steeghs D., & Wijnands R., 2006, ATel, 746, 1

[396] Sala G. & Greiner J., 2006, ATel, 791, 1

[397] Gehrels M.S.N., Steeghs D., Torres M.A.P., et al., 2005, ATel, 588, 1

[398] in 't Zand J., Jonker P., Mendez M., & Markwardt C., 2006, ATel, 915, 1

[399] Kinugasa K., Torii K., Hashimoto Y., et al., 1998, ApJ, 495, 435

[400] Voges W., Aschenbach B., Boller T., et al., 2000, IAU Circ., 7432, 1

[401] Migliari S., Fender R.P., Rupen M., et al., 2004, MNRAS, 351, 186

[402] Revnivtsev M., Sazonov S., Churazov E., & Trudolyubov S., 2006, A&A, 448, L49

[403] Douglas J.N., Bash F.N., Bozyan F.A., et al., 1996, AJ, 111, 1945

[404] Juett A.M. & Chakrabarty D., 2005, ApJ, 627, 926

[405] Iaria R., Di Salvo T., Burderi L., & Robba N.R., 2001, ApJ, 557, 24

[406] Jonker P.G. & van der Klis M., 2001, ApJL, 553, L43

[407] Hellier C. & Mason K.O., 1989, MNRAS, 239, 715

[408] Mason K.O. & Cordova F.A., 1982, ApJ, 262, 253

[409] Monet D. & et al. 1998, in The PMM USNO-A2.0 Catalog. (1998), 0–+

[410] Martocchia A., Motch C., & Negueruela I., 2005, A&A, 430, 245

[411] Casares J., Ribó M., Ribas I., et al., 2005, MNRAS, 364, 899

[412] Thompson T.W.J., Rothschild R.E., Tomsick J.A., & Marshall H.L., 2005, ApJ, 634, 1261

[413] Homer L., Charles P.A., & O'Donoghue D., 1998, MNRAS, 298, 497

[414] Kong A.K.H., Homer L., Kuulkers E., et al., 2000, MNRAS, 311, 405

[415] Safi-Harb S., Harrus I.M., Petre R., et al., 2001, ApJ, 561, 308

[416] Camilo F., Ransom S.M., Gaensler B.M., et al., 2006, ApJ, 637, 456

[417] Schmitz M., 1991, NED Team Report, 1, 1 (1991), 1, 1

[418] de Rosa A., Piro L., Tramacere A., et al., 2005, A&A, 438, 121

[419] Grandi P., Urry C.M., & Maraschi L., 2002, New A Rev., 46, 221

[420] Parmar A.N., Oosterbroek T., Sidoli L., Stella L., & Frontera F., 2001, A&A, 380, 490

[421] Deutsch E.W., Margon B., & Anderson S.F., 2000, ApJL, 530, L21

[422] Malizia A., Bassani L., Stephen J.B., et al., 2005, ApJL, 630, L157

[423] Foster R.S., Cadwell B.J., Wolszczan A., & Anderson S.B., 1995, ApJ, 454, 826

[424] Molkov S.V., Cherepashchuk A.M., Lutovinov A.A., et al., 2004, AstL, 30, 534

[425] Halpern J.P., Gotthelf E.V., Helfand D.J., et al., 2004, ATel, 289, 1

[426] Bamba A., Yokogawa J., Ueno M., et al., 2001, PASJ, 53, 1179

[427] Wachter S., Patel S.K., Kouveliotou C., et al., 2004, ApJ, 615, 887

[428] Morii M., Sato R., Kataoka J., & Kawai N., 2003, PASJ, 55, L45

[429] Vasisht G. & Gotthelf E.V., 1997, ApJL, 486, L129

[430] Sanbonmatsu K.Y. & Helfand D.J., 1992, AJ, 104, 2189

[431] Sguera V., Bird A.J., Dean A.J., et al., 2007, A&A, 462, 695

[432] Coe M.J., Fabregat J., Negueruela I., et al., 1996, MNRAS, 281, 333

[433] Piraino S., Santangelo A., Segreto A., et al., 2000, A&A, 357, 501

[434] Israel G.L., Negueruela I., Campana S., et al., 2001, A&A, 371, 1018

[435] Gotthelf E.V., Vasisht G., Boylan-Kolchin M., & Torii K., 2000, ApJL, 542, L37

[436] Helfand D.J., Collins B.F., & Gotthelf E.V., 2003, ApJ, 582, 783

[437] Livingstone M.A., Kaspi V.M., Gotthelf E.V., & Kuiper L., 2006, ApJ, 647, 1286

[438] Becker R.H. & Helfand D.J., 1984, ApJ, 283, 154

[439] Soffitta P., Tomsick J.A., Harmon B.A., et al., 1998, ApJL, 494, L203

[440] Lutovinov A.A. & Revnivtsev M.G., 2003, AstL, 29, 719

[441] Beuermann K., Harrison T.E., McArthur B.E., et al., 2004, A&A, 419, 291

[442] Corbet R.H.D. & Mukai K., 2002, ApJ, 577, 923

[443] Corbet R.H.D., Marshall F.E., Peele A.G., & Takeshima T., 1999, ApJ, 517, 956

[444] Harris D.E., Forman W., Gioa I.M., et al., 1996, VizieR Online Data Catalog, 9013, 0

[445] Bikmaev I.F., Sunyaev R.A., Revnivtsev M.G., & Burenin R.A., 2005, AstL, in press, astro-ph/0511405

[446] Paul B. & Rao A.R., 1998, A&A, 337, 815

[447] Takeshima T., Corbet R.H.D., Marshall F.E., et al., 1998, IAU Circ., 6826, 1

[448] Rupen M.P., Mioduszewski A.J., & Dhawan V., 2005, ATel, 530, 1

[449] Campana S., 2005, ATel, 535, 1

[450] Kaaret P., Morgan E.H., Vanderspek R., & Tomsick J.A., 2006, ApJ, 638, 963

[451] Kawai N. & Suzuki M., 2005, ATel, 534, 1

[452] Galloway D.K., Remillard R., & Morgan E., 2003, IAU Circ., 8081, 2

[453] Galloway D.K., Wang Z., & Morgan E.H., 2005, ApJ, 635, 1217

[454] Frail D.A., Kulkarni S.R., & Bloom J.S., 1999, Nature, 398, 127

[455] Esposito P., Mereghetti S., Tiengo A., et al., 2007, A&A, 461, 605

[456] Vrba F.J., Henden A.A., Luginbuhl C.B., et al., 2000, ApJL, 533, L17

[457] Rupen M.P., Dhawan V., & Mioduszewski A.J., 2002, IAU Circ., 7874, 1

[458] in 't Zand J.J.M., Miller J.M., Oosterbroek T., & Parmar A.N., 2002, A&A, 394, 553

[459] Chaty S., Mignani R.P., & Israel G.L., 2006, MNRAS, 365, 1387

[460] Cusumano G., di Salvo T., Burderi L., et al., 1998, A&A, 338, L79

[461] Baykal A., İnam S.C., & Beklen E., 2006, MNRAS, 369, 1760

[462] in 't Zand J.J.M., Baykal A., & Strohmayer T.E., 1998, ApJ, 496, 386

[463] Cox N.L.J., Kaper L., & Mokiem M.R., 2005, A&A, 436, 661

[464] Levine A.M., Rappaport S., Remillard R., & Savcheva A., 2004, ApJ, 617, 1284

[465] Morel T. & Grosdidier Y., 2005, MNRAS, 356, 665

[466] Wijnands R., Maitra D., Bailyn C., & Linares M., 2006, ATel, 871, 1

[467] Chevalier C. & Ilovaisky S.A., 1991, A&A, 251, L11

[468] Brinkmann W., Kotani T., & Kawai N., 2005, A&A, 431, 575

[469] Blundell K.M. & Bowler M.G., 2004, ApJL, 616, L159

[470] in 't Zand J.J.M., Jonker P.G., Nelemans G., et al., 2006, A&A, 448, 1101

[471] Corbet R.H.D., Hannikainen D.C., & Remillard R., 2004, ATel, 269, 1

[472] Martocchia A., Matt G., Belloni T., et al., 2006, A&A, 448, 677

[473] Harlaftis E.T. & Greiner J., 2004, A&A, 414, L13

[474] Juett A.M. & Chakrabarty D., 2006, ApJ, 646, 493

[475] Falanga M., Belloni T., & Campana S., 2006, A&A, 456, L5

[476] Sambruna R.M., 1997, ApJ, 487, 536

[477] Véron-Cetty M.-P. & Véron P., 2003, A&A, 412, 399

[478] Wang J., Wei J.Y., & He X.T., 2006, ApJ, 638, 106

[479] Andronov I.L., Baklanov A.V., & Burwitz V., 2006, A&A, 452, 941

[480] Rana V.R., Singh K.P., Barrett P.E., & Buckley D.A.H., 2005, ApJ, 625, 351

[481] Naik S., Callanan P.J., Paul B., & Dotani T., 2006, ApJ, 647, 1293

[482] Galloway D.K., Morgan E.H., & Levine A.M., 2004, ApJ, 613, 1164

[483] Tsygankov S.S. & Lutovinov A.A., 2005, AstL, 31, 88

[484] Evans D.A., Worrall D.M., Hardcastle M.J., et al., 2006, ApJ, 642, 96

[485] Liu F.K. & Zhang Y.H., 2002, A&A, 381, 757

[486] Masetti N., Orlandini M., Palazzi E., et al., 2006, A&A, 453, 295

[487] Mattana F., Götz D., Falanga M., et al., 2006, A&A, 460, L1

[488] Schulz N.S., Cui W., Canizares C.R., et al., 2002, ApJ, 565, 1141

[489] Ziólkowski J., 2005, MNRAS, 358, 851

[490] Zhou H.-Y. & Wang T.-G., 2002, Chinese J. Astron. Astrophys., 2, 501

[491] NED Team, 1992, NED Team Report, 1, 1 (1992), 1, 1

[492] Bykov A.M., Krassilchtchikov A.M., Uvarov Y.A., et al., 2006, ApJL, 649, L21

[493] Reig P. & Coe M.J., 1999, MNRAS, 302, 700

[494] Camero Arranz A., Wilson C.A., Connell P., et al., 2005, A&A, 441, 261

[495] Wilson C.A., Finger M.H., Coe M.J., et al., 2002, ApJ, 570, 287

[496] Weekes T.C. & Geary J.C., 1982, PASP, 94, 708

[497] Stark M.J. & Saia M., 2003, ApJL, 587, L101

[498] Lara L., Cotton W.D., Feretti L., et al., 2001, A&A, 370, 409

[499] Ballantyne D.R., 2005, MNRAS, 362, 1183

[500] Cutri R.M., Skrutskie M.F., van Dyk S., et al., 2003, The IRSA 2MASS All-Sky Point Source Catalog, NASA/IPAC Infrared Science Archive. (http://irsa.ipac.caltech.edu/applications/Gator/)

[501] Baykal A., Stark M.J., & Swank J.H., 2002, ApJ, 569, 903

[502] Sidoli L., Mereghetti S., Larsson S., et al., 2005, A&A, 440, 1033

[503] Falcone A., Tueller J., Markwardt C., et al., 2006, ATel, 846, 1

[504] Thorstensen J.R. & Taylor C.J., 2001, MNRAS, 326, 1235

[505] Halpern J.P., 2006, ATel, 847, 1

[506] Bonnet-Bidaud J.M., Mouchet M., de Martino D., et al., 2006, A&A, 445, 1037

[507] Motch C., Guillout P., Haberl F., et al., 1997, A&AS, 122, 201

[508] Mauche C.W., 2004, ApJ, 610, 422

[509] Harrison T.E., McNamara B.J., Szkody P., & Gilliland R.L., 2000, AJ, 120, 2649

[510] Costantini E., Freyberg M.J., & Predehl P., 2005, A&A, 444, 187

[511] Casares J., Charles P.A., & Kuulkers E., 1998, ApJL, 493, L39

[512] Stickel M., Lemke D., Klaas U., et al., 2004, A&A, 422, 39

[513] Dadina M., Bassani L., Cappi M., et al., 2001, A&A, 370, 70

[514] Ravasio M., Tagliaferri G., Ghisellini G., et al., 2003, A&A, 408, 479

[515] Hog E., Kuzmin A., Bastian U., et al., 1998, A&A, 335, L65

[516] Masetti N., Dal Fiume D., Amati L., et al., 2004, A&A, 423, 311

[517] Ribó M., Negueruela I., Blay P., et al., 2006, A&A, 449, 687

[518] Blay P., Negueruela I., Reig P., et al., 2006, A&A, 446, 1095

[519] Patterson J., Kemp J., Richman H.R., et al., 1998, PASP, 110, 415

[520] Barrett P., 1996, PASP, 108, 412

[521] Gibson R.R., Marshall H.L., Canizares C.R., & Lee J.C., 2005, ApJ, 627, 83

[522] Scott J.E., Kriss G.A., Lee J.C., et al., 2005, ApJ, 634, 193

[523] George I.M., Turner T.J., Netzer H., et al., 1998, ApJS, 114, 73

[524] Hwang U., Laming J.M., Badenes C., et al., 2004, ApJL, 615, L117

[525] Reed J.E., Hester J.J., Fabian A.C., & Winkler P.F., 1995, ApJ, 440, 706

Chapter 13
Spatial Distribution

13.1 Longitude & Latitude

Angular distributions, in Galactic coordinates, of the major classes of γ-ray sources detected by ISGRI are presented in Figs. 13.1–13.2. While detections are naturally biased towards regions of the sky that have been exposed the longest (i.e. the Galactic Plane and Bulge), the evolution of each type of source has an influence on its spatial distribution.

Stellar companions of HMXBs are young stars so these systems must remain close to sites of recent stellar formation (i.e. the Galactic Plane and spiral arms). Like birds on a wire, the HMXBs in Fig. 13.3 are ligned up along the Galactic Plane. High-mass X-ray binaries that have Galactic latitudes $b > 5$–10° are either nearby (e.g. X Per), which means their high latitude is simply an effect of projection, or they belong to the Small and Large Magellanic Clouds (SMC and LMC, respectively) whose stars have undergone a different evolution compared to those in the Milky Way.

It is clear from Fig. 13.3 that *INTEGRAL* has discovered many SG HMXBs: half of the SG HMXBs in the inner 90° are new. This underscores the ability of *INTEGRAL* to detect sources that are intrinsically absorbed to begin with, and that are further obscured by the dust and gas of the inner Galaxy.

The longitudinal distribution of HMXBs (Fig. 13.1) reflects the spiral structure of the Galaxy, with an uneven distribution along the Galactic Plane punctuated by peaks that are roughly consistent with the tangential directions to the inner spiral arms. Those HMXBs that have been detected at longitudes $|l| \gtrsim 90^\circ$ correspond to systems located around spiral arms near the Sun.

Because their optical companions belong to an old stellar population, LMXBs are found predominantly in the Galactic bulge (Fig. 13.4) and/or they have had time to migrate off the plane of the Milky Way ($|b| \gtrsim 3$–5°) (Fig. 13.2).

Miscellaneous sources (Fig. 13.5) group objects with all types of evolutionary his-

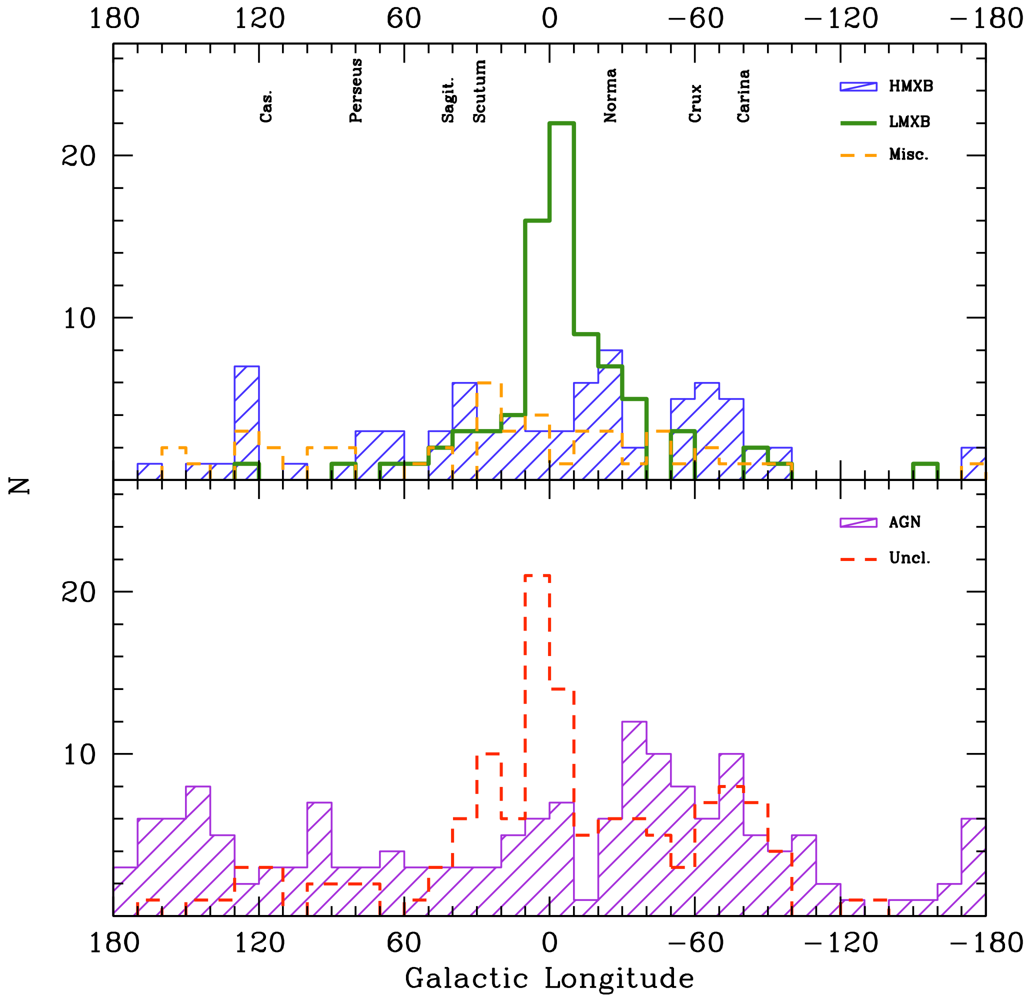

Figure *13.1: Distribution of Galactic longitudes for ISGRI sources where each bin represents* $l = 10°$. *The figure at the top presents the distributions of HMXBs (shaded blue histogram), LMXBs (thick green histogram), and miscellaneous sources (dashed orange histograms). Unclassified sources (dashed red histogram) and extragalactic sources (shaded purple histogram) are displayed in the lower figure. The directions to the spiral arm tangents are indicated.*

tories and ages. The distribution is still Galactic, with high latitudes in many cases stemming from their proximity to the Sun ($\langle d \rangle \sim 1$ kpc). Extragalactic sources are detected wherever there is enough exposure (Fig. 13.6), so the distribution is roughly flat in both longitude and latitude.

Unclassified sources have a distribution of Galactic latitudes that peaks in the central 3° from the Galactic Plane and decreases gradually, suggesting a population of sources that are Galactic rather than extragalactic in origin (Fig. 13.2). In terms of the latitude distribution of unclassified sources, the probability of statistical com-

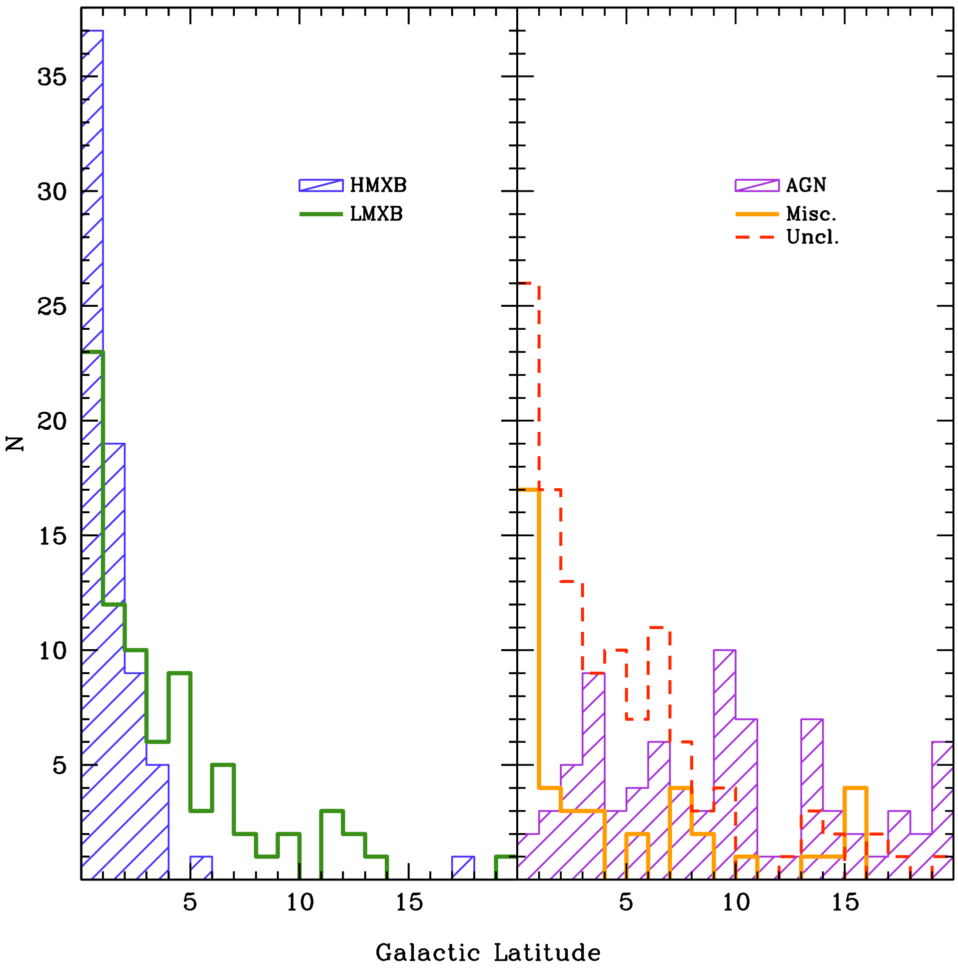

Figure *13.2: Latitudinal distribution (with 1°-bins, for $|b| < 20°$) of sources that have been detected by ISGRI. Shaded histograms are HMXBs (left) and AGN (right), and the clear histograms represent LMXBs (left) and unclassified sources (right). The distributions have been summed over the northern and southern Galactic hemispheres.*

patibility from a Kolmogorov-Smirnov (KS) test is nearly 40% with LMXBs, compared with 13% for miscellaneous sources, and less than 0.001% for either AGN or HMXBs.

While there are extragalactic sources among them, the population of unclassified sources shown in Fig. 13.7 is therefore likely to be composed primarily of Galactic sources such as LMXBs and miscellaneous sources. Since many of them are IGRs, the reasons they have avoided classification are: the companion stars to LMXBs are usually faint in the optical/IR spectrum; they are located near the Galactic Plane where absorption and source confusion prevent an identification; and, for many

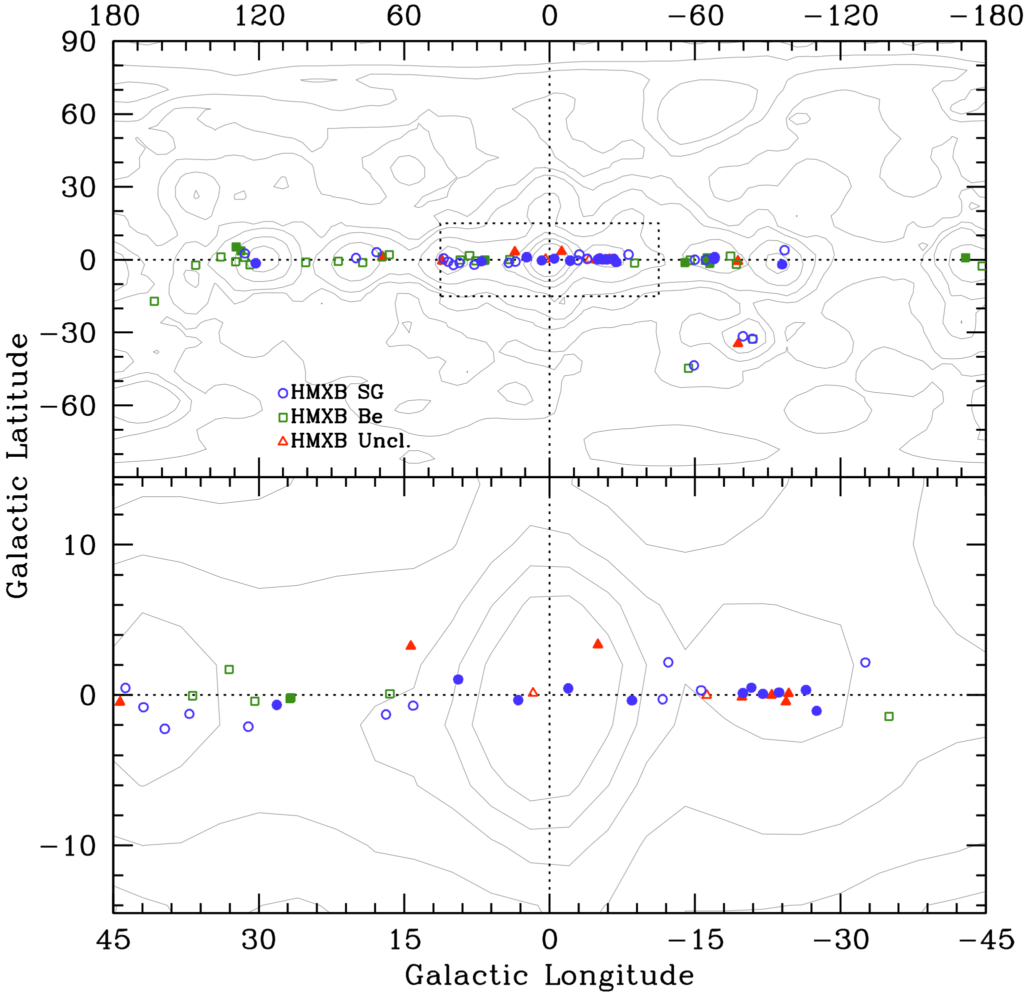

Figure *13.3: Spatial distribution of HMXBs whose companions are SG stars (blue circles), Be stars (green squares), or unknown (red triangles). Filled symbols represent IGR sources. The lower figure focuses on the inner Galaxy (boxed area in upper figure) with contours from the exposure map of Fig. 12.1.*

of these sources, their transient emission complicates efforts to perform follow-up observations. Recent improvements in ToO campaigns aimed at new IGRs have uncovered as many new transient LMXBs in the last year as during the first 3 years of observations combined.

13.2 Galactic Distribution

A histogram of galactocentric radii (Fig. 13.8) shows LMXBs peaked at the center and decreasing gradually. This is similar to the distribution of globular clusters (Bica et al. 2006) which harbor old KM-type companions of LMXBs. On the

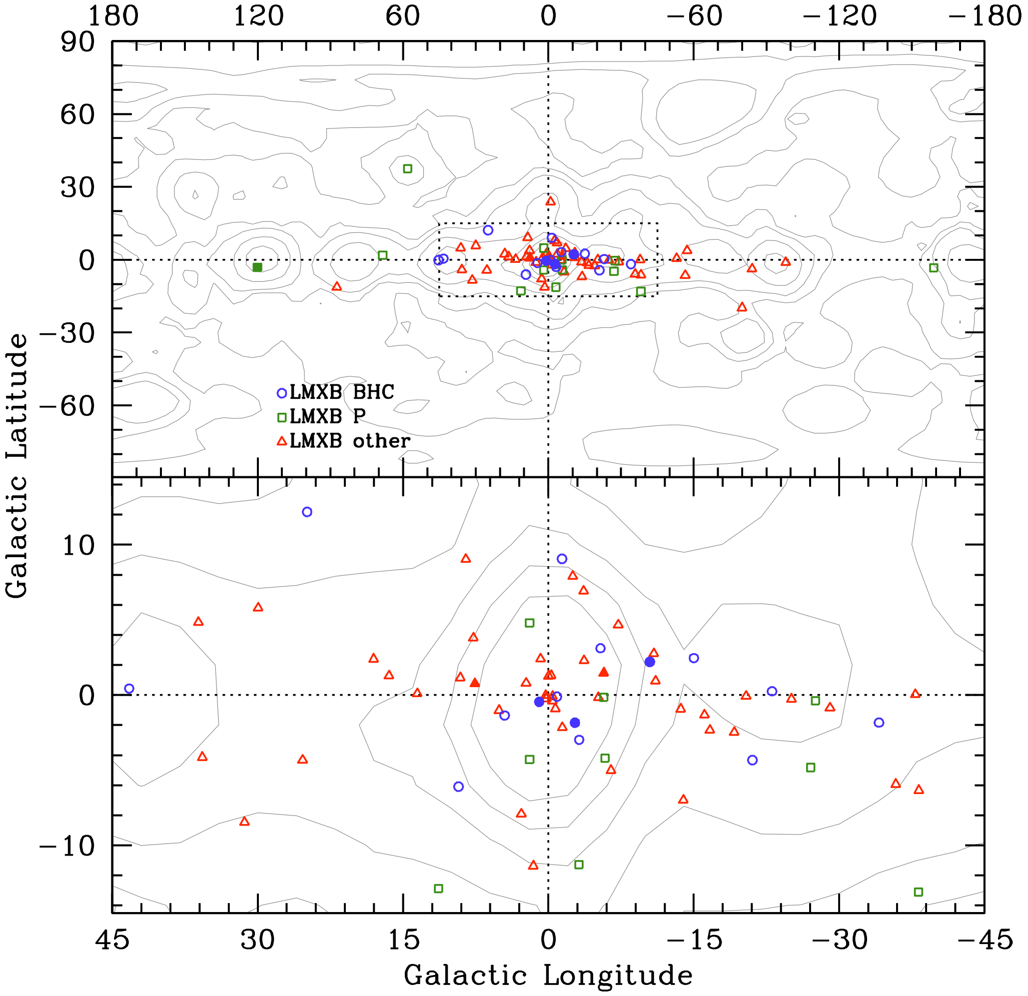

Figure *13.4: As in Fig. 13.3, but for LMXBs that are BHCs (blue circles), X-ray pulsars (green squares), and others (red triangles).*

other hand, HMXBs roughly follow the distributions from H II/CO surveys (Russeil 2003), the tracers of young star-forming regions: i.e. underabundant in the central few kpc with peaks at the spiral arms. According to a KS test, the probability is less than 0.01% that the galactocentric distributions of LMXBs and HMXBs are statistically compatible.

Following the procedure in Dean et al. (2005), we set the number of sources as a function of the distance in kpc above the Galactic Plane (h) according to:

$$N = k \cdot e^{-\alpha \cdot h} \tag{13.1}$$

where $\alpha \equiv 1/h_0$ describes the steepness of the exponential.

The values that we derive for the characteristic scale height (h_0) for HMXBs and

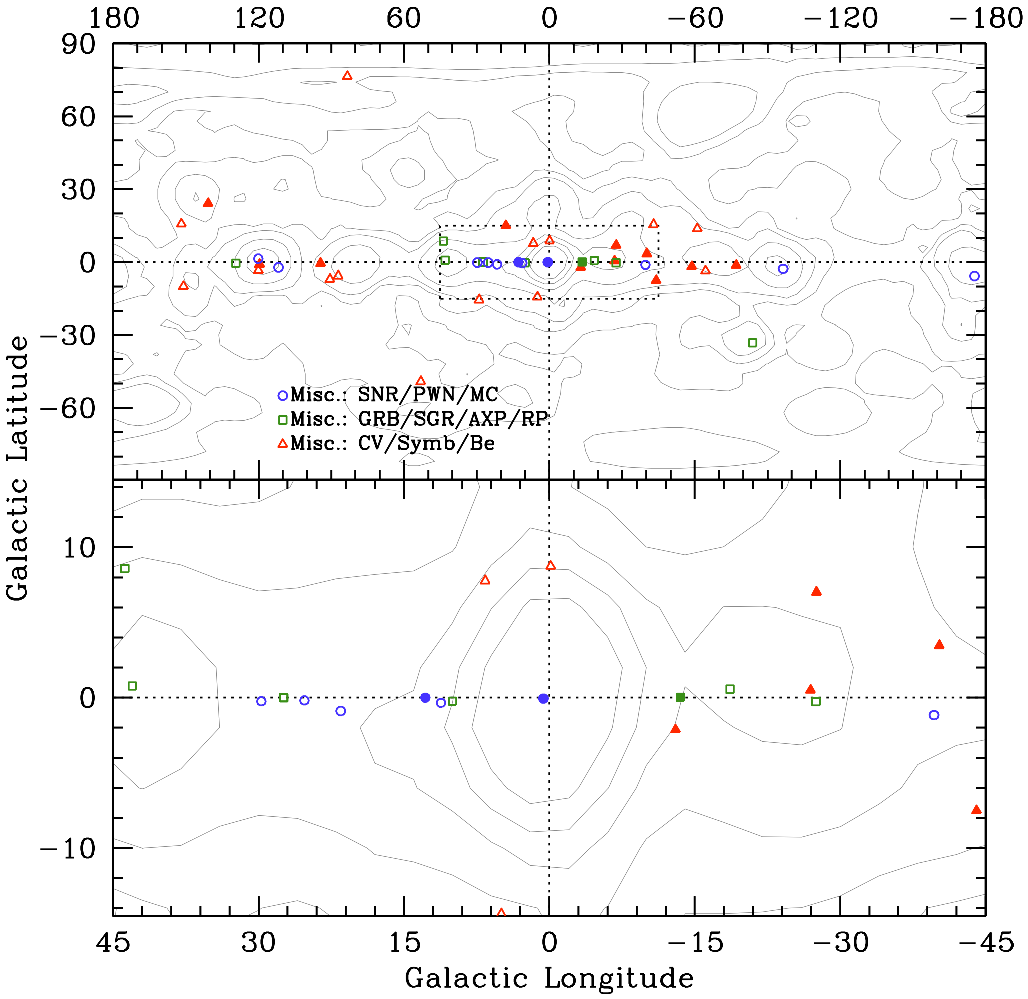

Figure *13.5: Same as Fig. 13.3, but for miscellaneous sources. Supernova remnants, pulsar wind nebulae, and molecular clouds are represented by blue circles. Green squares represent gamma-ray bursts, soft gamma repeaters, anomalous X-ray pulsars, and radio pulsars. Stellar objects such as cataclysmic variables, symbiotic stars, and Be stars are represented by red triangles.*

LMXBs are compatible with those of Grimm et al. (2002) and Dean et al. (2005). In determining the scale height for their unclassified IGRs, Dean et al. (2005) assumed a source distance of 8 kpc, which led them to conclude that a Galactic origin was likely for their unclassifieds. At a distance of 8.5 kpc, the unclassified sources in our sample have a characteristic scale height ($h_0 = 560^{+240}_{-130}$ pc) that is reminiscent of a thick disk population of LMXBs ($h_0 \sim 680$ pc), rather than the thin disk HMXBs ($h_0 \sim 134$ pc). However, the assumption of a Galactic distance is tenuous given what little we know about the unclassified IGRs. Furthermore, it is not surprising that assigning a typically Galactic value to a group of objects of unknown origin results in a Galactic distribution.

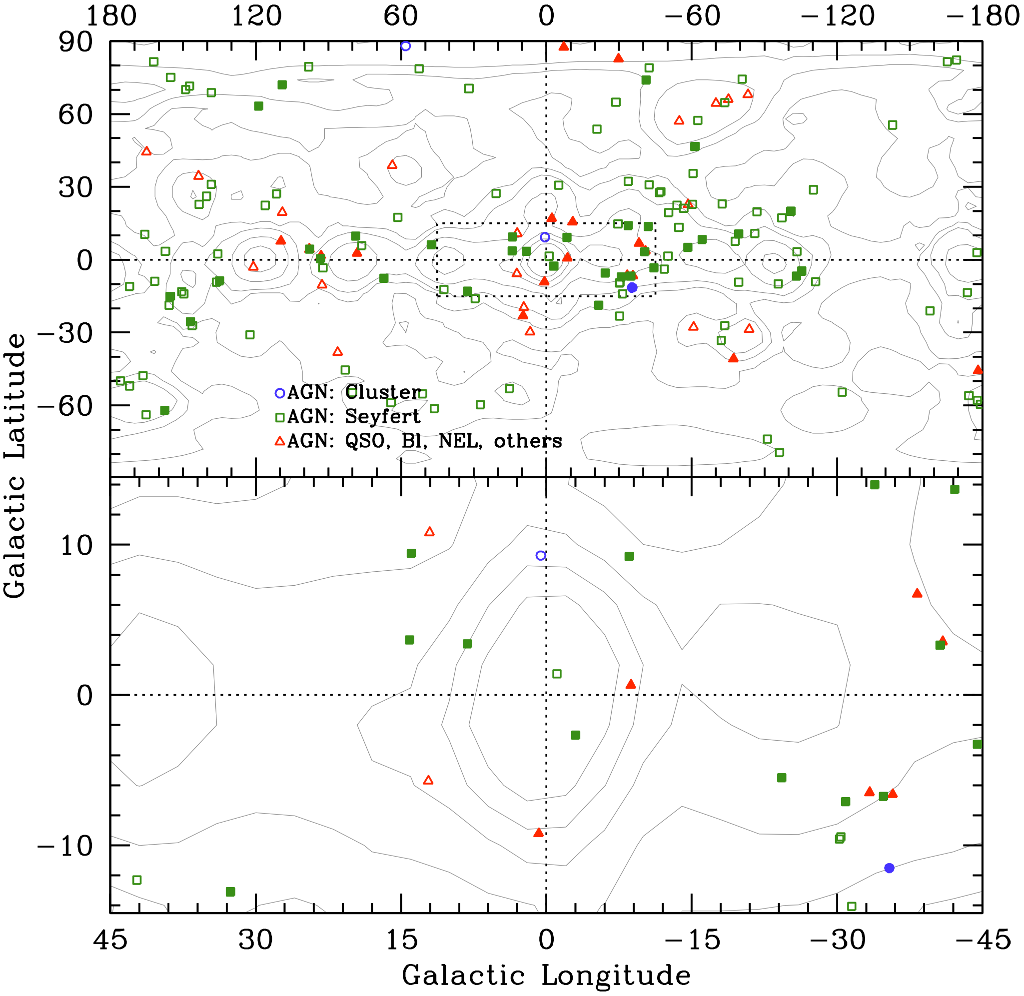

Figure *13.6: Same as Fig. 13.3, but for extragalactic sources. Blue circles denote clusters of galaxies, green squares represent Seyfert galaxies, and red triangles symbolize quasars, blazars, narrow-emission line galaxies, and others.*

In the central Galaxy, the distribution of LMXBs is compatible with the distribution of globular clusters (Bica et al. 2006) (Fig. 13.9). A slight asymmetry in the distribution of LMXBs suggests an association with the Galactic bar.

Figure 13.9 shows that the distribution of HMXBs in the Galaxy generally coincides with the distribution of massive star-forming regions from Russeil (2003). Lutovinov et al. (2005a) and Dean et al. (2005) found that the distribution of HMXBs was offset with respect to the directions of the spiral arm tangents. The type of Galactic model used (i.e. assumptions about the Sun-GC distance, the number of spiral arms and their pitch angles) can heavily influence the directions to the tangents. If the shift is real, it would be the signature of the time delay between the

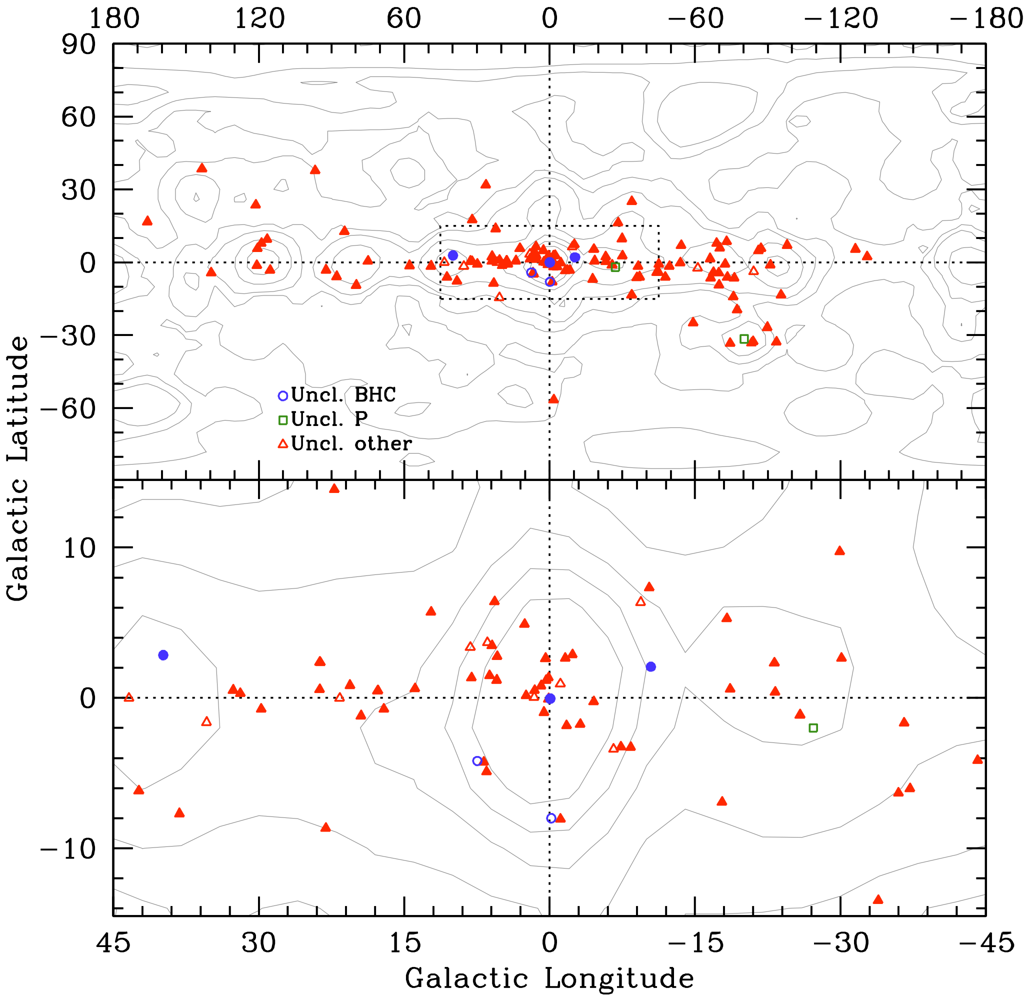

Figure *13.7: Same as Fig. 13.3, but for unclassified sources that are BHCs (blue circles), X-ray pulsars (green squares), and others (red triangles).*

formation of a binary system and the time when one of its stars becomes a compact object. For HMXBs, this corresponds to $\sim 10^7$ yr.

Differential rotation was introduced to the Galactic 4-armed model of Russeil (2003) in order to rewind time about 10^7 yr, corresponding to a rotation around the GC of $\sim 40°$ for a Galactic radius of 3 kpc. The purpose is to use the complexes that are currently active to deduce the locations that produced the current crop of HMXBs. Solid rotation of the inner 8.5-disk, and assigning each complex a statistical weight equal to the activity of the complex were also tested.

Kolmogorov-Smirnov tests suggest that the effects of Galactic rotation are negligible, even when only the most active sites are considered (Fig. 13.11). The conclusion is that even though the peak in the HMXB distribution does not coincide

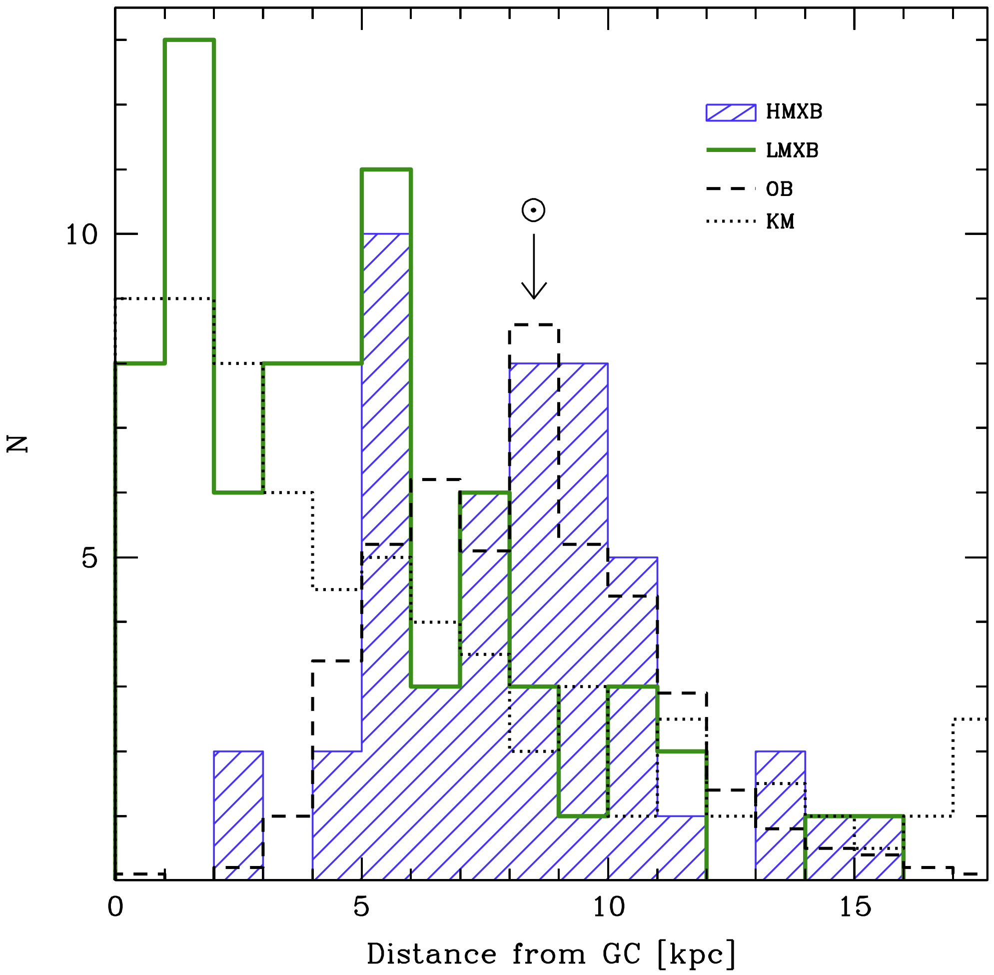

Figure *13.8: Distribution of galactocentric distances of HMXBs (49, shaded blue histogram) and LMXBs (74, red histogram). The dashed and dotted histograms (divided by 2) represent OB star-forming complexes from Russeil (2003) and globular clusters from Bica et al. (2006), respectively.*

with the tangent to the Norma Arm as defined by the model of Russeil (2003) (or others), the HMXBs are still closely associated with active sites of massive star formation.

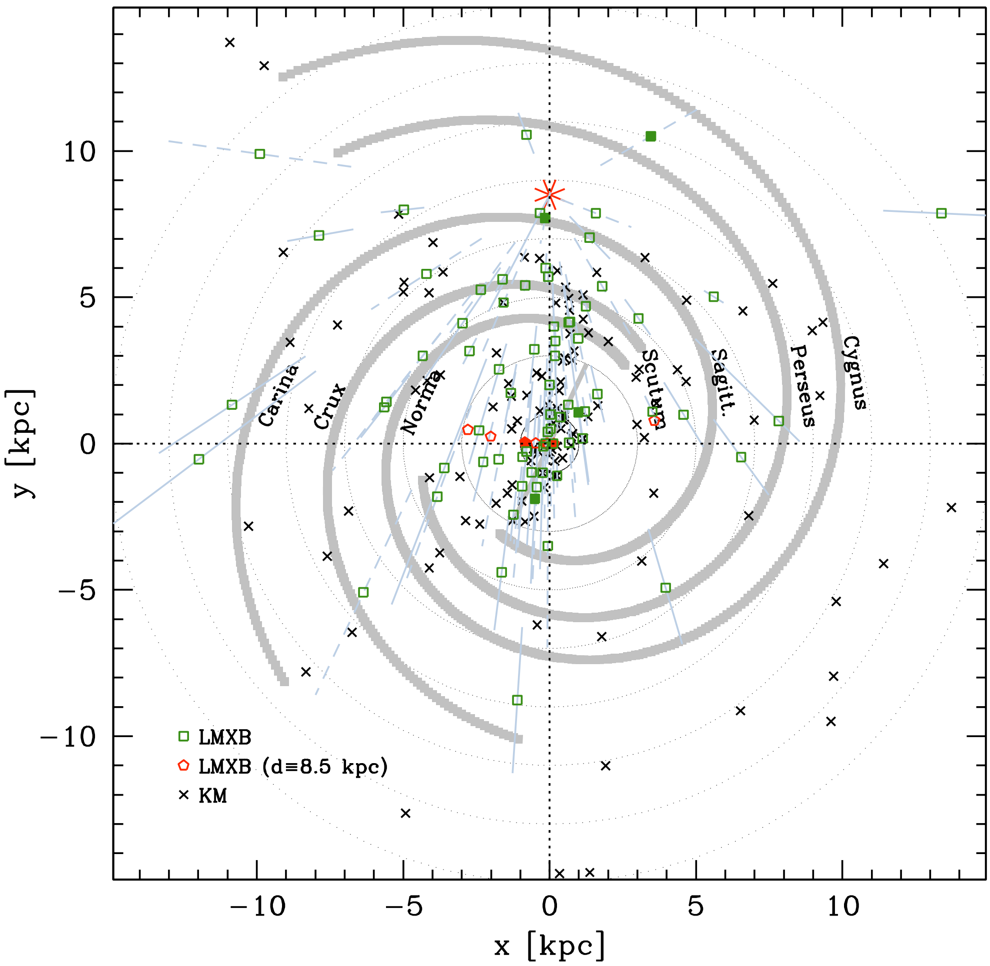

Figure *13.9: Face-on view of the Milky Way as seen from above with LMXBs whose distances are known (49, green squares) and the locations of old globular clusters from Bica et al. (2006) (153, black crosses). The error bars are known (solid lines) or are assumed equal to the square root of the distance (dashed lines). Those HMXBs with unknown distances (23, red pentagons) are placed at 8.5 kpc from the Sun (red star symbol) Filled symbols represent IGRs.*

13.3 Log(N)–Log(S)

Consider a disk of radius r with a distribution of N sources where n is the number of sources per element of surface. If the distribution is homogenous, then the number of sources that are expected in an annulus dr is:

$$dN = 2\pi r dr \cdot n$$

Suppose that each source is observed with a certain a flux:

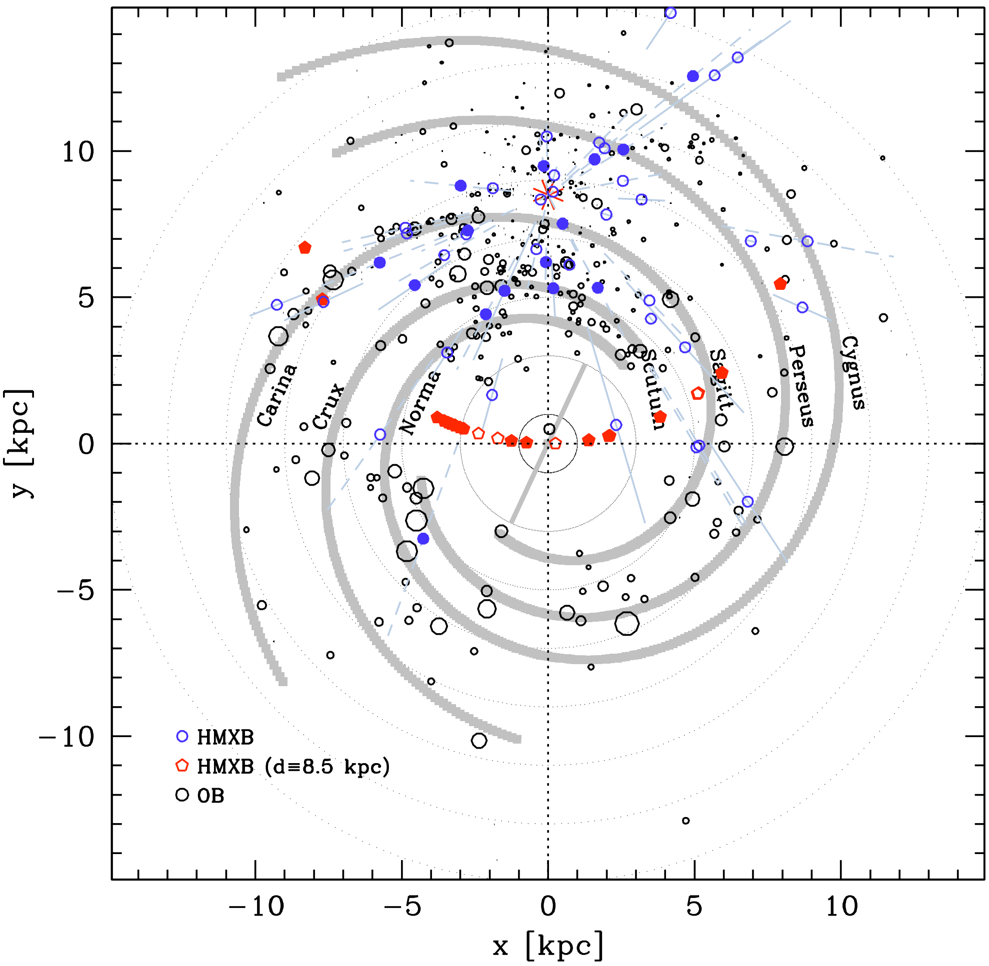

Figure *13.10: Galactic distribution of HMXBs whose distances are known (49, blue circles) and the locations of star-forming complexes from Russeil (2003) (464, black circles). The symbol size of the latter is proportional to the activity of the complex. The error bars are known (solid lines) or are assumed equal to the square root of the distance (dashed lines). A distance of 8.5 kpc is assigned to HMXBs whose distances are unknown (23, red pentagons). Filled symbols represent IGRs.*

$$
\begin{aligned}
S &= \frac{L}{4\pi r^2} \quad \Big\{ \quad dS = -\frac{L}{2\pi r^3} dr \\
\Rightarrow dN &= 2\pi r \left(-\frac{2\pi r^3}{L} dS \right) n = -\frac{4\pi^2 r^4 n}{L} dS = -\frac{Ln}{4S^2} dS \\
\Rightarrow N(S) &= -\frac{Ln}{4} \int_{\infty}^{S} \frac{dS}{S^2} \sim S^{-1}
\end{aligned}
$$

Thus, the slope and shape of the Log(N)–Log(S) function reflect the spatial dis-

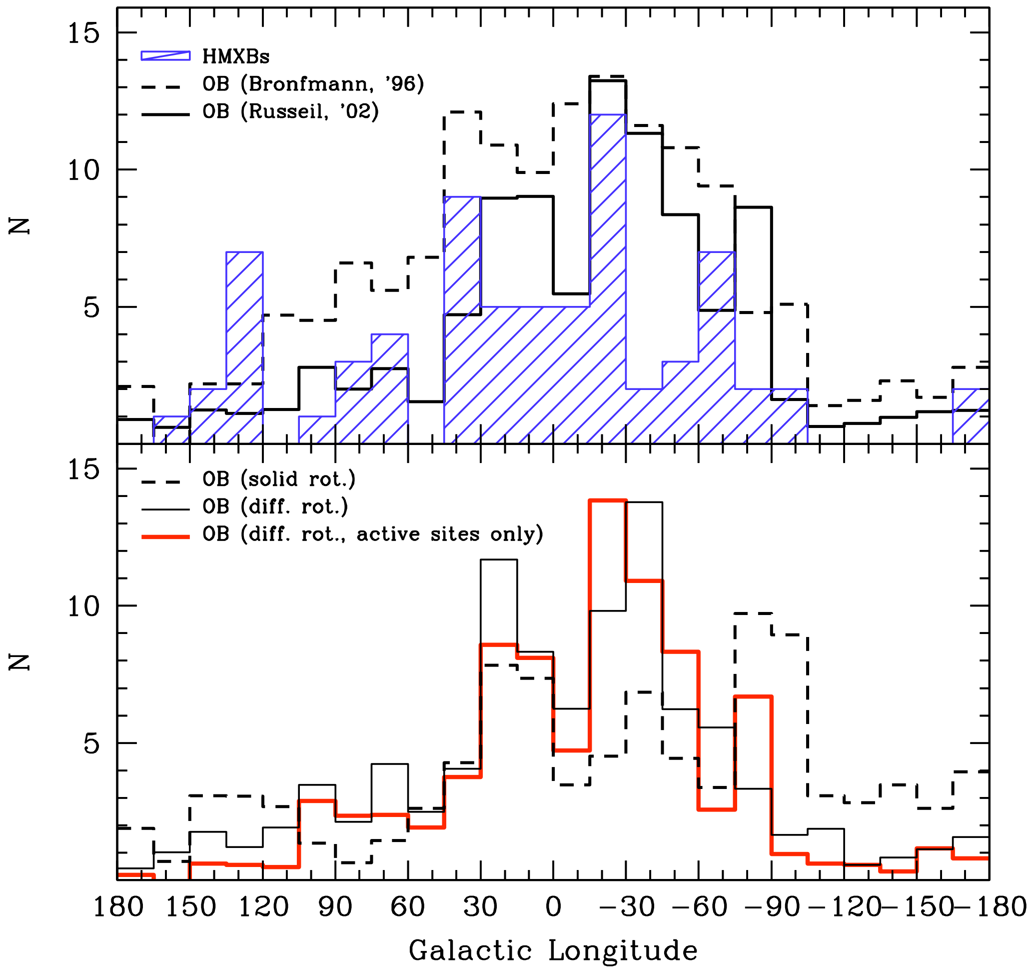

Figure *13.11:* top*: Histograms of Galactic longitudes integrated over the latitude for HMXBs with* $|b| < 6°$ *(shaded blue histogram) and star-forming regions from Russeil (2003) (thick black histogram, divided by 300) and Bronfman et al. (1996) (dashed black histogram, divided by 10).* bottom*: Same as above for the star-forming complexes (divided by 300) of Russeil (2003) featuring a solid Galactic rotation of* 40° *of the inner 8.5 kpc (dashed black histogram), a differential Galactic rotation with angles* ~ 40° *in the central 3 kpc and decreasing with radius (thin black histogram), and for a differential Galactic rotation focusing on the most active sites only (thick red histogram). Each complex has been assigned a statistical weight that is equal to its excitation parameter (measures the amount of ionizing photons).*

tribution, and by extension the origin and evolution, of detected sources. Similar reasoning for a spherical distribution (e.g. AGN) yields a slope of $-3/2$. For faint sources, an observational bias from limits in the instrumental sensitivity will lead to a deviation from the expected number-flux relation.

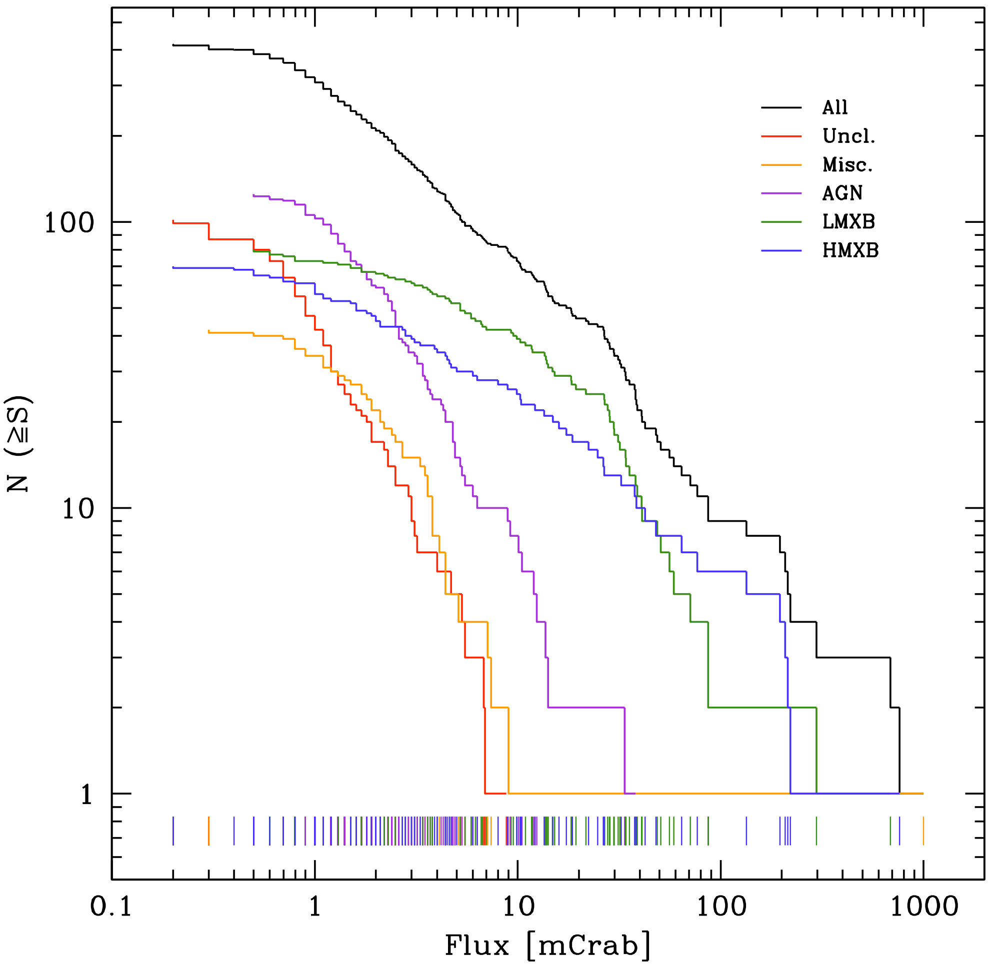

Figure *13.12: Log(N)–Log(S) functions for the various classes of objects in this sample with fluxes from Bird et al. (2007). Vertical lines represent the flux levels of individual sources.*

Constructing the Log(N)–Log(S) curve from the sample of ISGRI sources is not a straightforward exercise. The sources were culled from a series of publications that used different energy bands in their analyses. Source fluxes are therefore representative of a specific time and wavelength rather than an average. A systematic analysis of long-term mosaics in a given energy band is the best way to obtain time-averaged fluxes for a group of sources. However, surveys might miss short-lived sources, and the variability and transience of many γ-ray sources confuses the notion of an average flux.

Another complication stems from the non-uniformity of the exposure map. Faint sources are detected only when enough exposure is accumulated. It follows that

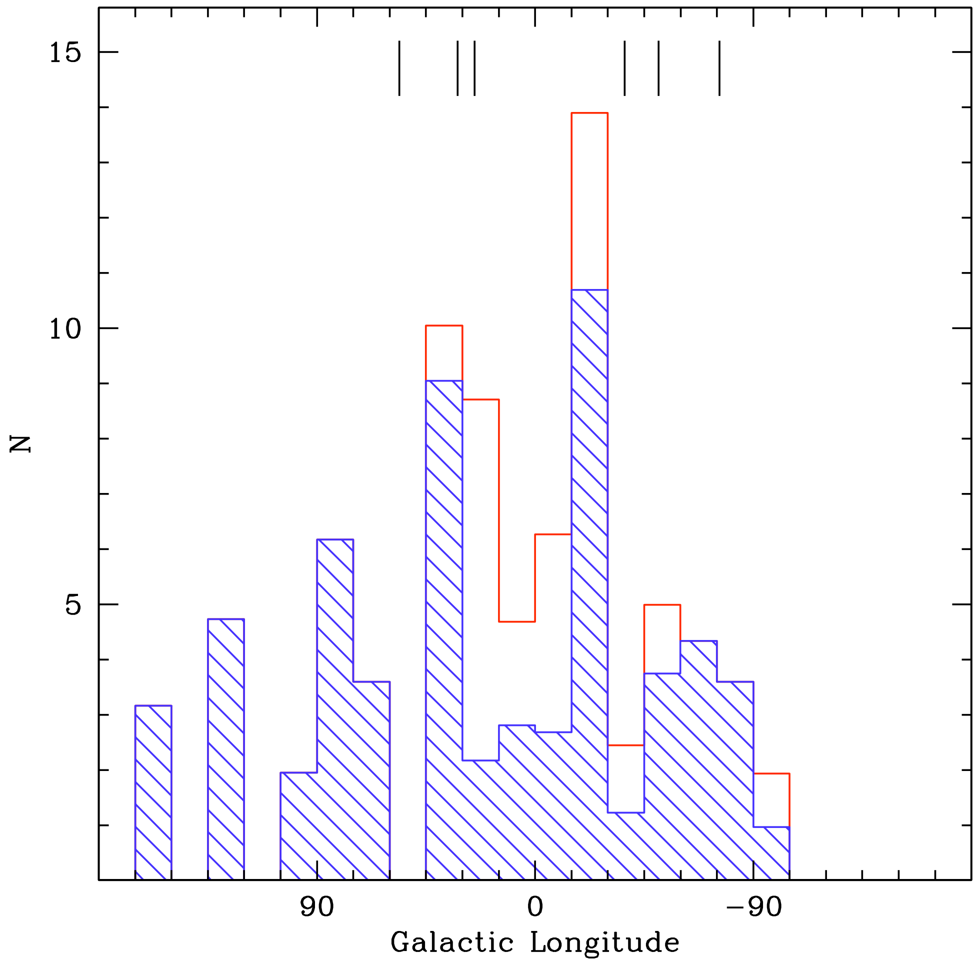

Figure *13.13: Normalized longitudinal distribution of HMXBs from Bird et al. (2006) assuming a slope of* -0.7 *for the Log(N)–Log(S) relation. The bin size is* $15°$. *The shaded histogram represents HMXBs, with the clear segments of each bin denoting unclassified sources situated near the Galactic plane* ($|b| < 2°$)*. Vertical lines correspond to the spiral arm tangents from Russeil (2003).*

ISGRI source detections are deficient in regions of the sky that are still under-exposed. Grimm et al. (2002) worked with a homogenous exposure map, and a systematically-produced set of fluxes in order to generate the Log(N)–Log(S) function for sources from *RXTE*/ASM.

Roughly 85% of the sources in this sample have a soft band (20–40 keV) flux listed in Bird et al. (2007), which were used to build the log(N)–log(S) curves displayed in Fig. 13.12. The flattening of the curves at low fluxes is a relic of the uneven exposure map. One way to account for this is to establish a minimum detectable flux at every location of space in relation to its exposure time. In this case, the number density is considered as a function of the minimum detectable flux. When properly accounted for, the number-flux relation of a cosmological distribution of sources (e.g. AGN) can be modeled by a power law with a slope of $-3/2$.

As long as the spatial distribution of a population of sources is well understood, one could use the expected Log(N)–Log(S) relation to normalize a distribution of sources from a survey taken with varying exposure times. For example, the longitudinal distribution of HMXBs (Fig. 13.1) shows that there are peaks at the inner spiral arm tangents, but the higher numbers of detected sources could simply be the product of more exposure time dedicated to these areas.

Fitting a power law to the exposure-corrected Log(N)–Log(S) relation for HMXBs from Bird et al. (2006) yields a slope of -0.7. The exposure map along the Galactic Plane from Bird et al. (2006) was split into 15°-bins where the exposure times of all pixels in that bin were averaged ($t_{\rm bin}$). Let $N_{\rm det}$ be the number of sources detected in each bin. If the Galactic Plane were evenly exposed with (e.g.) 1 Ms, the number of sources that we should detect can be expressed as:

$$N_{\rm norm} = N_{\rm det}\left(\frac{1\,{\rm Ms}}{t_{\rm bin}}\right)^{0.35}$$

Figure 13.13 displays the normalized HMXB distribution that results. Peaks at the inner arms are still observed, while the population of HMXBs in arms near the Sun (high longitudes, and lower exposures) is enhanced, and the number of sources in the heavily-exposed GC is reduced.

Chapter 14

Absorption & Modulations

14.1 Absorbed IGRs

On average, Galactic IGRs are more absorbed than the sources seen before *INTEGRAL* (by a factor of ~4) with a KS test yielding a probability of less than 0.01% that the two groups are drawn from the same parent distribution (Fig. 14.1). A large absorption is also a common feature of extragalactic IGRs. However, as a group, they are not more absorbed than pre-*INTEGRAL* AGN (Fig. 14.2).

Some of the observed column density is extrinsic given that many IGRs are located where interstellar absorption is expected to be high, such as along the Galactic Plane and towards the spiral arms. However, the highest value of Galactic N_H is $\sim 3 \cdot 10^{22}$ cm^{-2} (Dickey & Lockman 1990). Objects with $N_H \gtrsim 10^{23}$ cm^{-2} can not be explained by interstellar absorption alone. Most of the absorption is therefore intrinsic. Obscuring material is believed to surround the system and suppress the soft X-ray spectrum, while contributing to the X-ray luminosity whenever it is accreted.

The high average column density of Galactic IGRs is directly related to the disproportionate number of SG HMXBs, which tend to be heavily-obscured systems, that *INTEGRAL* has found.

14.2 The Absorption Map

Distant (or more luminous) sources could be expected to have a higher column density than nearby sources. There is a very weak to insignificant correlation between N_H and the distance or the luminosity for HMXBs (see Fig. 14.3).

For a column density N_H and an interstellar absorption N_H^G (Dickey & Lockman 1990), we define the normalized absorption parameter $\eta \equiv N_H/N_H^G$. The spatial distribution of η is presented in Fig. 14.4.

This absorption map can be used for highlighting potential clustering or asymme-

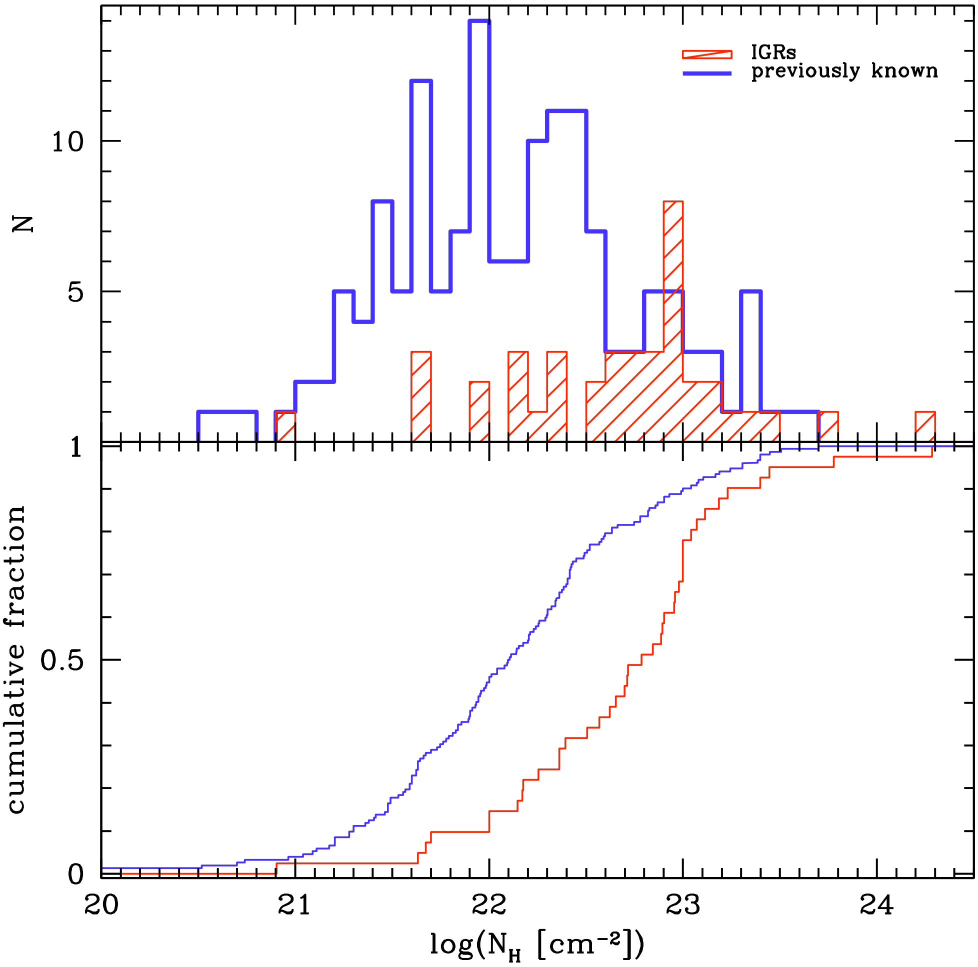

Figure *14.1: The distribution of reported column densities ($N_{\rm H}$) for Galactic sources (including sources in the Magellanic Clouds) that were previously known (152, clear histogram) and for IGRs (41, shaded histogram). The lower figure presents the results of the Kolmogorov-Smirnov test which yields a probability of $\lesssim 0.2\%$ of statistical compatibility between the $N_{\rm H}$ distribution of Galactic IGRs and that of previously known sources.*

tries in the local distribution of matter. Figure 14.4 shows that the Norma Arm hosts many of the most heavily-absorbed Galactic sources ($N_{\rm H} \gtrsim 10^{23}$ cm^{-2}). This region also happens to be the most active formation site of young supergiant stars (Bronfman et al. 1996). These stars are the precursors to the absorbed HMXBs that ISGRI is discovering preferentially in the Norma Arm. While the Galactic Bulge and the Scutum/Sagittarius Arms host some obscured sources, they are less numerous than in the Norma Arm. This image was named ESA's *INTEGRAL* Picture of the Month (May, 2007) and NASA's high-energy astrophysics Picture of the Week (June 11, 2007).

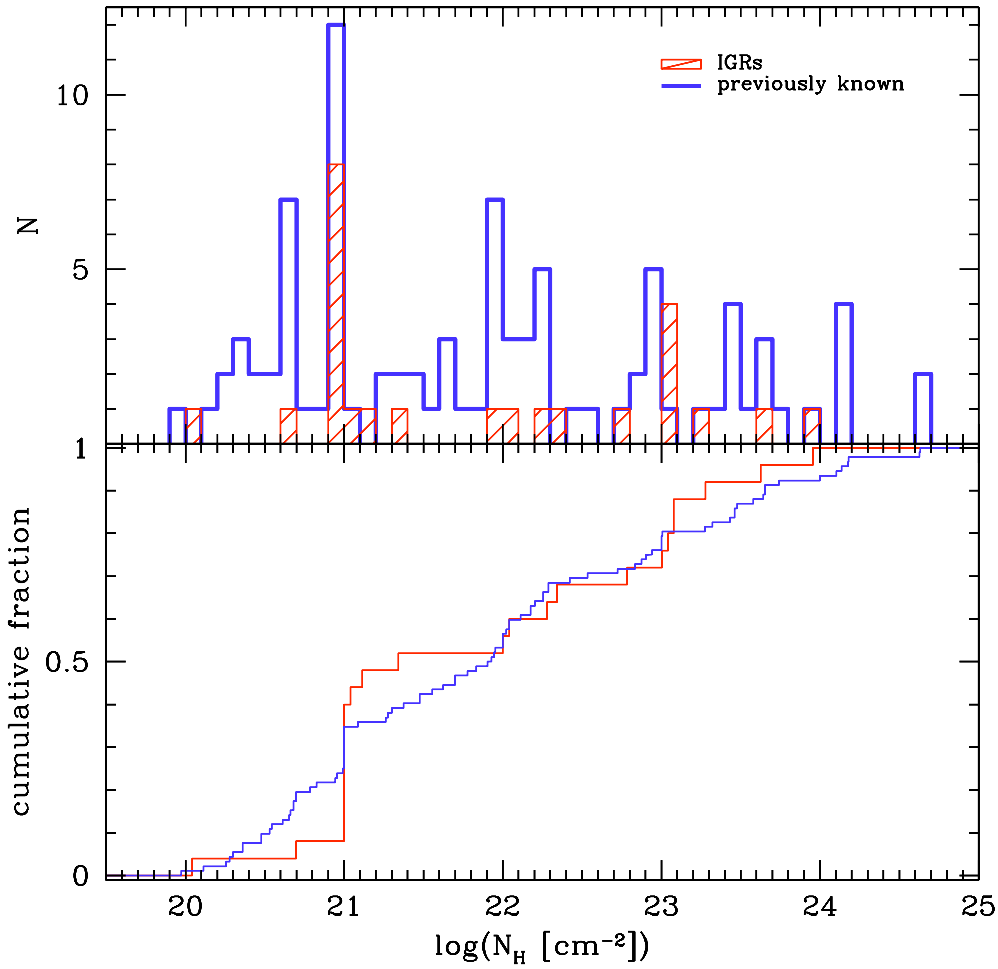

Figure *14.2: The distribution of reported column densities (N_H) for extragalactic sources that were previously known (92, clear histogram) and for IGRs (25, shaded histogram). The lower figure presents the results of the Kolmogorov-Smirnov test which yields a probability of* ~ 50% *of statistical compatibility between the N_H distribution of extragalactic IGRs and that of previously known sources.*

14.3 The P_S–N_H and P_O–N_H Diagrams for HMXBs

Most IGRs for which a pulsation has been measured have spin periods (P_S) in the range of 100–1000 s, or around 10 times longer than the average pulse period of pre-*INTEGRAL* sources. *INTEGRAL* and *XMM-Newton* feature long orbital periods around the Earth which means that a source can be observed for long periods of time without interruptions, so that pulsations on the order of a few hundreds of seconds or more can be detected. Supergiant HMXBs, which are well represented

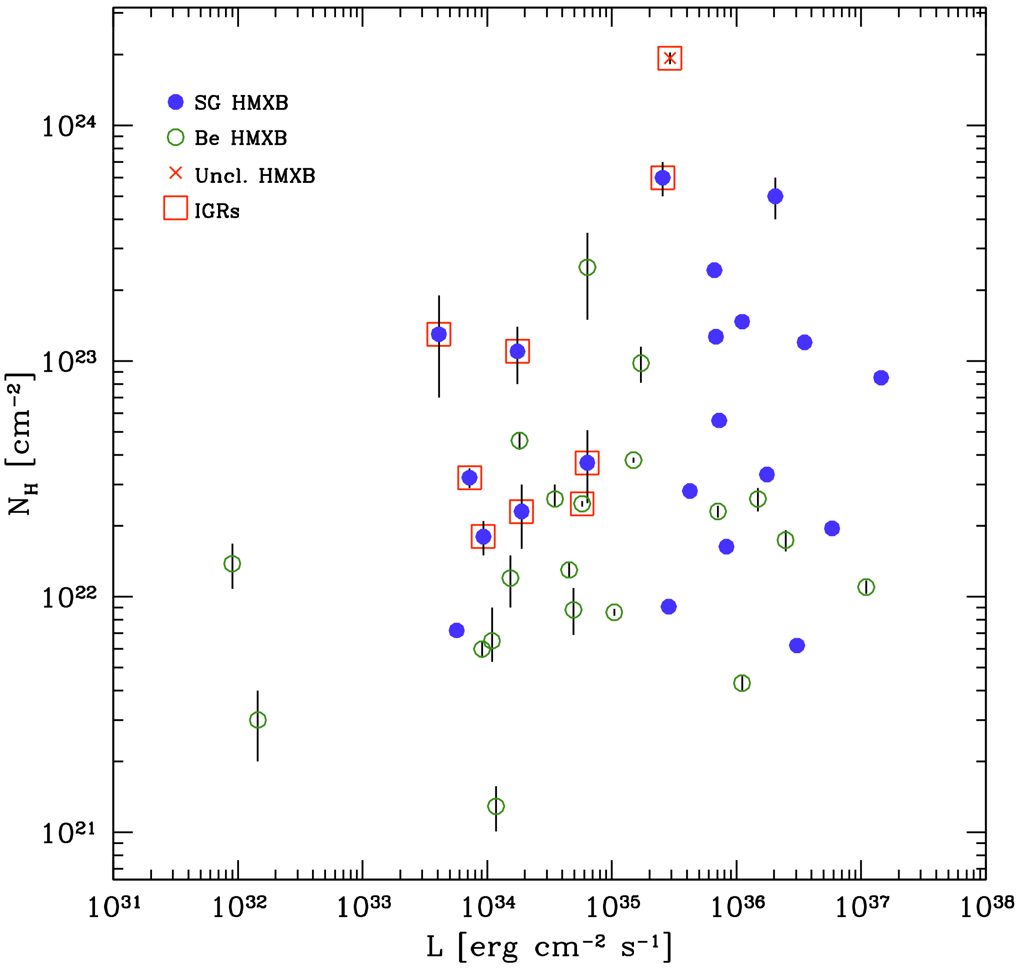

Figure *14.3: Reported column densities (N_H) for HMXBs as a function of the source luminosity as derived from the soft 20–40 keV band flux of Bird et al. (2007).*

among IGRs, tend to have long pulse periods (e.g. Corbet 1984).

The influx of new absorbed X-ray pulsars made it is possible to test for dependencies between the intrinsic column density and the modulations. The observed spin period of a NS in a HMXB is regulated by, among other things, the angular momentum of the wind of the stellar companion. Assuming a constant rate of spherically-symmetric accretion from a radiation-driven stellar wind, and assuming that the accreted material has an angular momentum that points in the same direction as the spin of the NS, the spin period will reach an equilibrium value $P_{eq} \propto \rho^{-3/7}$ (Waters & van Kerkwijk 1989). Using N_H as an estimate for the density of material available for accretion, and assuming that $P_S \sim P_{eq}$, we could find a similar relation: $P_S \propto N_H^{-3/7}$.

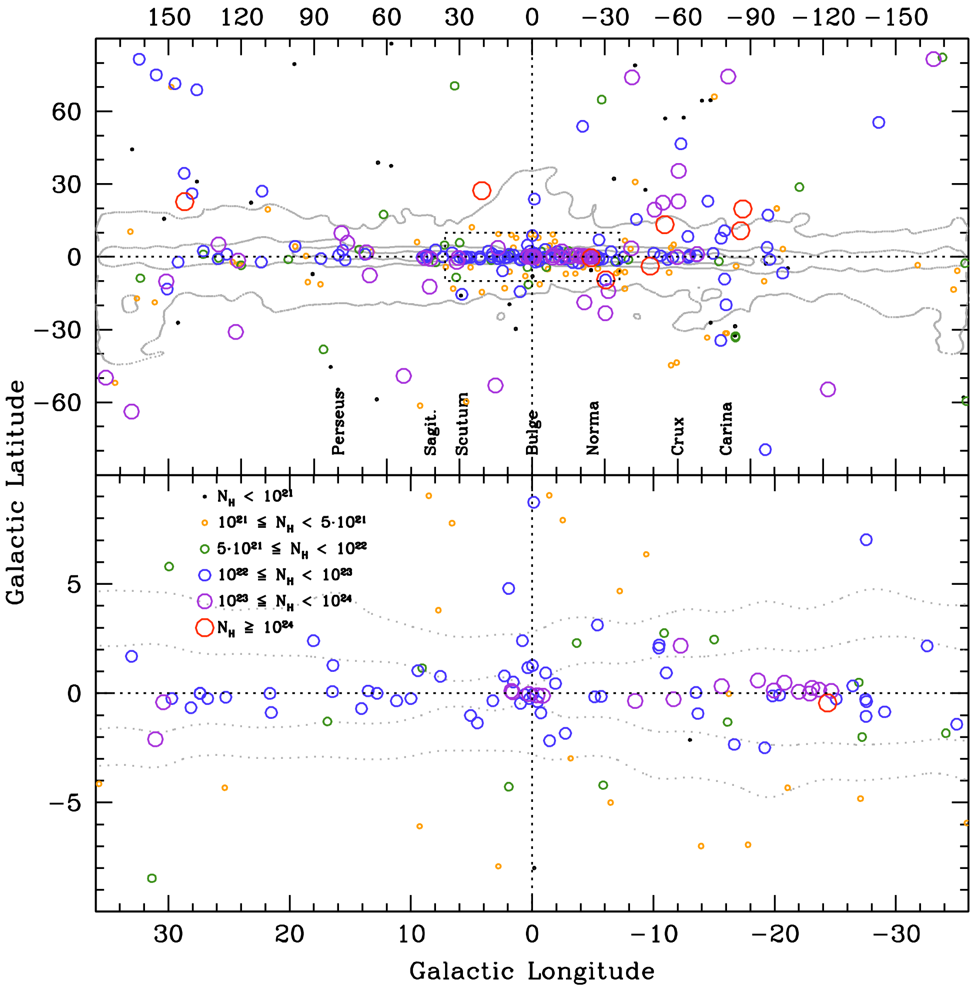

Figure *14.4: Spatial distribution, in Galactic coordinates, of all sources detected by ISGRI for which* $N_{\rm H}$ *has been reported. The symbol size is proportional to the published column density normalized by the expected Galactic absorption from (Dickey & Lockman 1990). The figure at the top shows the whole sky and includes extragalactic sources, while the figure at the bottom focuses on the Bulge region (boxed region in the figure at the top) and excludes extragalactic sources. Contours denote Galactic absorption levels of* 10^{21}, $5 \cdot 10^{21}$, *and* 10^{22} *cm*$^{-2}$ *(Dickey & Lockman 1990).*

High-mass X-ray binaries are segregated into distinct regions of a $P_{\rm S}$–$N_{\rm H}$ diagram (Fig. 14.5). This segregation could stem from the higher average $N_{\rm H}$ and longer average $P_{\rm S}$ of SG HMXBs compared to Be HMXBs. Even sources from the Magellanic Clouds seem to obey the rule, albeit with much lower column densities. The clear exceptions among SG HMXBs are Cen X-3 which, unlike the others, is a Roche-lobe overflow system, and OAO 1657−415 which might be transitioning from a wind-fed to a disk-fed system (Audley et al. 2006). There could be a weak positive correlation between the $N_{\rm H}$ and spin period for Galactic HMXBs. The slope of ~ 2.5 is different from the expected value of $-3/7$ and could indicate that

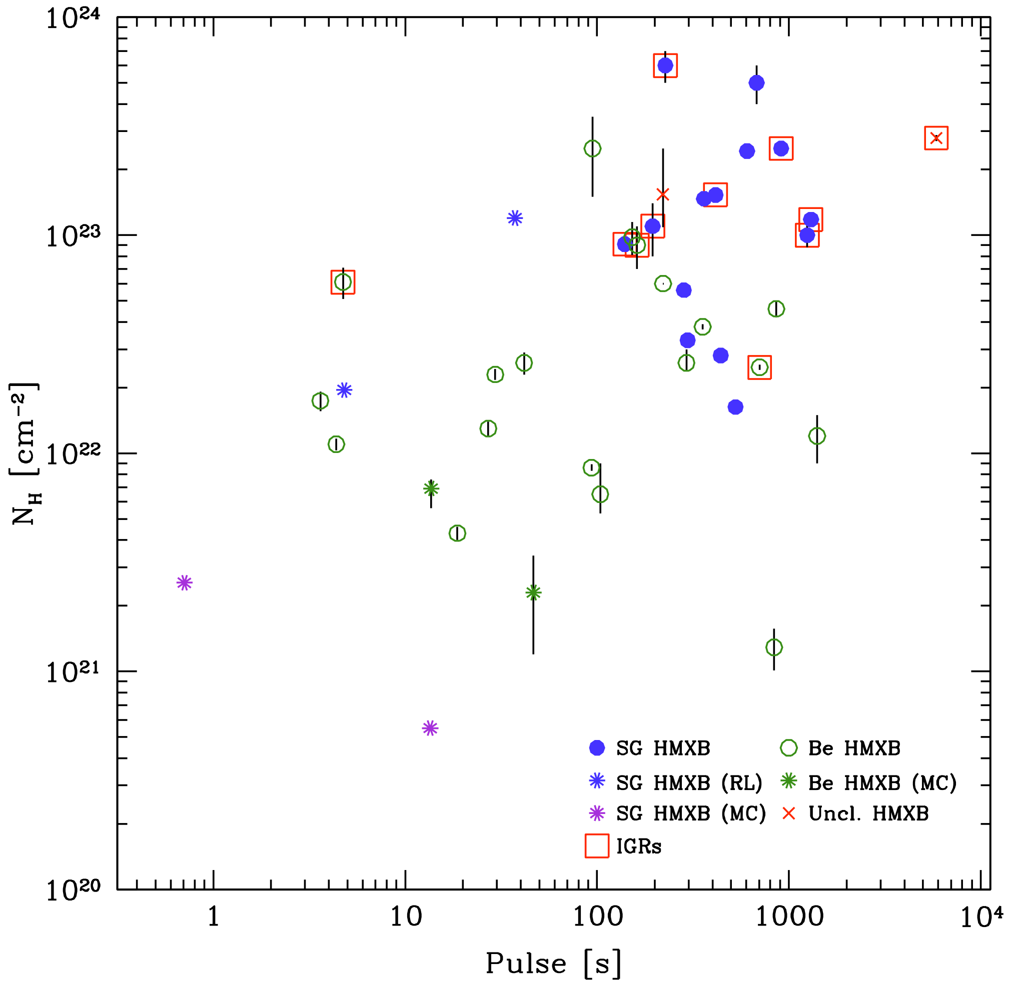

Figure *14.5: Spin period as a function of reported N_H value for HMXBs whose companions are OB supergiants (16, filled blue circles), Be stars (19, empty green circles), or unclassified (2, red crosses). IGRs are boxed and Magellanic Cloud (MC) sources are distinguished. Two SG HMXBs (Cen X-3 and OAO 1657−415) that are (or are transitioning to) Roche-lobe (RL) systems are symbolized by blue stars.*

the pulsars in Fig. 14.5 are spinning at periods that are longer than their equilibrium values would suggest.

Segregation is also observed among HMXBs with Be or SG companions in distributions of N_H and orbital period (Fig. 14.6). There also appears to be an anti-correlation of N_H and orbital period in Galactic HMXBs. In both types of systems, a shorter orbital period implies a compact object that is embedded deeper or spends more time in the dense regions of its stellar companion's wind resulting in more absorption.

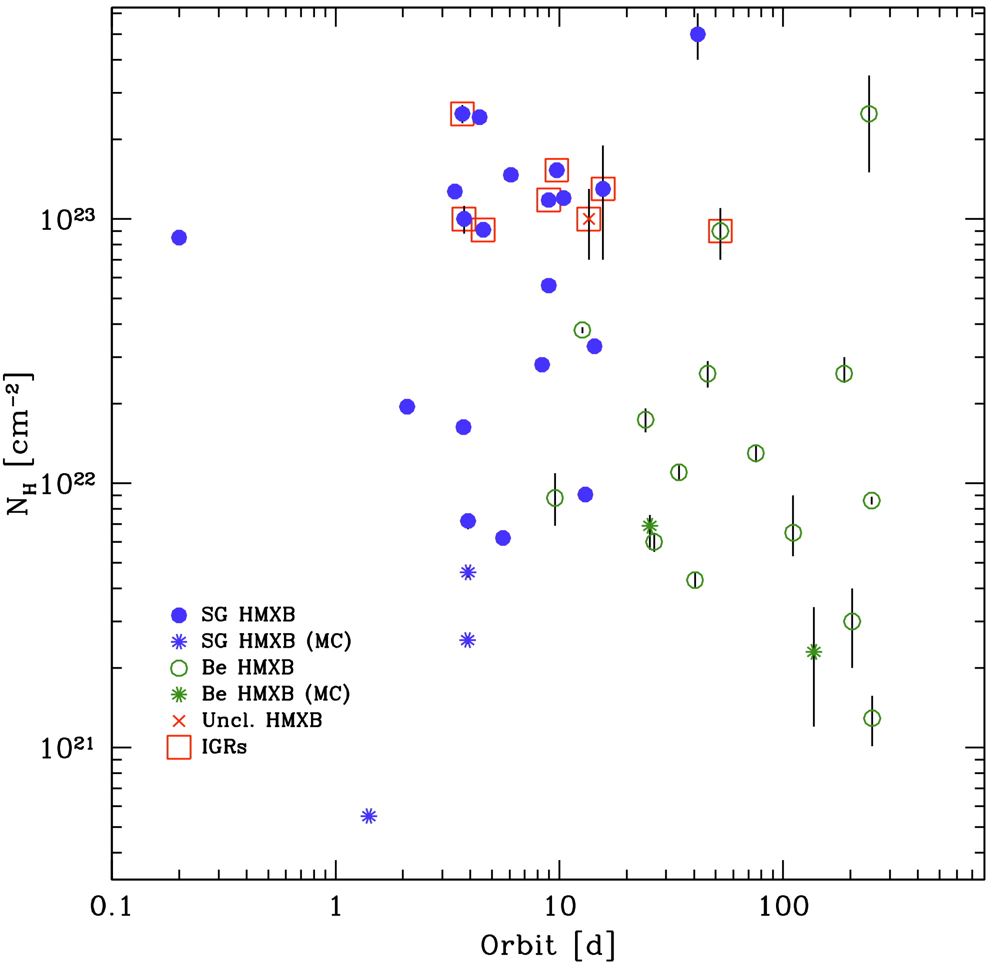

Figure *14.6: Orbital period versus reported N_H value for HMXBs whose companions are OB supergiants (20, filled blue circles), Be stars (15, empty green circles) or unclassified (1, red cross). IGRs are boxed and Magellanic Cloud sources are distinguished.*

These diagrams could serve as new tools to help distinguish between SG and Be HMXBs when only N_H and either the spin or orbital periods are known. This has been successfully used to predict a supergiant counterpart for 2 previously unclassified HMXBs (IGR J16358−4726 and IGR J19140+0951). If the trends underline a real physical effect, instead of being due to segregation of the groups into distinct locations of the plots, then they could help constrain models describing the influence of local absorbing matter on the modulations.

Chapter 15

Concluding Remarks

In 4 years, ISGRI has detected similar numbers of X-ray Binaries and Active Galactic Nuclei (AGN). The latter's numbers have increased recently given the increasing proportion of exposure time set aside for extragalactic fields. The former group contains new members of the class of HMXBs with supergiant stellar companions. Usually, this type of object presents strong intrinsic absorption which leads to a peak emission in an energy range that ISGRI is ideally suited to detect.

Many of the new SG HMXBs systems host neutrons stars with longer pulsations periods than average ($\sim$ 1 ks). The detection of such pulsation periods is made possible by the long orbital period of *INTEGRAL* which offers extended, uninterrupted coverage of a source during dozens of pulse cycles.

With the addition of these new systems, we are able to show for the first time that HMXBs are generally segregated in plots of intrinsic N_{H} versus the spin period of the pulsar, based on whether the companion is a Be or an OB supergiant star. There is an unexpected but weak correlation between the N_{H} and the spin period. A distinction among SG and Be HMXBs is also evident in the P_{O}–N_{H} diagram, with a tentative but expected anti-correlation between the intrinsic column density and the orbital period. Some HMXBs with unclassified counterparts can be assigned SG or Be companions based on their locations in the plots.

Galactic IGR sources are 4 times more absorbed than sources detected by ISGRI that were previously known. The spatial distribution of absorbed sources hints at a clustering towards the Norma Arm. This region is the Milky Way's most active nursery for the progenitors of stars that are likely to become absorbed HMXBs. Other authors have noted an offset in the peaks of the HMXB distribution and the spiral arm tangents. A Galactic rotation model was not able to improve upon the coincidence in the peaks in the distributions of HMXBs and OB star-forming complexes.

Only a handful of new Low-Mass X-ray Binaries (LMXBs) have been discovered. However, many sources remain unclassified and they appear to follow a spatial distribution typical of Galactic sources (especially LMXBs) rather than extragalactic sources. Interestingly, LMXBs in the central kpcs of the Galaxy appear to be associated with the Galactic Bar. The way that LMXBs are distributed in the Bulge could have implications for the study of distribution of 511 keV emission (G. Wiedenspointer, private communication).

Unclassified sources are usually a nuisance in population studies but they can also inform us about the limitations of the study. Classifying these sources requires a systematic campaign of follow-up observations of IGRs listed in the IBIS Survey catalogs, and ToO observations for transient sources announced through ATels. Observations of IGRs (either known or upcoming) should be proposed for every AO of the current flock of space telescopes. Given the history, and assuming that most of the persistent sources have already been found, there is a good chance that the next IGR will be a transient. It is imperative that ToOs are ready to be triggered immediately after an announcement is made (or much sooner, data rights permitting).

15.0.1 Scientific Article on the Parameters of IGRs

The results from the distributions of parameters of *INTEGRAL* sources were first presented publically at the Astrophysics Spring School (April, 2006) in Cargèse (Corsica), France, and at the 6th *INTEGRAL* Workshop in Moscow, Russia (July, 2006). By February, 2007, an article was accepted for publication in A&A as Bodaghee et al. (2007). A copy of the article is provided on the next several pages.

- Bodaghee A., Courvoisier T.J.-L., Rodriguez J., Beckmann V., Produit N., Hannikainen D., Kuulkers E., Willis D.R. & Wendt G.
  A description of sources detected by INTEGRAL during the first 4 years of observations
  A&A, Vol. 467-2, pp. 585–596, May, 2007
  also in: Proceedings of the 6th *INTEGRAL* Workshop, in press

A&A 467, 585–596 (2007)
DOI: 10.1051/0004-6361:20077091

Astronomy
&
Astrophysics

A description of sources detected by *INTEGRAL* during the first 4 years of observations*

A. Bodaghee[1,2], T. J.-L. Courvoisier[1,2], J. Rodriguez[3], V. Beckmann[4], N. Produit[1,2], D. Hannikainen[5], E. Kuulkers[6], D. R. Willis[1], and G. Wendt[1]

[1] *INTEGRAL* Science Data Centre, Chemin d'Ecogia 16, 1290 Versoix, Switzerland
e-mail: `arash.bodaghee@obs.unige.ch`
[2] Observatoire Astronomique de l'Université de Genève, Chemin des Maillettes 51, 1290 Sauverny, Switzerland
[3] CEA-Saclay/DSM/DAPNIA/SAp, 91191 Gif-sur-Yvette, France
[4] NASA Goddard Space Flight Center, Astrophysics Science Division, Greenbelt, MD 20771, USA
[5] Observatory, PO Box 14, 00014 University of Helsinki, Finland
[6] ISOC, ESA/ESAC, Urb. Villafranca del Castillo, PO Box 50727, 28080 Madrid, Spain

Received 12 January 2007 / Accepted 23 February 2007

ABSTRACT

Context. In its first 4 years of observing the sky above 20 keV, *INTEGRAL*-ISGRI has detected 500 sources, around half of which are new or unknown at these energies. Follow-up observations at other wavelengths revealed that some of these sources feature unusually large column densities, long pulsations, and other interesting characteristics.

Aims. We investigate where new and previously-known sources detected by ISGRI fit in the parameter space of high-energy objects, and we use the parameters to test correlations expected from theoretical predictions. For example, the influence of the local absorbing matter on periodic modulations is studied for Galactic High-Mass X-ray Binaries (HMXBs) with OB supergiant and Be companions. We examine the spatial distribution of different types of sources in the Milky Way using various projections of the Galactic plane, in order to highlight signatures of stellar evolution and to speculate on the origin of the group of sources whose classifications are still uncertain.

Methods. Parameters that are available in the literature, such as positions, photoelectric absorption (N_{H}), spin and orbital periods, and distances or redshifts, were collected for all sources detected by ISGRI. These values and their references are provided online.

Results. ISGRI has detected similar numbers of X-ray Binaries and Active Galactic Nuclei (AGN). The former group contains new members of the class of HMXBs with supergiant stellar companions. Usually, this type of object presents strong intrinsic absorption which leads to a peak emission in an energy range that ISGRI is ideally suited to detect. Thanks to these additional systems, we are able to show that HMXBs are generally segregated in plots of intrinsic N_{H} versus the orbital period of the system and versus the spin period of the pulsar, based on whether the companion is a Be or an OB supergiant star. We also find a tentative but expected anti-correlation between N_{H} and the orbital period, and a possible and unexpected correlation between the N_{H} and the spin period. While only a handful of new Low-Mass X-ray Binaries (LMXBs) have been discovered, there are many sources that remain unclassified and they appear to follow a spatial distribution typical of Galactic sources (especially LMXBs) rather than extragalactic sources.

Key words. gamma rays: observations – catalogs – X-rays: binaries – Galaxy: stellar content

1. Introduction

In just over 4 years, *INTEGRAL*-IBIS/ISGRI (Lebrun et al. 2003; Ubertini et al. 2003) has detected ~300 previously-known sources in the hard X to soft γ-ray band (20–100 keV), and discovered ~200 sources that were previously unknown at these energies. We will hereafter refer to the latter sources as IGRs[1] (for *INTEGRAL* Gamma-Ray sources). Generally, these sources were detected by creating long-exposure mosaic images captured by ISGRI (e.g., Bird et al. 2007). The *INTEGRAL* core programme (Winkler et al. 2003) is beginning to fill in underexposed regions of the sky.

Most of the sources that ISGRI has detected are Low and High-Mass X-ray Binaries (LMXBs and HMXBs, respectively), or Active Galactic Nuclei (AGN). Both LMXBs and HMXBs feature a compact object such as a neutron star (NS) or a black hole (BH) accreting material from a companion star: a faint old dwarf in LMXBs ($M \lesssim 1\ M_{\odot}$), a bright young giant in HMXBs ($M \gtrsim 10\ M_{\odot}$), or sometimes an intermediate-mass companion. Accretion typically occurs via Roche-lobe overflow in LMXBs or through the wind in HMXBs. An accretion disk can be found in both types of systems and is an important component of the optical/UV and X-ray emission from AGN and LMXBs.

Subclasses exist within the 3 most common groups. In the case of HMXBs, the spectral type of the stellar companion determines the sub-classification beyond the NS or BH nature of the compact object. A majority of HMXBs host main-sequence (MS) Be stars that have not filled their Roche lobe (Waters & van Kerkwijk 1989). These systems are usually transient with flares produced whenever the sometimes wide and eccentric orbit brings the compact object close to its companion. Persistent HMXBs are typically accompanied by an evolved supergiant (SG) O or B star whose wind steadily feeds the compact

---

* Table 1 and references are only available in electronic form at `http://www.aanda.org`

[1] An updated list of IGRs can be found at
`http://isdc.unige.ch/~rodrigue/html/igrsources.html`

object. Their variability stems from inhomegeneities in the wind. Similarly, LMXBs can be classified based on the type of compact object (NS or BH) it has. Neutron star LMXBs can be divided further into Z or Atoll sources depending on the tracks they follow in a color–color diagram. The 2 primary groups of AGN are Seyfert 1 and 2, with the latter being more absorbed and showing narrow emission lines only.

Our understanding of the different populations of *INTEGRAL* sources is limited by the large number of sources about which very little is known. Roughly half of all IGRs remain unclassified. The nature of these sources is difficult to elucidate given that many are faint or transient. Furthermore, the images, spectrum, and timing analysis gathered from a single energy range are usually insufficient to classify an object. Information from other wavelengths such as soft X-rays, infrared or radio are necessary to help identify the nature of a source. For example, radio emission can be the signature of a jet or pulsar, while the optical spectral type can help distinguish between LMXBs and HMXBs, and the redshift can place it at extragalactic distances. Follow-up observations with soft X-ray telescopes (i.e. *Chandra*, *RXTE*, *Suzaku*, *Swift* and *XMM-Newton*) can provide fine timing analyses which enable short-period modulations to be found, and they can describe the shape of the continuum below ISGRI's ~20 keV lower limit, in an energy range where potential photoelectric absorption (N_{H}) and iron fluorescence lines are detectable. Precise X-ray coordinates from *Chandra*, *Swift* or *XMM-Newton* can be used to search for counterparts in dedicated radio, optical, and IR observations or in catalogues. However, many sources are clustered in the Galactic center and along the plane, which, because of the density of stars and the amount of obscuring dust, can hinder the identification of the optical/IR counterpart.

Perhaps the most interesting result from follow-up observations is that a number of IGRs present column densities that are much higher than would be expected along the line of sight. These large absorptions are therefore intrinsic and could be the reason these sources eluded discovery with previous (softer) X-ray missions. The first new source discovered by *INTEGRAL* is IGR J16318−4848 (Courvoisier et al. 2003) which is one of the most absorbed Galactic sources known with $N_{\mathrm{H}} \sim 2 \times 10^{24}$ cm^{-2} or roughly 2 orders of magnitude more than the intervening Galactic material (Dickey & Lockman 1990). Since this discovery, other sources joined the growing class of heavily-obscured X-ray sources described by Walter et al. (2004) and Kuulkers (2005).

A certain number of these absorbed sources consist of X-ray pulsars: e.g. IGR J16320−4751 (Rodriguez et al. 2006), IGR J16393−4643 (Bodaghee et al. 2006), and IGR J17252−3616 (Zurita Heras et al. 2006). Their persistent emission, their long pulse periods (~1 ks), and their large column densities suggest that these systems are likely to be SG HMXBs, with the NS deeply embedded in the wind of its massive stellar companion (Walter et al. 2006). These kinds of systems are still a minority compared to Be HMXBs, but *INTEGRAL* is expanding their ranks.

Supergiant Fast X-ray Transients (SFXT: see Sguera et al. (2005) for a review) are another type of object whose numbers are increasing thanks to *INTEGRAL*. These objects are HMXBs whose X-ray emission is characterised by short strong outbursts (a peak flux of up to a Crab or more during a few seconds to a few hundred seconds), sometimes with recurrence timescales that can reach several hundred days. Despite the intensity of their outbursts, SFXTs are usually not detected in deep mosaic images because the accumulation of exposure time attenuates their significance. Therefore, the search for SFXTs involves scanning archival light curve data and short-exposure mosaic images for rapid bursts from known transients or at new locations.

ISGRI has also detected other types of Galactic objects such as Cataclysmic Variables (CVs), Supernova Remnants (SNRs), Pulsar Wind Nebulae (PWN), Anomalous X-ray Pulsars (AXPs), etc., which are referred to henceforth as Miscellaneous.

The most extensive catalogues of sources detected by ISGRI are the catalogues of Bird et al. (2006) and Bird et al. (2007). These catalogues represent fairly large and homogeneous samples that can be used to study the general characteristics of populations of high-energy sources (e.g. Lebrun et al. 2004; Dean et al. 2005; Lutovinov et al. 2005; Beckmann et al. 2006b).

This research presents the parameters of all sources detected by ISGRI and reported between its launch on Oct. 17, 2002, until Dec. 1, 2006. Absorption values, pulse and orbital periods, and distances or redshifts were collected from the literature and were used to study the populations of high-energy sources, to test various correlations expected from theoretical predictions, and to investigate where the new and previously-known sources detected by ISGRI fit in the parameter space of high-energy objects.

2. Data and analysis

We selected all sources from Version 27 of the *INTEGRAL* General Reference Catalogue (Ebisawa et al. 2003) which were detected by ISGRI (i.e. those with "ISGRI_FLAG==1"). These flags were set to the value of 1 as soon as confirmation of a detection by ISGRI is announced in an article, conference proceeding, Astronomer's Telegram or IAU circular. Therefore, the completeness of the sample is difficult to evaluate given that by definition, the present sample contains all sources that were detected above 20 keV while within the ISGRI FOV at some point during the last ~4 years, without considering the detection significance, nor the amount of exposure time that was required to make the detection.

The exposure map that can be seen in Fig. 1 was created by accumulating all public pointings in revolutions 30–484 (UTC: 11/1/2003–1/10/2006). Due to the core programme observation strategy, the Galactic centre (GC) is heavily exposed ($t_{\mathrm{exp}} > 10$ Ms) whereas some regions have less than 10 ks of exposure time dedicated to them. The exposure is uneven along the Galactic plane as well, with exposure biases in the directions of the spiral arms. The sensitivity limit of a source in the most exposed regions is as low as ~1 mCrab for a transient object detected at the 6σ level (Bird et al. 2006). In fact, some sources were detected only because the instrument serendipitously caught a flaring event. Using the fact that the Log(N)−Log(S) relation for extragalatic sources follows a power law with a slope of $-3/2$ (Forman et al. 1978), we can estimate a sensitivity limit of $\lesssim$5 mCrab (=3.78×10^{-11} erg cm^{-2} s^{-1} in 20–40 keV) for our sample based on where the distribution of AGN from Bird et al. (2006) deviates from the expected slope.

A number of IGRs have soft X-ray counterparts that were sometimes detected by earlier missions. For example, IGR J16393−4643 was known as AX J1639.0−4642 by *ASCA*, and IGR J17252−3616 as EXO 1722−360 by *EXOSAT*, and many IGRs have ROSAT counterparts (Stephen et al. 2006). Since ISGRI was the first to detect them above 20 keV, it is legitimate to group them together as a population of new soft γ-ray sources. They can then be compared to sources detected by ISGRI that were previously known to emit above 20 keV (e.g., Crab, Vela X-1, etc.). Note that the so-called previously-known

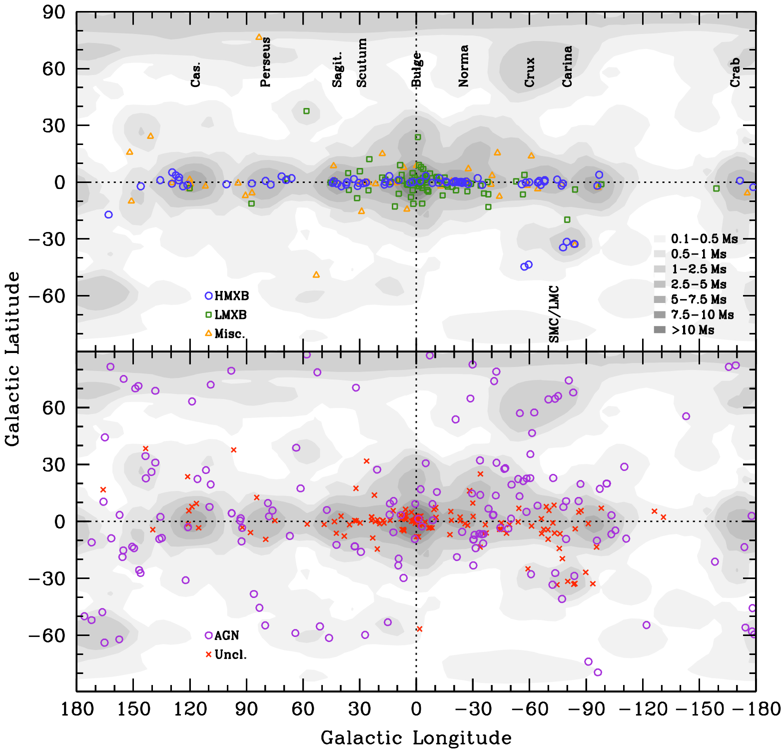

Fig. 1. Spatial distribution in Galactic coordinates of sources detected so far by ISGRI. The figure at the top presents the distributions of HMXBs (stars), LMXBs (squares) and miscellaneous sources (triangles). The figure at the bottom displays extragalactic sources (circles) and unclassified sources (crosses). The directions to the spiral arm tangents and other areas of interest are indicated, as are the cumulative exposure times at each location (from public data in revs. 30–484). The number of sources in each class is listed in Table 2.

sources actually include a few objects that were discovered after the launch of *INTEGRAL* (e.g. by *HETE*, *RXTE* or *Swift*).

The name or position of each source in our sample was queried to the SIMBAD and ADS servers for references that could provide any of the following parameters: position and error radius, classification, column density (N_H), spin period, orbital period, and distance (or redshift). Besides a rough X-ray position, very little is known about some sources, while other sources were so thoroughly studied that choices had to be made between sometimes conflicting values (notably N_H and distance). The index of parameters that we have constructed (see Table 1[2]) represents what we know about sources detected by ISGRI to date (until December 1, 2006). The structure of Table 1 is as follows:

- *Name*:
  Most sources have more than 1 name owing to detections by various instruments operating at different energies. As in Ebisawa et al. (2003), we selected names that are commonly used in high-energy astrophysics and that are accepted as an identifier in SIMBAD. This eases comparisons with other catalogs.
- *Position*:
  Source positions are from the X-rays unless a more accurate position at other wavelengths is known for a confirmed counterpart. Right Ascension and Declination in J2000 coordinates are given in “hh mm ss.s” and “deg arcmin arcsec” formats, respectively. The uncertainty (in arcmin) of the position from the reference is given as an individual entry, and it is reflected in the representation of the source positions. Galactic coordinates are also provided.
- *Absorption*:
  Column densities (in 10^{22} cm^{-2}) were gathered from the literature whenever a model fit to the X-ray spectrum required an absorption component. Extracting a single N_H for a source and comparing this value to those of other sources is not a straightforward exercise since intrinsic column densities are not static. A measurement made during flaring or quiescent periods, or at different orbital epochs, will heavily influence the N_H. The geometry of the system, the energy range of the satellite that gathered the data, and the model used to describe the resulting spectrum also affect the N_H value. Therefore, the uncertainties are often large or only upper limits are provided. Whenever possible, we selected the N_H value of the model that best fits a recent X-ray spectrum taken with a telescope that covers the soft X-ray domain well.
- *Modulations*:
  Spin periods (in seconds) and/or orbital periods (in days)

---

[2] Table 1 is only available in electronic form.

Table 2. The number of sources from each of the major classes detected by ISGRI are listed for new (≡IGRs) and previously-known sources. Miscellaneous (Misc.) sources are Galactic objects that are not X-ray binaries (e.g. CVs, SNRs, AXPs, etc.) and Uncl. refers to the group of sources that have yet to be classified.

	HMXBs	LMXBs	AGN	Misc.	Uncl.	Total
IGRs	32 (15%)	6 (3%)	50 (23%)	15 (7%)	111 (52%)	214
previously-known	46 (16%)	76 (27%)	113 (40%)	32 (11%)	18 (6%)	285
Total	78 (16%)	82 (16%)	163 (33%)	47 (9%)	129 (26%)	499

have been reported for a large number of Galactic objects detected by ISGRI. Some systems are known to spin down, so we selected the most recent value from *RXTE* whenever possible, even though this level of precision is not needed for the purpose of our study. The spin period can refer to the spin of the NS in X-ray binaries, or to the spin of the White Dwarf in CVs. The catalogs of Liu et al. (2000) and Liu et al. (2001), and the systematic analysis of *RXTE* data by Wen et al. (2006) are among the main references of spin and orbital periods in this work.

- *Distances*:
  The distances to extragalactic objects are given as a measure of the redshift (denoted by brackets). Objects in the Milky Way and Magellanic Clouds have distances in units of kpc. Opinions sometimes differ as to the distances of some Galactic sources. We favored distance measurements that were recent, precise and that were the least model-dependent. Even so, the distance uncertainties quoted in the literature can be large. The distance measurements are from, among others, White & van Paradijs (1996), Grimm et al. (2002), Jonker & Nelemans (2004), Bassani et al. (2006), Beckmann et al. (2006a), or from references in Liu et al. (2000) and Liu et al. (2001). Note that the distances in Grimm et al. (2002) sometimes represent an average over several competing distance estimates.
- *Type*:
  Source classifications are based on the concensus opinion in the literature. Peculiar behaviour, such as quasi-periodic oscillations, transience, and Z-track or Atoll shapes, are also noted since they can help us distinguish between systems within the same class. If the source classification has not yet been confirmed, it is simply called "unclassified". The transient identification of a source is given by any of the following: 1) the label was assigned by its discoverers or by other authors (e.g. "Discovery of a new *transient* IGR J..."); 2) the source has not been detected by anyone else since its discovery announcement, e.g. it is not listed in the all-data, all-sky catalogs of Bird et al. 2006, 2007); 3) the source is detected only in mosaic images of a single or a few consecutive revolutions according to Bird et al. (2007), but not in their all-data mosaic images.
- *References*:
  All parameters are referenced so that the reader can assess the methods that were used to determine the quoted values and uncertainties.

3. Results

3.1. Spatial distribution

Table 2 lists the major source populations detected by ISGRI that are either new (≡IGRs) or that were previously known. ISGRI has discovered many new HMXBs and AGN, but their proportions relative to the other classes are similar to what was known before the launch of *INTEGRAL*. Only a few LMXBs have been discovered by ISGRI. This is because LMXBs are generally less intrinsically obscured than HMXBs or AGN, and are therefore easier to detect with previous satellites. Around 50 sources have been detected that belong to the group of miscellaneous sources (i.e. CVs, SNRs, PWN, AXPs, etc.), while ~130 IGRs await classification.

The spatial distributions, in Galactic coordinates, of the major classes of γ-ray sources detected by ISGRI are presented in Fig. 1. Naturally, ISGRI detects sources in regions that are exposed. Given the heterogeneous exposure map of the sky gathered in the last 4 years of observations, detections are biased towards regions of the sky that have been exposed the longest (i.e. the Galactic plane and bulge).

However, Fig. 1 also demonstrates the effect that the evolution of each type of source has on its spatial distribution. Because their optical companions belong to an old stellar population, LMXBs are found predominantly in the Galactic bulge and/or they have had time to migrate off the plane of the Milky Way ($|b| \gtrsim$ 3–5°). On the other hand, the stellar companions of HMXBs are young stars, so these systems must remain close to sites of recent stellar formation. Thus, the angular distribution of HMXBs reflects the spiral structure of the Galaxy, with an uneven distribution along the Galactic plane punctuated by peaks that are roughly consistent with the tangential directions to the inner spiral arms. Those HMXBs that have been detected at longitudes $|l| \gtrsim 90°$ correspond to systems located around spiral arms near the Sun. Evolutionary signatures like these were noticed in the past by *Ginga* (Koyama et al. 1990), *RXTE* (Grimm et al. 2002), and more recently with *INTEGRAL* (Dean et al. 2005; Lutovinov et al. 2005), although their samples were smaller than the one presented here.

Another way to demonstrate the role of stellar evolution in shaping the spatial distributions of LMXBs and HMXBs is to plot the positions of sources whose distances are known on a spiral arm model of the Milky Way. Russeil (2003) developed the Galactic spiral arm model that we used. Their model is based on the locations of star-forming complexes that include groups of OB stars, molecular clouds, H II regions, and diffuse ionised gas. The locations of these complexes are derived from a variety of tracers such as Hα, CO, the radio continuum and absorption lines.

While the uncertainties on distances can be large, Fig. 2 shows that HMXBs tend to occupy the outer disk and arms where young stars are formed, whereas LMXBs are clustered near the bulge where old globular clusters reside. A histogram of galactocentric radii (Fig. 3) shows LMXBs peaked at the center and decreasing gradually, while HMXBs roughly follow the distributions from H II/CO surveys (Russeil 2003) which are underabundant in the central few kpc and peak at the spiral arms. According to a Kolmogorov-Smirnov (KS) test, the probability is less than 0.01% that the galactocentric distributions of LMXBs and HMXBs are statistically compatible.

The distribution of LMXBs in the central Galaxy suggests an association with the Galactic bar (Fig. 2). Low-mass X-ray

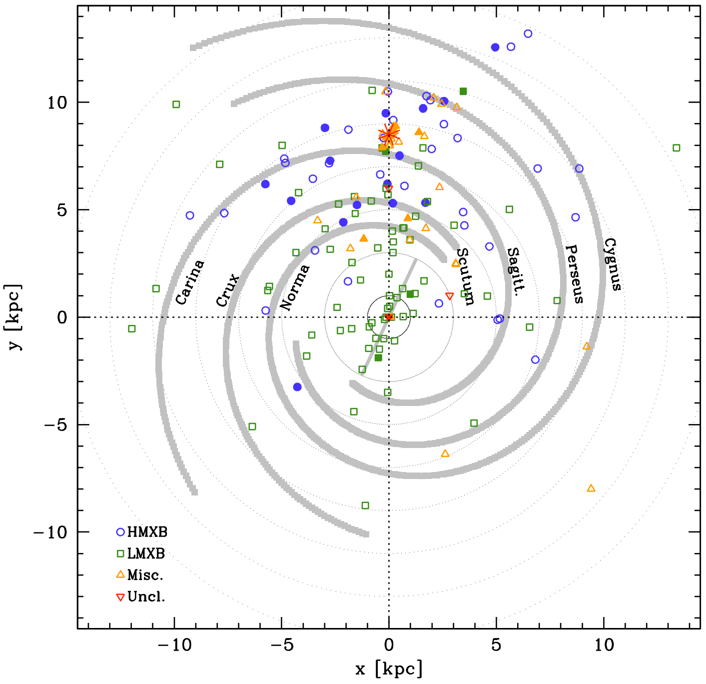

Fig. 2. Galactic distribution of HMXBs (49, circles), LMXBs (74, squares), miscellaneous sources (37, triangles), and unclassified sources (3, inverted triangles). Filled symbols represent IGR sources. Also plotted is the 4-arm Galactic spiral model from Russeil (2003) with the Sun located at 8.5 kpc from the centre. The concentric circles indicate radii of 1, 3, 5,..., kpc from the centre.

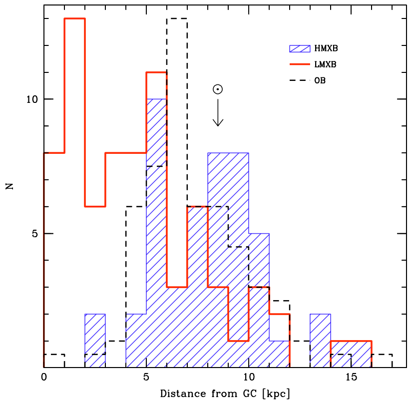

Fig. 3. Distribution of galactocentric distances of HMXBs (49, shaded histogram) and LMXBs (74, thick histogram). The dashed histogram represents OB star-forming complexes from Russeil (2003) (divided by 2).

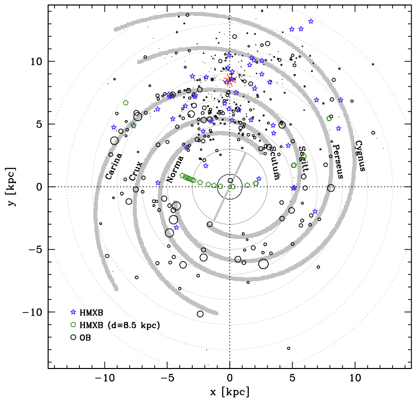

Fig. 4. Galactic distribution of HMXBs whose distance are known (49, star symbols) and the locations of star-forming complexes from Russeil (2003) (464, circles). The symbol size of the latter is proportional to the activity of the complex. HMXBs whose distances are unknown have been placed at 8.5 kpc (23, pentagons).

binaries whose distances are known and that have been detected by ISGRI are not prevalent on either side of the bar. Only 1 LMXB with a distance measurement has been detected in the Galactic center region bound by $0 < x < 3$ kpc and $-3 < y < 0$ kpc, indicating that the bar might be responsible for preventing an identification and distance measurement to be made for the faint counterparts to LMXBs situated behind it. As viewed from the Sun, the orientation of the bar leads to an apparent asymmetry of LMXBs in the central 3 kpc of the Galaxy ($|l| \lesssim 20°$): in this direction, ISGRI has detected 50% more LMXBs at negative longitudes than at positive longitudes. Maps of Galactic absorption are expected to be symmetrical in this region (Dickey & Lockman 1990).

In Fig. 4, we present the Galactic distribution of star-forming complexes Russeil (2003) with the symbol size proportional to the excitation parameter in that region (≡amount of ionising photons as determined from the radio continuum flux). High-mass

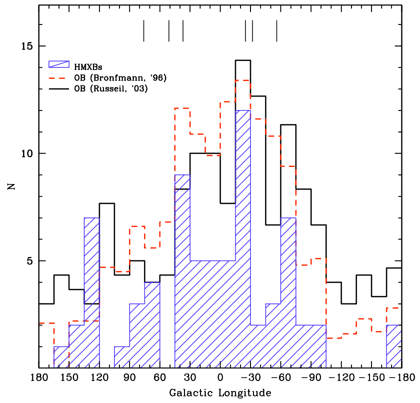

Fig. 5. Histograms of Galactic longitudes integrated over the latitude for HMXBs with $|b| < 6°$ (shaded histogram) and star-forming regions from Russeil (2003) (thick histogram, divided by 3) and from Bronfman et al. (1996) (dashed histogram, divided by 10). The vertical lines indicate the tangential directions of the 4-arm spiral model from Russeil (2003).

X-ray binaries whose distances are known are symbolised by stars, while those with unknown distances were assigned a distance of 8.5 kpc and are represented by pentagons. The 4-arm spiral model of Russeil (2003) is also drawn. Figure 5 presents histograms of Galactic longitudes (integrated over the latitude) of HMXBs (shaded histogram, with $|b| < 6°$, in order to exclude sources in the Magellanic Clouds). Also shown are angular distributions of star-forming complexes from Russeil (2003) (divided by 3, thick histogram), and of ultra-compact H II regions detected by *IRAS* (Bronfman et al. 1996) (divided by 10, dashed histogram).

In general, the distribution of HMXBs along the plane of the Milky Way coincides with the expected radial distribution of young massive star-forming regions. A KS test yields a probability of 22% that the distributions of HMXBs and *IRAS* sources (shaded and dashed histograms, respectively, in Fig. 5) are statistically compatible. Excluding HMXBs that lie outside the survey region covered by Bronfman et al. (1996) ($|b| < 2°$ for $|l| < 60°$, and $|b| < 4°$ elsewhere) increases the probability of statistical compatibility to 34%. Peaks at Galactic longitudes $l \sim \pm 30°$ are observed in both data sets corresponding to the direction of the inner spiral arm tangents (Norma and Scutum/Sagittarius arms). Bronfman et al. (1996) remark that the peaks in their distribution are also consistent with another active formation site of young, massive stars: a molecular ring situated at a radius of ∼3 kpc from the Galactic center.

At first glance, the distributions of star-forming complexes of Russeil (2003) and HMXBs are also compatible (thick histogram in Fig. 5). The KS test returns a probability of only 3% which is misleading given the large number of objects in Russeil (2003) that are not very active. When selecting complexes with an excitation parameter >10 pc cm^{-2}, which still represents 70% of the sample, the statistical compatibility improves to 41%.

Lutovinov et al. (2005) and Dean et al. (2005) found that the distribution of HMXBs was offset with respect to the directions of the spiral arm tangents. Lutovinov et al. (2005) note that ∼10 Myr must elapse before one of the stars in a binary system collapses into a NS or BH, and that Galactic rotation will induce changes in the apparent positions of the arms relative to the Sun. This implies a delay between the epoch of star formation and the time when the number of HMXBs reaches its maximum. The observed displacement could simply stem from uncertainties in the distances to the HMXBs. Another problem is that the exact location of the arms depends on which Galactic model is used. Changes in the Sun-GC distance or in the pitch angles of the arms affects the radial scaling and shifts the tangential directions.

The propagation of density waves is believed to promote star formation in the spiral arms (Lin et al. 1969). Depending on the distance to the GC, the spiral arm pattern has angular velocities in the range of $\Omega \sim 20$–60 Gyr^{-1} (Bissantz et al. 2003). Hence, in the last ∼10 Myr (corresponding roughly to the epoque when the inner spiral arms and the current density maxima of HMXBs overlapped), the inner arms of the Galaxy have rotated around the GC by ∼40°. Individual stars (such as the Sun) or groups of stars have negligible movement in this scenario. Instead, star-forming sites that are now active (e.g. from Russeil 2003) should be about ∼40° away from those regions that were active some 10 Myr ago and that produced the current crop of HMXBs. Therefore, in order to reproduce the distribution of active star-forming sites as they were some 10 Myr ago, we introduced differential Galactic rotation to "unwind" the distribution of current star-forming complexes from Russeil (2003). Kolmogorov-Smirnov tests suggest that the effects of Galactic rotation are negligible, even when only the most active sites are considered.

The distribution of angular distances from the Galactic plane (in degrees, for $|b| < 20°$) of sources detected by ISGRI is shown in Fig. 6. The distributions were summed over the northern and southern Galactic hemispheres. Shaded histograms are HMXBs (left) and AGN (right), and the thick histograms represent LMXBs (left) and miscellaneous sources (right). The distribution of unclassified sources is given by the dashed histogram. Not surprisingly, the spread of the latitude distributions is larger in LMXBs than it is in HMXBs owing to the relative youth of the optical primaries in the latter. Also expected is the distribution of AGN which is more or less flat and which roughly follows the exposure map. However, the Galactic plane ($|b| \lesssim 3°$) is noticeably deficient in AGN detections despite the fact that the exposure map is biased here. This highlights the difficulty in detecting AGN at high energies and at low latitudes; these objects tend to be intrinsically absorbed, they are further obscured by the Galactic plane, and their counterparts have to be identified within a crowded field. Sazonov et al. (2007) noted that the exclusion of sources in the Galactic plane region ($|b| < 5°$) from an all-sky survey resulted in only a marginal reduction in the number of identified AGN, whereas the number of unclassified sources dropped significantly.

It is useful to examine the unclassified sources as they help to define the limits of our study. Almost all of the sources that are unclassified have position accuracies that are no better than a few arcminutes. This precludes establishing an optical counterpart for many unclassified sources located in crowded regions such as the Galactic plane. The transient nature of many unclassified sources implies a lack of immediate follow-up observations that would permit a classification. Because of their transience, many unclassified sources appear fainter than average in long-exposure mosaic images. Masetti et al. (2006) suggest that up to half of all unclassified sources could be AGN situated behind the Galactic plane, whereas Dean et al. (2005), working on a smaller sample, favor a Galactic origin for the unclassified sources of Bird et al. (2004) based on the slope of the Log(N)–Log(S) relation and other factors.

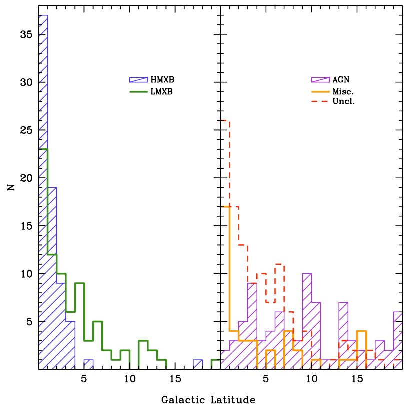

Fig. 6. Angular distribution (in degrees, for $|b| < 20°$) from the Galactic plane of sources that have been detected by ISGRI. Shaded histograms are HMXBs (*left*) and AGN (*right*), and the clear histograms represent LMXBs (*left*) and miscellaneous sources (*right*). The dashed histogram denotes unclassified sources. The distributions have been summed over the northern and southern Galactic hemispheres. The curves represent fits to the data from the model and parameters described in the text.

Unclassified sources have a distribution of Galactic latitudes that peaks in the central 3° from the Galactic plane and decreases gradually, suggesting a population of sources that are Galactic rather than extragalactic in origin (see Fig. 6). Many of the unclassified sources also happen to be transient, whereas AGN can vary but tend to emit persistently. Furthermore, the angular distribution of unclassified sources is very similar to the distribution of LMXBs with a KS-test probability of nearly 40% of statistical compatibility between unclassifieds and LMXBs, compared with 13% for miscellaneous sources, and less than 0.01% for either AGN or HMXBs.

While there are extragalactic sources among them, the population of unclassified sources is therefore likely to be composed primarily of Galactic sources such as LMXBs and miscellaneous sources. We are unable to elaborate on the proportions of the different classes, but it is clear from Fig. 6, and from the results of KS tests, that the unclassified sources are most similar to the LMXBs and miscellaneous sources in their distribution off the Galactic plane. The reasons they have avoided classification (and detection by previous missions) are: the companion stars to LMXBs are usually faint in the optical/IR spectrum; they are located near the Galactic plane where absorption and source confusion prevent an identification; and, for many of these sources, their transient emission complicates efforts to perform follow-up observations. Recent improvements in Target of Opportunity campaigns aimed at new IGRs have uncovered as many new LMXBs in the last year than during the first 3 years of observations combined.

Figure 7 presents the distributions of scale heights (in kpc) for HMXBs (shaded histogram) and LMXBs (clear histogram) whose distances are known. Sources from the Magellanic Clouds are excluded. Following the procedure in Dean et al. (2005), we set the number of sources as a function of the distance in kpc above the Galactic plane (h) according to $N = k \cdot \mathrm{e}^{-\alpha \cdot h}$ where $\alpha \equiv 1/h_0$ describes the steepness of the exponential. The parameters that best fit this model are listed in Table 3. The value that we derive for the characteristic scale height (h_0) of HMXBs is ~130 pc which is compatible with the value found by Grimm et al. (2002) with *RXTE* data, but slightly less than the value from Dean et al. (2005) (≳200 pc). The characteristic scale height that we derive for LMXBs (~600 pc) is larger than the scale heights found by Grimm et al. (2002) and Dean et al. (2005) which were closer to ~400 pc. This is probably due to the greater coverage of the sky and larger sample size of our study. Miscellaneous sources have a distribution that is more similar to HMXBs than it is to LMXBs.

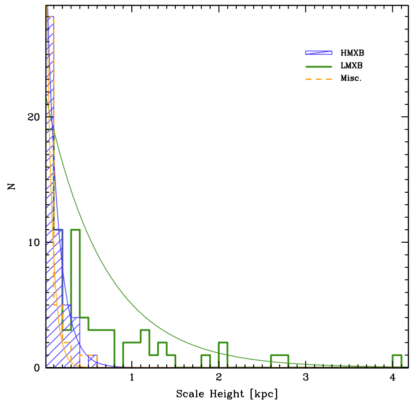

Fig. 7. Vertical scale height (in kpc) from the Galactic plane of HMXBs, LMXBs and miscellaneous sources whose distances are known. The distributions have been summed over the northern and southern Galactic hemispheres. Sources from the Magellanic Clouds are excluded. The curves represent the exponential model described in the text fit to the data (see Table 3 for parameters).

Table 3. Parameters from the model described in the text fit to the distributions of scale heights from the Galactic plane for HMXBs, LMXBs and miscellaneous sources whose distances are known. Objects from the Magellanic Clouds are excluded.

	k	α	h_0 [pc]
HMXBs	36 ± 3	7.5 ± 1.7	134^{+39}_{-25}
LMXBs	22 ± 3	1.5 ± 0.5	680^{+320}_{-160}
Misc.	41 ± 3	15 ± 4	66^{+23}_{-14}

3.2. Absorption

The column densities along the light of sight of some sources in our sample are higher than the value expected from radio maps (Dickey & Lockman 1990) which implies absorbing material intrinsic to the source. On average, Galactic IGRs are more absorbed than the sources seen before *INTEGRAL* (by a factor of ~4) with IGRs representing a sizable contingent of objects that have $N_{\mathrm{H}} \sim 10^{23}$ cm^{-2} (see Fig. 8). The average column density of sources that were previously known is $N_{\mathrm{H}} = 1.2 \times 10^{22}$ cm^{-2} ($\sigma \sim 0.7$) whereas IGRs have an average $N_{\mathrm{H}} = 4.8 \times 10^{22}$ cm^{-2} ($\sigma \sim 0.6$). A KS test yields a probability of less than 0.01% that the two distributions are statistically compatible.

The classified Galactic IGRs are mostly HMXBs (Table 2) which usually exhibit high column densities, either intrinsically due to the geometry of the system or extrinsically due to their location along the dusty Galactic plane. Note, however, that the

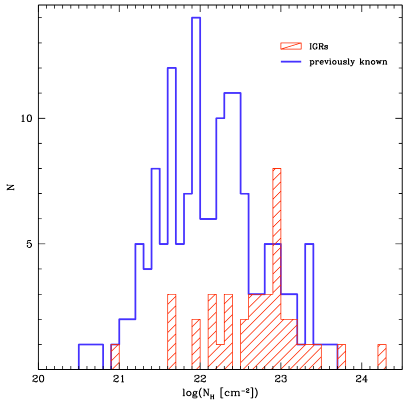

Fig. 8. The distribution of reported column densities (N_H) for Galactic sources (including sources in the Magellanic Clouds) detected by ISGRI that were previously known (152, clear histogram) and for IGRs (41, shaded histogram).

highest value of Galactic N_H is ~3 × 10^{22} cm^{-2} so objects with very large N_H can not be explained by interstellar absorption alone. Also keep in mind that the absorption from Dickey & Lockman (1990) tends to be underestimated given that local small-scale inhomogeneities and the contribution from molecular hydrogen are ignored. The main reason that more absorbed sources are being found is that by operating above 20 keV, ISGRI is immune to the absorption that prevented their discovery with earlier soft X-ray telescopes. A large absorption is also a common feature of extragalactic IGRs. However, our data show that as a group, they are not more absorbed than pre-*INTEGRAL* AGN, in agreement with the conclusions of Beckmann et al. (2006a) and Sazonov et al. (2007).

Figure 9 presents an all-sky map of sources detected by ISGRI with symbol sizes proportional to reported column densities (N_H). Contours of expected line-of-sight absorption (Dickey & Lockman 1990) are provided for levels of 10^{21}, 5 × 10^{21} and 10^{22} cm^{-2}. One of the benefits of such a map is that potential clustering or asymmetries in the local distribution of matter can be studied. The lower portion of Fig. 9 shows that the Norma Arm region hosts many of the most heavily-absorbed Galactic sources ($N_H \geq 10^{23}$ cm^{-2}) continuing a previously noted trend (e.g., Kuulkers 2005; Lutovinov et al. 2005; Walter et al. 2006). This region also happens to be the most active formation site of young supergiant stars (Bronfman et al. 1996). These stars are the precursors to the absorbed HMXBs that ISGRI is discovering in the Norma Arm. The Galactic Bulge and the Scutum/Sagittarius Arms are also represented by obscured sources but to a lesser extent than in the Norma Arm.

For sources whose distance are known, we did not find any clear dependence of the intrinsic N_H on the distance to the source, nor did we find a dependence of N_H with the luminosity as derived from the soft-band fluxes (20–40 keV) listed in Bird et al. (2007).

3.3. Modulations

The strong magnetic fields in some NS X-ray binaries can produce non-spherically symmetric patterns of emission. If the magnetic and rotation axes are misaligned, this results in pulsations in the X-ray light curve.

Most IGRs for which a pulsation has been measured have spin periods (P_s) in the range of 100–1000 s, or around 10 times longer than the average pulse period of pre-*INTEGRAL* sources (Fig. 10). There are notable IGRs that represent extreme cases: IGR J00291+5934 has a pulse period of only 1.7 ms making it the fastest accretion-powered pulsar ever observed (Galloway et al. 2005), whereas IGR J16358−4726 has a spin period as long as 6000 s (Lutovinov et al. 2005; Patel et al. 2006). One of the reasons that IGRs have longer pulse periods than average is because many of them are SG HMXBs which are wind-fed systems with strong magnetic fields that tend to have the longest pulse periods (e.g. Corbet 1984). Another reason is that *INTEGRAL* and *XMM-Newton* feature long orbital periods around the Earth. This means that the source can be observed for long periods of time without interruptions, so that pulsations on the order of a few hundreds of seconds or more can be detected. Meanwhile, the previously-known sources in Fig. 10 include millisecond pulsars and other LMXBs, radio pulsars, CVs, etc., which are underrepresented among IGRs. To illustrate this, we performed a KS test which returned a very low probability (0.0007%) of statistical compatibility between the distributions of 18 IGRs (shaded histogram) and 92 previously-known pulsars of all types (clear histogram) as they are presented in Fig. 10. The KS-test probability improved by an order of magnitude when IGRs were compared to 49 previously-known HMXBs, and it improved by 3 orders of magnitude when IGRs were compared to 14 previously-known SG HMXBs. So *INTEGRAL* is not just finding new pulsars that are HMXBs, but these HMXBs are predominantly long-period systems with SG companions.

The distribution of orbital periods (P_o) of IGRs exhibits a similar bimodal shape to that seen in the distribution of orbital periods known before *INTEGRAL* (Fig. 11). The probability of statistical compatibility is nearly 80% according to a KS test. The bimodal distribution represents 2 underlying populations: LMXBs (and miscellaneous sources) which tend to have short orbital periods, and HMXBs which tend to have longer orbital periods (Fig. 12).

In a Corbet P_s–P_o diagram (Corbet 1984), members of each subclass of HMXBs segregate into different regions of the plot owing to the complex feedback processes between the modulation periods and the dominant accretion mechanism. Figure 13 shows that the majority of IGRs are located among other known SG HMXBs. The figure also shows that Be HMXBs have longer orbital periods than SG HMXBs, in general. While this fact was already known (e.g. Stella et al. 1986), the discrepancy remains even though *INTEGRAL* has nearly doubled the number of such systems.

3.4. Modulations vs. absorption

Accretion affects the spin period of a NS. If the velocity at the corotation radius (the radius at which the magnetic field regulates the motion of matter) exceeds the Keplerian velocity, then material will be spun away taking angular momentum with it and the NS will slow down due to the “propellor mechanism” (Illarionov & Sunyaev 1975). For corotation velocities smaller than the Keplerian velocity, the material is able to accrete onto the NS magnetosphere which will either spin up or spin down the NS depending on whether the angular momentum of the accreted material has the same or an opposite direction as the NS spin (Waters & van Kerkwijk 1989). So the spin rate of the pulsar in

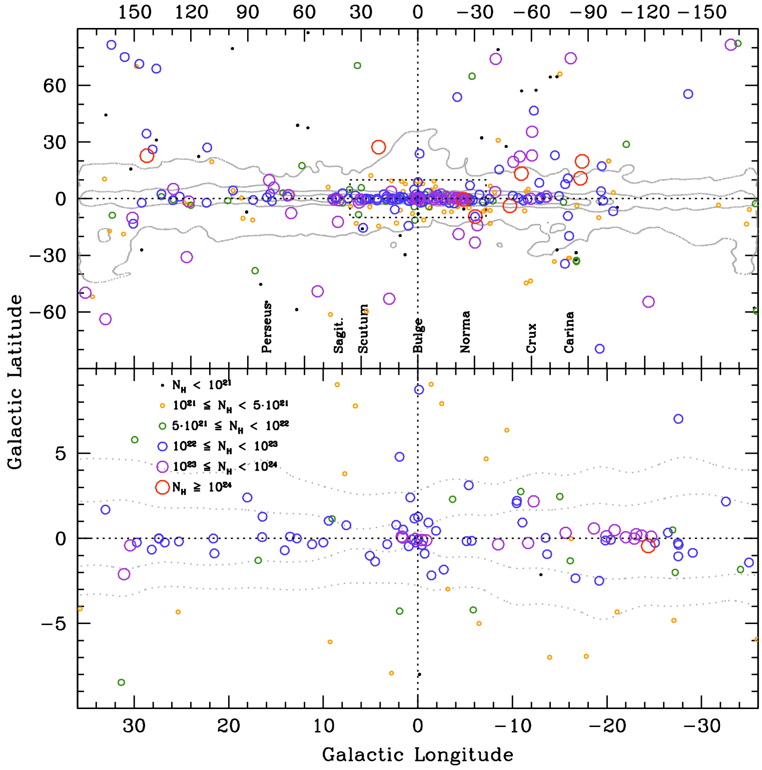

Fig. 9. Spatial distribution, in Galactic coordinates, of all sources detected by ISGRI for which N_H has been reported. The symbol size is proportional to the published column density. The figure at the top shows the whole sky and includes extragalactic sources, while the figure at the bottom focuses on the Bulge region (boxed region in the figure at the top) and excludes extragalactic sources. Contours denote Galactic absorption levels of 10^{21}, 5×10^{21}, and 10^{22} cm^{-2} (Dickey & Lockman 1990).

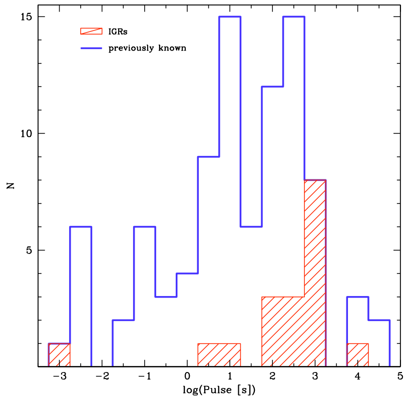

Fig. 10. Spin periods reported for sources detected by ISGRI that were previously known (92, clear histogram) and for IGRs (18, shaded histogram).

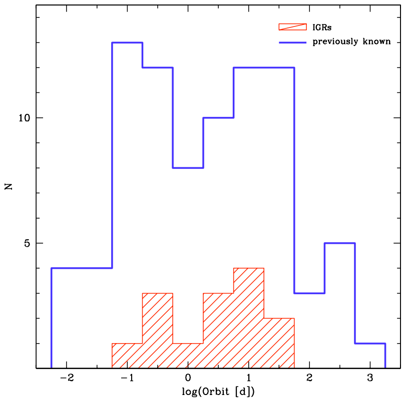

Fig. 11. Published orbital periods of sources detected by ISGRI. The clear histogram represents sources that were previously known (84) while the shaded histogram represents IGRs (14).

a HMXB is regulated by, among other things, the angular momentum of the wind of the stellar companion.

Assuming spherically-symmetric accretion from a radiation-driven wind of a SG star, the density of the wind as a function

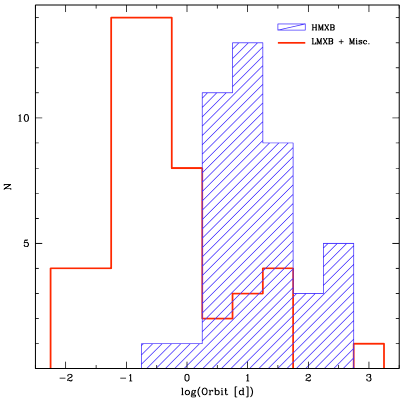

Fig. 12. Distribution of orbital periods of HMXBs (43, shaded histogram) compared with LMXBs and Miscellaneous sources (54, clear histogram).

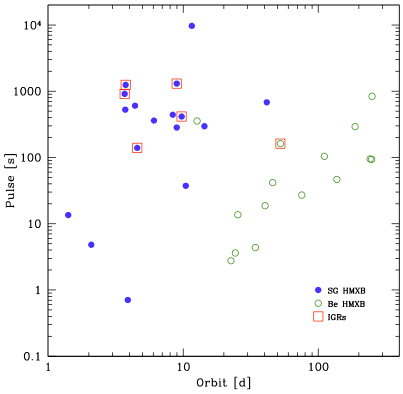

Fig. 13. Corbet diagram of spin vs. orbital period of HMXBs detected by ISGRI whose companions are OB supergiants (17, filled circles) or Be stars (15, empty circles). IGRs are boxed.

of radius is $\rho(r) \propto r^{-2}$. On the other hand, the structure of the winds of Be stars is believed to consist of dense slow equatorial outflows and thin fast polar winds (Lamers & Waters 1987). The density drops much faster with the radius ($\rho(r) \propto r^{-3}$) (Waters et al. 1988). Therefore, the winds of Be stars present stronger density and velocity gradients inside the capture radius of the NS, in both radial and azimuthal directions, which suggests that wind-fed accretion is more efficient at delivering angular momentum to the NS in Be HMXBs than it is in SG HMXBs (Waters & van Kerkwijk 1989).

Given the density structures described above, and assuming a steady accretion rate of material whose angular momentum has the same direction as the spin of the NS, the spin period of the NS will reach an equilibrium value $P_{\rm eq} \propto \rho^{-3/7}$. However, the present-day spin periods of NS in SG systems are much longer than predicted and are actually closer to $P_{\rm eq}$ of the stellar winds while the star was still on the MS (Waters & van Kerkwijk 1989). The equilibrium spin period in Be systems is constantly adjusting to the changing conditions in the winds (Waters & van Kerkwijk 1989). As with the SG systems, pulsars in Be systems are not currently spinning at $P_{\rm eq}$ but reflect the values of an earlier evolutionary stage (King 1991). So even though the transport of positive angular momentum through the wind is so inefficient that it can not spin up the pulsar to its expected equilibrium spin period, this does not influence how well the pulsar can be spun down by the "propellor mechanism" (Waters & van Kerkwijk 1989).

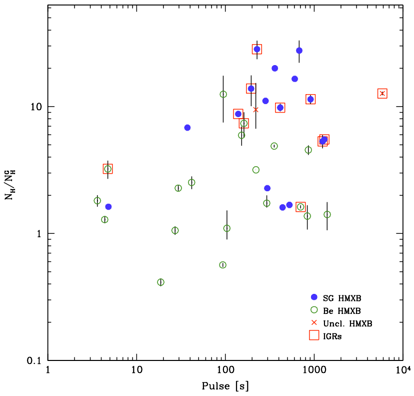

Fig. 14. Spin period as a function of reported $N_{\rm H}$ value (normalised by the expected Galactic value from (Dickey & Lockman 1990)) for HMXBs detected by ISGRI whose companions are OB supergiants (16, filled circles), Be stars (19, empty circles), or unclassified (2, crosses). IGRs are boxed and Magellanic Cloud sources are excluded.

With a few exceptions, HMXBs from the Milky Way that have been detected by ISGRI are segregated into distinct regions of a $P_{\rm s}$–$N_{\rm H}$ diagram (Fig. 14) stemming from the higher average $N_{\rm H}$ and longer average $P_{\rm s}$ of SG HMXBs compared to Be HMXBs. The SG HMXBs set apart from the others ($P_{\rm s} <$ 50 s) are Cen X-3 which is a Roche-lobe overflow system, and OAO 1657−415 which might be transitioning from a wind-fed to a disk-fed system (Audley et al. 2006). The $N_{\rm H}$ values of sources in Fig. 14 have been normalised by the line-of-sight values ($N_{\rm H}^{\rm G}$) from Dickey & Lockman (1990). This normalisation does not affect our conclusions but it helps to reduce the scatter in the vertical direction, particularly for nearby sources such as X Per.

There could be a weak positive correlation between the $N_{\rm H}$ and spin period for HMXBs as a group. There are no highly-absorbed sources ($N_{\rm H} > 10^{23}$ cm^{-2}) with spin periods shorter than a few tens of seconds, and there are no pulsars with $P_{\rm s} >$ 100 s that are poorly absorbed ($N_{\rm H} < 10^{22}$ cm^{-2}). A least-squares fit to the data yields $P_{\rm s} \propto N_{\rm H}^{5/7}$. If we consider the $N_{\rm H}$ to be a reliable estimate of the density of matter around the compact object, then the slope that we find contradicts the slope expected from the equilibrium values (∼−3/7). However, as noted above, the pulsars in Fig. 14 are spinning at periods that are longer than their equilibrium values would suggest.

Since Be HMXBs tend to have longer orbital periods than SG HMXBs (see Fig. 13), a distinction is also seen among the distributions of the $N_{\rm H}$ values and orbital periods of HMXBs with Be or SG companions (Fig. 15). There also appears to be an anti-correlation of $N_{\rm H}$ and orbital period: a least-squares fit to the data returns $P_{\rm o} \propto N_{\rm H}^{-3/7}$. In both types of systems, a shorter orbital period implies a compact object that is embedded deeper or spends more time in the dense regions of its stellar companion's wind resulting in more absorption. Therefore, Be HMXBs

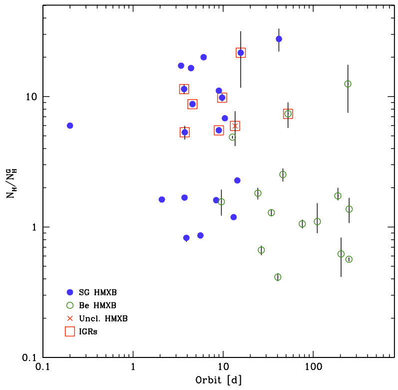

Fig. 15. Orbital period versus reported N_H value (normalised by the expected Galactic value from (Dickey & Lockman 1990)) for HMXBs detected by ISGRI whose companions are OB supergiants (20, filled circles), Be stars (15, empty circles) or unclassified (1, cross). IGRs are boxed and Magellanic Cloud sources are excluded.

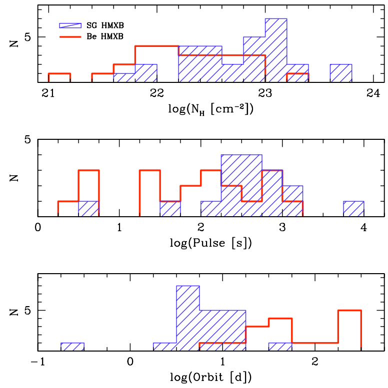

Fig. 16. Distribution of reported N_H (*top*), pulse periods (*middle*), and orbital periods (*bottom*) among HMXBs detected by ISGRI whose companions are OB supergiants (shaded histograms) or Be stars (clear histograms). Magellanic Cloud sources are excluded.

continue the trend set by SG HMXBs into long-orbital periodicity and low-N_H regions of the plot.

Spearman rank tests to the P_s–N_H and P_o–N_H distributions return weak positive and negative correlations with coefficients of 0.37 and −0.33, respectively, suggesting that the null hypothesis of mutual independence between N_H and P_s or P_o can be rejected. From Monte Carlo simulations, we determined that the probability of finding a Spearman rank coefficient $\gtrsim$0.33 is around 5%. Admittedly, the scatter in the data is large as can be seen in Figs. 14–15. Because there are large uncertainties in the N_H and practically no uncertainty in the spin and orbital periods, the slope from a least-squares fit will tend to overestimate the real slope. Futhermore, the conclusions that we derive for how divergent species of objects react to changes in the local absorbing matter are based on a simplification of the underlying physics. The inclinations of the systems and their eccentricities, for example, are ignored. Even if we can not fit a slope of −3/7 to the data in Fig. 14, the correlations that we find in Figs. 14–15 might simply be due to the segregation of the 2 populations into distinct regions of the plots, rather than being due to physical processes.

Nevertheless, as more sources are added to these diagrams, the potential trends that have emerged could help constrain models describing the influence of local absorbing matter on the modulations. Another advantage of these plots is that the probable designation of an unidentified source is much more likely to be correct than when only a single parameter is used. This is illustrated in Fig. 16 where distributions of the 3 parameters in question (N_H, P_s and P_o) are presented for SG and Be HMXBs. Other than in the orbital periods, and in the extremities of the N_H and P_s distributions, there is little that differentiates the 2 groups. A HMXB selected from an average bin in either N_H or P_s has a roughly equal probability of hosting a SG or Be star. However, a random HMXB in the N_H–P_s plot will tend to be located among other members of its group.

Therefore, these diagrams could serve as new tools to help distinguish between SG and Be HMXBs when only N_H and either the spin or orbital periods are known. For example, IGR J19140+0951 has an orbital period of around 13 days and $N_H \sim 10^{23}$ cm^{-2}. It is positioned among other SG HMXBs so its companion is probably an OB supergiant (boxed cross in Fig. 15). This designation has already been suggested based on other criteria such as the source's persistent emission (Rodriguez et al. 2005). Recent IR observations of the source indicate a spectral type of B0.5-Ia which confirms the supergiant nature of the companion (D. Hannikainen, private communication). Similarly, AX J1749.2−2725 which is currently an unclassified HMXB could have a SG companion based on its position in Fig. 14 ($N_H > 10^{23}$ cm^{-2} and pulse period over 100 s). The other unclassified HMXB in Fig. 14 is IGR J16358−4726, whose NS has an unusually long spin period suggesting a magnetar nature for the source (Patel et al. 2006). This object is clearly in the SG HMXB camp based on its position in the plot.

4. Summary and conclusions

We have compiled a catalogue of all ~500 sources that were detected by ISGRI during its first 4 years of observations. This includes published parameters such as positions, column densities, spin and orbital periods, and distances or redshifts. The primary aims of this catalogue were to gather in a single place the most important parameters of high-energy sources detected by ISGRI and to use this large sample to test against various theoretical predictions, to search for possible trends in the data, and to determine where new sources fit in the parameter space established by previously-known high-energy sources.

Clustered towards the spiral arm tangents and at low Galactic latitudes, HMXBs follow the distributions of tracers of star-forming regions. In contrast, most LMXBs are found in the Galactic bulge or have had time to migrate to high latitudes, typical of an older stellar population. The discrepancy is seen again in galactocentric profiles where the number of LMXBs gradually decreases from its maximum in the central kpcs, while HMXBs avoid the central kpcs and are overrepresented at the peaks of H II/CO distributions.

Over 200 new sources have been discovered by ISGRI but many of them remain unclassified. Although some may be AGN behind the plane, unclassified sources have a spatial distribution that resembles a Galactic population (notably LMXBs and CVs) rather than an extragalactic one. If the unclassified sources are composed primarily of LMXBs, as their spatial distributions and the transient emission of most them seem to suggest, then the reason they remain unclassified is because the faint optical/IR counterparts of such sources are difficult to identify in the crowded and obscure Galactic plane.

Since it operates above 20 keV and is unhindered by absorption, ISGRI is discovering many new HMXBs and AGN that are intrinsically absorbed ($N_{\rm H} \sim 10^{22}$–10^{24} cm^{-2}). On average, Galactic IGRs are more absorbed (by a factor of ~4) than sources that were previously known.

Spin periods for most IGR pulsars are between a few hundred to a few thousand seconds or somewhat longer than the average spin periods of sources known before *INTEGRAL*. The distribution of orbital periods for IGRs closely resembles the bimodal distribution set by previously-known sources. The peaks correspond to 2 underlying populations: LMXBs and miscellaneous sources such as CVs and SNRs which tend to have short orbital periods, and HMXBs which have longer orbital periods, in general. Almost all IGRs for which both spin and orbital periods have been measured are located in the region of wind-fed accretion in the Corbet diagram. This is a testament to the number of new SG HMXBs that *INTEGRAL* has discovered.

Thanks to the larger sample size of these new SG HMXBs, we were able to test for dependences of the spin and orbital periods of HMXBs on the amount of absorbing matter local to the source. While scatter is an issue, there is a clear segregation of HMXBs in both plots which could be used to help assign Be or SG sompanions to sources that are still unclassified. There could be trends in both the $P_{\rm s}$–$N_{\rm H}$ and $P_{\rm o}$–$N_{\rm H}$ diagrams. The possible correlation of $P_{\rm s} \propto N_{\rm H}^{5/7}$ appears to contradict the expected slope ($-3/7$, e.g. (Corbet 1984)) which confirms that current spin periods are longer than the predicted equilibrium values, and that the spin-up of the pulsar via the wind is not as effective as the spin-down via the "propellor mechanism". The potential anti-correlation in the $P_{\rm o}$–$N_{\rm H}$ plot means that the average column density varies inversely with the distance between the objects as one would expect. However, intrinsic absorption values can change and the potential trends we see, rather than being due to physical processes that make the parameters interdependent, could simply be the result of 2 populations of sources occupying different parameter spaces, i.e. SG HMXBs are generally more absorbed, they spin slower, and they have shorter orbits than Be HMXBs. Nevertheless, given $N_{\rm H}$ and either $P_{\rm s}$ or $P_{\rm o}$ for a HMXB, improves the chances of correctly predicting the type of counterpart it has, compared with relying on only a single parameter. Of course, confirmation of the spectral type of the donor star in a HMXB still requires an optical/IR observation.

This work takes advantage of multi-wavelength observations in order to understand the nature of IGRs, and to help clarify the mechanisms that govern each type of source. Among the challenges facing more detailed population studies is the limited sample size of each subclass. This can only be alleviated by using large-FOV instruments such as *INTEGRAL* to search for new sources, and by regularly observing each new source in other wavelengths so that the accumulation of evidence rules out all but a single type of object. Many of the new sources which have been classified are absorbed HMXBs with supergiant companions. The increasing number of these systems discovered by *INTEGRAL* could alter our view of the Galactic population of hard X-ray sources and the evolutionary scenarios of their massive stellar companions.

Acknowledgements. The authors thank the anonymous referee for their prompt review of the paper. A.B. thanks S.E. Shaw, S. Paltani and M. Türler for their input and discussions. A.B. also thanks R. Walter for useful discussions on the Galactic distribution of HMXBs. J.R. warmly thanks P. Laurent, A. Goldwurm and C. Gouiffes for a careful reading of the manuscript and useful comments. This publication uses observations obtained with the ESA science mission *INTEGRAL*. The *INTEGRAL* instrument and data centres were directly funded by ESA member states and the USA (NASA). This research has made use of: the SIMBAD database operated at CDS, Strasbourg, France; NASA's Astrophysics Data System Bibliographic Services; data obtained from the High Energy Astrophysics Science Archive Research Center (HEASARC) provided by NASA's Goddard Space Flight Center.

References

Audley, M. D., Nagase, F., Mitsuda, K., Angelini, L., & Kelley, R. L. 2006, MNRAS, 367, 1147
Bassani, L., Molina, M., Malizia, A., et al. 2006, ApJ, 636, L65
Beckmann, V., Gehrels, N., Shrader, C. R., & Soldi, S. 2006a, ApJ, 638, 642
Beckmann, V., Soldi, S., Shrader, C. R., Gehrels, N., & Produit, N. 2006b, ApJ, 652, 126
Bird, A. J., Barlow, E. J., Bassani, L., et al. 2004, ApJ, 607, L33
Bird, A. J., Barlow, E. J., Bassani, L., et al. 2006, ApJ, 636, 765
Bird, A. J., Malizia, A., Bazzano, A., et al. 2007, ApJ, in press [arXiv:astro-ph/0611493]
Bissantz, N., Englmaier, P., & Gerhard, O. 2003, MNRAS, 340, 949
Bodaghee, A., Walter, R., Zurita Heras, J. A., et al. 2006, A&A, 447, 1027
Bronfman, L., Nyman, L.-A., & May, J. 1996, A&AS, 115, 81
Corbet, R. H. D. 1984, A&A, 141, 91
Courvoisier, T. J.-L., Walter, R., Rodriguez, J., Bouchet, L., & Lutovinov, A. A. 2003, IAU Circ., 8063, 3
Dean, A. J., Bazzano, A., Hill, A. B., et al. 2005, A&A, 443, 485
Dickey, J. M., & Lockman, F. J. 1990, ARA&A, 28, 215
Ebisawa, K., Bourban, G., Bodaghee, A., Mowlavi, N., & Courvoisier, T. J.-L. 2003, A&A, 411, L59
Forman, W., Jones, C., Cominsky, L., et al. 1978, ApJS, 38, 357
Galloway, D. K., Markwardt, C. B., Morgan, E. H., Chakrabarty, D., & Strohmayer, T. E. 2005, ApJ, 622, L45
Grimm, H.-J., Gilfanov, M., & Sunyaev, R. 2002, A&A, 391, 923
Illarionov, A. F., & Sunyaev, R. A. 1975, A&A, 39, 185
Jonker, P. G., & Nelemans, G. 2004, MNRAS, 354, 355
King, A. R. 1991, MNRAS, 250, 3P
Koyama, K., Kawada, M., Kunieda, H., Tawara, Y., & Takeuchi, Y. 1990, Nature, 343, 148
Kuulkers, E. 2005, in Interacting Binaries: Accretion, Evolution, and Outcomes, ed. L. Burderi, L. A. Antonelli, F. D'Antona, T. di Salvo, G. L. Israel, L. Piersanti, A. Tornambè, & O. Straniero, AIP Conf. Proc., 797, 402
Lamers, H. J. G. L. M., & Waters, L. B. F. M. 1987, A&A, 182, 80
Lebrun, F., Leray, J. P., Lavocat, P., et al. 2003, A&A, 411, L141
Lebrun, F., Terrier, R., Bazzano, A., et al. 2004, Nature, 428, 293
Lin, C. C., Yuan, C., & Shu, F. H. 1969, ApJ, 155, 721
Liu, Q. Z., van Paradijs, J., & van den Heuvel, E. P. J. 2000, A&AS, 147, 25
Liu, Q. Z., van Paradijs, J., & van den Heuvel, E. P. J. 2001, A&A, 368, 1021
Lutovinov, A., Revnivtsev, M., Gilfanov, M., et al. 2005, A&A, 444, 821
Masetti, N., Morelli, L., Palazzi, E., et al. 2006, A&A, 459, 21
Patel, S. K., Zurita, J., Del Santo, M., et al. 2006, ApJ, in press [arXiv:astro-ph/0610768]
Rodriguez, J., Bodaghee, A., Kaaret, P., et al. 2006, MNRAS, 366, 274
Rodriguez, J., Cabanac, C., Hannikainen, D. C., et al. 2005, A&A, 432, 235
Russeil, D. 2003, A&A, 397, 133
Sazonov, S., Revnivtsev, M., Krivonos, R., Churazov, E., & Sunyaev, R. 2007, A&A, 462, 57
Sguera, V., Barlow, E. J., Bird, A. J., et al. 2005, A&A, 444, 221
Stella, L., White, N. E., & Rosner, R. 1986, ApJ, 308, 669
Stephen, J. B., Bassani, L., Malizia, A., et al. 2006, A&A, 445, 869
Ubertini, P., Lebrun, F., Di Cocco, G., et al. 2003, A&A, 411, L131
Walter, R., Courvoisier, T. J.-L., Foschini, L., et al. 2004, in The INTEGRAL Universe. Proceedings of the Fifth INTEGRAL Workshop, 16–20 February 2004, Munich, Germany, ed. B. Battrick, Scientific ed. V. Schoenfelder, G. Lichti, & C. Winkler (Noordwijk: ESA Publication Division), ESA SP-552, 417
Walter, R., Zurita Heras, J., Bassani, L., et al. 2006, A&A, 453, 133
Waters, L. B. F. M., van den Heuvel, E. P. J., Taylor, A. R., Habets, G. M. H. J., & Persi, P. 1988, A&A, 198, 200
Waters, L. B. F. M., & van Kerkwijk, M. H. 1989, A&A, 223, 196
Wen, L., Levine, A. M., Corbet, R. H. D., & Bradt, H. V. 2006, ApJS, 163, 372
White, N. E., & van Paradijs, J. 1996, ApJ, 473, L25
Winkler, C., Courvoisier, T. J.-L., Di Cocco, G., et al. 2003, A&A, 411, L1
Zurita Heras, J. A., de Cesare, G., Walter, R., et al. 2006, A&A, 448, 261

Part V

Other Scientific Contributions

Chapter 16

Scientist On Duty

This chapter describes the continuous monitoring of *INTEGRAL* scientific and instrumental data as it received in the "barn" of the ISDC. The ISDC must constantly follow observations in real time and react to interesting or unusual events such as a gamma-ray burst (GRB), a new X-ray source, or an outburst from a known source. In such cases, the data are quickly analyzed and an announcement is sent to the community in the form of an Astronomer's Telegram (ATel) or a GCN alert. A quick reaction time is crucial in order to ensure that scientists worldwide can observe this short-lived event at other wavelengths thereby shedding light on the object's nature.

16.1 Data Monitoring

Data from the *INTEGRAL* satellite is collected and archived at the ISDC. Given the variability and transience of almost all X-ray sources, the raw data must be processed and analyzed soon after it is received. The monitoring of *INTEGRAL* data in the barn requires both a technical and a scientific component.

The technical monitoring is performed by the operators (P. Haymoz, L. Martins, P. de Meynis, and J. Soldan) who are responsible for the reception and processing of raw data through the various pipelines. They also verify that instrumental parameters such as temperatures and voltages are within acceptable ranges. When necessary, they contact the Mission Operations Center (MOC) or the Principal Investigators (PIs) of the instruments. Once the raw data have been successfully received and processed, they are forwarded to the Interactive Operation Status Monitoring (IOSM), the Interactive Quick Look Analysis (IQLA), and the *INTEGRAL* Burst Alert System (IBAS) which require additional scientific input.

The Scientist on Duty (Scody) monitors the scientific aspects of incoming data. One of the duties of every scientist at the ISDC is to serve as Scody during consecutive spacecraft revolutions (1 week). The recurrence period is roughly 1 shift every 2–3 months. Responsibilities of the Scody include:

- checking the quality of each image that is received;
- verifying the behavior of the sources in each image to make sure that such activity (either their presence, their absence, or their variability) is well known;
- reacting to alerts from IBAS of possible GRBs and Soft-Gamma Repeaters (SGRs) in the IBIS FOV;
- alerting the community in case of a GRB or a new source;
- designating triggers from the SPI Anti-Coincidence Sheild (ACS) as potential GRBs;
- monitoring the instrumental shadowgrams and count rates;
- generating light curves of all sources detected in a revolution and comparing them to historical light curves;
- creating mosaics upon completion of a revolution and checking these for new sources; and
- writing the scientific report at the end of the revolution.

The IOSM provides the Scody with the most recent shadowgrams from IBIS, PICSIT, and JEM-X, as well as the SPI detector plane, snapshots from the OMC, and particle count rates. The shadowgrams are converted into ScW images and analyzed by IQLA which is a slimmer version of the standard OSA package. The energy ranges of the images are 3–10 and 10–30 keV for JEM-X (1 or 2), and 20–60 and 60–200 keV for ISGRI. Any new source detected in an image, or a known source that is flaring, will trigger an alert that the Scody must react to.

In reality, IQLA monitoring is done for Near-Real Time (NRT) data since it takes roughly 3 hours between the time when the instruments capture the data and when the images appear on the screen. However, events like GRBs are only visible in the X and γ-rays for a few seconds to a few minutes. Therefore, IBAS works independently of IQLA and will trigger an alert for a GRB using real-time data rather than the delayed NRT data. This is essential so that multiwavelength follow-up observations of GRBs are possible.

16.2 Announcements

Before any external announcements are made in the event of a GRB, a new source, or a known source in outburst, procedures are in place to contact all relevant researchers. First, the Operations Coordinators (N. Mowlavi and S.E. Shaw) are briefed. With their approval, the PIs of the observation are contacted. It is then up to the PIs to decide what to do with information received during their private observations.

Five ATels and 1 GCN were sent based on observations realized and analyzed during my shifts (2003–2006).

ATel #241 *INTEGRAL confirms the brightening of 4U 1724−307*

Bodaghee A. (ISDC, Geneva), Westergaard N.-J. (DSRI, Copenhagen), Capitanio F. (IASF, Roma), McBreen B. (UC Dublin), Roques J.-P. (CESR, Toulouse), Kuulkers E. (ESTEC, Noordwijk), Molkov S. (IKI, Moscow), Palumbo G.G.C. (Universita di Bologna) February 19, 2004

During an observation of the Galactic Center Deep Exposure performed between February 17 (07:03 UTC) and February 18 (00:01 UTC), JEM-X on board INTEGRAL detected a bright source at position (J2000) R.A. = $17^h27^m34^s$ Dec. = $-30°47.9'$ ($1'$ uncertainty) corresponding to 4U 1724−307. The source varies between 50 and 100 mCrab on time scales of hours in both the 3–10 and 10–30 keV bands. Between 3 and 20 keV the photon index is 2.7±0.4 and the flux is F(3–20) = $8 \cdot 10^{-10}$ ergs cm^{-2} s^{-1}. This confirms the report by Markwardt et al (ATel #237).

ATel #248 *GX 339−4 detected with INTEGRAL*

Kuulkers E. (ESA/ESTEC), Bodaghee A. (ISDC Geneva), Foschini L. (IASF/CNR Bologna), Guainazzi M. (ESA/Vilspa), Matt G. (Universiy of Roma), Israel G. (INAF - OA Roma), Nicastro F. (CfA), Oosterbroek T. (ESA/ESTEC), Parmar A. (ESA/ESTEC), Rodriguez J. (CEA/Saclay & ISDC Geneva), Walter R. (ISDC Geneva); February 19, 2004

GX 339−4 was in the field of view during an observation of IGR J16318−4848 with INTEGRAL (UT 2004 Feb. 18 03:41 – Feb. 18 17:29). Further to the increase in activity reported in the optical/radio (ATel #230) and X-rays (ATel #231, #236), we report the detection of GX 339−4 with JEM-X and ISGRI/IBIS onboard INTEGRAL. Between 2004 Feb 18 03:41 – 10:09 (UT) the average observed fluxes were ~37 mCrab, ~46 mCrab, ~24 mCrab, and ~38 mCrab, in, respectively the 3–10 keV, 10–31 keV (JEM-X), 20–60 keV, and 60–200 keV (ISGRI/IBIS) energy bands.

ATel #290 *Burst in 1E 1145.1−6141*

Bodaghee A. (ISDC), Mowlavi N. (ISDC), Ballet J. (CEN-Saclay); June 12, 2004

We report the brightening of the high-mass X-ray binary 1E 1145.1−6141 by a factor of 4 in 20–60 keV between June 10 (00:00 UTC) and June 11 (09:30 UTC), reaching about 130 mCrab in this energy range. The burst was recorded by the ISGRI detector on board INTEGRAL during an open observation of the Carina region. To our knowledge, no such burst has been mentioned in the literature so far, as the source is believed to be a persistent and steady X-ray pulsar with a flux up to 20–30 mCrabs (Grebenev et al., 1992, see also Ray & Chakrabarty, 2002). No increase is detected by ISGRI in 60–200 keV. In the only pointing for which 1E 1145.1−6141 was in the JEM-X FOV (June 11, 03:30 UTC), the flux is about 40 mCrab in 3–10 keV. Further observations during the Carina open program on June 12th show a decrease of the flux below

100 mCrab. This would indicate that 1E 1145.1−6141 went into an episode of burst of about 2 days.

GCN #3003 *GRB 050129: a weak long GRB detected with INTEGRAL*

Gotz D., Mereghetti S. (IASF, Milano), Bodaghee A., Shaw S.E., Beck M. (ISDC, Versoix), Borkowski J. (CAMK, Torun) on behalf of the IBAS Localization Team; January 31, 2005

A 20 s long GRB has been detected by IBAS in IBIS/ISGRI data at 20:03:03 UT on Jan. 29. Due to its faintness no automatic IBAS Alert has been delivered. Its coordinates (J2000) are:

R.A. = 252.7998

Dec. = −3.0788

with an uncertainty of 2.7′ radius (90% confidence level).

Its peak flux (20–200 keV, 1-s integration time) is about 0.26 ph ($3 \cdot 10^{-8}$ ergs) $\mathrm{cm^{-2}\,s^{-1}}$, which classifies it among the faintest INTEGRAL GRBs.

ATel #452 *INTEGRAL detected Aql X-1 in hard X-rays*

Grebenev S.A. (IKI, Moscow), Belanger G. (SEA, Saclay), Bodaghee A. (ISDC, Versoix), Lund N. (DSRI, Copenhagen), Hermsen W. (SRON, Utrecht; UvA, Amsterdam), Parmar A. (ESA/ESTEC, Noordwijk), Roques J.-P. (CESR, Toulouse), Mas-Hesse M. (LAEFF, Madrid); April 5, 2005

INTEGRAL observed the region near Aql X-1 on April 1.825–1.924, 2005 (UT) during the Galactic plane scan. The IBIS/ISGRI telescope detected the source at the flux level of 54±3 and 64±8 mCrab in the 18–45 and 45–80 keV bands, respectively. The source was as well detected in the standard 3–20 keV X-ray band with JEM-X at the flux level of about 35 mCrab. The combined spectrum can be well described with a single power law with a photon index of 1.98±0.06 in the broad 3–100 keV band.

Further observations will show if it is a temporal reactivation of the source in hard X-rays (a “mini-outburst” similar to that observed in March 2004) or the real beginning of a new X-ray outburst as was suspected by Maitra and Bailyn (ATel #450) from their optical and infrared observations.

ATel #592 *INTEGRAL detects XTE J1739−285*

Bodaghee A., Mowlavi N. (ISDC, Geneva), Kuulkers E. (ESA/ESAC, Spain), Wijnands R. (UvA, Netherlands), Shaw S.E. (Southampton, UK & ISDC, Geneva), Courvoisier T.J.-L. (ISDC, Geneva), Markwardt C. (NASA/GSFC, USA), Oosterbroek T., Orr A. (ESA/ESTEC, Netherlands), Paizis A. (ISDC, Geneva & IASF, Milano), Ebisawa K. (NASA/GSFC, USA), Kretschmar P. (ESA/ESAC, Spain); August 26, 2005

The JEM-X telescope on board INTEGRAL detected the X-ray transient XTE J1739−285 while monitoring the Galactic Bulge in revolution 350. The source was detected in three successive pointings of 30 minutes each, starting on 2005-08-25T14:40 UTC. The fluxes in the 3–10 keV band were about

120, 70 and 77 mCrabs, respectively, and about 70, 30 and 40 mCrabs in the 10–20 keV band. The source was not detected above 20 keV by the ISGRI instrument, with an upper limit of 5 mCrabs.

The source position (J2000) derived by JEM-X is R.A. = $17^h40.0^m$ and Dec. = $-28°30'$ (2' accuracy), which is within the 5' accuracy of the position derived by RXTE in 1999 (IAUC 7300). The spectrum can be modeled with a power law with a photon index of 2.9±0.1, yielding a flux of $1.8 \cdot 10^{-9}$ ergs cm^{-2} s^{-1} in the 2–10 keV band. Follow-up observations at other wavelengths are encouraged.

Part VI

Conclusions

Chapter 17

Conclusions & Perspectives

In the soft γ-rays, *INTEGRAL* is the most sensitive imager and spectrometer ever designed. For 4 years it has captured spectacular pictures of a Universe teeming with objects in which the laws of physics are pushed to their limits. Even so, some of the sources discovered by *INTEGRAL* represent extreme cases. For example, the most absorbed X-ray binary is IGR J16318−4848, and the accreting pulsar with the shortest spin period is IGR J00291+5934.

While ISGRI is well adapted to detect these sources in the γ-rays, multi-wavelength observations are necessary to shed light on the nature of each object. Spectra taken below ISGRI's threshold of 20 keV can reveal absorption and line features which provide clues to the distribution of matter around the X-ray source. Coherent pulsations and QPOs are easier to detect in the soft X-rays. These modulations inform us of the way matter is accreted onto the CO. Since more photons are emitted at lower energies, an arcsecond position accuracy can be achieved in the soft X-rays, which enables a stellar counterpart to be identified in optical and infrared images.

The study of IGR J16393−4643 represents an example of how multi-wavelength analyses can be used to determine the object class. By combining hard X/γ-ray data from *INTEGRAL*, soft X-ray data from *XMM-Newton*, with infrared and radio data, we demonstrated that IGR J16393−4643 is a heavily-absorbed ($N_{\mathrm{H}} \gtrsim 10^{23}\,\mathrm{cm}^{-2}$) HMXB where the CO accretes the wind of its SG companion. Once believed to be a BHC, the CO is actually a NS that spins with a rather long period of 912 s. A soft excess emission, iron fluorescence lines at 6.4 and 7.1 keV, and a cutoff around 15 keV are spectral characteristics commonly found in wind-fed X-ray pulsars. The 4″ error circle from *XMM-Newton* eliminates the radio counterpart that helped justify the BHC. Only 1 infrared object from 2MASS remains as a counterpart candidate.

Multi-wavelength analyses were also performed for IGR J16320−4751, IGR J17252−3616, and IGR J17497−2821. The first 2 are similar to IGR J16393−4643 in that they are absorbed X-ray binaries consisting of a slowly-rotating NS embedded in and accreting from the radial wind of a SG companion. *INTEGRAL*, *RXTE*, and radio observations of IGR J17497−2821 suggest a BHC.

Well over a hundred sources have been discovered so far by *INTEGRAL*, and over 300 objects that were previously known have been detected. Generally, these sources are found by creating deep ($\gtrsim$500 ks) mosaic images of several hundred to a few thousand IBIS-ISGRI pointings each lasting a few ks. Two years after *INTEGRAL*'s launch, the IBIS Survey Team generated mosaic images of the Galactic Plane where the sensitivity in the 20–100 keV band was as low as ~1 mCrab with a position accuracy of only ~0.7 arcminutes. The high quality of these images was made possible in part by implementing an up-to-date input catalog of relevant sources with precise positions, and by addressing the systematic uncertainties that accumulate over long exposure times.

With so many sources, there is an obvious need to synthesize the important facts about each source as they are announced. Two of the tools that were developed were the ISDC General Reference Catalog which lists the most accurate positions known for all ~1500 sources that *INTEGRAL* is capable of detecting, and the IGR Sources Page which is a Web database and circular for parameters and references of IGR sources.

Each of the 499 sources detected by ISGRI were researched in the literature in order to collect references that could provide a source classification, a photoelectric absorption value (N_H) from a soft X-ray spectrum, pulsation and/or orbital periods, and distances or redshifts. The primary aims of this catalog were to gather in a single place the most important parameters of *INTEGRAL* sources and to use this large sample to determine where new sources fit in the parameter space established by previously-known high-energy sources, to test various theoretical predictions, and to search for possible trends in the data.

By operating above 20 keV, ISGRI is unhindered by absorption so it is discovering many new HMXBs and AGN with high column densities ($N_H \sim 10^{22}$–10^{24} cm^{-2}). On average, Galactic IGRs are more absorbed (by a factor of ~4) than sources that were previously known. Spin periods for most IGR pulsars are between a few hundred to a few thousand seconds or somewhat longer than the average spin periods of sources known before *INTEGRAL*. The large column densities and long pulsation periods are testaments to the number of new SG HMXBs that *INTEGRAL* has discovered.

Thanks to the larger sample size of these new OB HMXBs, we were able to test for dependences of the spin and orbital periods of HMXBs on the amount of absorbing matter local to the source. There could be trends in both the P_S–N_H and P_O–N_H diagrams. The trends, rather than being due to physical processes that make the parameters inter-dependent, could simply be the result of 2 populations of sources occupying different regions of the plot.

More importantly, the 2 main classes of HMXBs are segregated in the P_S–N_H and

P_O–N_H diagrams which could be used to help assign Be or OB sompanions to HMXBs that are still unclassified. Both IGR J16358−4726 and IGR J19140+0951 are HMXBs where the spectral types of the donor stars are unknown, but their positions in these plots suggest that they are likely to be OB HMXBs. Obviously, confirmation of the spectral type of the donor star in a HMXB requires an optical/IR observation. Once again, the multi-wavelength approach provides the best hope for clarifying the identity of a high-energy emitter.

Evolutionary signatures are witnessed throughout the various spatial projections of *INTEGRAL* sources. Clustered towards the spiral arm tangents and at low Galactic latitudes, HMXBs follow the distributions of tracers of star-forming regions. On the other hand, LMXBs are found predominantly in the Galactic bulge or have had time to migrate to high latitudes, typical of an older stellar population. The discrepancy is seen again in galactocentric profiles where the number of LMXBs gradually decreases from its maximum in the central kpcs, while HMXBs avoid the central kpcs and are overrepresented at the peaks of H II/CO distributions.

As in Lutovinov et al. (2005a) and Dean et al. (2005), the density maxima of HMXBs is slightly offset with respect to the inner spiral arm tangents. This has been interpreted as a lag between the epoch of star formation and the formation of HMXBs. However, the position of the tangents depends strongly on the Galactic model involved. Massive star-forming regions and HMXBs have distributions that are statistically compatible. Galactic rotation of the current complexes, in order to deduce the locations in the Galaxy that were active star-forming regions some 10 Myr ago (or when the current HMXBs were created), does not improve the compatibility.

Among the challenges facing more detailed population studies is the daunting number of unclassified sources. If the unclassified sources are composed primarily of LMXBs, as their spatial distributions and the transient emission of most them seem to suggest, then they remain unclassified because their faint optical/IR counterparts of such sources are difficult to identify in the crowded and obscure Galactic plane unless they are in outburst.

Classifying such sources requires a dedicated effort to follow new IGRs during their outburst with ToO observations with the full complement of high-energy space telescopes, combined with a systematic campaign to propose observations for known IGRs that lack observations at other wavelengths. As part of the an ongoing project to help identify IGRs, any new source detections in the coming year (fulfilling certain conditions) will immediately be followed by *RXTE* ToO observations supplemented by simultaneous coverage from *Swift*. Combined with a *Chandra* ToO (Paizis et al. 2007), this endeavor has helped to categorize the transient IGR J17497−2821 as a BHC in a LMXB. A *Chandra* proposal for 6 persistent IGRs which appeared in both catalogs of Bird et al. (2004) and Bird et al. (2006), and that lacked a follow-up observation at low energies, was rejected. However, a more ambitious proposal (over 25 sources) by our competitors was accepted. Our sources are likely to be among their group. The end result is that we will soon have access to new parameters from *Chandra* for a dozen or more IGR sources that are currently unclassified.

This thesis has afforded the opportunity to study almost all types of X/γ-ray objects, beginning shortly after the launch of a major mission, and during a time when high-energy astronomy is at its zenith. The scope has gone from the analysis of individual IGRs across a broad spectral range, to the general characteristics of the different populations of *INTEGRAL* sources. Hopefully, the fruits of this research will help us to better understand (and open new questions about) the different types of high-energy sources, in particular the origin and evolution of Galactic X-ray binaries, with a special emphasis on the growing class of SG absorbed X-ray pulsars and the possible interactions between material surrounding the X-ray source and modulations in its light curve.

Bibliography

Audley, M. D., Nagase, F., Mitsuda, K., Angelini, L., & Kelley, R. L. 2006, MNRAS, 367, 1147

Barlow, E. J., Knigge, C., Bird, A. J., et al. 2006, MNRAS, 372, 224

Bassani, L., Malizia, A., Stephen, J. B., et al. 2004, The Astronomer's Telegram, 232, 1

Beckmann, V., Gehrels, N., Shrader, C. R., & Soldi, S. 2006a, ApJ, 638, 642

Beckmann, V., Soldi, S., Shrader, C. R., Gehrels, N., & Produit, N. 2006b, ApJ, 652, 126

Bélanger, G., Goldwurm, A., Goldoni, P., et al. 2004, ApJL, 601, L163

Bica, E., Bonatto, C., Barbuy, B., & Ortolani, S. 2006, A&A, 450, 105

Bird, A. J., Barlow, E. J., Bassani, L., et al. 2006, ApJ, 636, 765

Bird, A. J., Barlow, E. J., Bassani, L., et al. 2004, ApJL, 607, L33

Bird, A. J., Malizia, A., Bazzano, A., et al. 2007, ApJS, 170, 175

Bodaghee, A., Courvoisier, T. J.-L., Rodriguez, J., et al. 2007, A&A, 467, 585

Bodaghee, A., Walter, R., Lund, N., & Rohlfs, R. 2004, in ESA SP-552: 5th INTEGRAL Workshop on the INTEGRAL Universe, ed. V. Schoenfelder, G. Lichti, & C. Winkler, 833–+

Bodaghee, A., Walter, R., Zurita Heras, J. A., et al. 2006, A&A, 447, 1027

Bronfman, L., Nyman, L.-A., & May, J. 1996, A&AS, 115, 81

Combi, J. A., Ribó, M., Mirabel, I. F., & Sugizaki, M. 2004, A&A, 422, 1031

Corbet, R., Barbier, L., Barthelmy, S., et al. 2005, The Astronomer's Telegram, 649, 1

Corbet, R. H. D. 1984, A&A, 141, 91

Corbet, R. H. D. 1986, MNRAS, 220, 1047

Courvoisier, T. J.-L., Walter, R., Beckmann, V., et al. 2003a, A&A, 411, L53

Courvoisier, T. J.-L., Walter, R., Rodriguez, J., Bouchet, L., & Lutovinov, A. A. 2003b, IAU Circ., 8063, 3

Cutri, R. M., Skrutskie, M. F., van Dyk, S., et al. 2003, VizieR Online Data Catalog, 2246, 0

Dean, A. J., Bazzano, A., Hill, A. B., et al. 2005, A&A, 443, 485

Di Cocco, G., Caroli, E., Celesti, E., et al. 2003, A&A, 411, L189

Dickey, J. M. & Lockman, F. J. 1990, ARA&A, 28, 215

Diehl, R., Halloin, H., Kretschmer, K., et al. 2006, Nature, 439, 45

Ebisawa, K., Bourban, G., Bodaghee, A., Mowlavi, N., & Courvoisier, T. J.-L. 2003, A&A, 411, L59

Ghosh, P. & Lamb, F. K. 1979, ApJ, 234, 296

Giacconi, R., Gursky, H., Paolini, F. R., & Rossi, B. B. 1962, Physical Review Letters, 9, 439

Grimm, H.-J., Gilfanov, M., & Sunyaev, R. 2002, A&A, 391, 923

Haberl, F. & White, N. E. 1990, ApJ, 361, 225

Hajdas, W., Bühler, P., Eggel, C., et al. 2003, A&A, 411, L43

Hartman, R. C., Bertsch, D. L., Bloom, S. D., et al. 1999, ApJS, 123, 79

Hickox, R. C., Narayan, R., & Kallman, T. R. 2004, ApJ, 614, 881

Horne, J. H. & Baliunas, S. L. 1986, ApJ, 302, 757

Illarionov, A. F. & Sunyaev, R. A. 1975, A&A, 39, 185

in ’t Zand, J. J. M., Ubertini, P., Capitanio, F., & Del Santo, M. 2003, IAU Circ., 8077, 2

Itoh, T., Kokubun, M., Yuasa, T., et al. 2006, The Astronomer’s Telegram, 914, 1

Jansen, F., Lumb, D., Altieri, B., et al. 2001, A&A, 365, L1

Jensen, P. L., Clausen, K., Cassi, C., et al. 2003, A&A, 411, L7

Kuulkers, E. 2005, in AIP Conf. Proc. 797: Interacting Binaries: Accretion, Evolution, and Outcomes, ed. L. Burderi, L. A. Antonelli, F. D’Antona, T. di Salvo, G. L. Israel, L. Piersanti, A. Tornambè, & O. Straniero, 402–409

Kuulkers, E., Chenevez, J., Shaw, S., et al. 2006, The Astronomer’s Telegram, 888, 1

Lebrun, F., Leray, J. P., Lavocat, P., et al. 2003, A&A, 411, L141

Lewin, W. H. G. & van der Klis, M. 2006, Compact stellar X-ray sources (Compact stellar X-ray sources)

Lund, N., Budtz-Jørgensen, C., Westergaard, N. J., et al. 2003, A&A, 411, L231

Lutovinov, A., Revnivtsev, M., Gilfanov, M., et al. 2005a, A&A, 444, 821

Lutovinov, A., Rodriguez, J., Revnivtsev, M., & Shtykovskiy, P. 2005b, A&A, 433, L41

Malizia, A., Bassani, L., di Cocco, G., et al. 2004, The Astronomer's Telegram, 227, 1

Mas-Hesse, J. M., Giménez, A., Culhane, J. L., et al. 2003, A&A, 411, L261

Matt, G. 2002, MNRAS, 337, 147

Monet, D. G., Levine, S. E., Canzian, B., et al. 2003, AJ, 125, 984

Much, R., Barr, P., Hansson, L., et al. 2003, A&A, 411, L49

Ochsenbein, F., Bauer, P., & Marcout, J. 2000, A&AS, 143, 23

Orellana, M. & Romero, G. E. 2005, Ap&SS, 297, 167

Paizis, A., Nowak, M. A., Chaty, S., et al. 2007, ApJL, 657, L109

Revnivtsev, M. G., Sunyaev, R. A., Varshalovich, D. A., et al. 2004, Astronomy Letters, 30, 382

Rodriguez, J., Bel, M. C., Tomsick, J. A., et al. 2007, ApJL, 655, L97

Rodriguez, J., Bodaghee, A., Kaaret, P., et al. 2006, MNRAS, 366, 274

Rodriguez, J., Tomsick, J. A., Foschini, L., et al. 2003, A&A, 407, L41

Russeil, D. 2003, A&A, 397, 133

Sakano, M., Koyama, K., Murakami, H., Maeda, Y., & Yamauchi, S. 2002, ApJS, 138, 19

Sguera, V., Bird, A. J., Dean, A. J., et al. 2006, The Astronomer's Telegram, 873, 1

Soldi, S., Walter, R., Eckert, D., et al. 2006, The Astronomer's Telegram, 885, 1

Strüder, L., Briel, U., Dennerl, K., et al. 2001, A&A, 365, L18

Sugizaki, M., Mitsuda, K., Kaneda, H., et al. 2001, ApJS, 134, 77

Sunyaev, R. & Revnivtsev, M. 2000, A&A, 358, 617

Takeuchi, Y., Koyama, K., & Warwick, R. S. 1990, PASJ, 42, 287

Tawara, Y., Yamauchi, S., Awaki, H., et al. 1989, PASJ, 41, 473

Thompson, T. W. J., Tomsick, J. A., Rothschild, R. E., in't Zand, J. J. M., & Walter, R. 2006, ApJ, 649, 373

Titarchuk, L. 1994, ApJ, 434, 570

Tomsick, J. A., Lingenfelter, R., Walter, R., et al. 2003, IAU Circ., 8076, 1

Turner, M. J. L., Abbey, A., Arnaud, M., et al. 2001, A&A, 365, L27

Ubertini, P., Lebrun, F., Di Cocco, G., et al. 2003, A&A, 411, L131

Vedrenne, G., Roques, J.-P., Schönfelder, V., et al. 2003, A&A, 411, L63

Voges, W., Aschenbach, B., Boller, T., et al. 1999, A&A, 349, 389

Walter, R., Bodaghee, A., Barlow, E. J., et al. 2004a, The Astronomer's Telegram, 229, 1

Walter, R., Courvoisier, T. J.-L., Foschini, L., et al. 2004b, in The INTEGRAL Universe. Proceedings of the Fifth INTEGRAL Workshop. 16-20 February 2004, Munich, Germany. Editor: B. Battrick, Scientific Editors: V. Schoenfelder, G. Lichti, & C. Winkler. ESA SP-552, Noordwijk: ESA Publication Division, ISBN 92-9092-863-8, 2004, p. 417-422., 417–422

Walter, R., Zurita Heras, J., Bassani, L., et al. 2006, A&A, 453, 133

Warwick, R. S., Norton, A. J., Turner, M. J. L., Watson, M. G., & Willingale, R. 1988, MNRAS, 232, 551

Waters, L. B. F. M. & van Kerkwijk, M. H. 1989, A&A, 223, 196

White, N. E., Nagase, F., & Parmar, A. N. 1995, X-ray binaries (Cambridge Astrophysics Series, Cambridge, MA: Cambridge University Press, |c1995, edited by Lewin, Walter H.G.; Van Paradijs, Jan; Van den Heuvel, Edward P.J.), 1–57

Winkler, C., Courvoisier, T. J.-L., Di Cocco, G., et al. 2003, A&A, 411, L1

Zurita Heras, J. A., de Cesare, G., Walter, R., et al. 2006, A&A, 448, 261

Chapter 18
Acknowledgments

This thesis was not an independent achievement. The scientific discourse does not allow much room for expressions of gratitude to those who provided the emotional and technical support that were necessary to produce this work. I would like to rectify that with the following declarations.

Thank you Isabelle for so many reasons that it would take at least another 4 years to list them all. Your years of waiting patiently as the wife of a perennial student are over: I am finally done with school! It's time for me to get a real job and let you "relax" for a while...

Thanks to our families who were supportive thoughout my academic career, whether I was preparing for medical school or shifting gears to graduate studies in astrophysics. Even if you claimed that you grasped only a fraction of what I described, you looked interested and it was apparent that I made you proud. Special thanks to Parvine Huguenin, and the Entezam, Dreifuss, and Nicollier families.

I can't thank Professor Thierry Courvoisier enough for providing this opportunity to me. I was given what every graduate student craves: resources and autonomy. If that weren't enough, the ISDC is an incredibly beautiful place to work, and the friendships that took root there will persist even if we are swept to different places.

Speaking of which, I sincerely thank Jerome Rodriguez for helping me overcome Benny Hill's chicanery, and just as importantly, for the fantastic skiing and so-called "GRB meetings." Thanks George "Norm" Wendt for *Lost*, "Honest" Simon Shaw for his betting scandals, and Dave"M-Budget" Willis for his constant stream of wit. Thanks for all the laughs and may we continue to have more.

I appreciate the jury members (Dr. Jacques Paul of CEA/Saclay, Prof. Georges Meynet of the Geneva Observatory, and Dr. Stéphane Paltani of the ISDC) accepting to oversee my thesis, expressing confidence in my work and for providing useful comments.

From the ISDC, I thank: Ada for her great attitude and the tip about an amazing and remote beach on Crete; Juan for his support that stretches back to my *el Presidente* days; Simona for listening to my rants without rolling her eyes and for making the best tiramisu ever; Dominique and Christel for our shared experiences; Bruce for understanding what it's like to be a liberal American patriot these days; Nicolas P. for helping out or having coffee any time I asked; Franca, Marie-Claude, Martine and Isabelle for their patience with me and their presence during tea; Nami for remaining completely serene when things heated up in the Barn; Mark, a fellow rice enthusiast, for his interest in my collection of weird movies; Patrick for the bike rides; Pavel for the lunch trips to the curry house; Marc for his tutoring of SuperMongo; Stéphane for his reaction to *Requiem for a Dream*; Ken for introducing me to INTEGRAL science; Volker for being the world's smartest and most gracious chauffeur; Daniel for proving that a systems manager can also be approachable; Ingo and Peter for the Software Beer Meetings; Linda, Mohamed, Philippe, Mathias, Reiner, Nicolas M., Masha, Sandrine, J.C., Pierre, Petr, Piotr, Sandrine, Osmi, Dirk, Carla and Marc A. for always saying hi every time our paths crossed.

Outside the ISDC, I thank Olivia, Leila, Isabelle P., Mona, Leona, Joey and Ben, Carol and Mike of Saddleback, Isabel, Eva and Yann, Céline and JF, Ioana, Iavor, Victor, Gerald, Pickwick's Pub, the softball team, the staff of the Red Cross at Ecogia, and everybody else that I've neglected to thank.

Part VII

Appendix

Appendix A
Software

There are 2 steps in the creation of the ISDC General Reference Catalog (GRC). The first step involves the Perl script `make_ascii_submit.pl` which requires 2 input files. The first is called `CAT_sources.txt` and has the format (1 source per line, parameters separated by ampersands):

NAME (most commonly used name)
RA (J2000 right ascension in hh mm ss)
DEC (J2000 declination in dd mm ss)
ALIAS (aliases and comments)
POSREF (position reference code from ADS)
TYPE (source classification)

The second is called `model_file.txt` which describe the source parameters in the following format (1 source per line with parameters separated by tabs or spaces):

"NAME" (must be the same as in `CAT_sources.txt`, in quotes, and spaces replaced by underscores)
SOURCE_ID (unique, unchangeable source identifier in the GRC)
ERROR (position error in degrees)
CLASS (HEASARC class code)
ISGRI_FLAG JEMX_FLAG SPI_FLAG PICSIT_FLAG (instrument detection flags: 1≡detected, 0≡not detected)
PULSE PUER1 PUER2 PUREF (spin period [s], lower and upper uncertainties, and reference code from ADS)
ORBIT ORER1 ORER2 ORREF (orbital period [d], lower and upper uncertainties, and reference code from ADS)
DIST DIER1 DIER2 DIREF (distance or redshift, lower and upper uncertainties, and reference code from ADS)
NHER1 NHER2 NHREF NHGAL (lower and upper uncertainty on absorption [10^{22} cm^{-2}], reference code from ADS, and N_H from Dickey & Lockman (1990))
SOFT SFER HARD HDER SIG EXP (20–40 and 40–80 keV fluxes and errors, significance, and exposure time from Bird et al. (2007))
MODEL NH GAMMA1 (ECUT/EFOLD GAMMA2) NORM (SED model and

parameters in XSPEC format)

Before running, the latest RMF and ARF files must be set in the parameter file `make_ascii_submit.par` (N.B.: for ISGRI, the penultimate version of the RMF should be used since its spectral binning is finer than in the latest one).

Three output files are produced by `make_ascii_submit.pl`: `catalog.tex`, `catalog.html` and `catalog.ascii` which are the TEX, HTML and ASCII versions of the catalog, respectively.

The second step in the creation of the GRC invokes the C-language script `make_isdc_cat.c`. This code creates the FITS version of the catalog that is used in QLA and in OSA. This contributed script is an officially-delivered ISDC software suite so it is rigorously tested across different computing platforms. The idea is to enable anyone to create a catalog.

The ASCII file `catalog.ascii` that was created by `make_ascii_submit.pl` is 1 of 2 input files of `make_isdc_cat.c`. The second input file (`comments.txt`) simply lists the changes since the last release. It is automatically inserted at the end of the FITS header.

A schematic view of the main steps is shown below:

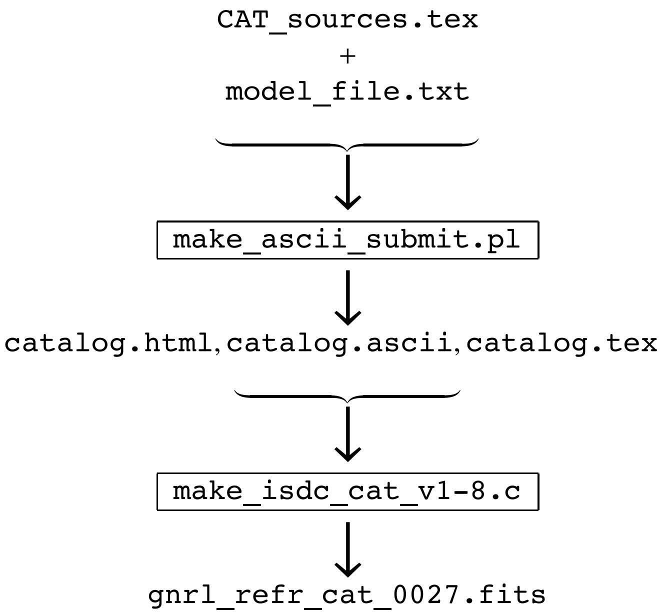

Appendix B
Publications

2003

- Ebisawa K., Bourban G., Bodaghee A., Mowlavi N., Courvoisier T.J.-L., 2003, *High-energy sources before INTEGRAL: The INTEGRAL Reference Catalog*, A&A, Vol. 411, pp. 59–62

2004

- Malizia A., Bassani L., Di Cocco G., Stephen J.B., Walter R., Bodaghee A., Bazzano A., 2004, *IGR J16393−4643 a possible X-ray counterpart to 3EG J1639−4702 discovered by INTEGRAL*, ATel #227
- Walter R., Bodaghee A., Barlow E.J., Bird A.J., Dean A.J., Hill A.B., Shaw S.E., Bazzano A., Ubertini P., Bassani L., Malizia A., Stephen J.B., Bélanger G., Lebrun F., Terrier R., 2004, *14 New Unidentified INTEGRAL Sources*, ATel #229
- Bassani L., Malizia A., Stephen J.B., Bazzano A., Ubertini P., Barlow E.J., Bird A.J., Dean A.J., Hill A.B., Shaw S.E., Walter R., Bodaghee A., Bélanger G., Lebrun F., Terrier R., Much R., 2004, *17 New Identified INTEGRAL Sources*, ATel #232
- Bodaghee A., Foschini L., Guainazzi M., Matt G., Israel G., Nicastro F., Oosterbroek T., Parmar A.N., Rodriguez J., Walter R., 2004, *GX 339-4 detected with INTEGRAL*, ATel #240
- Bodaghee A., Westergaard N.J., McBreen B., Roques J.-P., Kuulkers E., Molkov S., Pulumbo G.G.C., 2004, *INTEGRAL confirms the brightening of 4U 1724-307*, ATel #241
- Bodaghee A., Mowlavi N., Ballet J., 2004, *Burst in 1E 1145.1-6141*, ATel #290
- Bird A.J., Barlow E.J., Bassani L., Bazzano A., Bodaghee A., Capitanio F., Cocchi M., Del Santo M., Dean A.J., Hill A.B., Lebrun F., Malaguti G., Malizia A., Much R., Shaw S.E., Stephen J.B., Terrier R., Ubertini P., Walter R.,

2004, *The first IBIS/ISGRI soft gamma-ray galactic plane survey catalog*, The Astrophysical Journal, Vol. 607-1, pp. 33–37

- Walter R., Bird A.J., Bodaghee A., Lebrun F., Lund N., Ubertini P., Westergaard N.J., 2004, *The INTEGRAL Milky Way*, Proceedings of the 5th INTEGRAL Workshop, ESA-SP 552, pp. 525–528

- Bodaghee A., Walter R., Lund N., Rohlfs R., 2004, *Systematics of ISGRI and JEM-X mosaic images*, Proceedings of the 5th INTEGRAL Workshop, ESA-SP 552, pp. 833–836

- Shaw S.E., Mowlavi N., Ebisawa K., Paizis A., Rodriguez J., Zurita Heras J.A., Walter R., Türler M., Soldan J., Sauvageon A., Produit N., Pottschmidt K., Meynis P., Martins L., Lerusse L., Kreykenbohm I., Kretschmar P., Haymoz P., Favre P., Dubath P., Deluit S., Courvoisier T.J.-L., Chernyakova M., Bodaghee A., Beckmann V., 2004, *Scientific Performance of the ISDC Quick Look Analysis*, Proceedings of the 5th INTEGRAL Workshop, ESA-SP 552, pp. 897–890

- Lund N., Westergaard N.J., Budtz-Jorgensen C., Chenevez J., Brandt S., Walter R., Kretschmar P., Bodaghee A., 2004, *Obscured galactic X-ray sources*, Proceedings of the 5th INTEGRAL Workshop, ESA-SP 552

2005

- Gotz D., Mereghetti S., Bodaghee A., S.E. Shaw, M. Beck, J. Borkowski on behalf of the IBAS Localization Team, 2005, *GRB 050129: a weak long GRB detected with INTEGRAL*, GCN 3003

- Grebenev S.A., Bélanger G., Bodaghee A., Lund N., Hermsen W., Parmar A.N., Roques J.-P., Mas-Hesse J.M., 2005, *INTEGRAL detected Aql X-1 in hard X-rays*, ATel #452

- Bodaghee A., Mowlavi N., Kuulkers K., Wijnands R., Shaw S.E., Courvoisier T.J.-L., Markwardt C., Oosterbroek T., Orr A., Paizis A., Ebisawa K., Kretschmar P., 2005, *INTEGRAL detects XTE J1739-285*, ATel #592

2006

- Bird A.J., Barlow E.J., Bassani L., Bazzano A., Bélanger G., Bodaghee A., Capitanio F., Dean A.J., Hill A.B., Lebrun F., Malizia A., Mas-Hesse J.M., Molina M., Moran L., Renaud M., Sguera V., Shaw S.E., Stephen J.B., Terrier R., Ubertini P., Walter R., Willis D.R., Winkler C., 2006, *The 2nd IBIS/ISGRI soft gamma-ray survey catalog*, The Astrophysical Journal, Vol. 636-2, pp. 765–776

- Bodaghee A., Walter R., Zurita Heras J.A., Bird A.J., Courvoisier T.J.-L., Malizia A., Terrier R., Ubertini P., 2006, *IGR J16393−4643: a new heavily-obscured X-ray pulsar*, A&A, Vol. 447-3, pp. 1027–1034, also in: Proceedings of the "The X-ray Universe 2005", ESA-SP 6048, pp. 345-346

- Zurita Heras J.A., de Cesare G., Walter R., Bodaghee A., Bélanger G., Courvoisier T.J.-L., Shaw S.E., Stephen J.B., 2006, *IGR J17252−3616: an accreting pulsar observed by INTEGRAL and XMM-Newton*, A&A, Vol. 448-1, pp. 261–270, also in: Proceedings of the "The X-ray Universe 2005", ESA-SP 6048, pp. 315-316

- Rodriguez J., Bodaghee A., Kaaret P., Tomsick J.A., Kuulkers E., Malaguti G., Petrucci P.-O., Cabanac C., Chernyakova M., Corbel S., Deluit S., Di Cocco G., Ebisawa K., Goldwurm A., Henri G., Lebrun F., Paizis A., Walter R., Foschini L., 2006, *INTEGRAL and XMM-Newton observations of the X-ray pulsar IGR J16320−4751/AX J1631.9−4752*, MNRAS, Vol. 366-1, pp. 274–282

- Walter R., Zurita Heras J.A., Bassani L., Bazzano A., Bodaghee A., Dean A.J., Dubath P., Parmar A.N., Renaud M., Ubertini P., 2006, *XMM-Newton and INTEGRAL observations of new absorbed supergiant high-mass X-ray binaries*, A&A, Vol. 453-1, pp. 133–143

2007

- Rodriguez J., Cadolle Bel M., Tomsick J.A., Corbel S., Brocksopp C., Paizis A., Shaw S.E., Bodaghee A., 2007, *The discovery outburst of the X-ray transient IGR J17497−2821 observed with RXTE and ATCA* ApJL, Vol. 655, pp. 97–100

- Bodaghee A., Courvoisier T.J.-L., Rodriguez J., Beckmann V., Produit N., Hannikainen D., Kuulkers E., Willis D.R., Wendt G., 2007, *A description of the parameters of sources detected by INTEGRAL in the first 4 years of observations* A&A, Vol. 467-2, pp. 585–596, also in: Proceedings of the 6th INTEGRAL Workshop, in press

Appendix C
Glossary

- *A* Atoll Source
- *AGN* Active Galactic Nucleus/Nuclei
- *AO* Announcement of Opportunity
- *ATel* Astronomer's Telegram
- *AXP* Anomalous X-ray Pulsar
- *AU* Astronomical Unit
- *Be* B Emission-line Star
- *BH* Black Hole
- *BHC* Black Hole Candidate
- *CO* Compact Object
- *CP* Core Program
- *CV* Cataclysmic Variable: IP ≡ Intermediate Polar
- *DN* Dwarf Nova
- *E* Eclipsing
- *EPIC* European Photon Imaging Camera
- *FCFOV* Fully-Coded Field Of View
- *FITS* Flexible Image Transport System
- *FOV* Field Of View
- *FTOOLS* FITS-based software utilities
- *FWHM* Full Width at Half Maximum
- *GCDE* Galactic Center Deep Exposure

- *GCN* Gamma-ray Coordinates Network
- *GP* General Program
- *GPS* Galactic Plane Scan
- *GRB* Gamma-Ray Burst
- *GRC* ISDC General Reference Catalog
- *GRS* Gamma-Ray Source
- *GS* Ground Segment
- *GUI* Graphical User Interface
- *HMXB* High Mass X-ray Binary
- *IAUC* International Astronomical Union Circulars
- *IBAS INTEGRAL* Burst Alert System
- *IBIS* Imager on Board *INTEGRAL* Satellite
- *INTEGRAL* INTErnational Gamma-Ray Astrophysics Laboratory
- *IOSM* Interactive Operations Status Monitoring
- *IQLA* Interactive Quick Look Analysis
- *IREM INTEGRAL* Radiation Environment Monitor
- *ISGRI INTEGRAL* Soft Gamma-Ray Imager
- *ISDC INTEGRAL* Science Data Center
- *ISOC INTEGRAL* Science Operations Center
- *ISWT INTEGRAL* Science Working Team
- *JEM-X* Joint European Monitor for X-rays
- *KP* Key Program
- *LMC* Large Magellanic Cloud
- *LMXB* Low Mass X-ray Binary
- *MOC* Mission Operations Center
- *MS* Main Sequence
- *muQSO* Micro-Quasar
- *NRT* Near Real Time
- *OSA* Off-line Scientific Analysis

- *OG* Observation Group
- *OMC* Optical Monitoring Camera
- *OSA* Offline Science Analysis
- *PCFOV* Partially-Coded Field Of View
- *PI* Principal Investigator
- *PICsIT* Pixellated Imaging Cesium-Iodide Telescope
- *PWN* Pulsar Wind Nebula
- *QLA* Quick Look Analysis
- *QSO* Quasi-Stellar Object or Quasar
- *RL* Roche Lobe
- *RLO* Roche-Lobe Overflow
- *RXTE* Rossi X-ray Timing Explorer
- *SC* Spacecraft
- *Scody* Scientist On Duty
- *ScW* Science Window
- *SMC* Small Magellanic Cloud
- *SFXT* Supergiant Fast X-ray Transient
- *SG* Supergiant (O or B-type) Star
- *SGR* Soft Gamma Repeater
- *SNR* Supernova Remnant
- *SPI* Spectrometer on board *INTEGRAL* satellite
- *SW* Software
- *TAC* Time Allocation Committee
- *ToO* Target of Opportunity
- *XMM* X-ray Multi-Mirror space telescope
- *XRB* X-ray Binary
- *WD* White Dwarf

Figures

Tables